Magmatic Processes at Various Scales in the Lower Oceanic Crust of the Samail Ophiolite (Sultanate of Oman)

Von der Naturwissenschaftlichen Fakultät der
Gottfried Wilhelm Leibniz Universität Hannover

zur Erlangung des Grades
Doktor der Naturwissenschaften
(Dr. rer. nat.)

genehmigte Dissertation

von

Dominik Mock, M. Sc.

2021

Referent: apl. Prof. Dr. rer. nat. Jürgen Koepke

Korreferent: Benoît Ildefonse, Directeur de Recherche
Korreferentin: Prof. Dr. Ambre Luguet

Tag der Promotion: 07.12.2021

Magmatic Processes at Various Scales in the Lower Oceanic Crust of the Samail Ophiolite (Sultanate of Oman)

**Présentée par Dominik MOCK
Le 07 décembre 2021**

**Sous la direction de Benoît ILDEFONSE
et Jürgen KOEPKE**

Devant le jury composé de

Ambre LUGUET, Prof. Dr., Rheinische Friedrich-Wilhelms-Universität Bonn	Rapporteur
Mike CHEADLE, Prof. Dr., University of Wyoming	Rapporteur
Marguerite GODARD, Directeur de Recherche, Université de Montpellier	Examinateur
Jutta WINSEMANN, Prof. Dr., Leibniz Universität Hannover	Examinateur, Président du jury
Benoît ILDEFONSE, Directeur de Recherche, Université Montpellier	Directeur de thèse
Jürgen KOEPKE, Prof. Dr., Leibniz Universität Hannover	Directeur de thèse
François HOLTZ, Prof. Dr., Leibniz Universität Hannover	Invité

UNIVERSITÉ DE MONTPELLIER

Acknowledgments

Abstract

Oceanic crust covers more than two thirds of the Earth's surface and mid-ocean ridges, where it is formed, are the most important zones for mass and energy exchange between litho-, bio-, and hydrosphere on our planet. Nonetheless, mid-ocean ridges are still widely mysterious and our knowledge on magmatic processes taking place beneath them is very limited. A detailed knowledge on those processes is essential to understand the formation of lower oceanic crust and, thereby, its role in the System Earth. Two end-member models of crustal accretion are competing: (1) the gabbro glacier model explains crustal accretion from a subsiding crystal mush of the cumulates from the axial melt lens and (2) the sheeted sill model suggests that the lower crust is accreted by in-situ crystallizing melt sills within the lower crust. The Samail ophiolite in the Sultanate of Oman is regarded as ancient oceanic lithosphere formed at a fast-spreading ridge. With its coherent stratigraphy covering the upper mantle, the layered, foliated, and varitextured gabbros, as well as the sheeted dykes and the pillow basalts (from base to top), Wadi Gideah in the Samail ophiolite provides an ideal field laboratory for investigating ancient oceanic crust.

A profile crossing the entire gabbroic section from the axial melt lens at 5000 m above the base of the Moho transition zone (maM) down to the crust/mantle transition in Wadi Gideah was analyzed with a focus on the microstructural features of the lower crust. The variations in grain size and in fabric strength and symmetry with depth were interpreted as indicators for a hybrid accretion model, where the upper third of the gabbroic crust accretes by vertical magmatic flow either from the axial melt lens down- or from the underlying crystal mush upward and the lower two thirds of the crust crystallized in-situ. Vertical flow is indicated by steep foliations observed in the field and accompanied by a significant lineation component that disappears at 3500 maM. Beneath this horizon, the fabric strength and the degree of lineation gradually increase down section indicating magmatic deformation of previously emplaced crystal mush by the underlying convecting mantle.

Two approximately 400 m long drill cores were obtained in the lower crust of Wadi Gideah: GT1A covering an interval from 1173 down to 815 maM and GT2A covering the transition from the foliated to the layered gabbros at 2695 down to 2300 maM. GT1A was sampled with a high spatial resolution of about 2 m on average (16 m maximum) and petrological, geochemical, and microstructural tools were applied for detailed investigations. Indicators of fractional crystallization and melt evolution at depth were documented, indicating that in-situ crystallization has formed the layered gabbro section as proposed from the surface profile. Parallel variations in the phase compositions and their fabric symmetry were observed in both drill cores which could result from changes in physical properties (e.g., viscosity) of a melt with chemical evolution, thereby, also affecting deformation mechanisms. Local core/rim zonation in clinopyroxene and an increased lineation of plagioclase and clinopyroxene crystals indicate porous melt flow in a narrow horizon of drill core GT1A.

Igneous layering is a ubiquitous feature of the lower oceanic crust at fast-spreading mid-ocean ridges and two types were investigated: decimeter scale gradual modal layering from Wadi Somerah and modal layering pronounced by millimeter scale bands being enriched in olivine from Wadi Wariyah. The formation of the former can be explained by crystal-laden density currents slumping from the inclined wall of a melt sill leading to density-controlled phase segregation. The latter is most consistent with the formation by Liesegang banding where the diffusion of elements from the melt toward a crystallization front is not able to keep pace with the cooling of the magma, thus, these elements are supersaturated at a certain distance from the crystallization front leading to the formation of a new crystal band. The preferred growth of larger grains on the expense of smaller ones and shearing of the lower crust by mantle convection might emphasize initial heterogeneities to well-developed modal layering.

Zusammenfassung

Ozeanische Kruste bedeckt über zwei Drittel der Erdoberfläche und Mittelozeanische Rücken, an denen sie gebildet wird, sind die weltweit wichtigsten Austauschzonen von Masse und Energie zwischen Litho-, Bio- und Hydrosphäre. Dennoch sind Mittelozeanische Rücken wenig erforscht und unser Verständnis der magmatischen Prozesse, die unter ihnen stattfinden, ist eingeschränkt. Detailliertes Wissen über diese Prozesse ist essenziell, um die Bildung unterer ozeanischer Kruste, und damit deren Rolle im System Erde, zu erfassen. Zwei Modelle zur Krustenakkretion existieren: (1) das *gabbro glacier model* erklärt die Akkretion unterer Kruste durch einen abwärtsgleitenden Kristallbrei aus dem Kumulat der axialen Schmelzlinse. (2) das *sheeted sill model* erklärt die Akkretion der unteren Kruste durch in-situ-Kristallisation. Der Samail Ophiolith im Sultanat Oman wird als ehemalige ozeanische Kruste angesehen, die an einem schnellspreizenden Rücken gebildet wurde. Mit seiner kohärenten Stratigraphie, die den oberen Mantel, die lagigen, foliierten und variabel texturierten Gabbros, sowie die sheeted dykes und die Kissenlaven abdeckt (von unten nach oben), bildet das Wadi Gideah im Samail Ophiolith ein ideales Feldlabor zur Untersuchung unterer ozeanischer Kruste.

Ein Profil, das die gesamten Gabbros von der axialen Schmelzlinse bei 5000 m über der Moho-Übergangszone (maM) bis hinab zur Kruste/Mantel-Zone in Wadi Gideah abdeckt, wurde mit Fokus auf die Mikrostrukturen der unteren Kruste analysiert. Die Tiefenänderung in Korngröße und Gefügeausprägung und –symmetrie werden als Indikatoren eines hybriden Akkretionsmodells interpretiert, in dem das obere Drittel der gabbroiden Kruste aus einem vertikalen magmatischen Fluss entweder aus der axialen Schmelzlinse oder aus dem darunterliegenden Kristallbrei gebildet wird und die unteren zwei Drittel der Kruste in-situ kristallisiert sind. Vertikale Schmelzbewegung wird durch steile Foliationen, die von deutlicher Lineation begleitet werden, suggeriert. Letztere verschwindet bei 3500 maM. Darunter verstärken sich Gefüge und seine Symmetrie graduell, was auf magmatische Deformation des Kristallbreis durch Konvektion des darunterliegenden Mantels hindeutet.

Zwei annähernd 400 m lange Bohrkerne wurden im Wadi Gideah genommen: GT1A deckt ein Intervall zwischen 1173 und 815 maM ab, GT2A deckt die Übergangszone von lagigen zu foliierten Gabbros von 2695 bis hinab auf 2300 maM ab. GT1A wurde mit hoher räumlicher Auflösung von durchschnittlich etwa 2 m (maximal 16 m) beprobt und petrologisch, geochemisch sowie mikrostrukturell untersucht. Es wurden Hinweise auf fraktionierte Kristallisation und Schmelzentwicklung in der Tiefe dokumentiert, die zeigen, dass die lagigen Gabbros in-situ kristallisierten, wie aus dem Oberflächen-Profil abgeleitet. Parallele Variationen in Mineralchemismus und -gefüge wurden in beiden Bohrkernen beobachtet und könnten durch Änderungen der physikalischen Eigenschaften einer Schmelze (z.B. Viskosität), einhergehend mit Änderungen im Chemismus, erklärt werden. Lokale Zonierung im Klinopyroxen und stärkere Lineation von Plagioklas und Klinopyroxen deuten auf porösen Schmelzfluss in einem schmalen Bereich von GT1A hin.

Magmatische Lagen sind eine allgegenwärtige Eigenschaft schnellspreizender unterer ozeanischer Kruste und es wurden zwei Typen untersucht: graduelle Änderungen des Modalbestands im Dezimetermaßstab in Wadi Somerah und modale Lagenbildung durch olivinreiche Bänder im Millimetermaßstab in Wadi Wariyah. Die Bildung des ersteren kann durch das Abrutschen kristallgeladener Magmenströme von den Wänden einer Schmelzlinse erklärt werden, das eine dichtegetriebene Phasentrennung verursacht. Letzteres lässt sich am besten durch Liesegang-Bänderung erklären, bei der es durch Verlangsamung von Diffusion bei einer gewissen Distanz von der Kristallisationsfront zu Übersättigung mineralbildender Elemente kommt, die dort zu einem neuen Kristallband kristallisieren. Das bevorzugte Wachstum großer Kristalle auf Kosten von kleineren sowie Scherung der unteren Kruste durch Mantelkonvektion kann ursprüngliche Heterogenitäten im Modalbestand zu stark ausgeprägten Lagen weiterentwickeln.

Résumé

La croûte océanique couvre plus des deux tiers de la surface de la Terre et se forme au niveau des dorsales médio-océaniques qui représentent des zones importantes pour les échanges de masse et d'énergie entre la litho-, la bio- et l'hydrosphère de notre planète. Néanmoins, les processus magmatiques qui s'y déroulent restent encore un mystère et les connaissances à ce sujet sont limitées. Pourtant, une connaissance détaillée de ces processus est essentielle pour comprendre la formation de la croûte océanique inférieure et, par conséquent, son rôle dans le système Terre. Deux modèles d'accrétion crustale sont en compétition : (1) le « *gabbro glacier model* » explique l'accrétion crustale par la subsidence d'une bouillie cristalline associée à un cumulat provenant de la lentille de fusion axiale et (2) le « *sheeted sill model* » suggère que l'accrétion crustale résulte de la cristallisation *in-situ* du magma sous forme de sills au sein de la croûte inférieure. L'ophiolite de Samail située dans le Sultanat d'Oman est considérée comme une ancienne lithosphère océanique formée sur une dorsale à propagation rapide. Le Wadi Gideah, présentant une stratigraphie cohérente couvrant l'ensemble des lithologies d'une croute océanique ancienne, constitue une laboratoire idéal pour cette étude.

Un profil traversant toute la section gabbroïque, allant de la lentille de fusion axiale située à 5000 m au-dessus de la base de la zone de transition du Moho (maM) jusqu'à la transition croûte/manteau dans le Wadi Gideah, a été analysé en mettant l'accent sur les caractéristiques microstructurales. Les variations en termes de taille de grain, d'intensité de la déformation (fabrique)et de symétrie avec la profondeur ont été interprétées comme indicateurs d'un modèle d'accrétion hybride. Marqué par une foliation sub-verticale et une importante linéation, le tier supérieur de la croûte gabbroïque s'accrète par écoulement magmatique vertical, soit vers le bas à partir de la lentille de fusion axiale, soit vers le haut, à partir du « crystal mush ». La linéation marquée dans le premier tier disparait à 3500 maM. Les deux tiers inférieurs cristallisent in-situ et l'intensification progressive de la déformation sous l'horizon 3500 maM, indique que le « crystal mush » préexistant subit une déformation au stade magmatique par le manteau convectif sous-jacent.

Deux carottes de forage d'environ 400 m de long ont été obtenues dans la croûte inférieure du Wadi Gideah: GT1A couvrant un intervalle de 1173 à 815 maM et GT2A couvrant la transition des gabbros foliés à lités de 2695 jusqu'à 2300 maM. GT1A a été échantillonné avec une haute résolution spatiale d'environ 2 m (16 m maximum) et étudié à l'aide d'outils pétrologiques, géochimiques et microstructuraux. Des indicateurs de cristallisation fractionnée et d'évolution du magma en profondeur ont été documentés, indiquant que les grabbros lités résultent d'une cristallisation *in-situ* tel que proposé à partir du profil de surface. L'évolution de la composition des phases et de l'intensité et la symétrie de la défomation est similaire dans les deux carottes ce qui pourraient résulter de changements dans les propriétés physiques (p. ex. la viscosité) d'un magma évoluant chimiquement e masse fondue avec une évolution chimique, affectant ainsi également les mécanismes de déformation. La zonation locale cœur/bordure dans le clinopyroxène et une linéation croissante des cristaux de plagioclase et de clinopyroxène indiquent un écoulement du magma dans un milieu poreux au niveau d'un horizon étroit de la carotte de forage GT1A.

La stratification ignée est une caractéristique omniprésente de la croûte océanique inférieure au niveau des dorsales médio-océaniques à propagation rapide et deux types ont été étudiés : la stratification modale progressive à l'échelle décimétrique du Wadi Somerah et la stratification modale prononcée par des bandes à l'échelle millimétrique enrichies en olivine du Wadi Wariyah. La formation du premier peut s'expliquer par des courants de densité chargés de cristaux s'effondrant de la paroi inclinée d'un sill conduisant à une ségrégation de phase par densité. Le second est plus cohérent avec du « Liesegang banding », où la diffusion des éléments depuis le magma (ou la zone fondue ?)vers un front de cristallisation n'est pas en mesure de suivre la vitesse de refroidissement du magma. Ces

éléments sont ainsi sursaturés à une certaine distance du front de cristallisation conduisant à la formation d'une nouvelle bande cristalline. La croissance préférentielledes gros grains au détriment des plus petits et le cisaillement de la croûte inférieure par convection du manteau pourraient accentuer les hétérogénéités présentes initialement pour arriver à une stratification modale bien développée.

Content

1   Introduction

Two thirds of Earth's surface are still mysterious and not well understood. Covered by thousands of meters of sea water, oceanic crust escapes from geological field studies as they were performed on every continent during the past centuries. Nowadays, after several space missions and by the application of extraordinary telescopes, there are extraterrestrial bodies which are described and understood in more detail than the outermost few kilometers of the solid Earth beneath the oceans. By developing ocean drilling programs, seismic, gravimetric, and magnetic tools, earth scientists described the properties of oceanic crust in many details. However, a fundamental understanding of how oceanic crust accretes and which magmatic, hydrothermal, and tectonic processes play a role during crustal formation is still missing.

Ophiolites – complexes of more or less intact oceanic crust obducted on land – provide insights into oceanic crust and allow its sampling without diving through a water column of several hundred or thousand meters. However, erosion and weathering lead to an underrepresentation of weathering-sensitive lithologies and sampling outcrops in the field may result in incoherent sample suites. Obtaining and describing coherent sections of oceanic crust by drilling into the Samail ophiolite in the Sultanate of Oman, the largest and best-preserved ophiolite complex in the world (e.g., Nicolas et al., 1988), is therefore the main goal of the international Oman Drilling Project (OmanDP).

This thesis presents a compilation of both surface samples covering an entire lower crustal profile and drilled samples from two 400 m long drill cores obtained in the Samail ophiolite, providing insights from the km- down to the mm-scale. The applied multi-methodical approach combines petrographic, petrological, geochemical, and microstructural tools and therefore provides insights into both mechanical and chemical processes that have occurred during the accretion of lower oceanic crust. Although the results of this thesis are on the first order representative for the sampled areas, the similarity of the rocks analyzed to those from other locations of oceanic crust around the world indicates that the conclusions drawn by this study might also be applicable to a wide range of both ancient and recent oceanic crust on Earth.

1.1   Oceanic crust

1.1.1   Importance for mass and energy exchange on Earth

The Earth's surface is covered by oceans to an extend of about 70% which means that more than two thirds of the surface of our planet is inaccessible for classical geological investigation. In the absence of any knowledge of the seafloor – only the assumption that the sea could be as deep as the highest mountains are high, made on a physical basis – people started to systematically investigate the depth of the oceans and the morphology of their bottoms in the mid of the nineteenth century (Maury, 1860). For the first time, they figured out that the seafloor is no plane area but that its morphology is as complex as the one of continental plates, with sea mounts, valleys, and mountain chains (Maury, 1860). Captain Maury's expedition in 1860 revealed the existence of the Mid-Atlantic Ridge for the first time – obviously not knowing that he discovered the piece of a mountain chain spreading over the entire globe. Areas where oceanic crust is formed, the mid-ocean ridges (MOR), span a network of about 65,000 km over the world (Searle, 2013) and are responsible for the formation of two thirds of Earth's surface. These divergent plate boundaries, which divide the floor of every ocean on the planet, furthermore produce approximately 20 km³ of melt per year (Searle, 2013). With their enormous magmatic impact and the gravitation-driven ridge-push away from the spreading axis, MORs host two

of the three key processes for plate tectonics. Therefore, their importance for the system Earth is undeniable.

Nowadays, it is clear that oceanic crust does not only display a complex surface structure, but also provides living space to a still unknown, but high, number of animals and microbes. Furthermore, oceanic crust may preserve tons of ores. Thus, it is considered as a source of resources humanity will probably need in future (e.g., Pirajno, 1992). As far as we know today, MORs are the oceanic areas being most enriched in ores and habitats. Both formation of ore deposits and creation of living space is strictly correlated to the interaction of seawater with the lithosphere: seawater may enter oceanic crust through fault zones and can reach depths of several kilometers where the crust is hot and heat becomes exchanged between the lithosphere and the seawater. This hydrothermal activity is expected to be the most efficient cooling mechanism of the young oceanic crust formed at a MOR (e.g., Coogan et al., 2006). The hot water can transport metals from the crust upwards and when it gets in contact with cold seawater, metals may precipitate. The deposited metals form large ore deposits which are being investigated, for example, at the Southwest-Indian Ridge (e.g., German et al., 1998; Keith et al., 2016). At the same time, the water rising from the lithosphere heats the surrounding seawater to temperatures of about 250 to 350°C (e.g., Bemis et al., 2012). Close to the exchanges between hot water from the crust and the cold seawater, some bacteria, corals and even animals grow and form a diverse biotope in a few kilometers water depth. This means that MORs are the most interesting regions for possible sub-sea mining and at the same time they are areas to be protected in order to save life on Earth. This ambivalence makes clear why a best-possible understanding of the processes taking place along and beneath MORs is required and why studies on oceanic crust are essential to shape the future of human beings on our planet.

1.1.2 Fast-spreading mid-ocean ridges

Magma supply beneath the MOR is a key parameter affecting the spreading rate perpendicular to the axis. Three types are commonly distinguished: fast-spreading, slow-spreading, and ultraslow-spreading MORs. Because magmatic activity is weak at slow and ultraslow MORs, their spreading is dominated by tectonic processes and strong plastic deformation. Efficient magma supply beneath a ridge leads to faster spreading (e.g., Chen, 1992; Bown and White, 1994; Dick et al., 2003; Cannat et al., 2009; Ildefonse et al., 2014) and dominates the processes at fast-spreading MORs where the tectonic component is weaker. The strong tectonic deformation taking place at slow- and ultraslow-spreading MORs leads to a complex structure of the crust accompanied by only small fractions of magmatic basalts and gabbros. Slow-spread crust is therefore significantly different from fast-spread crust. The latter, on which this study focuses, is assumed to form a relatively constant stratigraphy along the ridge axis with pillow lavas and sheeted dykes forming the upper
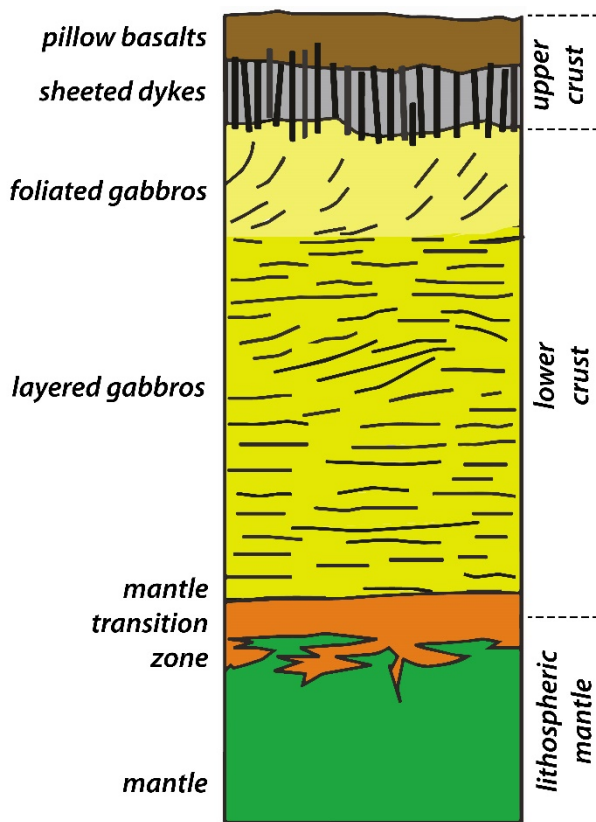
Figure 1-1   Draft of fast-spread oceanic crust as suggested by the participants of the Penrose field conference on ophiolites in 1972.

modified after Dick et al. (2006)

17

crust, varitextured, foliated, and layered gabbros forming the lower crust that transitions through a several hundred meters thick zone into the upper mantle (Figure 1-1; Penrose model; Anonymous, 1972). This model is based on studies of ophiolites, which are fragments of oceanic crust that was obducted onto the continent (see chapter 1.3.1).

The most famous example for a recent fast-spreading MOR is the East-Pacific Rise (EPR) which crosses the southern part of the Pacific Ocean from the Antarctic plate to the Gulf of California. Crustal fragments produced at the EPR or the spreading ridge itself were already the destination of many ship-based expeditions for both seismic and petrological or geochemical studies (e.g., Detrick et al., 1987; Vera et al., 1990; Marjanović et al., 2015; Gillis et al., 2014b; Koepke et al., 2011). Such expeditions played and play a pivotal role in testing predictions about lower oceanic crust made on the basis of studies on ancient oceanic lithosphere. These are introduced and discussed in more detail in chapter 1.2. Lithological features that were only known from ophiolites before, could be confirmed by drilling into recent oceanic crust, such as the existence of modally layered gabbros in the deeper sections of lower oceanic crust (Gillis et al., 2014b).

Those observations are very important not only in extending our knowledge of recent oceanic lithosphere, but also because they significantly increase the confidence into ophiolite complexes as reliable analogues for recent oceanic crust. The good agreement between lithological features observed in the Samail ophiolite and at the EPR, as well as detailed descriptions of an axial melt lens at the dyke/gabbro transition in Oman (e.g., Müller et al., 2017) and at the EPR (e.g., Detrick et al., 1987) provide fundamental evidence that the Samail ophiolite can be used (with some considerations described in chapter 1.3.1) as analogue for recent fast-spread oceanic crust.

1.1.3   The Oman Drilling Project

As the Oman ophiolite is regarded as representing fast-spread oceanic crust formed at a supra-subduction zone-related fast-spreading center (see chapter 1.3.1), detailed studies of its lithologies, composition, and both primary and secondary formation or alteration mechanisms can also help to better understand recent oceanic crust and its role in geochemical, mass, and energy cycles on Earth. Seven scientific objectives of the Oman Drilling Project (OmanDP) are listed on its website (www.omandrilling.ac.uk):

1) *"Quantify the nature and timing of solid upwelling beneath a spreading ridge using crystal shape and lattice preferred orientation data systematically collected on core from the periphery of a mantle diapir.*

2) *Quantify the nature and structural relationships of melt transport features in the shallow mantle, to evaluate mechanisms that focus transport from a melting region 100's of kilometers wide into a zone 2 kilometers wide where igneous oceanic crust is formed.*

3) *Quantify chemical variability deformation structures in the crust-mantle transition zone and plutonic lower crust, to determine the depth of crystallization, the nature of ductile flow, and mechanisms of melt transport.*

4) *Quantify hydrothermal alteration and cooling of the plutonic lower crust using mineral compositions, diffusion profiles, and stable isotopes to determine the importance of hydrothermal convection in heat and mass transfer.*

5) *Investigate processes in the critical "dike-gabbro transition" via study of cross-cutting igneous relationships, metamorphic mineral assemblages, and geochemical alteration.*

6) *Quantify mass transfer from subducted sediments into overlying peridotite at the "leading edge of the mantle wedge" via petrologic and geochemical studies, with special focus on carbon cycling.*

7) *Systematic and detailed study of ongoing, subsurface alteration of mantle peridotite, including fluid compositions, flow rates and hydrology, characterization of fracture and vein spacing, studies of mineral assemblages formed by carbonation, hydration (serpentinization) and oxidation and resulting mass transfer, and characterization of the subsurface microbial biosphere that derives energy from catalysis of low temperature alteration in this unique and fundamentally important environment."*

These show that the findings of the OmanDP not only point to a better understanding of primary magmatic formation processes beneath fast-spreading MORs, but also to a clear identification and an understanding of secondary processes modifying the formed crust und the underlying mantle. This includes exchange mechanisms between the lithosphere and atmo-, hydro-, and biosphere at different regimes with conditions ranging from ~1350°C and ~700 MPa in the upper mantle down to atmospheric conditions at the surface. It also includes tectonic environments from the active spreading center via the deep see and subduction zones to surficial weathering (Kelemen et al., 2020).

Drilling and coring helps to achieve a best-possible quality of the won data, since the stratigraphy of the samples is (a high recovery presumed) undeniable coherent und provides a much higher spatial resolution than surface sampling where large gaps between "adjacent" samples are practically unavoidable. Obviously, it may be misleading to expect coherency of the cores with respect to the initial stratigraphy of the crust, since faulting and tectonic thrusting may have deformed the obducted crustal fragment. Therefore, intense field studies were necessary to identify the best drill sites, depths and angles.

In total, fifteen drill sites were chosen in order to obtain samples from the sheeted dyke/gabbro transition (Gabbro Traverse (GT) 3A), the foliated/layered gabbro transition (GT2A), the layered gabbros (GT1A), the crust/mantle boundary (sites CM1A and B, CM2A and B), the active alteration of the mantle (sites BA1A to D, BA2A, BA3A, BA4A) and the basal thrust of the ophiolite (site BT1A). Nine of those sites were sampled by diamond coring in order to get coherent drill cores, each with a length of 300 to 400 m. Drilling was performed in two phases from December 2016 to March 2017 and from November 2017 to March 2018. The obtained drill cores were described during two description phases on board of the Japanese drilling vessel CHIKYU (see chapter 2.2).

1.1.4 Objectives of this study

This study aims to collect and provide indicators which help to constrain magmatic processes beneath fast-spreading MORs at both the crustal and the small magma chamber scale. Those processes may vary from km-scale magma emplacement mechanisms down to mm- or dm-scale dynamics within a magma chamber. Both large and small scale mechanisms beneath fast-spreading MORs are insufficiently understood to explain all features observed within both ancient and recent oceanic crust. This study approaches these objectives by different methods applied to samples that are distributed over different scales of the gabbro sequence of the Samail ophiolite (Oman). The four content chapters (chapters 3 to 6) focus on different sections of the lower crust and shed light on magmatic processes at various scales. Although the Samail ophiolite can be considered as representing ancient oceanic crust (e.g., Nicolas, 1989), it is stated again that crustal properties like thickness, scales and the presence of particular crustal units, or its chemistry, can vary even along single ridge segments (Searle, 2013). Therefore, the conclusions drawn from this study are primarily applicable to the analyzed rocks

of this thesis. Nevertheless, the similarity of the Samail ophiolite to recent oceanic fast-spread crust (see chapter 1.3.1) emphasizes its potential to also represent recent oceanic fast-spreading systems, as it is stated in more detail in chapter 6.2. The conclusions of this study can be tested in terms of plausibility and consistency with data from other fast-spread oceanic crustal systems and, thereby, are a precious contribution to the scientific community.

Chapter 3 presents a microstructural study on the gabbroic section of the Wadi Gideah reference profile (see chapter 1.3.3) which covers the entire lower oceanic crust exposed in Wadi Gideah of the southernmost Wadi Tayin massif of the Samail ophiolite. Microstructural and textural data, including grain size distributions, are used to constrain the magmatic processes occurring beneath fast-spreading MORs with a special focus on crustal accretion mechanisms existing in literature (see chapter 1.2). The key feature of this chapter is a high data density along an entire crustal section which was never achieved in previous studies and which is, as documented in the chapter, a key parameter to reliably constrain magmatic processes within the lower oceanic crust.

Chapter 4 presents and discusses the results obtained from drill core GT1A of the OmanDP. This also includes a compilation of the data won by the OmanDP Science Team during the initial core description on the Japanes drilling vessel CHIKYU which are an essential addition of the data won during the preparation of this thesis. The data set includes petrographic, petrologic, mineral and whole rock geochemical, and microstructural data with a unique spatial resolution of up to 2 m (depending on the applied analytical method) over a crustal section of approximately 400 m in height. The layered gabbro section has never been sampled and analyzed in so much detail and the obtained data can contribute to a substantial improvement of our understanding of lower crustal magmatic processes at the meter scale.

Chapter 5 is a report of the data obtained so far from drill core GT2A of the OmanDP. The 400 m long core covers a section of the transition between foliated and layered gabbros and provides samples from both crustal units. The obtained data set includes petrographic, petrologic, and microstructural data which are presented as a data report here.

Chapter 6 focuses explicitly on samples from two layered sequences from the lower crust showing modal layering, i.e., cyclic changes in mineral proportions, on the dm- and the mm-scale. The sequences were sampled with a spatial resolution of <10 cm or covering 11 mm-scale layers coherently, respectively. Petrographic, Petrologic, and microstructural analyses were applied to both sequences, the dm-layere sequence was additionally analyzed in terms of mineral trace element geochemistry. Cooling rates were obtained by trace element diffusion modeling in both sequences. The chapter aimed on constraining layer-forming processes potentially occurring within the lower oceanic crust, where modal layering is a ubiquitous feature.

1.2 Accretion of lower oceanic crust at fast-spreading mid-ocean ridges

The formation of the gabbroic units of oceanic crust is still part of scientific debate. Because one major objective of this thesis is the description of magmatic processes beneath fast-spreading MORs, the current context established by several crustal accretion models is described in the following.

The proposed models have to be consistent with field observations on ophiolite complexes, with samples from both paleo and recent oceanic crust, implications by seismic studies at recent MORs, and also thermodynamic constraints. A key question is where the rising partial melt from the asthenosphere crystallizes forming the plutonic lower oceanic crust. First models by Cann (1974) or Pallister and Hopson (1981) suggested that a large magma chamber beneath a MOR with a thickness and a width of several kilometers spans from the dyke/gabbro down to the crust/mantle transition and slowly crystallizes forming the entire thickness of the plutonic crust. This model easily explained the occurrence of igneous modal layering within the lower gabbros, since such structures were already known from large continental layered intrusions like Skaergaard (Greenland), Sept Iles (Canada) or Bushveld (South Africa); see chapter 1.4 for further details. The so-called "infinite-onion" models of Cann (1974) and Pallister and Hopson (1981) only differed by the shape they proposed for the magma chamber: while Cann (1974) suggested that the chamber is thinning upwards leading to a Δ-shaped chamber, Pallister and Hopson (1981) suggested a V-shaped chamber thinning towards its bottom.

However, by performing seismic studies at the recent EPR, e.g., Detrick et al. (1987) and Vera et al. (1990) found that there is no melt-rich zone with the dimensions suggested by the infinite-onion models beneath the MOR, which should have been detected by significantly slower seismic velocities through a melt-rich magma chamber. These workers only found a relatively small (a few hundred meters thick and at maximum 3-4 km wide) melt-rich volume which extended along the ridge axis for tens of kilometers. This axial melt lens (AML) was found to contain a high amount of melt whereas the region below appeared as a crystal mush with only a small melt fraction (e.g., Detrick et al., 1987; Vera et al., 1990; Canales et al., 2003).

These findings led to the creation of alternative accretion models. The two most-popular end-member models are the "gabbro glacier model" (Figure 1-2a) and the "sheeted sill model" (Figure 1-2c). The former was established in the early 1990's by Quick and Denlinger (1993), Henstock et al. (1993), and Phipps Morgan and Chen (1993) who suggested that crystallization only occurs within the AML. The cumulates from the bottom of the AML form a crystal mush that moves down- and sidewards to the MTZ as a "gabbro glacier". This model is in good agreement with structural field observations from the Samail ophiolite (e.g., Pallister and Hopson, 1981) with foliation of the gabbro sections changing from steep directly beneath the AML to nearly horizontal, Moho-parallel in the deeper sections. The sheeted sill model (e.g., Bedard et al., 1988; Kelemen et al., 1997; Korenaga and Kelemen, 1997; Kelemen and Aharanov, 1998) also suggests that cumulates from the AML can subside and form the uppermost part of the gabbros. But the broad majority of the lower crust is here assumed to crystallize *in situ* within relatively small melt lenses randomly distributed, mostly on- but occasionally also off-axis, along the lower crust (e.g., Kelemen et al., 1997). The model was initially based on the occurrence of decameter high gabbroic sills within the ultramafics of the MTZ in the Oman ophiolite (Kelemen et al., 1997). However, the latent heat released by their crystallization would hamper further nucleation (e.g., Maclennan et al., 2005) and needs to be removed from the system in order to enable the crust to solidify. Both models, as well as a hybrid model combining ductile cumulate flow from the AML with crystallizing sill intrusions randomly distributed throughout the crust (Figure 1-2b; Boudier et al., 1996), are scientifically debated.
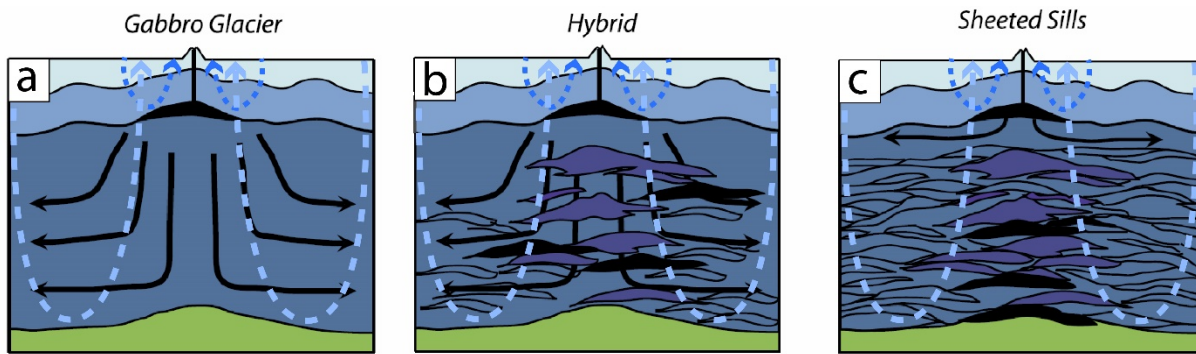
Figure 1-2   *Cartoons of accretion models established by e.g., Henstock et al. (1993; gabbro glacier), Kelemen et al. (1997; sheeted sills), and Boudier et al. (1996; hybrid). See text for further explanations.*
modified after VanTongeren et al. (2015)

There is support found for both end-member models, not only by ophiolite studies but also by ongoing investigations at recent fast-spreading centers. The key argument against the *in situ* crystallization of sills are the low cooling rates calculated by Mg or Ca diffusion in plagioclase and olivine, respectively, which can record sub-solidus cooling processes of a rock containing one of those phases and additionally clinopyroxene serving as semi-infinite reservoir for the diffused trace elements (Onorato et al., 1981; Dodson, 1986; Köhler and Brey, 1990b;Coogan et al., 2002a, 2007; Shejwalkar and Coogan, 2013; Faak et al., 2014). Coogan et al. (2002a, 2007) used the Ca-in-olivine speedometer to determine the cooling of gabbros in Wadi Abyad (Oman) as a function of height above the MTZ. They found a generally decreasing trend of cooling rate with $\log[dT/dt; °C\ yr^{-1}] \approx -1$ at the dyke/gabbro transition and $\log[dT/dt; °C\ yr^{-1}] \approx -4$ at the crustal base. The decreasing trend is confirmed at the recent Hess Deep tectonic window at the EPR where Faak et al. (2015) applied the Mg-in-plagioclase speedometer to the upper 800 m of the gabbroic section. Cooling significantly slows down from $\log[dT/dt; °C\ yr^{-1}] \approx -0.5$ at the dyke/gabbro transition to $\log[dT/dt; °C\ yr^{-1}] \approx -3.5$ at 800 m below. They interpret the decreasing cooling rate down section and the generally very slow cooling in the lower gabbros as indicators for cooling mostly occurring within the AML and the deeper parts of the crust being conductively, and so less efficiently, cooled. In turn, this supports the gabbro glacier model since the *in situ* crystallization of the sheeted sill model requires relatively fast cooling of the lower crust for removing heat (e.g., Maclennan et al., 2005).

A variable cooling rate without significant decrease along the crust of Wadi Khafifah (Oman) was modeled by VanTongeren et al. (2008) who also used the Ca-in-olivine speedometer. VanTongeren et al. (2008) calculated cooling rates between $\log[dT/dt; °C\ yr^{-1}] \approx -2$ to $\log[dT/dt; °C\ yr^{-1}] \approx 0$ without a clear down section trend. They interpret the absence of a clear trend and the generally faster cooling as supporting an efficient cooling of the lower crust by convective heat removal which fulfills the thermodynamic requirement of the sheeted sill model. The lower crustal cooling rate profile of VanTongeren et al. (2008) was extended by Dygert et al. (2017) to the mantle section between the Moho and the metamorphic sole north of Wadi Khafifah. They applied a REE-in-two-clinopyroxene thermometer (Liang et al., 2013), the two-pyroxene solvus thermometer (Brey and Koehler, 1990), and a cation exchange thermometer (Köhler and Brey, 1990a) to samples covering 10 km of the mantle section and found that cooling close to the Moho is as fast as modeled by VanTongeren et al. (2008)) and that the cooling rate decreases from the Moho down to the metamorphic sole. Dygert et al. (2017) infer from those findings that deep hydrothermal activity efficiently cools the lower crust close to the ridge axis, in turn cooling the underlying mantle convectively. The latter is suggested by the decreasing cooling rates along the analyzed mantle section.

Hasenclever et al. (2014) modeled cooling rates in the lower crust along the ridge axis numerically, taking the occurrence of hydrothermal activity into account, as it was considered by many authors (e.g., Bosch et al., 2004; VanTongeren et al., 2008; Zihlmann et al., 2018). Deep hydrothermal activity is indicated by the presence of large hydrothermal fault zones described in Oman (e.g., Zihlmann et al., 2018) and the presence of high temperature alteration phases, like brown amphiboles, or magnesio-hornblende, in some outcrops from the lower crust (e.g., Bosch et al., 2004; Currin et al., 2018b). Very high Cl contents in magmatic amphiboles at the crustal base are interpreted as indicator for the presence of seawater in the deep crust (Currin et al., 2018b) potentially serving as cooling mechanism at magmatic temperatures on-axis. Hasenclever et al. (2014) conclude that the removal of heat from the lower parts of oceanic crust can be sufficient to enable *in situ* crystallization, therefore supporting the sheeted sill model.

Geophysical support for this model is also provided by seismic studies at recent fast-spreading MORs. Seismic reflection patterns obtained at the EPR (Canales et al., 2012; Marjanovic et al., 2014), at the Juan de Fuca Ridge (Canales et al., 2009), and at the Galápagos Spreading Center (Boddupalli and Canales, 2019) suggest the existence of deep crustal melt reservoirs, as the findings of Carbotte et al. (2021) do.

Perk et al. (2007) applied petrological and geochemical techniques to samples from Pito Deep and Hess Deep at the EPR and found that the data from the former are more consistent with a subsidence accretion whereas data from the latter indicate a hybrid accretion with a subsidence mechanism in the upper and sill accretion in the lower part of the gabbros. Subsidence at Pito Deep is also suggested by Brown et al. (2019) obtaining textural and fabric data from the upper gabbros. An increasing strength of crystallographic preferred orientations and intracrystalline strain of plagioclase crystals down section is interpreted as indicating submagmatic flow from the AML downward. However, they make clear that these findings are restricted to the uppermost 800 m of the plutonic crust and do not give indication on the processes having occurred below.

Those are best- accessible in ophiolites, because sampling recent fast-spread oceanic crust rarely reached deeper gabbroic sections, yet. Browning (1984) found indicators for *in situ* crystallization from decameter scale cyclic fractionation trends observed over a cumulate sequence of 600 m in Wadi Bani Kharus of the Samail ophiolite. From the Wadi Gideah reference profile, Müller (2016) and Mueller et al. (2017) concluded that crystallization of gabbroic sills occurred deep in the lower crust, combined with cumulates subsiding from the AML and accreting shallower parts of the gabbroic section. These findings are based on clear fractionation trends of whole rock and phase composition within the lowermost 3500 m of the crust which imply that upward migrating melt evolved at depth by fractional crystallization. This hypothesis is supported by crystallographic preferred orientations (Müller, 2016) as further shown in chapter 3 of this thesis. Large scale fractionating trends as found in Wadi Gideah are, however, not observed in other wadis of the Samail ophiolite, such as Wadi Bani Kharus (Browning, 1984) or Wadi Abyad (Coogan et al., 2002b) emphasizing that the composition of fast-spread lower oceanic crust must be expected to be more variable between different localities than the very simplistic Penrose model (Figure 1-1; Anonymous, 1972) indicates (Gess et al., 2018).

1.3   The Samail ophiolite

The Samail ophiolite is a mountain range of about 600 km in length covering an area of approximately 20,000 km² along the northeastern coast of the Sultanate of Oman and the United Arabian Emirates (Figure 1-3). With its enormous dimensions and the well-preserved complete series of crustal units compared to other ophiolites, it provides the ideal field laboratory for performing studies on natural samples from the oceanic lithosphere (Nicolas, 1989). In order to assess whether the results obtained by such a study are plausible and whether implications on magmatic processes

beneath recent fast-spreading centers are justified, it is inescapable to consider the formation environment of the Samail ophiolite and its tectonic emplacement.

The ophiolite can be separated into the northern, the central, and the southern massifs and it contains twelve massifs in total (Figure 1-3). While the extrusive sheeted dykes and lavas are dominant in the northern and central massifs, they consume only small volumes in the southern massifs Sumail and Wadi Tayin, where the present study was conducted. Here, voluminous parts of the ophiolite are gabbros and harzburgitic mantle rocks. The gabbros are typically overprinted by magmatic deformation inducing a foliation and also mineral lineation (e.g., Nicolas et al., 2000). Foliation mostly parallels the magmatic layering, where present; high-temperature plastic deformation is generally negligible (Nicolas et al., 2000). The clear indication that present deformation is magmatic and the nearly absence of plastic deformation gives evidence that the constraints on primary magmatic processes from microstructural data obtained in Oman, as done in chapter 3 of this thesis, are reliable.

1.3.1   Formation of the Samail Ophiolite

The Samail ophiolite is regarded as a fragment of ancient oceanic lithosphere formed during the late Cretaceous in the Tethyan ocean about 95 Ma ago (e.g., Tilton et al., 1981; Rioux et al., 2013). Its paleo half-spreading rate was estimated to range between 50 and 100 mm per year (e.g., Hacker et al., 1997; Rioux et al., 2012a), defining it as fast-spreading mid-ocean ridge. Whereas the crust forming the ophiolite was considered for a long time to have accreted beneath a typical mid-ocean ridge, Pearce et al. (1981) found geological and geochemical evidence that the formation of the present lithologies was affected by subduction fluids indicating that the Samail crust was formed in a supra-subduction environment. This indicates that the ophiolite was part of a submarine arc-basin complex. As Ernewein et al. (1988) deduced from the Salahi block in the northern part of the ophiolite, it must have formed during several, subsequent magmatic stages. These authors defined three different types of volcanism, named V1, V2 and V3 (Figure 1-4), which are still used to characterize the complex evolution of the Samail ophiolite. Crystallization ages of zircons obtained by $^{206}Pb/^{238}U$ dating suggest that the magmatic stages V1 and V2 occurred very shortly after each other at about 96.40 ± 0.17 to 95.50 ± 0.17 Ma (V1; Rioux et al., 2012b) and 96.4 ± 0.3 to 95.2 ± 0.3 Ma (Goodenough et al., 2010), respectively, meaning that the whole magmatic formation of the ophiolite can be ascribed to the middle Cretaceous at about 95 Ma.

As Godard et al. (2003) confirmed by trace element analyses, including rare earth elements (REE), the V1 lavas are very similar to normal mid-ocean ridge basalts (N-MORB) only with slightly enriched light REE patterns. They are assumed to result from a typical MOR-like magmatism indicating that the melt results from partial decompression melting of the underlying mantle during adiabatic ascent of the asthenospheric mantle (e.g., Searle, 2013). These melts mainly crystallized Harzburgite, Dunite, (olivine-) gabbro and basalt (Goodenough et al., 2014). Wehrlite, anorthosite or troctolite are present, but display only minor constituents of the magmatic stage V1.

In contrast, the V2 lavas display chondrite-normalized REE patterns with decreasing REE contents from heavy to light REEs (Godard et al., 2003) being generally more depleted than those of stage V1 (Ernewein et al., 1988). They do not match the typical N-MORB pattern and moreover show different and more fractioned lithologies with huge bodies of plagiogranite, tonalite or trondhjemite. Dunite, wehrlite and clinopyroxenite are present and the gabbros are compositionally very heterogeneous (Goodenough et al., 2014). The magmatic stage V2 crystallized not only plagioclase, clinopyroxene and olivine, but also orthopyroxene, quartz and amphibole. The latter indicate that the melts of the V2 magmatism were more hydrous than those of stage one (Goodenough et al., 2014).
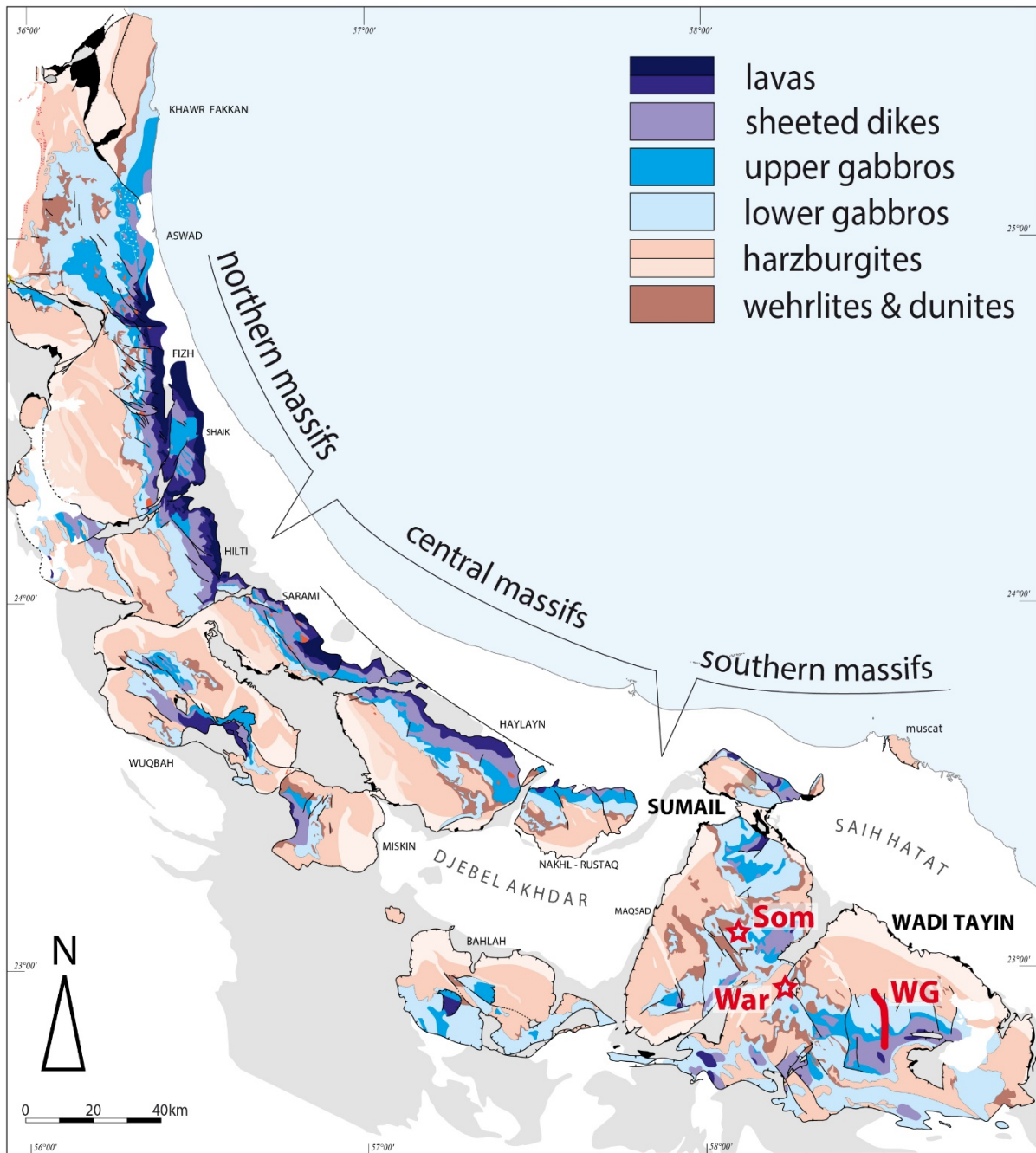
Figure 1-3   Simplified geological map of the Samail ophiolite at the northeastern coast of the Sultanate of Oman. Red stars give sample locations in Wadi Somerah (Som) and Wadi Wariyah (War) of chapter 6, the red line symbolizes the north-south tending Wadi Gideah (WG) where samples for the chapters 3-5 were collected. Note that the samples for this thesis were only collected in the southernmost massifs Sumail and Wadi Tayin.

Map modified after Nicolas et al. (2000)

It was highly debated for a long time, whether the complete ophiolite formed at a normal MOR spreading center (e.g., Boudier et al., 2000) or the subduction, which was arguably involved at least during the V2 magmatism, was initiated subsequently after an open spreading system (e.g., Juteau et al., 1988). MacLeod et al. (2013) ruled out both possibilities by modeling water contents during both magmatic phases V1 and V2 and found that the water content also during stage V1 was significantly elevated compared to N-MORB indicating that the magmatism forming the Samail Ophiolite always was related to a supra-subduction environment, maybe in a marginal basin (MacLeod et al., 2013).

Being related to a supra-subduction zone (SSZ) may explain differences between the crust from Oman compared to some recent fast-spreading MORs like EPR. These differences have to be considered when applying the Samail ophiolite as an analogue for modern oceanic crust. A key difference is the elevated water content of 0.4 to 0.8 wt% in the primary magma forming the Oman crust (MacLeod et al., 2013; Müller et al., 2017) in comparison to typical mantle-sourced MORB melts being assumed as nearly dry (e.g., Bell and Rossman, 1992; Searle, 2013). The presence of water in the parental melt of Oman provides a plausible explanation for the occurrence of large wehrlite bodies in V2 and much smaller wehrlitic dykelets within the V1 lower crust: as Gaetani et al. (1993) and Feig et al. (2006) figured out, water has a strong influence on the order of phase stabilization in basaltic melts: increased water activities suppress the nucleation of plagioclase, leading to the crystallization of the wehrlitic major constituents olivine and clinopyroxene prior to plagioclase. Koepke et al. (2009) applied those findings experimentally to the parental melt of Oman and found that wehrlites from Oman may have formed due to the slightly elevated water contents in both magmatic stages.

The formation of anorthosites, with a (nearly) monomineralic plagioclase assemblage, requires a different explanation. Nicolas and Boudier (2011) distinguished two different types of anorthosite close to the root zone of the sheeted dyke complex: fat anorthosite layers showing shearing and stretching as well as swarms of thin anorthosite layers alternating with (anorthositic) gabbros and showing a remarkable lamination. The authors suggest that the fat anorthosite bodies are cumulates of plagioclase crystallizing first in a magma chamber and settling to its bottom. When new melt replenishes the chamber, it passes the anorthosite layer at its base and swirls the deposited plagioclase crystals which follow convection cells and become lineated during the transport in such a cell. The newly deposited anorthosite layer is then only a few centimeters thin showing the observed lamination. This hypothesis is, however, not consistent with the modeling of plagioclase sinking velocities in primitive basaltic melt from the lower crust which is shown in chapter 6.5.2.2 of this thesis. As shown there, plagioclase with An_{80} is buoyant or even floats in a primitive basaltic magma. This effect should become even stronger during fractionation, because of a decreasing An component in plagioclase and increasing Fe content in the melt, which leads to a strengthening of the density contrast between plagioclase and melt. Nonetheless, a density-controlled phase segregation, as described in chapter 6.5.2.3, may play an important role in forming anorthositic assemblages.

Troctolite consisting to a very major extend of olivine and plagioclase, and usually only containing traces of clinopyroxene, was observed as plutonic lithology not only in the Samail ophiolite (e.g., Pallister and Hopson, 1981) but also at the Hess Deep Rift at the EPR (e.g., Arai and Matsukage, 1996; Gillis et al., 2014b). However, whereas troctolites, with variable olivine/plagioclase ratios, are a major constituent of the layered gabbro sequence at Hess Deep, Pallister and Hopson (1981) describe them as a volumetrically minor variant in Oman. For troctolites at the EPR, Arai and Matsukage (1996) suggested that they formed as an
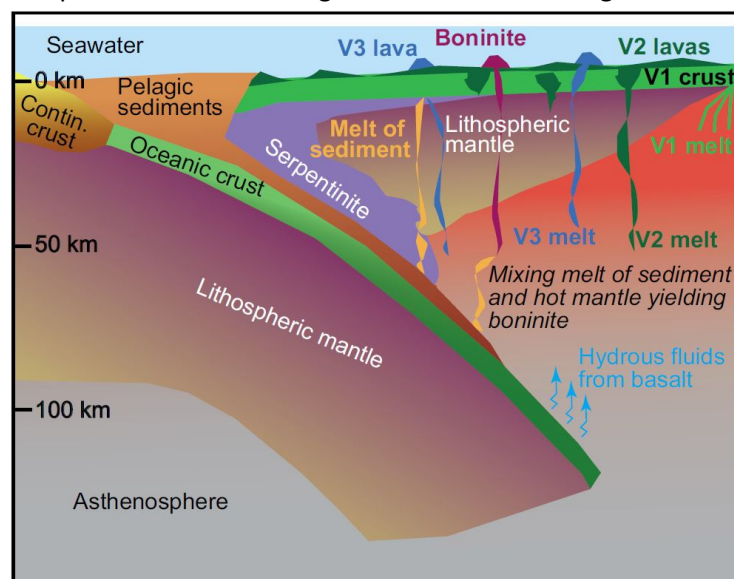
Figure 1-4   Model of melt source and emplacement of different volcanic stages during formation of the Oman oceanic crust.

Haase et al., 2015

26

interaction product from injected melt with the harzburgitic wall rock of the shallow mantle. The reaction of the melt with the host rock is assumed to gradually evolve the mantle harzburgite to dunite, troctolite, olivine gabbro, and finally gabbro (Arai and Matsukage, 1996). This hypothesis implies an evolution in phase chemistry from one to the next of the phases listed above. The high recovery of the coherent drill cores obtained for the chapters 4 and 5 of this thesis provides a good opportunity to test this hypothesis.

The mantle transition zone (MTZ) of the Samail ophiolite contains large dunite bodies, which can have either pure olivine assemblages or additional interstitial plagioclase or pyroxene (e.g., Koga et al., 2001). Rospabe et al. (2019) studied a suite of both dunite types petrologically and chemically and suggested that the dunite bodies from the MTZ are a result of partial melting of the mantle harzburgite, such that orthopyroxene is removed and pure dunite with some fractionated melt remains. The melt is either extracted by compaction leaving a pure dunite behind or fractionates *in situ* leading to interstitial growth of later phases, such as plagioclase and clinopyroxene. With their study, Rospabe et al. (2019) have shown that melt/rock interaction plays an important role within the MTZ and that small amounts of interstitial melt can crystallize *in situ* confirming earlier findings by Koga et al. (2001), Abily and Ceuleneer (2013), or Rospabe et al. (2017).

As described above, the magmatic stage V2 of the Samail ophiolite also contains large amounts of more evolved lithologies, such as plagiogranites or boninites. By the presence of biotite, muscovite, and K-feldspar in plagiogranites from the Samail ophiolite, Haase et al. (2015) rule out their formation (they call them leucogranites in their study) by pure fractional crystallization of mafic melt. Instead, they suggest the formation of those bodies by partial melting of pelagic sediments being sunk during subduction beneath the crust formed during the stage V1. The partial melting of pelagic sediments is indicated by low Nd and Hf isotope ratios which Haase et al. (2015) found in their samples, as well as an extreme enrichment of fluid-mobile elements such as Rb, K, and Pb. Identifying the products of the V2 magmatism as results from partially molten sediments is in good agreement with the later findings of de Graaff et al. (2019), who interpret a more radiogenic Pb composition in plagioclase as indicator for a melt derived from sediments of more altered oceanic crust. Although their study lacks a comprehensive data set of boninite geochemical data, Haase et al. (2015) suggest by comparison of their boninitic samples from Oman with the findings by Bedard (1999), König et al. (2010), and Zhao and Asimow (2014) that they result from interaction of the hydrous sedimentary melt with overlying mantle wedge. This is in agreement with the incompatible element signature of the boninitic magmas obtained in Oman. These processes are visualized in Figure 1-4.

Although the traces of the magmatic stage V2 are conspicuous over wide regions of the Samail ophiolite, they are quite rare in the southernmost massifs Sumail and Wadi Tayin, where the samples for this thesis were collected. This thesis only deals with plutonic rocks formed during the magmatic stage V1. The paucity of V2-related rocks in the sampled areas implies that – having the consequences of the elevated water content in the parental melt described above in mind – the findings of the presented study can be seen as closely related to the processes taking place beneath fast-spreading MORs.

1.3.2   Tectonic emplacement of the Samail ophiolite

Due to its higher density, oceanic crust is usually subducted below continental crust at a convergent plate boundary. Therefore, the obduction of the Samail oceanic crust fragment onto the continental Arabian peninsula required a mechanism that overcame the gravity-driven subduction. Boudier et al. (1988) suggested that an intra-oceanic thrust close to the early spreading center formed enabling overthrusting of the ophiolite sequence, comprising oceanic crust, lithospheric mantle, and

the earlier formed metamorphic sole (c.f., chapter 1.3.1; Guilmette et al., 2018) onto older oceanic crust (Figure 1-5b). They stated that a "situation, where a hot lithospheric plate is inclined only a few degrees above a weak asthenosphere, represents an excellent potential thrust surface if oceanic extension should rapidly change to compression." (Boudier et al., 1988). Once the ophiolite section is thrusted, compression will move it over the passive margin onto the Arabian peninsula (Figure 1-5c).

However, a working model for the tectonic emplacement of the Samail ophiolite has to reconcile several field observations and geochronological data as compiled by Warren et al. (2005). Main criteria are the dates of the formation of the metamorphic sole (about 104 Ma; Guilmette et al., 2018), of the ophiolite formation (about 96 Ma; e.g., Tilton et al., 1981; Hacker et al., 1997; Warren et al., 2005), and of the metamorphic peak of eclogite, formed at the subducting slab of the continental margin (82-79 Ma; e.g., El-Shazly et al., 2001; Warren et al., 2003).

El-Shazly et al. (2001) and Warren et al. (2005) described the tectonic emplacement of the ophiolite complex onto the Oman margin and assumed that the metamorphic sole was formed during the thrusting of the ophiolite. However, Guilmette et al. (2018) dated the age of the metamorphic sole about 8 Ma earlier than the ophiolite formation and inferred that the sole formed at a depth of about 35 km in the subduction zone that later initiated the formation of the Samail crust (Figure 1-5a). Nonetheless, thrusting the Samail crust together with the underlying lithospheric mantle and the metamorphic sole southwest-wards onto young oceanic crust still is a plausible obduction mechanism (El-Shazly et al., 2001; Figure 1-5b and c). Ongoing compression from southwest to northeast led to the obduction of the continental

Figure 1-5   Tectonic emplacement of the Samail ophiolite synthesized and simplified after Guilmette et al. (2018; a)-b)) and El-Shazly et al. (2001; b)-e)). Sm = Samail ophiolite; mtl = mantle; Hw = Hawasina sediments; ms = metamorphic sole; ecl = eclogite. Note the failing continental subduction resulting in exhumation of the formed eclogites. Arrows symbolize nappe movements. Dashed rectangle in c) represents section shown in d) and e). See text for details.

slope sediments of the Hawasina basin, the Samail crust with the underlying mantle, and the metamorphic sole onto the thin margin of the Arabian plate. The load of the ophiolite on the continental margin triggered intracontinental thrusting and, combined with the ongoing convergent plate movement, initiated a northeast-dipping subduction zone (El-Shazly et al., 2001; Figure 1-5d).

This led to the formation of blueschist and eclogite facies rocks at depths of >15 km. The thicker continental crust approaching from southwest choked the continental subduction due to its positive buoyancy (Cloos, 1993). When subduction ceased, the metamorphic products of the lower plate became exhumed such that the high P/T metamorphic blueschists and eclogites can be found nowadays in the Saih Hatat north of the Wadi Tayin massif (e.g., Gregory et al., 1998).

Warren et al. (2005) discussed the potentially erroneous $^{40}Ar/^{39}Ar$ and Sm-Nd ages of up to 110 Ma for the metamorphic peak of the subducted continental plate presented in previous studies (e.g., El-Shazly and Lanphere, 1992; Gray et al., 2004a; Gray et al., 2004b) which were used to support an alternative emplacement model including a southwest-dipping subduction zone (e.g., Gregory et al., 1998; Gray and Gregory, 2000). Warren et al. (2005) stated that these data are probably erroneous due to extraneous Ar and that peak metamorphism ages clustering at about 80 Ma are more reliable, supporting the tectonic emplacement model by El-Shazly et al. (2001) described above. However, the disagreement in terms of age and the resulting formation mechanism of the metamorphic sole with the findings of Guilmette et al. (2018) makes clear that the entire emplacement history of the Samail ophiolite is still debated.

1.3.3   The Wadi Gideah reference profile

With respect to the different magmatic and tectonic stages the Samail Ophiolite experienced, its representability of recent oceanic crust or even of a coherent crustal section is restricted to areas fulfilling several criteria. As shown above, the second volcanic stage forming parts of the ophiolite's crust can clearly be ascribed to the supra-subduction setting, therefore, being not representative for recent EPR-type of a MOR (e.g., Ernewein et al., 1988; Godard et al., 2003; Goodenough et al., 2014). Furthermore, the tectonic emplacement of the crustal fragment led to intense faulting and thrusting of the crust such that its initial stratigraphy is strongly disturbed at many locations and not coherent anymore Figure 1-3.

A location to investigate the Oman paleo crust as a useful analogue of recent oceanic crust thus requires a dominant V1 signature and ideally contains every primary lithological unit (from bottom to top: mantle transition zone, layered gabbros, foliated gabbros, varitextured gabbros, (frozen) axial melt lens, sheeted dykes, pillow basalts) being typical for a coherent section of fast-spread oceanic crust (Figure 1-1) without significant faulting. Wadi Gideah in the southernmost Wadi Tayin block of the Samail Ophiolite tends southwards and cuts the entire crustal section from the mantle transition zone to the pillow basalts (Pallister and Hopson, 1981). The crustal block is gently dipping to the south with an average dip angle of 28° (Pallister and Hopson, 1981). As the south of the ophiolite is arguably less affected by the supra-subduction zone-related V2 magmatism, the lithologies found here show a typical MOR signature, although a slightly increased water activity must be taken into account (e.g., MacLeod et al., 2013; Müller et al., 2017). On the basis of these features, Wadi Gideah was chosen as a reference profile along the lower crust of Oman and was sampled at the surface during several field campaigns between 2010 and 2015 (Koepke et al., 2017).

The sample suite contains 293 samples which were analyzed using petrographic, petrological, geochemical, and microstructural techniques. The obtained data comprise major, minor, and trace elements of the bulk rock. Minerals were analyzed in terms of major, minor, and trace elements with implications on crystallization temperatures, as well as crystallographic preferred orientations (CPO). Beside primary lithologies, a focus of this profile were hydrothermal fault zones in order to provide a complete image of the formation processes from the magma emplacement to its cooling possibly achieved by deep hydrothermal activity (Koepke et al., 2017).

On the basis of information won during the field campaigns for sampling the profile, two drill sites of the Oman Drilling Project were placed into Wadi Gideah (see chapter 1.1.3). The corresponding drill cores, each having a length of 400 m and covering the layered gabbros (GT1A) or the foliated/layered gabbro transition (GT2A), respectively, are subject of this study (see chapters 4 and 5). Using the detailed maps available for Wadi Gideah (e.g., Nicolas et al., 2000) and with the help of the preliminary field studies, the cores can be embedded into the reference profile and provide the perfect opportunity to complete the image captured on the crustal scale with two detailed sections being sampled on the meter- or even centimeter scale.

1.4   Igneous layering – a review of layer-forming processes

Modal layering is a key feature of the deeper parts of lower oceanic crust, not only in the Samail ophiolite (e.g., Pallister and Hopson, 1981), but also in recent fast-spread oceanic crust (e.g., Gillis et al., 2014b). However, studies focusing on the formation of layering within the lower oceanic crust are rare (e.g., Jousselin et al., 2012). As an important indicator for magmatic processes occurring during lower oceanic crust accretion, layer-forming mechanisms within oceanic crust are one of the key topics of this thesis (see chapter 6). In order to provide an appropriate background on the mechanisms suggested to form different types of layering, some key findings on layered intrusions from the past decades are compiled here. The given context should also help to evaluate the reliability of the interpretations proposed in chapter 6.

Although layering is a well-known feature of several large igneous intrusive bodies, its formation is often scientifically debated and moreover variable from one location to the other or even from one zone to the other at the same location. The complexity of layer-forming processes is well represented by the very different appearances layering can have. Before describing different types of layering, a definition of the term *layer* and *layering* is introduced here following the suggestion by Irvine (1982): "[…] a layer is a sheetlike cumulate unit that is a distinctive entity in its compositional and (or) textural features." and "Layering is here defined as the overall structure and fabric of cumulates manifest through combinations of layers, laminae, and lamination." These definitions were also adapted by more recent layering studies (e.g., Namur et al., 2015).

Therefore, a layered igneous body can be seen as an intrusive body that preserves cyclic changes, independent of their scales, in compositional or textural properties. Typical and well-known examples for such properties can be changes in grain size (e.g., Duke Island, USA; Irvine, 1974), chemical composition (c.f., cryptic layering; e.g., Skaergaard, Greenland; Wager and Brown, 1968; Sept Iles, Canada; Namur et al., 2010) or in the modal proportions (i.e., phase abundances) as it is not only known from several continental intrusions (e.g., Bushveld, South Africa; Cawthorn, 1996; Panzhihua, China; Zhou et al., 2005) but also from the lower oceanic crust from both ancient (e.g., Samail ophiolite, Oman; Pallister and Hopson, 1981) and recent fast-spreading systems (Hess Deep, East Pacific Rise; Gillis et al., 2014b). As described in chapter 1.2, the layered features of lower oceanic crust lead to early crustal formation models based on the findings on large continental intrusive bodies which have been falsified by seismic studies in the 1980's (e.g., Detrick et al., 1987). Although their findings suggested that the active magmatic system beneath fast oceanic spreading centers must be assumed to be smaller than the majority of prominent continental layered intrusions, the high amount of scientific studies at the latter can help to understand the layered features found within oceanic systems.

In order to set the findings presented in chapter 6 into an appropriate scientific context, some well-described layer-forming processes and exemplary locations are presented in the following. The reader is also referred to the Supporting Information to chapter 6 (Table S-1) where layer-forming processes, compiled after the reviews by Naslund and McBirney (1996) and Namur et al. (2015), are listed. The following layer-forming processes and their description are geared to the review paper by Namur et al. (2015). They suggest to distinguish those layer-forming processes which "involve internal movement of melt, mush and crystals within the magma chamber" (dynamic layer-forming processes) from those which "occur during crystallization as a result of changing the conditions of crystallization or by self-organization of the mineral assemblage in the crystal mush" (non-dynamic layer-forming processes; Namur et al., 2015).

1.4.1 Dynamic layer-forming processes

Mechanical sorting

Sorting mechanisms by mechanical processes are strongly correlated to the physical properties of both solid and liquid phase of a magma. Grain size, the density contrast between crystals and melt, as well as the viscosity of the melt may control whether a crystal sinks, floats or is buoyant within the surrounding melt. This correlation between solid and liquid phase is described by Stoke's law:

$$V = 2r^2g(\rho_1 - \rho_2)/9\eta$$

where *V* is the settling or floating velocity, *r* is the radius of a grain, *g* is the gravity constant, ρ_1 and ρ_2 are the densities of the crystal or the liquid, respectively, and η is the viscosity of the liquid. Depending on these properties, crystals may segregate by their density and grain size with larger and denser crystals at the base grading to smaller, less dense crystals at the top of a layer. Crystal settling was suggested to have taken place in the Skaergaard intrusion (Wager and Brown, 1968) or – by grain size sorting – in the Duke Island peridotite (Irvine, 1974). While relatively dense phases like olivine, clinopyroxene, or spinel will sink in a mafic melt, plagioclase often has a density smaller than the surrounding basic melt, thus, tending to float and potentially forming anorthositic layers at the top of a magma chamber, as suggested for the Sept Iles intrusion by e.g., Namur et al. (2011).

The negative density contrast between plagioclase and most basic melt compositions, as it was for instance experimentally shown for the Skaergaard intrusion by McBirney and Noyes (1979), is a critical feature that can be adapted to many other mafic layered intrusions containing plagioclase as a major constituent to the mineral assemblage. In these cases, crystal settling from the melt as explained above cannot work physically for plagioclase. Irvine et al. (1998) argue that the floating of plagioclase in the melt can be hampered under some circumstances, although plagioclase is less dense than the surrounding melt. Such circumstances can be fulfilled when crystal settling does not occur by homogeneous sinking of crystals from a cooling melt but by crystal-laden magma currents slumping down the wall of a magma chamber. In such a dynamic system, density-controlled phase segregation can occur, as it is known from submarine turbidites, and at the same time, the aggregation of plagioclase with denser phases would hamper their flotation. Therefore, the concept of density currents can potentially be of importance in mafic layered intrusions where plagioclase is present as a major phase at the bottom of a layer. Wager and Brown (1968) and Irvine (1987) suggested this mechanism to have formed the gradual modal layers of the Upper Zone of the Skaergaard intrusion, which is also indicated by well-pronounced trough structures.

Convection-related layering-forming processes

Convection cells can form in magma chambers with a sufficient density gradient from the base to the top of the chamber, either provoked by significant temperature or compositional differences or both (e.g., Marsh, 1989). Magma moving in such a convective current has the potential to keep crystals in suspension that would sink in a static magma (e.g., Sparks et al., 1993). Density-controlled settling velocities of different phases in a multi-saturated system can lead to modal layering, as it is suggested for the Khibina alkaline massif by Kogarko and Khapaev (1987). If convection is not continuous but intermittent, the cyclicity of convection and the resulting differences in convection velocity can lead to periodic settling of crystals when convection slows down or stops while they were carried in suspension during faster convection. Intermittent convection was suggested to have formed the modal layering of the Stillwater intrusion (Hess and Smith, 1960) or sharply contrasting alternating plagioclase- and clinopyroxene-rich layers of the middle zone of the Skaergaard intrusion (Naslund et al., 1991).

In more complex systems, double-diffusive convection may occur and potentially leads to the formation of a stratified liquid which crystallizes igneous bodies with distinct layers from every

stratigraphic unit. Assumed that a magma chamber is compositionally stratified, a density gradient from its top to the bottom will develop driven by compositional differences. As a second parameter, the chamber may be cooled heterogeneously with faster cooling at its roof. The resulting temperature gradient will lead to different diffusion velocities within the magma chamber with slower diffusion at its roof. Compositional and thermic homogenization of the melt is then hampered by different diffusion rates leading to a stepwise stratified magma chamber. The discrete units formed by double-diffusive convection can form internal convection cells which crystallize as discrete layers with different modal proportions and potentially also compositions (Namur et al., 2015).

Magma injection and magma mixing

An event of magma injection and the mixing of several magmas can result in layer formation by several possibilities. In case the involved magmas contain crystal loads contrasting in phase proportions and/or types, the crystals may segregate by their density contrast and settle down to discrete layers with contrasting modal proportions (e.g., Naslund and McBirney, 1996). An alternative way to form layering by magma injection can be the differentiation of the liquid after each pulse of fresh, more primitive magma. This process was suggested by Irvine and Smith (1967) for the Muskox intrusion where a layer is made of a base-to-top sequence from dunite via harzburgite to orthopyroxenite. Injection of hot magma into a cumulate with much lower temperature can also lead to the formation of quench-horizons potentially with small grain sizes compared to the host rock. This process leading to grain size layering was described in the Kap Edward Holm intrusion (Tegner and Wilson, 1991) and was also suggested by Namur et al. (2011); Namur et al. (2010) to have taken place during formation of the Sept Iles intrusion.

When density and temperature are sufficiently different between a magma chamber and an injecting magma, the magma injection can lead to a stratified magma chamber (Raedeke and McCallum, 1984). Proceeding crystallization and hence fractionation of the denser liquid then leads to a decrease in its density such that at a certain time the two liquids, now being similar in density, start to homogenize and form a hybrid melt crystallizing different phases than the injected liquid. This creates differences in modal abundances from the lower to the upper cumulate pile and may form modal layering when the injection of denser melt repeats. Raedeke and McCallum (1984) explained the occurrence of micro-layers with different phase abundances in the Stillwater complex by such a process.

Magma injection and mixing is also considered to form monomineralic layers as they are known from the Muskox (e.g., Irvine, 1975), Stillwater (Lipin, 1993), and Bushveld layered intrusion (Harney et al., 1990). To form monomineralic lithologies, the injection of a magma is supposed to shift the bulk melt composition to the stability field of a single phase which then crystallizes and may cumulate as monomineralic layer (e.g., Irvine, 1977).

Liquid and fluid migration in a crystal mush

The migration of liquid through a crystal mush potentially leads to the formation of modal layering, presumed that the liquid is in disequilibrium with the solids of the crystal mush. In this case, the migrating liquid can lead to dissolution of one or more phases from the mush along the migration path. As Namur et al. (2013) have shown, this process can be regarded as being responsible for the formation of layering in the Skaergaard intrusion. Also in the Stillwater intrusion, disequilibrium between solids and a migrating liquid is suggested to have formed anorthositic and troctolitic assemblages (e.g., Boudreau and McCallum, 1992; Meurer et al., 1997).

Similarly, a free fluid phase entering a crystal mush can provoke partial melting and is considered by some authors to have formed modal layering. Boudreau (1999) suggested that the olivine-bearing

rocks from the troctolitic subzone in zone I of the Stillwater complex may have formed by fluid infiltration of a gabbronoritic crystal mush leading to partial melting and to the formation of troctolites.

Liquid immiscibility

When liquid immiscibility occurs, a melt separates into two melts with significantly different compositions (e.g., tholeiitic melt separates into ferrobasaltic and rhyolitic melts; Charlier et al., 2013). Although some questions concerning the scales of liquid immiscibility and the location in a magma chamber where this process can take place are still unsolved, the separation of immiscible melts which crystallize separately can play an important role in the formation of layering. For instance, immiscible melts were found in melt inclusions from the Skaergaard layered intrusion (Jakobsen et al., 2005) or in the Sept Iles intrusion (Charlier et al., 2011; Namur et al., 2012).

1.4.2   Non-dynamic layer-forming processes

Changes of intensive parameters of crystallization

The conditions within a magma chamber can change during its crystallization, i.e., changing nucleation rate, oxygen fugacity, pressure, or temperature. Similar to changes in magma composition, as described as dynamic layer-forming process, changing crystallization parameters are also able to shift the melt composition from the cotectic into the stabilization field of a certain phase, thus, leading to changes in the crystallizing mineral assemblage. If such changes occur multiple times during the crystallization of a magma body, the resulting phase assemblage may become stratified resulting in distinct modal layering.

Assuming that minerals with different crystal structures have different growth rates, Wager (1959) suggested that the modal layering in the Bushveld intrusion was formed by the different growth rates of chromite, orthopyroxene, and plagioclase. An increased nucleation rate of feldspar and nepheline compared to pyroxene resulting from increased vapor pressures was suggested by Sørensen and Larsen (1987) to have formed the layering of the Ilimaussaq intrusion in Greenland.

As suggested by the models of McBirney and Noyes (1979) and Hort et al. (1993), oscillatory nucleation can occur at the base of a magma chamber when elements being compatible with the major phase(s) at the crystallization front diffuse from the melt to the minerals at the crystallization front. Whereas the region directly in front of these crystals is heated by the latent heat of crystallization and moreover undersaturated in the diffused elements, those elements may create a new crystallization front at a certain distance from the former one, where the melt is then supersaturated, due to a lower temperature. This process may repeat several times during crystallization and creates mm-scale modal layering (Liesegang banding; Liesegang, 1896; Boudreau, 1995).

Also changes in the pressure of a magma chamber during crystallization can cause differences in the mineral assemblage precipitated from a magma. In the system forsterite – hematite – anorthite – quartz, increasing the pressure from 1 bar to 10 kbar leads to a significant expansion of the stability fields of spinel and orthopyroxene to the expense of olivine and plagioclase (Osborn, 1978). Changing pressure was therefore suggested to have played a role in several basic layered intrusions, including the anorthosite and magnetitite layers in Bushveld (Cawthorn and Ashwal, 2009). Such changes in pressure can be provoked by several chamber in- and external mechanisms, including vapor exsolution, magma replenishment, eruptions from the chamber and external tectonic events (see reviews by Naslund and McBirney, 1996 and Namur et al., 2015).

The stability fields of phases that contain multivalent cations are highly sensitive to changes in the oxygen fugacity (e.g., Toplis and Carroll, 1995). A good example of a layered intrusion that is suggested to have formed under changing oxygen fugacity conditions is the Panzhihua intrusion in

China. In a stratigraphic interval of about 100 m that is assumed to have formed during a recharge event of primitive magmas (Pang et al., 2009), decimeter-scale layers of Fe-Ti oxides alternate with gabbroic layers being depleted in oxides. The oxide content in those Fe-Ti oxide layers is mostly higher than 70 %, but is significantly lower in the gabbroic layers with 5 to 30 % and both gradual or sharp layer boundaries (Namur et al., 2015). While gravitational sorting was suggested to explain the formation of layering on the decameter-scale in the lower zone of the Panzhihua intrusion (Pang et al., 2008), the decimeter-scale layering of oxide- and gabbroic layers described above requires an additional explanation (Namur et al., 2015). Referring to the experimental findings of Toplis and Carroll (1995), they suggest that changes in oxygen fugacity would be able to shift the liquidus composition of the magma from the cotectic into the stability field of magnetite which then crystallizes solely and settles down to form more or less monomineralic oxide layers. Its fractionation from the magma (and possibly also the reaction of the magma with the carbonate wall rock; Ganino et al., 2008) drives the magma composition back to the cotectic resulting in the formation of gabbroic layers.

Processes of equilibration in the crystal mush

Compaction of a crystal mush under the influence of gravity can already form a rough layering, driven by sizes and densities of the present phases (Coats, 1936; Boudreau and McBirney, 1997). Although a planar fabric can be produced under the influence of pure shear during compaction (e.g., Meurer and Boudreau, 1998), a simple shear component is required to increase the fabric strength and to form a strong lamination (Higgins, 1991). Simple shearing of a compacted crystal mush is suggested to have formed the modal layering within gabbroic sills of the crust/mantle transition of the Samail ophiolite, Oman (Jousselin et al., 2012). As Benn and Allard (1989) already suggested, deformation by shearing has played a role in deforming the layered gabbros from Oman. Jousselin et al. (2012) have shown that the deformation intensity, i.e., the fabric symmetry induced by magmatic and/or plastic deformation, correlates with the intensity of the observed layering, indicating that simple shear can transform initially homogeneous rocks into layered bodies.

In a compacting crystal mush, crystals can be dissolved or precipitated due to their pressure sensitiveness and depending on local variations in the stress of compaction (Namur et al., 2015). Therefore, dissolution-precipitation of minerals has the potential to re-organize mineral abundances and to develop initial weak heterogeneities into distinct layers (Boudreau and McBirney, 1997). Dick and Sinton (1979) suggested that layers of pyroxenite and dunite in ophiolites have formed due to the higher sensitivity of olivine to high pressure and the differences in the free energy of pyroxenes depending on modal abundances: since olivine tends to dissolve more easily than pyroxene, pyroxenes in an assemblage of low pyroxene and high olivine contents are subject to a greater stress than in an assemblage of high pyroxene and low olivine contents. Pyroxenes dissolved in the former assemblage will then precipitate in regions of the latter one, leading to the segregation of olivine and pyroxene and finally to the formation of pyroxenite and dunite layers.

Inhomogeneity not only in modal proportions but also in grain sizes has the potential to form layers or to enhance formerly created layering (e.g., Boudreau, 1995). Since the solubility of small crystals is higher than the solubility of large grains of the same phase, the larger ones can grow at the expense of the smaller ones which tend to dissolve. The result can be a grain size layering or even the absence of a phase in a region where small crystals dissolved and their components migrated to larger grains during their growth (c.f., Ostwald ripening; e.g., Boudreau and McBirney, 1997). An example where this process could have taken place is the inch-scale layering in the Stillwater intrusion (Boudreau, 1987) or in the Skaergaard intrusion (McBirney et al., 1990; Boudreau and McBirney, 1997).

The layer-forming processes by dissolution-reprecipitation described above are based on the diffusion of mineral components through the non-moving liquid of a crystal mush. The dimensions of

the resulting layering are therefore restricted to the diffusion distances of the involved components and are restricted to the mm- to cm-scales (Boudreau and McBirney, 1997). However, if the liquid is moving, the distances of element transport and the effectiveness to remove or add components from or to a system is increased such that the intensity and the dimensions of the resulting layering are potentially increased (Namur et al., 2015).

Modal and cryptic layering due to chemical diffusion in the crystal mush

Cryptic layering, i.e., rhythmic chemical variation, accompanies modal layering in the upper critical zone of the Bushveld complex where chromitite layers are overlain by silicate cumulates comprised of pyroxenite, norite, and anorthosite from bottom to top (Naldrett et al., 1986). Cryptic variation is most pronounced by the Mg# (Mg/Mg+Fe x 100; molar basis) of orthopyroxene which decreases from the base to the top of the silicate cumulates. The Mg# of accessory Cr-spinels within the silicate layers is variable and generally lower than the constant values in the Cr-spinels of the chromitite layers (Naldrett et al., 1986). However, other minerals show compositional variations that are intuitively contradictory to the compositional changes of the Cr-spinels: Na_2O in plagioclases from the silicate layers is constant, contrasting with the variable Mg# in Cr-spinel mentioned above, and intercumulus plagioclase crystals from the chromitite layers are depleted in Li, K, and Rb whereas light rare earth elements are relatively enriched in the same crystals (Namur et al., 2015). An explanation for this behavior is suggested by Namur et al. (2015) who argue that peritectic reactions between chromite, silicates, and inter-cumulus melt could result in redox gradients. Such a gradient may trigger Na diffusion that benefits from the high diffusivity of Na^+ cations compared to other cations (Zhang et al., 2010).

Namur et al. (2015) suggest that such a chemical diffusion can also produce changes in the mineral assemblage of a crystal mush, hence leading to the formation of layering. They show at the example of the haplobasaltic system diopside (Di) – anorthite (An) – albite (Ab) that the addition or removal of Na to or from the system has significant effects of the modal proportions of plagioclase and diopside in a crystal mush, therefore, providing a plausible mechanism for the formation of anorthositic and pyroxenitic silicate layers.

1.4.3 Conclusions

The reasons of layer formation appear to be as variable as the layer appearances. It may help to subdivide layer-forming processes into a scheme, as Namur et al. (2015) suggested to distinguish dynamic and non-dynamic layer forming processes. Nonetheless, the high amount of intensive studies on igneous layering makes clear that we are not able yet – and possibly will never be – to explain the occurrence of layering by a single, universal process. At the opposite, the data obtained by the studies on layered intrusions indicate that careful investigations in the field and of the obtained samples are necessary to approach the best-possible understanding of how the layering at a particular location was formed.

This conclusion is the basis of the study presented in chapter 6, where multiple analytical methods were applied to profiles covering modal layering from two different locations in the Samail ophiolite with a very high spatial resolution. The findings on layering formation compiled above and reviewed in detail by, Naslund and McBirney (1996) and Namur et al. (2015) helped to get an understanding of what mechanisms can play a role during crystallization and cooling of a magma chamber. The results from the analyzed profiles in chapter 6 were interpreted with respect to those findings constraining a small number of mechanisms being possibly responsible for observed layering in the lower oceanic crust of the Samail ophiolite.

2 Materials and Methods

2.1 Surface sampling and coring

This study deals with samples from the three wadis Gideah, Somerah, and Wariyah. Wadi Gideah and Wadi Wariyah are located in the southernmost Wadi Tayin block of the Samail ophiolite whereas Wadi Somerah is located in the Samail block (Figure 1-3). Four field campaigns were performed to collect the samples of the reference profile in Wadi Gideah (chapter 3). The samples analyzed in Chapter 3 are a subset of 68 samples from the reference profile initially containing 293 samples (Müller, 2016; Koepke et al., submitted). The profile has also been described petrographically, petrologically (Koepke et al., submitted), thermometrically (Müller et al., submitted), and geochemically (Garbe-Schönberg et al., submitted). The samples analyzed microstructurally in Chapter 3 represent a cross section through the gabbroic units in Wadi Gideah from the MTZ to the AML with an average spacing of 81 m between adjacent samples (min. 1 m, max. 389 m). Since the initial intention was only to perform petro-geochemical analyses on those samples, they were not taken as oriented samples. The interpretation of the won data is therefore restricted to the relative changes in structural features along the crustal section. The fabrics of every samples cannot be directly oriented into the crustal context with respect to the sheeted dyke orientation or the orientation of the Moho. However, detailed field studies (e.g., Pallister and Hopson, 1981; Nicolas et al., 1996; VanTongeren et al., 2015) provide reliable data on the general orientation of foliation and lineation as dominant fabrics in the gabbros of the Wadi Tayin block. Therefore, a general treatment whether, e.g., the foliation of a sample is steep or horizontal, or the lineation in a thin section is parallel or normal to the paleo-spreading axis is possible by embedding our samples into the maps and cross-sections by Pallister and Hopson (1981) and Nicolas et al. (1996); Nicolas et al. (2000).

In 2010, the outcrops in Wadi Somerah (N 23°5'34.66", E 58°6'14.62") and Wadi Wariyah (N 22°59'0.42", E 58°15'54.68") were sampled in order to perform a highly resolved study on the formation of igneous layering in the lower crust of the Oman ophiolite (Chapter 6). The outcrop in Wadi Somerah is located in the middle of the layered gabbro section and shows modal layering pronounced by olivine abundance at the dm-scale. Twenty-nine thin sections were polished covering 5 complete layers and the olivine-rich base of a sixth layer. The layering is nearly horizontal and individual layers are traceable along the entire southern outcrop face of about 80 m (Figure 6-2a). The much smaller western face of the outcrop preserves sheared and partially discordant layers (Figure 6-11). Wadi Wariyah was subject of several studies before (e.g., Nicolas, 2003; Bosch et al., 2004; Currin et al., 2018a) describing several features of the outcrop. Olivine and plagioclase foliation is here parallel to the igneous layering (Nicolas, 2003), the gabbroic host rock is cross-cut by different types of dykes (Bosch et al., 2004): white veins with a thickness of ~0.1 mm contain prehnite indicating hydrothermal alteration at the low temperature regime. Dark mm-thick veins contain plagioclase and both green and brown amphiboles. Gabbroic cm-thick dykes cross-cut the layering (Figure 6-2c). These dykes show fringes of brown amphibole at their margins. The occurrence of brown amphiboles in both plagioclase-amphibole veins and gabbroic dykes indicate that hydrothermal activity occurred at high temperatures (850-1030°C) at the magmatic regime (Bosch et al., 2004). The mm-scale layering observed in this outcrop is described by mm- to cm-thick olivine-rich bands and was rarely documented in Oman before. A hand piece showing such a layering (Figure 6-2d) was collected at the mouth of Wadi Wariyah about 300 m away from the outcrop. Its rectangular shape implies that it was not transported over a long distance but can be assumed to represent the layered gabbros of the described outcrop. Its stratigraphic height is very close to the MTZ (~100 m above the MTZ). A large wehrlite intrusion was

observed close to the location where the sample was collected. Two thin sections from the hand piece were prepared and analyzed for this study (Chapter 6).

The drill cores GT1A and GT2A have been obtained in the frame of the Oman Drilling Project (see Chapter 1.1.3). As part of the gabbro traverse (GT), both drill sites are located in the Wadi Gideah such that the results can be embedded into the data from the Wadi Gideah reference profile (chapter 1.3.3). Drill core GT1A (N 22°53'32.1", E 58°30'54.2414"; chapter 4) covers 403.05 m of the layered gabbros with its top at a stratigraphic height of 1173 maM (meters above the base of the MTZ). Drill core GT2A (N 22°51'47.5812", E 58°31'11.8812"; chapter 6) cored 406.55 m and covers the transition from the layered to the foliated gabbros. These units can be distinguished by their significantly different grain sizes (coarse in the layered, fine in the foliated gabbros) and the alternating changes in grain size along the core indicate that the units transition over a mixed zone of several hundred meters into each other as already deduced from field observations (e.g., Pallister and Hopson, 1981; Nicolas et al., 1996). The drill hole GT2A was inclined by 30° from the vertical tending towards 54° north-east in order to cross a large hydrothermal greenshist vein which was mapped in the field (Kelemen et al., 2020).

2.2 Core description and sampling on CHIKYU

The obtained drill cores GT1A and GT2A have been described and analyzed on board of the Japanese drilling vessel CHIKYU between the 15th of July and the 15th of August 2017. The core sections were cut normal to the lineation and, if visible, parallel to the foliation of the rocks. Whereas one half of every section was used for description and further sampling on board, the other one of every core became archived for future investigations. The description was performed with a focus of igneous and alteration petrology, structural geology, seismic and physical properties and geochemistry (Kelemen et al., 2020; see chapter 4.2.1). Quarter core sample pieces with a length ranging from 5 to 25 cm were collected by the author during two sampling parties on board. A subset of 15 samples was kindly provided by Benoît Ildefonse to improve the spatial resolution of the obtained data and to fill potential gaps within the semple suite. Their sample name starts with "OM-DP-BI". The supplemental tables S-1 and S-2 list the collected samples with some key information, including depth in the drill hole, the projected height above the base of the MTZ, lithology, and performed analyses. The lithologies were defined from phase abundances following the categorization of Gillis et al. (2014c).

2.3 Calculation of crustal depths in Wadi Gideah

Projecting the height of the individual samples from both the reference profile and the cored samples requires some presumptions. Müller (2016) recalculated the height above the base of the MTZ of every sample from the reference profile using their GPS coordinates. An average dip angle of the entire Wadi Gideah lithologies after Pallister and Hopson (1981) was used to project the stratigraphic height above the base of the MTZ (HaM) of very sample. By knowledge of the bore hole top locations of GT1A and GT2A in the crustal frame, the height above the base of the MTZ of every drilled section can be calculated from the depth in the bore hole. However, for a proper projection into the crustal reference frame, the tilt of 28° of the Wadi Gideah area (Pallister and Hopson, 1981) has to be taken into account also here. For GT1A, the HaM of the samples was calculated following

$$\text{HaM}_{sample} = H_{Top} - (D_{BH} \times \cos(28)) \quad \text{Eq. 1}$$

with H_{Top} = HaM of the top of the bore hole (= 1173 m for GT1A) and D_{BH} = depth of the sample in the bore hole. The vertical drilling into the tilted ophiolite block leads to a reduction of the net drilled

crustal depth interval by about 47 m to 356 instead of 405 m. It covers a crustal section from 1173 to 817 maM.

The inclination of bore hole GT2A by 30° from the vertical leads to a much weaker effect of the crustal tilt on the drilled depth interval. The north-eastern orientation of the bore hole does not exactly equalize the southern dipping of the crustal block, although its inclination of 30° matches the ophiolite tilt of 28° very well. However, a three-dimensional animation using Adobe Dimension has shown that, regardless of the misfit between the orientation of the bore hole and the orientation of the crustal tilt, 406 meter along the drill core can be assumed to closely fit 406 meter in the crust. With respect to possible errors in defining the exact crustal height of the bore hole top above the Moho, the HaM of the GT2A samples was calculated by the simple equation

$$HaM_{sample} = H_{Top} - D_{BH} \qquad Eq.\ 2$$

with H_{Top} = 2695 m for GT2A. Drill core GT2A is assumed to cover a crustal section from 2695 to 2289 maM.

2.4 Sample preparation and analytical techniques

2.4.1 Thin section and rock powder preparation

The samples of this study were prepared as standard polished thin sections in the preparation workshop of the Institute of Mineralogy at Hannover. The long axis of the thin section is generally oriented parallel to the drill core (exceptions are the samples 152-2-65-68 in GT1A and 28-3-34-37, 42-1-36-38, and 51-2-81-84 in GT2A). If visible, the thin sections were cut perpendicular to the foliation and parallel to the lineation. The thickness of the thin section is 50 µm in order to prevent penetration of the glass holder during laser ablation analyses. A subset of 15 thin sections from GT1A (chapter 4) was shared by B. Ildefonse in order to increase the spatial resolution along the core. These were polished in the preparation laboratory of Géosciences Montpellier to a thickness of 30 µm. The thin sections used for electron backscattered diffraction analysis were fine-polished in the preparation laboratory of Géosciences Montpellier. The thin sections were coated with 20 nm carbon for BSE imaging and EDX analyses with the scanning electron microscope and for element analyses with the electron microprobe.

A selection of samples from drill core GT1A was prepared not only as thin section but also as rock powder for bulk rock chemical analysis. These samples were in a first step crushed by a hydraulic press and subsequently milled using the ball mill of the Institute of Mineralogy at Hannover. Nano-milling as required for best-possible homogenization and preparation of powder tablets (Garbe-Schönberg and Müller, 2014; see chapters 2.4.5 and 6.3.2) was performed in the milling laboratory of the Institute of Geo Sciences at Kiel.

2.4.2 Optical and electron microscopy

All thin sections were photographed under both plane- and cross-polarized transmitted light using a Nikon D800 camera equipped with macro lens Sigma EX 70mm f2.8 DG. The high-resolution images were used as overview photographs from the entire thin sections for further analyses. Moreover, digital point counting using the software JMicroVision was applied to every thin section of the drill cores GT1 and GT2 using these thin section photographs. A number of 500 points was distributed randomly over the thin section (or domain, where one section contained several domains)

and defined using the identifiers olivine, clinopyroxene, plagioclase, orthopyroxene, brown amphibole, green amphibole, opaque, and not identified. The resulting values were normalized to 100 in order to achieve reliable modal abundances of the primary mineralogical phases. Note that this method was only applied to the drill cores described in chapters 4 and 5. The modal abundances in the samples from the Wadi Gideah reference profile (chapter 3) and from the sampled layered gabbros in chapter 6 were estimated using EBSD technique or visual estimation, as described in both chapters in detail.

A Leica Leitz DMRP transmission binocular was used for petrographic investigations. Photomicrographs were acquired using a Leica digital camera attached to the microscope which was controlled using the Leica Application Suite v4.12.0. Detailed backscattered electron (BSE) images were acquired using a JEOL SEM 7610 FPlus equipped with a field emission gun for high resolution images. The scanning electron microscope (SEM) is furthermore equipped with two energy-dispersive X-ray (EDX) detectors of the type Bruker Quantax X-Flash 6I60. EDX element mappings were performed in order to get semi-quantitative information on element distribution within the samples. The SEM was controlled by the JEOL software PC-SEM v4.0.0.6 for adjustment of the beam parameters and for acquisition of BSE images. An accelerating voltage of 15 kV and a probe current of 20 nA were used. The working distance was 15 mm which is the height the EDX detectors are calibrated for. EDX map scanning parameters were controlled with the Bruker Esprit 2.2 software. The scan speed and the number of scans per frame were adapted with respect to a practicable measurement time. In order to achieve a sufficient quality of the element maps, the dwell time of every pixel was ≥8 µs and every frame was scanned over at least three cycles.

2.4.3   Electron probe micro analysis (EPMA)

The Cameca SX 100 microprobe of the Institute of Mineralogy in Hannover was used for quantitative wavelength-dispersive X-ray analyses (WDS) on major and minor elements. The microprobe is equipped with five WDS spectrometers and controlled by the Peaksight software. The analyzed elements and the used crystals with corresponding measurement times on the peak and both background are listed in Table 2-1. An accelerating voltage of 15 kV and a beam current of 15 nA were used, the beam was defocused to 2 µm for olivine and plagioclase analyses and to 20 µm for pyroxene analyses in order to integrate potential exsolution lamellae. A matrix correction was applied following the PAP scheme (Pouchou and Pichoir, 1991).

Measurements were performed on both core and rim of a grain. Analyses with a total of 100 wt% (±2) after standard correction of every element oxide were considered for further processing. The result tables of every sample including the obtained standard analyses and detection limits are provided in the electronic supplement. Data outside this given range were removed from the data set.

Table 2-1   Configuration of microprobe analysis settings for the phases olivine, clinopyroxene and plagioclase.

element[a]	Olivine			Clinopyroxene			Plagioclase		
	crystal[b]	peak time [s]	background time[c] [s]	crystal[b]	peak time [s]	background time [s]	crystal[b]	peak time [s]	background time [s]
Si	TAP	10	5	TAP	10	5	TAP	10	5
Fe	LLIF	10	5	LLIF	10	5	LLIF	10	5
Mg	TAP	10	5	TAP	10	5	TAP	10	5
Al	TAP	20	10	TAP	10	5	TAP	10	5
Ca	PET	30	15	PET	10	5	PET	20	10
Na	TAP	20	10	TAP	10	5	TAP	10	5
K	LPET	10	5	LPET	10	5	LPET	20	10
Ti	LPET	10	5	LPET	10	5	n.d.	n.d.	n.d.
Mn	LLIF	10	5	LLIF	10	5	LLIF	10	5
Ni	LLIF	10	5	n.d.	n.d.	n.d.	n.d.	n.d.	n.d.
Cr	n.d.	n.d.	n.d.	PET	10	5	n.d.	n.d.	n.d.

[a] results given as element oxides estimated by stoichiometry: SiO_2, FeO, MgO, Al_2O_3, CaO, Na_2O, K_2O, TiO_2, Mn_3O_4, NiO, Cr_2O_3

[b] crystals used for quantification with TAP = thallium acid phthalate, LLIF = large lithium fluoride, (L)PET = (large) pentaerythritol

[c] measurement time on both backgrounds

n.d. = not determined

2.4.4   Electron backscattered diffraction

Microstructures of the samples were measured using electron backscattered diffraction (EBSD; e.g., Prior et al., 2009). Analyses were performed at Géosciences Montpellier using the JEOL JSM 5600 equipped with an Oxford/Nordlys EBSD detector and controlled by the Aztec software. The SEM was used at an accelerating voltage of 15 kV. The step size (i.e., the spatial resolution of the measurement) depended on the grain size and ranged between 9 and 35 µm with smaller step sizes for fine-grained samples. Every pixel with a mean angular deviation (i.e., the angle between the measured diffraction pattern and the indexing solution proposed by the Aztec software) of ≤1° is counted as indexed raw data point. The detailed procedure of processing the EBSD data is given in chapter 3.3.2. If not indicated elsewise, the data processing followed this procedure in every chapter of this thesis.

2.4.5   Mineral trace element geochemistry

Trace element compositions of clinopyroxene and plagioclase were obtained for the chapters 4 and 6, with a focus on the rare earth element (REE) compositions, using laser ablation inductively-coupled plasma mass spectroscopy (LA-ICP-MS). Measurements were performed in-situ on selected thin sections at the Institute of Geosciences of the Christian-Albrechts-Universiät zu Kiel. Samples were selected with a focus on fresh, un-altered minerals. For chapter 4, (olivine) gabbro was analyzed, as well as troctolitic, anorthositic, and wehrlitic samples in order to provide a better understanding of

how those lithologies form. For a better understanding of layer-forming mechanisms, samples from both the top and the bottom of several decimeter scale layers were analyzed in chapter 6.

The used laser system is a 193 nm ArF excimer laser ablation system (GeoLasPro HD, Coherent) with a Zurich-type low dispersion high capacity laser ablation cell (Garbe-Schönberg and Müller, 2014) and coupled to an Agilent 7900s quadrupole inductively-coupled plasma mass spectrometer. We used a 10 Hz pulsed beam with a fluence of 12 Jm^{-2} and a crater diameter of 32 µm for clinopyroxene. The conditions were increased to 16 Hz pulse rate, fluence of 18 Jcm^{-2} and a crater diameter of 120 µm for plagioclase due to the very low amounts of – especially heavy – REEs in plagioclase compared to clinopyroxene. The large crater diameter hampered a distinct core/rim differentiation for plagioclase analyses, whereas clinopyroxene was measured on core and rim of every grain separately. At least four grains per phase and thin section or domain were analyzed in order to provide reliable statistics for average calculations.The cell was flushed with 1.0 L min^{-1} as carrier gas with the addition of 14 mL min^{-1} H_2 in order to increase the sensitivity and to prevent oxide formation (e.g., Garbe-Schönberg and Müller, 2014).

By application of the internal standardization method using CaO contents measured by EPMA as internal standard, initial data processing and adjusting the integration intervals was done with the GLITTER software package. For initial calibration, NIST SRM612 was used. The micro-analytical reference materials BIR-1P, BHVO-2P, JGb-1P, and JF-1P, prepared as nano-particulate pellets (Garbe-Schönberg and Müller, 2014), were used for a second matrix matched calibration step. All calibration and accuracy data are compiled in the electronic supplement of this thesis. For chondrite normalization of REE contents, the chondrite composition published by McDonough and Sun (1995) was used.

2.4.6   Bulk rock geochemistry

Major element analyses for the bulk rock powders was performed by X-ray fluorescence analysis (XRF). 600 mg of the sample powder are mixed with 3.6 g $Li_2B_4O_7$ and molten in a platinum crucible at 1100 °C in order to form fused glass discs. The XRF was performed using a Malvern Zetium 1 kW wavelength-dispersive spectrometer, equipped with five spectrometer crystals (PE, LiF 200, LiF 220, Ge 111, PX-1) to analyse major element contents quantitatively. Trace elements were measured on nano-particulate pressed powder pellets of the crushed rocks (Garbe-Schönberg and Müller, 2014)using the LA-ICP-MS system described in chapter 2.4.5.

3 A reference section through fast-spread lower oceanic crust, Wadi Gideah, Samail Ophiolite (Sultanate of Oman): Insights from Crystallographic Preferred Orientations

Dominik Mock [1,2]*, Benoît Ildefonse [2], Tim Müller [1], Jürgen Koepke [1]

[1] Institut für Mineralogie, Leibniz Universität Hannover, Germany

[2] Géosciences Montpellier, Université de Montpellier, CNRS, Montpellier, France

Corresponding author: Dominik Mock (d.mock@mineralogie.uni-hannover.de)

Abstract

We established a 5000 m thick profile through the paleo lower oceanic crust of the Samail ophiolite (Sultanate of Oman, Wadi Gideah), in order to investigate accretion processes beneath fast-spreading mid-ocean ridges. The Samail ophiolite is regarded as best on-land analogue for fast-spread oceanic crust, and Wadi Gideah allows sampling of the entire lower crust along the Wadi bed. Here, we provide microstructural constraints to lower crustal accretion beneath fast-spreading mid-ocean ridges, which reveal changing microstructures and fabrics with depth. Grain size coarsening occurs from the foliated to the layered gabbro section. A ~350 m thick zone of gabbroic rocks from the profile top, interpreted as frozen fillings of the axial melt lens and defined as varitextured gabbros, shows intergranular textures without crystallographic preferred orientations. Rocks from the varitextured/foliated gabbro transition (~500 m thick) and from the upper foliated gabbros (~600 m) are foliated and lineated. The lineation is absent or very weak in the underlying ~800 m thick lower foliated gabbros. In layered gabbros, the fabric gradually strengthens and becomes more lineated down section with local scattering at small spatial scales. This implies distinct accretion mechanisms in the deep and shallow plutonic crust. For the layered and lower foliated gabbros, our data suggest in-situ crystallizing individual magma reservoirs. Dominant lineation in the upper foliated gabbros and the varitextured/foliated gabbro transition suggests vertically transported crystal-laden melts or mushes being consistent with subsiding crystal mushes from the axial melt lens, and/or crystallizing upward migrating melt expelled from the crystal mush beneath.

3.1 Introduction

Based on marine geophysics, seafloor geology, and ophiolite studies, the classical picture of a uniformly layered oceanic crust (with basaltic lava flows, basaltic sheeted dikes, and gabbros, from top to bottom) emerged in the early 1970's (Anonymous, 1972). About 50 years later, our vision of the architecture of the ocean crust has considerably evolved, with a continuously growing understanding of its variability at the global scale. This variability results from various modes of accretion that are controlled by magma supply to the ridge, which in turn is related on the first order to spreading rate (e.g., Chen, 1992; Bown and White, 1994; Dick et al., 2003; Coogan et al., 2007; Cannat et al., 2009; Ildefonse et al., 2014; Karson et al., 2015).

A significant feature of the lower fast-spreading oceanic crust is a coherent modal layering. This is well-known from ophiolites since decades (Nicolas, 1989) and was studied in more details for the Samail ophiolite more recently, in order to shed light on the emplacement mechanism of deep crystal mushes and on the layer-forming processes. (e.g., Jousselin et al., 2012; Mock et al., 2020c). The occurrence of modal layering in lower crustal gabbros was also confirmed in 2014 from recent fast-spread crust by an IODP (International Ocean Discovery Program) Expedition into the lowermost crust at Hess Deep in the Eastern Pacific (Gillis et al., 2014b). The steady-state axial magma reservoir, and related crustal accretion mechanism(s) that are necessary to account for the production of a continuous, layered crust at mid-ocean ridges, were first conceptualized as relatively large magma bodies, up to ~10 to 20 km large across the ridge axis, and ~4 km thick at the axis, lying below the sheeted dike complex (e.g., Cann, 1974; Pallister and Hopson, 1981; Nicolas et al., 1988). These models were largely constrained by observations made in ophiolites and were different in terms of magma chamber shape and symmetry (i.e., Δ-shaped in Cann, 1974 or V-shaped in Pallister and Hopson, 1981). Using thermal constraints, Sleep, 1975 proposed that most of the chamber was filled with magmatic mush, and that melt-rich magma would be limited to the top, below the sheeted dykes. This prediction was confirmed a few years later, with the first seismic reflection images of the top of a thin axial magma chamber beneath the Valu Fa ridge in the Lau Basin (Morton and Sleep, 1985) and the East Pacific Rise (e.g., Herron et al., 1980; Hale et al., 1982; Detrick et al., 1987; Vera et al., 1990). Below this axial magma lens was pictured a seismically attenuated domain, which was inferred to correspond to a melt-poor magmatic mush (e.g., Orcutt et al., 1976; Harding et al., 1989; Caress et al., 1992; Dunn et al., 2000). About 30 years ago, two competing end-member models were then proposed for building the lower, gabbroic crust in this domain: the "gabbro glacier model" (Henstock et al., 1993; Phipps Morgan and Chen, 1993; Quick and Denlinger, 1993) postulates that the entire lower crust is formed by flow of mushy material downward and outward from the single, shallow axial magma lens, and the "sheeted sill model" focuses on in-situ formation of the lower crust by sill intrusions with a small region of cumulates from the axial melt lens beneath the sheeted dikes (Kelemen et al., 1997; Kelemen and Aharanov, 1998). A combination of these two end-member models was proposed by Boudier et al. (1996). While the gabbro glacier model does not require deep hydrothermal circulation close to the ridge axis, a deep cooling system is needed to sustain a sheeted sill model (e.g., Maclennan et al., 2005). Therefore, the estimation of cooling rates along the lower oceanic crust play a pivotal role in the evaluation of possible accretion mechanisms.

These accretion models can be used for predicting contrasted vertical trends of petrology, deformation, cooling rates, and alteration in the gabbroic crust (e.g., Ildefonse et al., 2010), which still remain to be fully tested in ophiolites and by deep drilling in intact fast-spread crust (e.g., Teagle et al., 2012; Ildefonse et al., 2014). Coogan et al. (2002a, 2007) and Faak et al. (2015) investigated cooling rates as a function of depth in the Samail ophiolite and at the EPR, respectively, and found that the cooling rate decreases down section, as predicted by thermal modeling of Maclennan et al. (2005) for a conductively cooled gabbro glacier. They argue that the slow cooling rates, in particular within the

lower crust of the Samail ophiolite (Coogan et al., 2002a, 2007), do not facilitate in-situ crystallization because the latent crystallization heat is assumed to prevent a significant amount of crystallization in a slowly cooled environment.

Petrological studies in the Samail ophiolite suggest deep in-situ intrusions as the main accretion mechanism for the lower crust (e.g., Kelemen et al., 1997; Müller, 2016; Koepke et al., 2017). While Kelemen et al. (1997) studied gabbroic sills that intruded mantle rocks in the crust-mantle transition zone, and also used petrological data by Browning (1984), Müller (2016) and Koepke et al. (2017) sampled a profile over the entire lower crust along Wadi Gideah in the Wadi Tayin block. Along this profile, Mg#s in bulk rock, olivine and clinopyroxene, as well as the anorthite content in plagioclase show decreasing trends up section indicating melt fractionation along the lower crust, as expected to occur within crystallizing sills. The low, and down section decreasing cooling rates in the lower crust documented by Coogan et al. (2002a, 2007) are inconsistent with the interpretation of sill crystallization at depth. In contrast, the variable faster cooling rates obtained for layered gabbros of the Samail ophiolite by VanTongeren et al. (2008) indicate that the thermodynamic requirement of latent heat removal from the lower crust enabling in-situ crystallization can be fulfilled.

Because rock fabrics provide helpful information on deformation processes, which in turn can be interpreted in terms of crustal accretion mechanisms, Nicolas et al. (2009) and Morales et al. (2011) investigated microstructures in gabbros and anorthosites, respectively, from the root zone of the sheeted dyke complex and the underlying foliated gabbros in the Samail ophiolite. They found crystallographic preferred orientations (CPO) which indicate subsiding of a crystal mush from the axial melt lens, consistent with the gabbro glacier mechanism forming the upper part of the lower crust in the Samail ophiolite. This conclusion is consistent with the results of Brown et al. (2019), who analyzed microstructures in the upper 800 m of the recent lower oceanic crust from Pito Deep at the EPR. They propose that the analyzed gabbroic rocks crystallized within the axial melt lens (AML) and subsequently subsided from the AML downward to form at least the upper 800 m of the plutonic crust. Similarly, Perk et al. (2007) investigated the microstructures, petrology and geochemistry of the uppermost 1000 m below the sheeted dike complex at Pito Deep, and concluded that gabbros might have crystallized at shallow depths, and subsequently subsided and formed the observed foliated and layered textures within the uppermost 1000 m of the gabbros. However, they compare their data with those from Hess Deep and suggest that the formation of the latter may have occurred by subsiding crystal mush in the shallow part of the lower crust, and by in-situ crystallization deeper in the crust. VanTongeren et al. (2015) studied plagioclase CPO along the entire lower crust in Wadi Khafifah (Wadi Tayin block, Samail ophiolite) and found no down section trends, neither in fabric strength nor in lineation orientation that are predicted in the gabbro glacier model. Hence, their data support the sheeted sill model for the studied crustal section. Seismic experiments performed at the Juan de Fuca Ridge (Canales et al., 2009), the Galapagos Spreading Center (Boddupalli and Canales, 2019) and the EPR (Marjanovic et al., 2014; Marjanović et al., 2015) provide evidence for the occurrence of small melt sills within the lower crust supporting the possibility of in-situ crystallization beneath the spreading center. A weakness of most of the abovementioned studies is that they either cover only parts of the lower oceanic crust (e.g., Perk et al., 2007; Nicolas et al., 2009; Morales et al., 2011; Faak et al., 2015; Brown et al., 2019) or provide a relatively low spatial resolution along the crust (Coogan et al., 2002a, 2007; VanTongeren et al., 2015; VanTongeren et al., 2008) making well-founded, unequivocal interpretations in terms of lower crustal accretion difficult.

Our objective in this paper is to test fast-spread crust accretion models by quantifying the vertical variability of CPO and Crystal Size Distribution (CSD) of primary silicate phases (plagioclase, clinopyroxene, olivine) in gabbroic rocks, as a qualitative proxy for strain and cooling, in the lower oceanic crust Wadi Gideah in the Samail ophiolite (Oeser et al., 2012; Garbe-Schoenberg et al., 2014;

Müller et al., 2014; Müller, 2016; Koepke et al., 2017). Our data provide a high spatial resolution along the entire gabbroic section exposed at Wadi Gideah. A further increase of the spatial resolution will also be reached in upcoming publications by integrating drill core data in the frame of the Oman Drilling Project (see below; Kelemen et al., 2020). For the drill sites within the layered gabbro and in the transition between layered and foliated gabbro, the Wadi Gideah was chosen because it displays a continuous crustal section from the crust/mantle boundary to the sheeted dike horizon in a region (the southern Wadi Tayin massif) that is arguably not disturbed by any secondary magmatic event such as large intrusions of wehrlites or gabbronorites (e.g., Goodenough et al., 2014), and which shows petrographic/petrologic features similar to gabbros from the East Pacific Rise (e.g., Koepke et al., 2011; Mueller et al., 2017; Müller et al., 2014).

3.2 Geological background: the Wadi Gideah reference section

The samples investigated here are a subset of a sample suite collected over four field campaigns along Wadi Gideah in the Wadi Tayin block of the Samail ophiolite (e.g., Pallister and Hopson, 1981; Nicolas et al., 2000; Figure 3-1), with the aim of constructing a complete analytical dataset for a reference section in an analogue to fast-spreading centers (Oeser et al., 2012; Garbe-Schoenberg et al., 2014; Müller et al., 2014; Müller, 2016; Koepke et al., 2017). Beside the microstructural data presented herein, the results of detailed petrographic and petrological, trace element and isotopic, as well as crystallization temperature studies will be published soon qualifying the Wadi Gideah section as a reference section of lower fast-spread crust in the Samail ophiolite. This reference section also provides the opportunity to integrate data from the drill cores GT1 and GT2 of the Oman Drilling Project (Kelemen et al., 2020), which are located in the same Wadi. The 400 m long gabbro sections from drill sites GT1 and GT2 are located in the layered gabbros and in the layered/foliated gabbro transition of the Wadi Gideah, respectively. Wadi Gideah drains southward from a divide located in the harzburgites of the mantle horizon (Figure 3-1A). The crustal section dips gently ~28° to the south (Pallister and Hopson, 1981), a value which is representative of the whole Wadi Tayin block (Nicolas et al., 1996).

3.3 Materials and Methods

3.3.1 Sample material

A subset of 68 samples (out of 293 samples for the whole reference section) was used for measuring CPO and CSD in this study (Table 3-1). The samples were initially obtained for geochemical analysis only, and were not oriented in the field with respect to the structural context. They were cut perpendicular to the foliation and parallel to the lineation of the samples, when visible. The analyzed samples span the entire lower crustal section, with 44 samples from the lower, layered gabbros (LG) and the Moho transition zone (MTZ), 16 samples from the foliated gabbros (FG), 5 samples from a transition zone between varitextured and foliated gabbros (VG/FG TZ), and 3 samples which are considered to represent the frozen AML (e.g., Mueller et al., 2017;Figure 3-1,Table 3-1). Wadi Gideah approximately parallels the inferred ridge axis which was mapped by Nicolas et al. (2000) about 10 km east of Wadi Gideah. The height above the base of the MTZ (in meters above MTZ; mam), was recalculated for each sample using the average 28° tilt of the section and the GPS coordinates of the
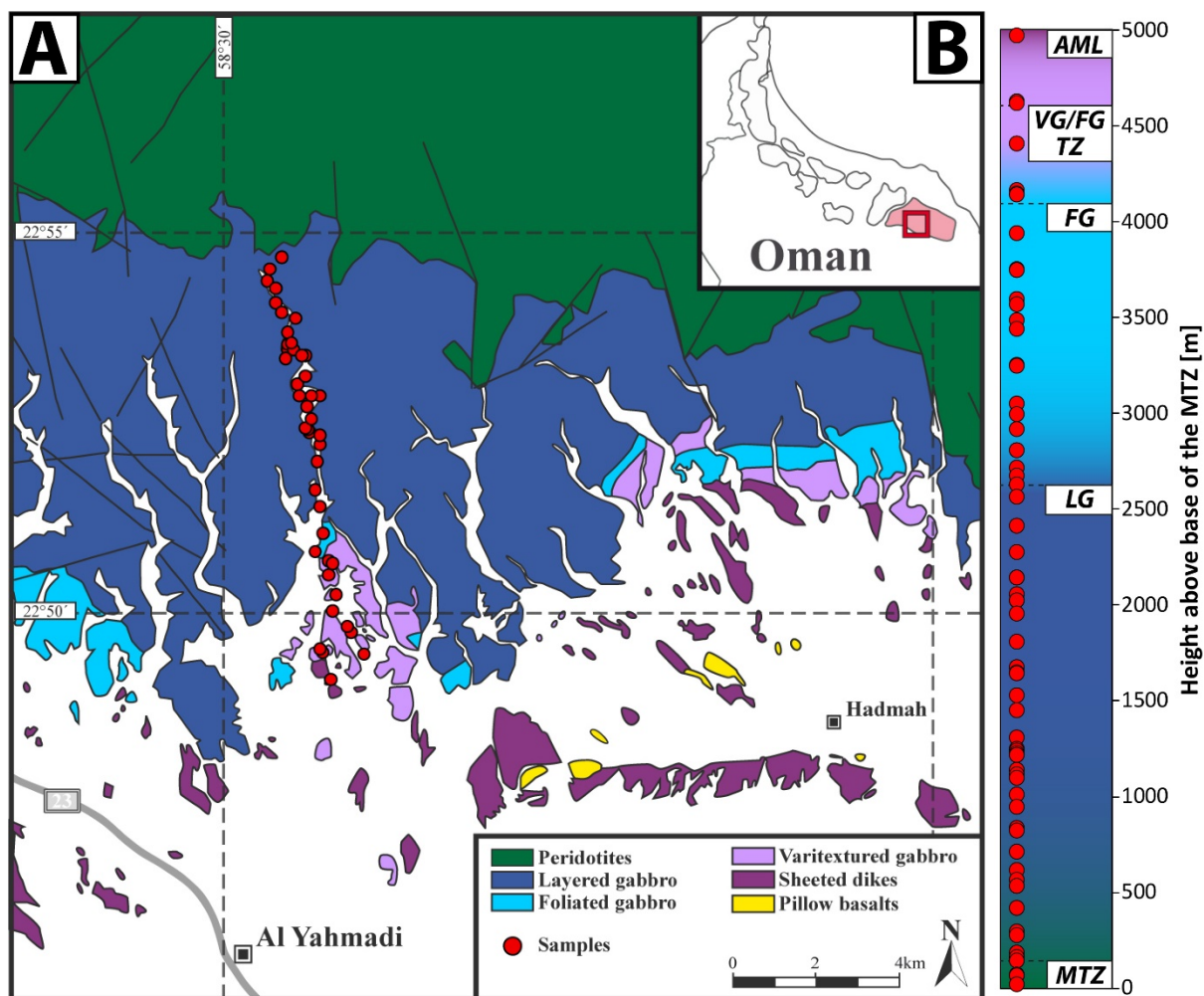
Figure 3-1 A) Simplified geological map (modified after Peters et al., 2005) of the working area in the Wadi Gideah, Wadi Tayin massif, Samail ophiolite. Red circles mark locations of the analyzed samples along the Wadi, crossing the entire crustal sequence from the mantle transition zone to the sheeted dikes (see depth plot on the right for more details; AML = axial melt lens, VG/FG TZ = varitextured/foliated gabbro transition zone, FG = foliated gabbro, LG = layered gabbro, MTZ = mantle transition zone). B) Overview of the entire ophiolite complex at the north-eastern coast of the Sultanate of Oman. The light red southernmost block is the Wadi Tayin massif, the red rectangle gives the cutout of A).

sample locations. The vertical interval between each sample averages 81 m (and ranges from 1 to 389 m). Samples were not oriented in the field because they were initially taken for geochemical analyses. The foliation measured in the field indicate average dips of 26° and 74° to the South-West for the layered gabbros and foliated gabbros, respectively, steepening from the lower to the upper foliated gabbros (e.g., Pallister and Hopson, 1981; Nicolas et al., 1996; Nicolas et al., 2000; VanTongeren et al., 2015). This is consistent with the general structure of the gabbroic crust described in Oman, with sub-horizontal layered gabbros, subparallel to the crust-mantle boundary, and steep foliated gabbros (e.g., Nicolas et al., 2000). Mineral foliations in the LG unit are subparallel to the dm-scale layering. The orientation of the modal layering was measured by Zihlmann et al. (2018) in a stratigraphic horizon <500 m above and below a large fault zone at approximately 1200 mam in Wadi Gideah and is 154/38° dipping to the South-East. This is consistent with previous field studies in the Wadi Tayin massif (e.g., Pallister and Hopson, 1981). Regardless of the dm-scale modal layering, which can hardly be observed in thin sections, LG and FG can be distinguished at the thin section scale by their grain size, which is ~200 μm on average for plagioclase in the foliated and ~310 μm on average in the layered gabbros.

The LG transition to FG upward, at about 2600 mam, through a diffuse, <100 m thick zone where LG and FG are mixed, and where the foliation rapidly steepens, as commonly described in many sections of the ophiolite (e.g., MacLeod and Yaouancq, 2000). Up-section, FG give way to varitextured gabbros from ~4150 mam. These isotropic rocks are called "varitextured" due to their strong heterogeneity in texture. They are highly variable in grain size, texture and chemical/modal composition (e.g., MacLeod and Yaouancq, 2000; France et al., 2009).

3.3.2 Crystallographic preferred orientations

Plagioclase, clinopyroxene and olivine CPO were measured using the Electron Back-Scattered Diffraction (EBSD) technique (e.g., Prior et al., 2009), using a JEOL JSM-5600 Scanning Electron Microscope (SEM) at Géosciences Montpellier. The system is equipped with an Oxford/Nordlys EBSD detector; the diffraction patterns were collected using the Channel 5® software suite, and later the AZtec software from Oxford Instruments. The SEM was used at an accelerating voltage of 15 kV. Crystallographic orientation maps were obtained for each sample, covering about 80% of a thin section (2.5 cm x 4 cm) with a sampling step size ranging from 14 to 35 μm. The indexing rate (fraction of patterns that are automatically indexed during mapping) ranges from ~25 % to 94 % in the raw maps (75 % on average). The raw data contains all indexed pixels with a mean angular deviation (i.e., the angle between the acquired diffraction pattern and the indexing solution proposed by the software) ≤1°. A first stage of post-acquisition data processing was done using the Tango software of the Channel 5® suite to increase the quality of the maps. It consists of removing isolated pixels (either non-indexed, or indexed as a given phase and surrounded by pixels indexed for another phase), and filling non-indexed pixels that have a minimum of 5 neighbor pixels with the same orientation. The EBSD data sets were then processed using MTEX (version 5.2.3), a free Matlab toolbox for analyzing and modeling crystallographic orientations (http://mtex-toolbox.github.io; Hielscher and Schaeben, 2008; Bachmann et al., 2010). We used MTEX to identify grains and produce maps from the EBSD data, calculate pole figures of plagioclase, clinopyroxene and olivine, analyze the crystallographic misorientations within grains, and calculate CPO strength and symmetry indices. A minimum of 100 grains is required to provide accurate fabric strength analyses (Ismaıl and Mainprice, 1998). We therefore plotted only data and contoured pole figures from measurements were at least 100 grains of a phase have been analyzed.

Grains were identified from the EBSD data by choosing a 10° threshold, over which the misorientation between two adjacent pixels indexed for the same phase is assumed to be a grain boundary. Grains that have a surface smaller than 5 pixels could be erroneous measurements, and were removed from the data set. Twins in plagioclase have been distinguished from grain boundaries by filtering out the 180° (± 5°) misorientations between adjacent grains around the twin rotation axes (crystallographic axes and poles [100], (100), [010], (010), [001] and (001)). Twins in clinopyroxene have been distinguished from grain boundaries by filtering out the 180° (± 5°) misorientations between adjacent grains around the crystallographic axes [100] and [001]. Pole figures were calculated using both the pixel data set from EBSD map data, and the average crystallographic orientation for each grain or each twinned domain in case of twinned grains. The second option can be preferred to avoid the overrepresentation of larger grains when the grain size distribution is heterogeneous at the thin section scale. We used this second option for clinopyroxene and plagioclase, and the pixel data (first option) for olivine. The intense mesh-serpentinization of olivine leads to misguided separation of primary grains into several "subgrains". Therefore, the average orientation option is misleading for olivine. The CPO strength for each phase is determined using both the J index (J) of the Orientation Distribution Function that is exclusively based on crystallographic orientations (e.g. Bunge, 1982; Mainprice and Silver, 1993), and the M-index (Skemer et al., 2005), based on the misorientation angle

distribution. J varies between 1 (for a uniform distribution) to infinite (for a single crystal); M varies from 0 to 1 (see Mainprice et al., 2015, for the details of J and M calculations, and for a comparison between these two indexes). The Orientation Distribution Function was calculated using the "de la Vallee Poussin" kernel with a halfwidth of 10° (Schaeben, 1999; Mainprice et al., 2015).

The symmetry of the CPOs is determined using the BA-index (BA) for plagioclase and BC-indices (BC) for clinopyroxene and olivine, which are calculated from the Point (P), Girdle (G) and Random (R) indices that are themselves calculated from the eigenvalues ($\lambda 1 \geq \lambda 2 \geq \lambda 3$, with $\lambda 1 + \lambda 2 + \lambda 3 = 1$) of the orientation tensor for each pole figure (Vollmer, 1990; Satsukawa et al., 2013; Mainprice et al., 2015):

$$P = \lambda_1 - \lambda_3, \ G = 2(\lambda_2 - \lambda_3), \ R = 3\lambda_3, \qquad \text{Eq. 3.1a}$$
$$BA = \tfrac{1}{2}[2 - \{P_{(010)}/(G_{(010)} + P_{(010)})\} - \{P_{[100]}/(G_{[100]} + P_{[100]})\}], \qquad \text{Eq. 3.1b}$$
$$BC = \tfrac{1}{2}\,[2 - \{P_{(010)}/(G_{(010)} + P_{(010)})\} - \{P_{[001]}/(G_{[001]} + P_{[001]})\}]. \qquad \text{Eq. 3.1c}$$

In a plagioclase CPO that results from magmatic flow, the foliation is classically marked by a preferred orientation of planes (010), and the lineation by a preferred orientation of axes [100] (e.g., Satsukawa et al., 2013; Mock et al., 2020c). BA is 0 for a perfect axial-B CPO, an oblate (planar) fabric defined by a strong point alignment of (010) with a girdle distribution of [100], and it is 1 for a perfect axial-A CPO, a prolate (linear) fabric with a strong point maximum concentration of [100], and parallel girdle distributions of (010) and (001). BA is 0.5 for the intermediate p-type CPO with point maxima in [100], (010) and (001) (Satsukawa et al., 2013). With pyroxene and olivine, the situation is similar, except for the magmatic lineation that is then marked by the preferred orientation of [001] axes. Hence we use BC, to characterize the variations between a perfect oblate (BC = 0) and a perfect prolate (BC = 1) CPO. BA and BC are only presented for those samples that show a significant CPO. Therefore, a few samples with pole figures indicating no fabric are not included into BA or BC plots.

In EBSD maps, the misorientation within grains is quantified using four parameters, the misorientation to the mean (M2M), the grain orientation spread (GOS), the kernel average misorientation (KAM), and the grain average misorientation (GAM). M2M is, for each pixel within a grain, the angle between the crystallographic orientation of that pixel and the average crystallographic orientation of the grain. It visualizes the misorientation between domains separated by subgrain boundaries or the progressive misorientation related to undulose extinction in optical microscopy. The GOS is, for each grain, the average M2M. The KAM is, for each pixel, the average misorientation (lower than 10°) of the nearest n neighbors (n = 4 here, see Wright et al., 2011 for a review of misorientation parameters). The GAM is, for each grain, the average KAM.

3.3.3   Crystal size distributions

For the determination of CSD, we used the software CSDCorrections 1.60 provided by Higgins (2000). The inserted parameters length, width, area and angle of every plagioclase crystal were obtained by EBSD measurements. We used the ellipse minor axis length for the calculation. An average value of the plagioclase roundness was calculated from the EBSD data used for the CSD determination with the software. On the basis of the 2-dimensional (2D) data obtained for every indexed grain, we calculated the 3-dimensional (3D) aspect ratio of plagioclase following the procedure proposed by Higgins (1994) normed to 1 for the short axis length. Using the equation

$$L_{Intermediate}/L_{Short} = l/w \qquad \text{Eq. 3.2}$$

where L is the 3D length of the indexed parameter, l is the 2D length and w the 2D width of the grain, the ratio of the 3D intermediate to short axis was calculated for every plagioclase grain with a width of at least 30 μm (= thin section thickness; c.f., Higgins, 2000). For calculating the 3D long axis length, we used the skewness defined by

$$skewness = (mean(w/l)_{2D} - mode(w/l)_{2D}) \, / \, SD(w/l)_{2D} \qquad Eq.\ 3.3$$

(Higgins, 1994) where (w/l)2D is the ratio of the 2 dimensional parameters width to length and SD is the standard deviation. The ratio of the 3D intermediate to long axes lengths could be determined using Figure 5 in Higgins, 1994. Hence, the 3D long axis length was calculated by division of the 3D intermediate length (obtained from Eq. 2) by the 3D intermediate to long axis ratio (obtained from Eq. 3). With these data, a first calculation of the CSD was performed for a massive fabric. The resulting alignment factor was then used as qualifier of fabric (i.e., lineation intensity) for a second CSD calculation taking the previously calculated lineation intensity into account.

3.4 Results

The parameters calculated from the EBSD data are presented for plagioclase, clinopyroxene, and olivine in the Supplementary Table 1 (Mock et al., 2020b). Examples of maps from varitextured, foliated and layered gabbros are presented in Figure 3-2.
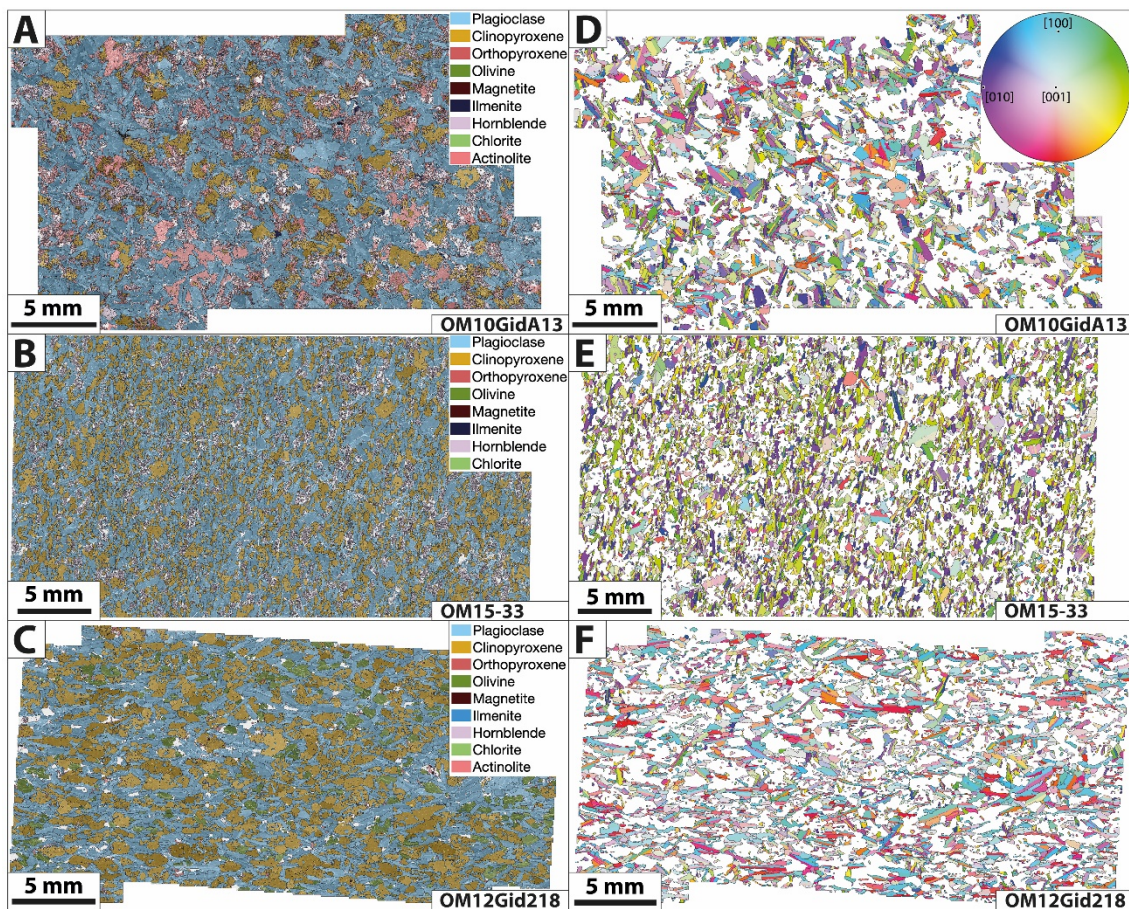
Figure 3-2   A – C: Phase maps acquired by EBSD representing a varitextured gabbro (A), a foliated gabbro (B), and a layered gabbro (C). D – F: orientation maps of plagioclase from the same samples. The inverse pole figure color coding uses the x axis of the maps (horizontal) as a reference direction. Sample names and scale bars are given at the base of each image.

3.4.1 General observations

The lithological units are defined following previous field studies (e.g., Pallister and Hopson, 1981; Nicolas et al., 1996), and are consistent with field observations along the Wadi Gideah section (Oeser et al., 2012; Garbe-Schoenberg et al., 2014; Müller et al., 2014; Müller, 2016; Koepke et al., 2017). The samples located between 4969 and 4627 mam which we interpret as frozen fillings of the dynamic AML are fine-grained, isotropic gabbros which we named dolerite in this study, and one anorthosite in sample OM10_Gid_A12_2a (Table 1). Below the AML, the varitextured gabbros (VG) transition to the FG unit over the VG/FG TZ from 4617 to 4144 mam. Olivine gabbros and olivine-bearing gabbros with occasional poikilitic hornblende or clinopyroxene containing plagioclase and variable grain sizes characterize this unit. Orthopyroxene and granular oxides are present in some of the samples. Both hornblende and oxide are also present in the underlying FG unit from 4138 to 2671 mam which mainly consist of plagioclase and clinopyroxene. Some relicts of highly altered olivine and small amounts of orthopyroxene in some samples complete the mineral compositions in the FG unit. These rocks show a strong foliation and their grain sizes are constantly smaller than below within the LG unit. The occurrence of oxides, hornblende and orthopyroxene systematically decreases down section in the FG unit. These phases are nearly absent in the LG unit below, which is dominated by mainly olivine gabbros
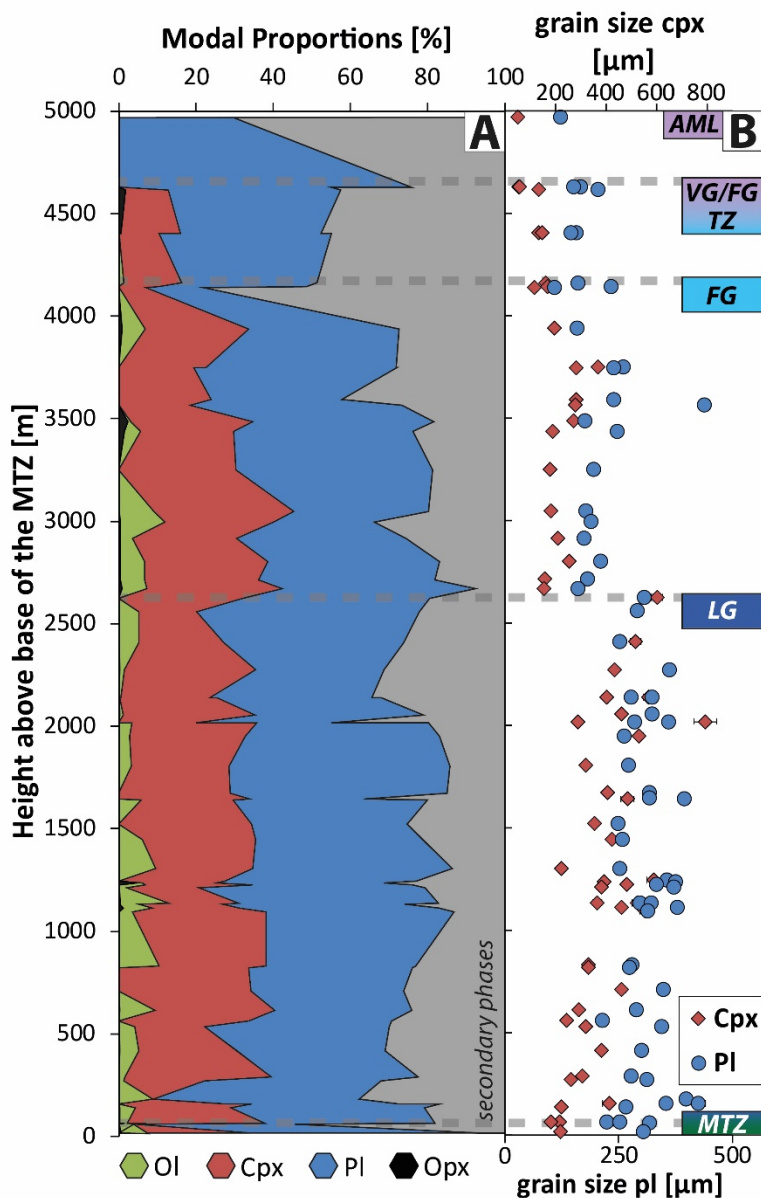
Figure 3-3 A) Modal proportions of the phases plagioclase (blue), clinopyroxene (red), olivine (green), orthopyroxene (black), and secondary phases (grey) estimated by EBSD analysis. B) 2D grain sizes of plagioclase (blue circles) and clinopyroxene (red diamonds); A and B plotted versus height above base of the MTZ. The grain size is plotted as diameter of a circle with the area of the analyzed grain. Black bars give the standard error (smaller than the symbol in most cases). Note different axes for plagioclase and clinopyroxene. Lithological units are given at the right (see text for definition of the abbreviations). Dashed horizontal lines mark transitions between lithological units.

with minor gabbro from 2625 to 180 mam. The average grain size of the LG unit is clearly higher than in the FG unit, and their fabric is not only foliated but also shows an increasing lineation intensity down section. Samples from the MTZ come from 157 to 16 mam and show gabbro, olivine gabbro and troctolite. They have variable grain sizes, locally with cm-sized plagioclase and clinopyroxene. Their fabric symmetry reveals both foliation and lineation, which are best-defined by plagioclase preferred orientations.

As shown in Figures Figure 3-2 and Figure 3-3A, secondary phases (e.g., actinolite, chlorite, hornblende) represent a significant fraction of the modal composition, indicating a degree of alteration between 10 and 80 % that decreases down section. In particular, the olivine content (up to 16.7 %) has to be taken with caution since olivine is highly sensitive to serpentinization leading to the underestimation of the primary olivine abundance by the EBSD. Regardless of the sensitivity of olivine to serpentinization and the increasing degree of alteration up section, the primary olivine content decreases up section, as observed petrographically. Along the entire crust, plagioclase (15 – 76 %) and clinopyroxene (0 – 38 %) form the most abundant primary phases, both showing significant variability along the sampled section. Orthopyroxene was found in several samples with low abundances (up to 6 % in a single sample from the LG unit); it is more abundant in the FG and VG units. The primary oxide content (magnetite and ilmenite) is generally low, reaching a maximum of 1.5 % in sample OM10-Gid-A17-1 within the FG unit. The abundance of secondary phases, hence the degree of alteration, increases above 3000 mam at the expense of the primary major components plagioclase and clinopyroxene, which both show decreasing contents above 3000 mam. Grain size (Figure 3-3B) is given by the diameter of the equivalent circle (i.e., with the same area as the corresponding grain). Plagioclase and clinopyroxene grain sizes are significantly coarser in the LG unit (beneath 2600 mam) compared to the FG unit and the VG/FG TZ (Figure 3-3B). The plagioclase average grain size in the VG/FG TZ and FG unit is about 200 µm; it increases to 310 µm in the LG unit beneath 2600 mam. Clinopyroxene forms coarser grains with 258 µm on average above 2600 mam, and 410 µm on average below. The deformation features indicate that brittle or plastic deformations are very weak or absent in most of the samples and that magmatic deformation is dominant throughout the entire section. This is mostly indicated by very low misorientation angles (Figure 3-7) and the paucity of petrographic indicators for plastic deformation, such as kink banding or undulose extinction in olivine. The dominance of magmatic deformation implies that the microstructures we observe in our samples can be ascribed to the primary emplacement of crustal material and are not or only weakly affected by any late stage tectonic process.

3.4.2 Crystal Size Distributions

CSD results for plagioclase are shown in Figure 3-4. They are displayed in a conventional way (Figure 3-4C) with the population density (n; the number of crystals per volume in a size bin divided by the width of the size bin; Marsh, 1988; Garrido et al., 2001) as a function of the binned crystal size (3D length of the crystals). The CSD plots show linear trends in the mid to large grain sizes and a decreased population density of the finer grains leading to roughly convex upward trends (Figure 3-4C). Regression lines were calculated using at least three data points and taking a best fit quality of Q > 0.1 into account, as suggested by the CSDCorrections software (Higgins, 2000) for an acceptable regression quality. While the linear regression includes the maximum population density at small grain sizes within most of the gabbros of the AML, VG/FG TZ and FG units, it is restricted to the larger crystal sizes in the LG unit and the MTZ. The slopes of the regression lines as well as their intercept with the y-axis were plotted for every sample (Figure 3-4A and B). Marsh (1988) defined the slope of the regression line as measure of the product of overall population growth rate and mean age. The intercept with the
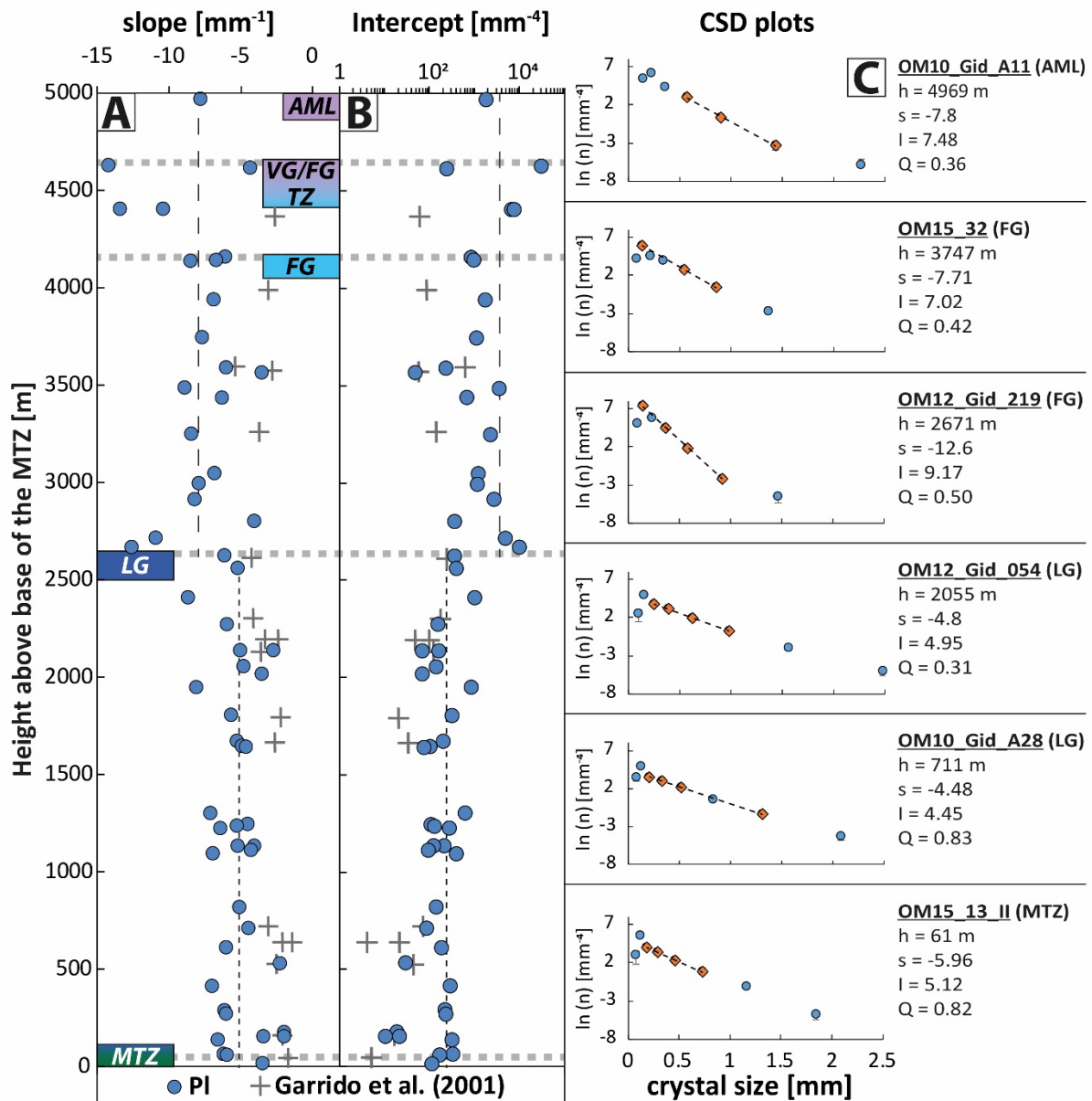
Figure 3-4 Results of crystal size distribution analysis. Slope (A) and intercept with y-axis (B) of the regression line interpolated from at least three data points of the crystal size distribution calculated after Higgins (2000). Blue circles are plagioclase data of this study, red crosses are data from Garrido et al. (2001). Dashed vertical lines give mean from the samples above 2600, dotted lines below 2600 m above the Moho (mam). C) shows representative CSD plots for plagioclase selected for every crustal unit. y-axis gives the population density which is the number of crystals per volume divided by the width of the size bin given on the x-axis (Marsh, 1988). Orange diamonds are used for calculating the regression line (dashed line). Sample name and corresponding crustal unit are given beside each plot. h = height above base of the MTZ, s = slope, I = y-axis intercept, Q = quality of the regression given by the CSDCorrections software (Higgins, 2000); Qmax = 1, Q > 0.1 is acceptable. Lithological units are given at the right. Dotted horizontal lines mark transitions between lithological units.

y-axis is defined as the nucleation density. The slope of the regression line reflects the nucleation rate (steeper slope means faster nucleation) for a constant growth rate (Marsh, 1988). It provides implications on the cooling rate of the systems since nucleation exponentially increases with faster cooling (e.g., Garrido et al., 2001).

Consistently with the 2D grain sizes obtained by EBSD, both plots show shifts at 2600 mam towards gentler slopes (Figure 3-4A) or lower intercepts (Figure 3-4B). The average slope in the

samples from the AML and the FG unit is -7.97; the steepest slope of -14.2 is in the VG/FG TZ unit, and the gentlest slope of -3.54 is in the FG unit. In the LG and MTZ samples, the average slope is -5.14, with the steepest slope of -8.66 in the uppermost LG unit and the gentlest slope of -1.98 in the lowermost LG above the MTZ. The intercept of the regression lines is plotted on a logarithmic scale in order to consider both very low and very high population densities. Its mean is 3663 mm-4 in the units above 2600 m with a minimum of 47 mm-4 in the upper FG unit and a maximum of 29437 mm-4 in the VG/FG TZ unit. In the sections below 2600 m, the mean of the intercept is 223 mm-4 with a minimum of 10.5 mm-4 in the lowermost and a maximum of 982 mm-4 in the uppermost LG. Maxima of the interception correspond to the lowest (and therefore steepest) slope and vice versa.

3.4.3   Fabric strength

The J and M indices show similar trends along the sampled section (Figure 3-5A). For the sake of simplicity, we describe and discuss the fabric strength using J only. Values of J calculated from average orientation data are slightly lower than those calculated from the pixel data, but show the same relative trends, which we focus on in this study. The depth plots of J for plagioclase and clinopyroxene are given in Figure 3-5A. With its low number of reliable results, due to the high degree of serpentinization and/or relatively small number of grains, the depth plot of J for olivine is meaningless, and is not presented. Plagioclase data show two distinct trends along the crustal section: the upper part from the dike/gabbro transition at 5000 mam down to 3500 mam is characterized by low and relatively stable J, up to 2.1. The second part beneath 3500 mam shows a stronger scattering, and higher values of J up to 5.1. Because of the significant change in the middle of the FG unit, which is also seen in the symmetry indices (described below), we decided to distinguish the upper foliated gabbros (UFG), where fabric strength is constantly weak, from the lower foliated gabbros (LFG) with increasing and more scattered fabric strengths. J for clinopyroxene shows a similar behavior with relatively stable values <2.5 from the dike/gabbro transition down to about 2600 mam (Figure 3-5A). In the layered gabbros below 2600 mam, it is more scattered, and is generally higher, up to 4.84. There is a gentle trend of increasing fabric strength for both plagioclase and clinopyroxene with depth from the top of the LG unit to about 1000 mam. In the lowermost 1000 meters, close to the MTZ, the fabric strength of both phases remains more or less constant, and gently decreases in the MTZ samples.

3.4.4   Pole figures and symmetry

Representative pole figures for plagioclase and olivine CPO are shown in Figure 3-5C and a compilation of all pole figures is available in the PANGAEA database (Mock et al., 2020b). The trace of the foliation, corresponding to the preferred orientation of plagioclase (010), is plotted on pole figures of every phase. Plagioclase shows point maxima of (010) along the entire section, mostly correlated with point to girdle distributions of [100]. For quantifying the CPO symmetry, we used BA and BC for plagioclase and clinopyroxene, respectively (Figure 3-5B). Distinct trends along the crustal section are observed for both phases: the upper 1500 m of the section are dominated by more or less constant indices with an intermediate symmetry in the section from 5000 down to 3500 mam (BA ≈ 0.4 for plagioclase and BC ≈ 0.5 for clinopyroxene). These data indicate that a significant lineation is present within the VG/FG TZ and UFG units as already shown by the pole figures (Figure 3-5C). At ~3000-3500 mam, a foliation-dominated fabric is represented by a clear minimum of the symmetry indices in both phases (BA = 0.06 for plagioclase and BC = 0.13 for clinopyroxene). Below this horizon, the lineation component gradually becomes stronger down section in both phases, with intermediate to slightly lineated symmetries at the base of the crust with a BA of up to 0.68 for plagioclase and a BC of up to

0.64 for clinopyroxene. Most olivine CPO show [010] point distributions and [001] girdles, or also [001] point maxima. A few of the samples below 1446 mam have CPO with [100][010] point maxima, parallel to the [100](010) plagioclase CPO (e.g., sample OM15_19AII in Figure 3-5C).

The pole figure J indices (pfJ) of plagioclase and clinopyroxene (Figure 3-6) plotted versus the crustal height behave similar to J with very low values in the AML, the VG/FG TZ and the UFG unit. In the LFG and LG units, the values are widely scattered. The pfJ of those axes that represent the lineation ([100] in plagioclase, [001] in clinopyroxene) show slight increases down section from 3500 to 1000 mam.
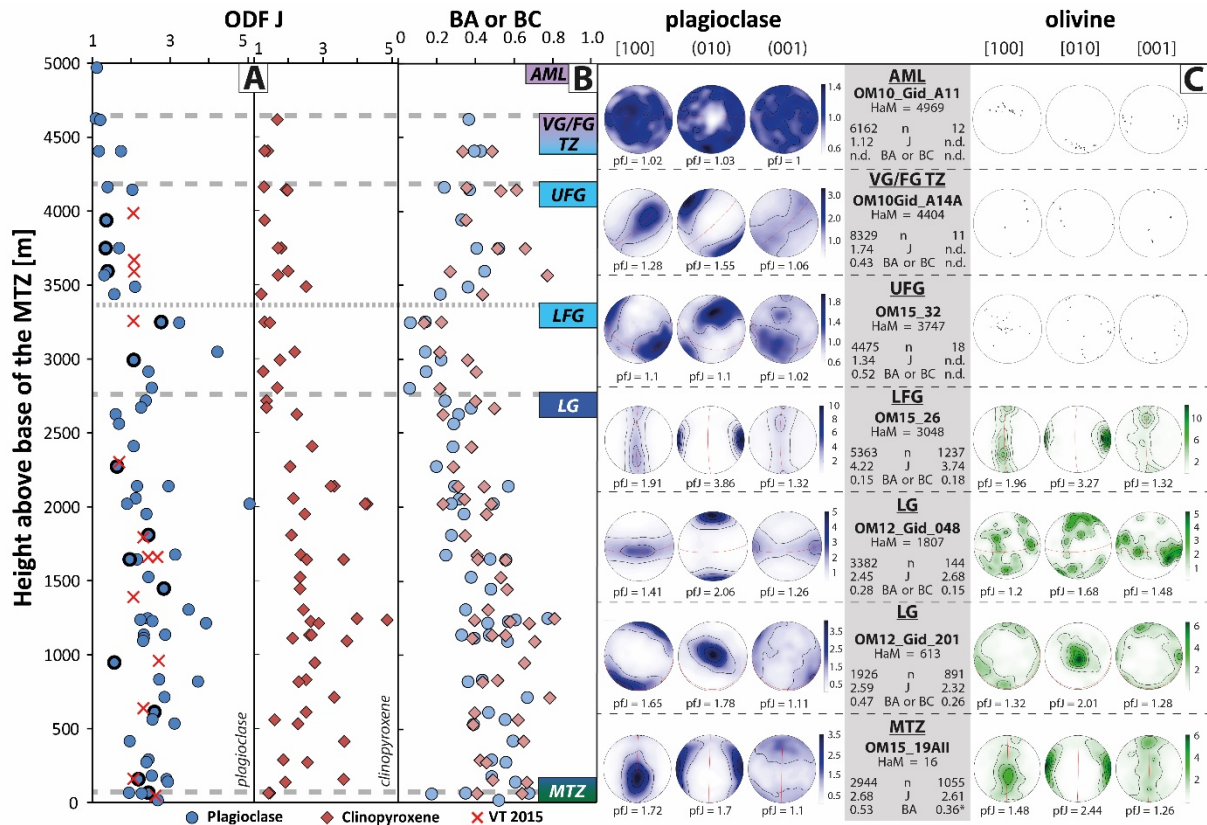
Figure 3-5 J indices (A) and BA or BC indices (B) of plagioclase and clinopyroxene plotted versus height above base of the MTZ. Plots show correlating trends with changes at 3500 m. Blue circles are plagioclase data, red diamonds are clinopyroxene data. Red crosses in A) are plagioclase data from VanTongeren et al. (2015; VT 2015). Plagioclase data with thicker contours are selected samples close to the stratigraphic height of VanTongeren's data. Their lower spatial resolution conceals a down section trend. Dashed horizontal lines mark transitions between lithological units. C) pole figures of [100], (010) and (001) of plagioclase (left, blue) and of [100], [010] and [001] of olivine (right, green) arranged by height above base of the MTZ. Representative pole figures for every lithological unit are selected. Sample information are given in the grey box with HaM = Height above the base of the MTZ in meters, n = number of indexed crystals, J = J-index of the orientation distribution function, BA = BA index, BC = BC index, pfJ = J-index of each pole figure (see text for details). Red line represents plagioclase foliation perpendicular to point maximum in (010). Note different color bars. Only the pole figures from samples with more than 100 indexed grains are plotted as contoured figures. n.d. means not determined due to very weak CPO visible in the pole figure. * indicates that we present the BA index for olivine, because the olivine fabric is most pronounced by [100][010] here. We separated the FG unit into upper foliated gabbros (UFG) and lower foliated gabbros (LFG) with respect to significantly differing fabric data; see text for details.

55

Table 3-1   *Fabric and misorientation data of the primary phases plagioclase, clinopyroxene, and olivine of the analyzed samples along Wadi Gideah arranged by height above the base of the MTZ.*

Sample	Unit[a]	lithology[b]	Height [mam][c]	Modal Proportions [%][d]						ODF J[e]			BA[f]		BC[f]	GOS[g]						GAM[h]					
				Pl	Cpx	Ol	Opx	Ox	sec	Pl	Cpx	Ol	Pl	Cpx	Ol	Pl	std err	Cpx	std err	Ol	std err	Pl	std err	Cpx	std err	Ol	std err
OM10_Gid_A11	AML	dol	4969	29.63	0.06	0.03	0	0.02	70.26	1.12						0.68	0.01	0.44	0.06	1.09	0.26	0.46	0.00	0.48	0.06	0.68	0.12
OM10_Gid_A12_2a	AML	an	4627	75.57	0.02	0.06	0.01	0.03	24.31	1.10						1.02	0.01	0.70	0.08	0.96	0.19	0.70	0.00	0.67	0.10	0.85	0.13
OM10_Gid_A12_2d	AML	dol	4627	54.72	0.08	0.1	0.01	0.03	45.07	1.09						0.74	0.00	0.39	0.03	0.69	0.05	0.56	0.00	0.41	0.04	0.50	0.05
OM10_Gid_A13	VG/FG TZ	ol-opx-hbl-b d-ox gb	4617	44.56	11	0.01	1.76	0.3	42.37	1.21	1.68		0.37			0.39	0.01	0.40	0.01	0.46	0.05	0.28	0.00	0.35	0.00	0.51	0.14
OM10_Gid_A14a	VG/FG TZ	ol-opx-hbl-b d-ox gb	4404	36.4	15.29	0.01	0.58	0.18	47.53	1.74	1.40		0.43	0.34		0.40	0.00	0.46	0.01	0.42	0.06	0.31	0.00	0.36	0.00	0.52	0.07
OM10_Gid_A14b	VG/FG TZ	hbl-ox-gb	4404	44.52	10.32	0.04	0	0.31	44.79	1.16	1.29		0.40	0.49		0.44	0.00	0.61	0.01	0.65	0.05	0.36	0.00	0.47	0.00	0.67	0.05
OM12_Gid_214	VG/FG TZ	ol-b d-ox gb	4161	34.89	14.88	1.36	0	0.24	48.61	1.39	1.28	3.86	0.24	0.35	0.68	0.39	0.00	0.38	0.01	0.31	0.03	0.34	0.00	0.30	0.00	0.26	0.02
OM10_Gid_A15	VG/FG TZ	hbl-ox-gb	4144	37.58	10.3	0.04	0	1.42	50.65	2.03	1.92		0.37	0.62		0.37	0.00	0.49	0.01	0.48	0.09	0.33	0.00	0.39	0.00	0.41	0.05
OM15_30	UFG	hbl-b d-ox gb	4138	14.69	6.84	0.11	0.01	0.75	77.61		1.95			0.53				0.40	0.01	0.63	0.11			0.32	0.00	0.60	0.09
OM10_Gid_A16	UFG	hbl-opx-b d-ox ol-gb	3939	38.86	26.88	6.01	0.78	0.02	27.45	1.36	1.30	1.86	0.33	0.35	0.47	0.48	0.00	0.51	0.01	0.44	0.02	0.40	0.00	0.43	0.00	0.40	0.00
OM10_Gid_A17	UFG	hbl-b ox-gb	3749	49.32	22.46	0.02	0	0.15	28.06	1.68	1.78		0.41	0.66		0.42	0.01	0.43	0.01	0.49	0.06	0.35	0.00	0.38	0.01	0.60	0.13
OM15_32	UFG	hbl-ox-gb	3747	51.95	19.15	0.03	0	1.07	27.79	1.34	1.68		0.52	0.52		0.53	0.01	0.45	0.01	1.07	0.24	0.35	0.00	0.32	0.01	0.75	0.09
OM10_Gid_A17_2	UFG	hbl-b ox-gb	3592	33.78	23.87	0.04	0	0.08	42.22	1.39	1.97		0.45	0.27		0.68	0.01	0.70	0.01	0.60	0.06	0.50	0.01	0.60	0.01	0.58	0.05
OM10_Gid_A17_1	UFG	hbl-b ox-gb	3565	53.98	18.1	0.13	0	1.53	26.25	1.31	1.69		0.52	0.77		0.56	0.01	0.60	0.01	0.66	0.04	0.41	0.01	0.48	0.01	0.66	0.03
OM15_27	LFG	ol-opx-hbl-b d-ox gb	3486	46.63	31.5	0.76	2.31	0.44	18.36	2.09	2.50		0.36	0.43		0.29	0.00	0.38	0.01	0.66	0.07	0.20	0.00	0.29	0.01	0.47	0.05
OM10_Gid_A18	LFG	hbl-opx-b ox-ol-gb	3438	46.36	24.12	4.18	1.41	0.04	23.89	1.56	1.20	2.37	0.22	0.44	0.58	0.33	0.00	0.40	0.01	0.43	0.01	0.30	0.00	0.38	0.00	0.43	0.01
OM15_33	LFG	d-ox hbl-gb	3249	50.75	30.38	0.01	0.01	0.05	18.79	2.76	1.31		0.14	0.23		0.42	0.00	0.37	0.01	0.90	0.18	0.37	0.00	0.29	0.00	0.63	0.11
OM10_Gid_A18_1	LFG	gb	3245	41.63	29.71	0	0	0	28.66																		
OM15_26	LFG	ol-gb	3048	34.93	36.18	9.02	0.12	0.04	19.71	4.22	2.18	5.08	0.15	0.22	0.17	0.29	0.00	0.29	0.00	0.48	0.02	0.24	0.00	0.23	0.00	0.30	0.00
OM12_Gid_217	LFG	ol-gb	2994	26.07	27.98	11.6	0.35	0.26	33.73	2.06	1.74	5.97	0.22	0.36	0.14	0.48	0.01	0.46	0.01	0.90	0.03	0.35	0.00	0.29	0.00	0.53	0.02
OM10_Gid_A18_2a	LFG	ol-gb	2915	43.88	26.98	3.07	0.43	0.01	25.64	2.44	1.26		0.15	0.41		0.36	0.00	0.57	0.01	0.52	0.03	0.25	0.00	0.34	0.00	0.35	0.01
OM12_Gid_218	LFG	ol-gb	2803	44.48	31.79	6.34	0.34	0.14	16.9	2.52	1.67	3.13	0.06	0.22	0.18	0.32	0.00	0.48	0.02	0.46	0.02	0.22	0.00	0.23	0.00	0.33	0.01

table 1 continued

Sample	Group	Type	No.																										
OM10_Gid_A19	LFG	ol-gb	2715	45.78	29.38	6.28	0.46	0.01	18.09	2.37	1.36	2.13	0.24	0.40	0.14	0.36	0.00	0.44	0.00	0.58	0.03	0.27	0.00	0.39	0.00	0.43	0.01		
OM12_Gid_219	LFG	ol-gb	2671	49.87	35.11	6.47	0.78	0.07	7.71	2.26	1.36	2.15	0.38	0.50	0.44	0.27	0.00	0.27	0.00	0.38	0.02	0.25	0.00	0.24	0.00	0.31	0.01		
OM12_Gid_57	LG	gb	2625	48.29	32.19	0	0	0	19.5	1.60	2.23		0.32	0.23		0.26	0.00	0.29	0.01			0.24	0.00	0.26	0.01				
OM15_24	LG	ol-gb	2560	57.61	14.88	5.08	0.15	0.07	22.21	1.69		7.45	0.29		0.24	0.27	0.00			0.79	0.09	0.21	0.00			0.37	0.01		
OM10_Gid_A20	LG	ol-gb	2409	46.59	22.02	5.11	0.11	0.01	26.17	2.06	2.67		0.29	0.38		0.31	0.00	0.39	0.02			0.27	0.00	0.33	0.02				
OM12_Gid_055	LG	ol-gb	2274	33.27	33.86	1.27	0.23	0.03	31.32	1.64	2.05		0.20	0.29		0.32	0.01	0.32	0.01			0.26	0.00	0.29	0.00				
OM10_Gid_A21	LG	ol-gb	2139	41.9	23.07	0.55	0.01	0.01	34.46	2.14	3.31		0.30	0.31		0.51	0.01	0.50	0.01			0.43	0.00	0.46	0.01				
OM11_Gid_A21a	LG	ol-b d-ox gb	2139	42.35	24.99	0.27	0.05	0.32	32.01	2.96	3.21		0.57	0.45		0.51	0.01	0.62	0.02			0.37	0.00	0.42	0.01				
OM12_Gid_054	LG	ol-b gb	2055	43.49	34.15	0.98	0.19	0	21.19	2.11	2.14		0.32	0.34		0.28	0.01	0.32	0.01			0.23	0.00	0.26	0.00				
OM12_Gid_052	LG	gb	2019	35.08	20.01	0.01	0	0	44.89	5.05	4.26		0.49	0.48		0.61	0.01	0.58	0.02			0.50	0.01	0.45	0.01				
OM12_Gid_053	LG	ol-gb	2019	44.36	32.39	3.35	0.04	0.01	19.84	1.89	4.20		0.28	0.23		0.43	0.01	0.61	0.05			0.32	0.00	0.43	0.03				
OM11_Gid_A22	LG	ol-gb	1951	50.32	29.85	2.68	0.17	0	16.98	2.39	2.47		0.34	0.46		0.25	0.00	0.39	0.01			0.23	0.00	0.28	0.00				
OM12_Gid_048	LG	ol-gb	1807	57.21	25.26	3.21	0.09	0	14.24	2.45	2.08	4.42	0.28	0.35	0.31	0.31	0.00	0.44	0.01	0.60	0.04	0.25	0.00	0.38	0.00	0.49	0.01		
OM10_Gid_A23	LG	ol-b gb	1674	56.2	28.88	0.01	0	0	14.92	3.13	2.34		0.25	0.41		0.32	0.00	0.46	0.01			0.28	0.00	0.35	0.01				
OM12_Gid_045	LG	gb	1645	29.55	33.87	0	0	0.11	36.47	2.15	3.58		0.48	0.41		0.45	0.01	0.44	0.01			0.34	0.00	0.32	0.01				
OM12_Gid_044	LG	ol-gb	1642	50.3	23.87	5.69	0.09	0	20.05	1.95	2.51	4.91	0.56	0.56	0.41	0.40	0.01	0.46	0.02	0.77	0.04	0.31	0.00	0.34	0.01	0.58	0.01		
OM12_Gid_040	LG	gb	1523	40.32	34.39	0	0.01	0	25.29	2.45	2.32		0.38	0.53		0.40	0.01	0.74	0.03			0.32	0.00	0.56	0.02				
OM10_Gid_A24	LG	ol-gb	1446	43.14	29.37	5.99	0.12	0	21.36	2.84	2.34	4.34	0.48	0.56	0.19	0.39	0.01	0.56	0.02	1.31	0.07	0.30	0.00	0.42	0.01	0.62	0.02		
OM12_Gid_039	LG	ol-gb	1304	51.59	25.1	9.44	0.17	0	13.7	3.48	2.42	2.82	0.35	0.47	0.19	0.41	0.01	0.45	0.01	0.86	0.03	0.32	0.00	0.36	0.00	0.56	0.01		
OM12_Gid_026	LG	gb	1246	49.47	27.47	0	0.05	0.04	22.97	2.43	3.97		0.78	0.81		0.49	0.01	0.55	0.02			0.38	0.00	0.40	0.01				
OM12_Gid_027	LG	ol-opx-b gb	1237	43.5	19.17	1.47	4.59	0.01	31.25	2.23	4.84		0.61	0.40		0.33	0.00	0.39	0.01			0.29	0.00	0.38	0.01				
OM10_Gid_A25	LG	ol-gb	1225	41.38	27.9	6.75	0.05	0	23.91	2.55	2.64	5.44	0.57	0.58	0.49	0.40	0.01	0.59	0.02	1.25	0.09	0.35	0.00	0.50	0.01	0.70	0.02		
OM12_Gid_025	LG	ol-b gb	1212	58.54	18.75	1.89	0.09	0	20.73	3.93	2.87		0.47	0.68		0.36	0.01	0.58	0.04			0.28	0.00	0.34	0.01				
OM12_Gid_038	LG	ol-gb	1136	51.71	18.11	12.63	0.35	0	17.2	2.31	2.60	2.08	0.48	0.56	0.46	0.39	0.01	0.46	0.02	0.71	0.03	0.34	0.00	0.34	0.01	0.53	0.01		
OM15_1	LG	opx-b ol-gb	1134	47.09	21.73	5.01	0.19	0	25.97	2.86	2.66	5.49	0.33	0.49	0.27	0.33	0.01	0.43	0.02	0.71	0.06	0.27	0.00	0.27	0.01	0.40	0.01		
OM15_2	LG	opx-b ol-gb	1114	51.64	22.59	7.56	1.09	0.01	17.11	2.32	2.12	4.52	0.40	0.38	0.23	0.42	0.01	0.42	0.02	1.19	0.08	0.32	0.00	0.28	0.01	0.57	0.02		
OM10_Gid_A26	LG	ol-gb	1094	48.63	34.61	3.47	0.06	0	13.23	2.30	3.68		0.57	0.71		0.37	0.01	0.55	0.02			0.31	0.00	0.50	0.01				
OM12_Gid_035	LG	gb	1006	0.76	22.01	0	0	0.58	76.65																				

table 1 continued

Sample	unit[a]	lith[b]	h[c]	pl	cpx	ol	opx	ox	sec	J pl	J cpx	J ol	BA pl	BC cpx	ol	GOS pl	err	GOS cpx	err	GOS ol	err	GAM pl	err	GAM cpx	err	GAM ol	err
OM11_Gid_A26	LG	ol-gb	945	49.27	27.09	2.82	0.03	0	20.8																		
OM11_Gid_A27	LG	ol-gb	831	38.7	27.78	10.21	0.17	0	23.13	2.72	2.50	2.89	0.44	0.52	0.34	0.43	*0.01*	0.59	*0.02*	1.12	*0.05*	0.39	*0.00*	0.42	*0.01*	0.67	*0.01*
OM10_Gid_A27	LG	gb	819	42.33	33.67	0.01	0	0	23.98	3.71	2.29		0.37	0.44		0.66	*0.01*	0.65	*0.02*			0.44	*0.00*	0.40	*0.01*		
OM10_Gid_A28	LG	gb	711	39.6	34.18	0	0	0	26.22	2.85	3.31		0.67	0.79		0.81	*0.01*	0.80	*0.03*			0.59	*0.01*	0.52	*0.01*		
OM12_Gid_201	LG	ol-gb	613	35.58	31.01	9.02	0.3	0	24.09	2.59	2.50	3.07	0.47	0.40	0.15	0.54	*0.01*	0.64	*0.02*	0.96	*0.03*	0.42	*0.00*	0.38	*0.01*	0.61	*0.01*
OM10_Gid_A29	LG	gb	560	36.29	32.91	0	0	2.03	28.77	2.54	1.59		0.56	0.62		0.57	*0.01*	0.66	*0.01*			0.45	*0.00*	0.48	*0.00*		
OM11_Gid_A29	LG	ol-gb	532	47.73	18.2	3.96	0.16	0	29.96	3.12	2.27	2.38	0.39	0.39	0.70	0.52	*0.01*	0.59	*0.02*	0.89	*0.04*	0.40	*0.00*	0.42	*0.01*	0.61	*0.01*
OM11_Gid_A29_2	LG	ol-gb	416	38.1	25.64	5.02	0.19	0	31.05	1.96	3.60	4.01	0.60	0.65	0.48	0.41	*0.01*	0.55	*0.02*	1.13	*0.07*	0.35	*0.00*	0.42	*0.01*	0.65	*0.02*
OM15_10	LG	ol-gb	291	38.1	37.76	1.64	0.01	0.01	22.48	2.45	1.84	7.41	0.49	0.42	0.34	0.45	*0.01*	0.53	*0.01*	0.75	*0.06*	0.31	*0.00*	0.29	*0.00*	0.42	*0.02*
OM10_Gid_A30	LG	ol-b gb	272	45.36	20.96	1.25	0.01	0.51	31.91	2.39	2.54	5.16	0.56	0.46	0.29	0.80	*0.01*	0.75	*0.02*	0.71	*0.05*	0.53	*0.01*	0.51	*0.01*	0.52	*0.02*
OM15_21	LG	tr	180	53.29	0.11	8.84	0	0.12	37.63	2.52		3.89	0.49		0.41	0.61	*0.01*			0.99	*0.03*	0.40	*0.00*			0.59	*0.01*
OM15_15C_II	MTZ	gb	157	43.73	27.29	0	0	1.99	27	2.91			0.46			0.46	*0.01*					0.33	*0.00*				
OM15_15D_II	MTZ	gb	157	48.23	33.97	0	0.02	1.06	16.7	2.18	3.59		0.49	0.49		0.61	*0.01*	0.87	*0.04*			0.43	*0.01*	0.56	*0.01*		
OM10_Gid_A31	MTZ	ol-gb	138	50.23	24.67	3.98	0.3	0	20.82	2.95	1.90	3.52	0.61	0.67	0.32	0.50	*0.01*	0.63	*0.01*	0.67	*0.02*	0.30	*0.00*	0.42	*0.00*	0.52	*0.01*
OM15_18	MTZ	ol-b gb	65	44.03	35.69	1.96	0.18	0	18.13	2.44	1.46	3.51	0.35	0.41	0.35	0.39	*0.01*	0.44	*0.01*	0.51	*0.03*	0.23	*0.00*	0.24	*0.00*	0.30	*0.01*
OM10_Gid_A32	MTZ	ol-gb	64	45	23.14	5.57	1.41	0	24.87	1.94	1.42	2.54	0.68	0.64	0.26	0.45	*0.01*	0.48	*0.01*	0.56	*0.02*	0.28	*0.00*	0.36	*0.00*	0.35	*0.00*
OM15_13_II	MTZ	tr	61	40.99	0.79	3.78	0.03	0.07	54.34	2.27			0.18			0.42	*0.01*					0.35	*0.00*				
OM15_19AII	MTZ	ol-gb	16	59.2	26.3	7.06	0.56	0	6.88	2.68	1.80	3.03	0.53	0.60	0.27	0.38	*0.01*	0.43	*0.01*	0.48	*0.02*	0.28	*0.00*	0.31	*0.00*	0.35	*0.01*

[a] geological unit where the sample was taken: AML = axial melt lens, VG/FG TZ = varitextured/foliated gabbro transition zone, UFG = upper foliated gabbro, LFG = lower foliated gabbro, LG = layered gabbro, MTZ = mantle transition zone

[b] lithology estimated by primary modal proportions after Gillis et al. (2014)a with ol=olivine, opx=orthopyroxene, ox=oxide, hbl=hornblende, gb=gabbro, tr=troctolite, an=anorthosite, dol=dolerite; -b=bearing (1%-5%), d-=disseminated (1%-2%)

[c] crustal height of the sample in meters above the Moho

[d] phase proportions in % of all acquired pixels; pl = plagioclase, cpx = clinopyroxene, ol = olivine, opx = orthopyroxene, ox = oxides (ilmenite and magnetite), sec = summarized secondary alteration phases (hornblende, chlorite, actinolite); note that oxides may also be socondary products of serpentinization

[e] J index of the orientation distribution function quantifying the fabric strength of the phase per sample with 1 = random fabric and infinity = single crystal; J index of Pl and Cpx have been calculated using grain data, J index of olivine was calculated using grid data

[f] BA or BC index quantifying the pole figure symmetry of plagioclase and clinopyroxene, respectively. Varies between 0 and 1 with 0 = purely foliated and 1 = purely lineated symmetry; BA of Pl and Cpx have been calculated using grain data, BA of olivine was calculated using grid data

[g] grain orientation spread calculated as the angle between the crystallographic orientation of an individual pixel and the crystallographic orientation of the corresponding grain averaged per phase and sample

[h] grain average misorientation calculated as the average misorientation between individual pixel and its four nearest neighbored pixels averaged per phase and sample

italic values are standard errors (std err) of the corresponding GOS or GAM, respectively

empty cells belong to data sets which have not been used for plots due to bad data quality or a general lack of grains

Figure 3-6 pfJ indices of the three crystallographic axes 100, 010 and 001 of plagioclase (A-C) and clinopyroxene (D-F) plotted versus height above the base of the MTZ. Blue circles are plagioclase, red diamonds are clinopyroxene data. Red crosses are plagioclase data from VanTongeren et al. (2015). Lithological units are given at the right. Dashed horizontal lines mark transitions between lithological units. We separated the FG unit into upper foliated gabbros (UFG) and lower foliated gabbros (LFG) with respect to significantly differing fabric data; see text for details.

3.4.5   Misorientation

The deformation within grains is quantified using the GOS and GAM (Figure 3-7A and B). Generally, the GOS does not vary much in our sample suite. However, similarly to J, the GOS in plagioclase and clinopyroxene decreases at the transition from the UFG to LFG units and slightly increases down section from 3500 mam. The GOS in olivine is generally more scattered. It tends to increase down section with maxima of about 1.3° between 1500 and 1000 mam. Below 1000 mam, the olivine GOS decreases to 0.5° at the MTZ. The sample average GOS in both clinopyroxene and plagioclase are relatively constant at about 0.5° from 5000 down to 3500 mam where they decrease to 0.3°, and gradually increase down section to 0.8° at 800 mam. Below 800 mam, they decrease to 0.5° at the MTZ reproducing the trend observed in olivine. The sample average GAM in all three phases is more scattered than the GOS between 5000 and 3500 mam. Similar to the GOS, the GAM increases below 3500 mam towards a maximum of about 0.7° in olivine and 0.5 or 0.6° in clinopyroxene and plagioclase, respectively. Below 800 mam, the GAM of all phases gradually decreases to about 0.4° at the MTZ. Misorientation in olivine is generally higher than in the other phases. The gradual increase in the LG unit reproduces the increase of J along this section (Figures Figure 3-5 and Figure 3-7).
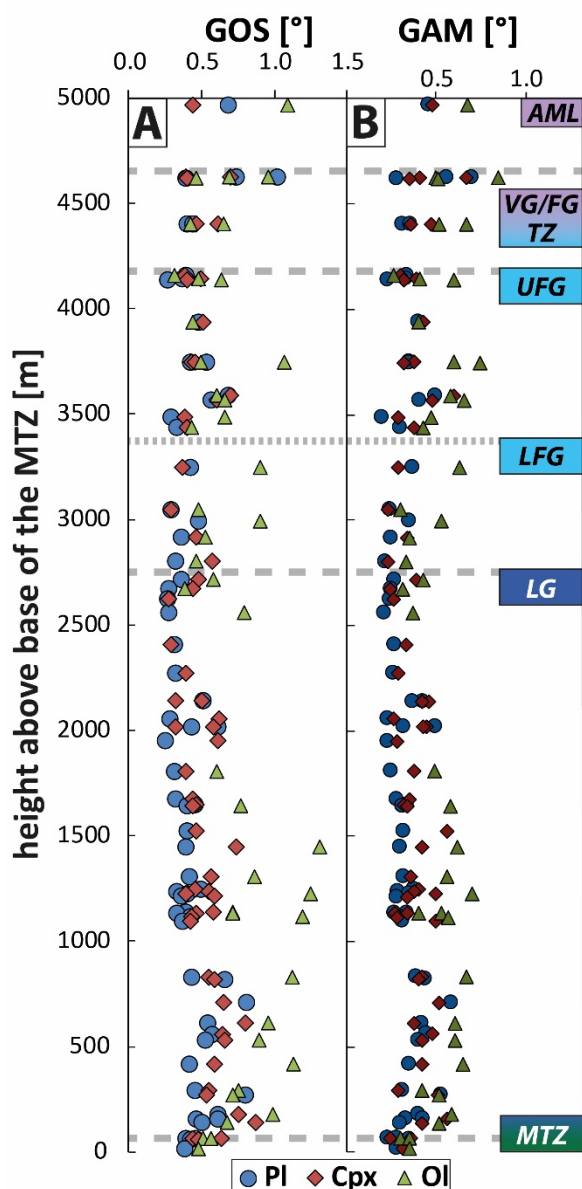
Figure 3-7   Depth plots of A) the grain orientation spread (GOS) of plagioclase, clinopyroxene, and olivine representing the degree of intracrystalline deformation averaged per phase and sample and B) the grain average misorientation (GAM) of plagioclase, clinopyroxene, and olivine representing the intensity of sub-grain formation averaged per phase and sample. Dashed horizontal lines mark transitions between lithological units.

3.5   Discussion

As summarized in the introduction, apparently contradictory conclusions in several published studies lead to a still on-going debate about the lower fast-spread oceanic crust accretion mechanism(s). Our results obtained in Wadi Gideah provide an opportunity to test the accretion models presented in the introduction in terms of consistency with the microstructural features of the primary phases plagioclase, clinopyroxene and olivine. Magmatic deformation is the most dominant type of deformation in our profile. Low values (≤1°) for the mean angular deviation in all samples emphasize the high data quality, and the relatively high spatial resolution (one sample every 81 m on average) is unique for an entire crustal profile. Compared to previous fabric studies, the high density of our data allows us to identify trends along the crust that were not documented before. This qualifies this section to constrain crustal accretion processes for fast-spreading ridge systems beneath the paleo spreading center that produced the Samail ophiolite. Table 2 provides an overview of the crustal units

we identified in our reference section and compiles microstructural key features and their implications on magmatic processes leading to the emplacement of every unit.

Table 3-2   *Crustal units with some microstructural key features. See text for details.*

crustal unit[a]	Upper boundary (interpolated) [mam][b]	thickness [m]	general presence of foliation[c]	which mineral(s) mark the foliation?[d]	general presence of lineation[c]	which mineral(s) mark the lineation?[d]	comment	magmatic process
AML	5010	388	no		no		no fabric	frozen melt
VG/FG TZ	4622	481	weak	pl, (cpx)	weak	pl	1 sample shows only weak foliation and no lineation (sample OM10_Gid_A13)	in part frozen melt lens, in part mush suspension
UFG	4141	616					1 sample shows neither fol nor lin (OM10_Gid_A17_1)	mush suspension
LFG	3525	877	strong	pl, cpx, ol (if present)	no		uppermost (OM15_27) and lowermost (OM12_Gid_219) sample show also weak lineation in pl	more sill intrusions, not affected by mantle convection
LG	2648	2480	strong	pl, (occasionally cpx, ol)	weak-strong	pl, (occasionally cpx, ol)	intensity of lineation increases down section; individual samples fall off this trend (e.g., OM12_Gid_026; OM10_Gid_A26)	sill intrusion, in-situ; increasingly affected by down section
MTZ	168	168	weak-strong	pl, ol, (occasionally cpx)	no-strong	pl, (occasionally cpx, ol)	variable fabrics within the MTZ with differing lineation intensities	sill intrusion, sills with more melt are less affected by manltle convection

[a] AML = axial melt lens, VG/FG TZ = varitextured gabbro/foliated gabbro transition zone, UFG = upper foliated gabbros, LFG = lower foliated gabbros, LG = layered gabbros, MTZ = mantle transition zone

[b] crustal height of the upper boundary of every unit in meters above the base of the MTZ [mam]

[c] non-quantitative identifier of the present foliation or lineation with no, weak, strong, or very strong

[d] pl = plagioclase, cpx = clinopyroxene, ol = olivine

3.5.1 Re-evaluating end-member accretion models

Both microstructural features and CSD data show correlated changes within the FG unit between 2600 and 3500 mam (Figures Figure 3-3 – Figure 3-7). The changes at 2600 mam coincide with the transition between the FG and the LG units. Changes at ~3500 mam are located within the FG unit, separating the UFG unit from the LFG unit. The gabbro glacier model (e.g., Henstock et al., 1993) implies microstructural features that should be observed along the crust as a result of ductile flow. Primary phases are expected in the gabbro glacier model to show a sub-vertical lineation close to the AML gradually rotating to horizontal and Moho-parallel at greater depths. Mineral lineations are described and measured in many field studies in Oman (e.g., Pallister and Hopson, 1981; Nicolas et al., 2000), and were used as an argument supporting a gabbro glacier model (e.g., Quick and Denlinger, 1993). Since the samples in our study were initially taken for geochemical analysis, they are not oriented and we are not able to use thin section orientations to document the global lineation trend at the crustal scale. However, both BA and BC, for pole figures of plagioclase and clinopyroxene, respectively, do not evolve continuously from oblate to prolate symmetry (i.e., from [100] girdles to [100] point maxima in plagioclase) down section as could be expected in a scenario involving ductile flow from the AML (Figure 3-5B). Instead, BA and BC show significant variations between adjacent samples. A similar conclusion was drawn by VanTongeren et al., 2015 using plagioclase CPO of gabbros from Wadi Khafifah (data points included in Figure 3-5A). The CPO strength in our study shows an increasing down section trend that may appear consistent with a subsiding crystal mush being transported in a ductile flow. However, the intuitive suggestion that the fabric strength continuously increases within such an environment is questionable. When cumulate mushes from the AML subside, the strength of a fabric does not necessarily depend on the transport distance. As pointed out by Vernon (2000), other parameters like melt fraction, viscosity of the melt and habit of the solids may control if and how strongly the crystals become aligned. Since the mechanical environment and the physical parameters of an assumed subsiding crystal mush may vary along the crust, fabric strength can also be variable along a crustal section with increasing strain. We therefore argue that a critical parameter is not necessarily the fabric strength but its symmetry. The latter varies along the crustal section: lineation is present in the VG/FG TZ and UFG unit, it is weak or even absent in the LFG unit, and increases with strong scattering in the LG unit. This behavior cannot be easily explained by local differences in physical properties of a crystal mush that is deformed by a gabbro glacier at the crustal scale. It rather suggests that the deformation regime changes along the studied profile.

The low J in the AML region, the VG/FG TZ and the UFG unit indicates a random fabric in the samples from the frozen AML to weak CPO showing both foliation and lineation in the samples from the VG/FG TZ and the UFG unit. Müller et al. (2017) studied an outcrop representing a frozen AML at the Southern end of Wadi Gideah, where our samples from the AML were taken, and found indicators for multiple sequences of heating and cooling events as well as dynamic vertical movement processes during the lifetime of the AML. They have also reported evidence for the AML intruding into the sheeted dikes at its highest position and for assimilation of hydrothermally altered roof material during relatively fast cooling of the AML resulting in the formation of the VG unit. France et al. (2009) and Müller et al. (2017) also showed that the geochemistry of most of the VG unit corresponds to frozen melts rather than to cumulate rocks. This indicates a regime with locally high melt fraction where crystals are free to rotate and previous crystal alignment, if present, is destroyed by melt perturbation or movement (e.g., Vernon, 2000), possibly resulting in the weak fabrics of our samples from the AML and the VG/FG TZ.

If we posit that crystallization of the lower crust occurred only, or at least to a major extent, in the AML, a mechanism is required to explain clear textural differences between the VG/FG TZ and FG

units and the LG unit. We observe a substantial and abrupt change from small to coarser grain sizes of plagioclase and clinopyroxene at the transition from the FG to LG units (Figure 3-3). The smaller grain sizes qualitatively imply a faster cooling of the VG/FG TZ and FG units and a slower cooled LG unit. Although this reflects in principle the findings of Coogan et al. (2002a, 2007), who documented by diffusion modeling that the cooling rate decreases down section in the lower crust of the Oman, they described a gradually decreasing trend. Our findings that grain sizes abruptly increase from the LFG to the LG units are similar to the results of Garrido et al. (2001) who studied plagioclase CSD in Wadi Khafifah. The plagioclase CSD in our study calls for a conditional change leading to abruptly smaller crystals above 2600 mam (Figure 3-4) and therefore confirms observations by Garrido et al. (2001) who found a significant change in plagioclase grain size at 2000 mam in Wadi Khafifah. Taking the slight variations in the crustal section thickness in the Wadi Tayin massif into account (e.g., Nicolas et al., 1996), the change in crystal size can be assumed to occur at a similar relative crustal height. As a general implication, Garrido et al. (2001) concluded that the difference in grain size is due to varying cooling rates along the crust with an abruptly accelerated cooling above 2000 m (in Wadi Khafifah) compared to the region below. Faster cooling of the uppermost gabbros is also consistent with the interpretation of Nicolas et al. (2009) deduced from gabbros below the root zone of the sheeted dyke complex that these must have been expelled fast through the wall of the AML therefore preserving textures of a fast cooling. Quick and Denlinger (1993) proposed that grain size is inversely related to strain, and found that the least strain predicted for uppermost gabbros is consistent with the high textural variety of the rocks near the AML. However, if grain size was inversely related to strain, the increasing strain down section in a subsiding mush should cause a gradual decrease of the grain size. The observed abrupt coarsening of grain sizes at 2600 mam does not agree with this expectation.

We found that the scenario of a downward ductile flow, inherent in the gabbro glacier model, is consistent with our microstructural data in the uppermost 1500 m of the gabbroic crust where small grained textures (Figure 3-3B) can be explained by an efficient hydrothermal cooling of the AML. Moreover, the observed foliated and lineated fabrics (Figure 3-5B and C), reflecting the possible impact of shearing, are consistent with a downward flow model. This scenario is however not applicable to coarser grained regions below (Figure 3-3B), which show substantial scattering in the fabric strength, which tends to decrease in the lowermost 1000 m of the crust (Figure 3-5A). CPO in the LFG and LG units reflect variable degrees of lineation and foliation at the meter scale along the lower crust, as revealed by the down section plots of BA and BC (Figure 3-5B and C).

MacLeod and Yaouancq (2000), VanTongeren et al. (2015), and Morris et al. (2019) suggested an alternative model for the accretion of the gabbros beneath the AML. They interpret steep foliation in the FG unit of Wadi Abyad (MacLeod and Yaouancq, 2000), Wadi Khafifah (VanTongeren et al., 2015), and wadis Somrah, Khafifah and Abyad (Morris et al., 2019) as resulting from upward migrating melt aligning the solid phases of the crystal mush. Their model of upward migrating melt is restricted to the FG unit in all sampled sections, where macroscopic foliations in the field are generally steep. Both steep foliations below the AML documented by Pallister and Hopson (1981) or Morales et al. (2011) and our observations from EBSD measurements also agree with this hypothesis in the VG/FG TZ and UFG unit where the pole figures indicate that plagioclase (and to a minor extend also clinopyroxene) fabrics are lineated. This upward flow model is also in agreement with the more efficient cooling of those gabbroic units as indicated by our CSD analyses and also the study of Garrido et al. (2001).

Whereas the uniform subsidence in a gabbro glacier model should result in consistent trends in pole figure symmetry with depth, a down-section trend in a sheeted sill model can be more complex and variable. Crystallization of the gabbros within small melt bodies of variable size and at various depths is not expected to result in clear microstructural or textural trends since small regions crystallize individually and not necessarily in a depth- or time-related sequence (VanTongeren et al., 2015). The

relatively low CPO strength of all phases in the gabbros of the AML, VG/FG TZ and the UFG unit (Figure 3-5A) could be interpreted as being consistent with the individual crystallization of small melt-rich magma bodies. However, the globally steep foliations in the upper foliated gabbros of the Oman ophiolite (e.g., Pallister and Hopson, 1981; MacLeod and Yaouancq, 2000; Nicolas et al., 2009), and observed in Wadi Gideah appear inconsistent with in-situ crystallization of individual sills in the UFG unit. In contrast to the uppermost 1500 m, the fabric strength in the gabbros below 3500 mam tends to increase downward, with strong scattering (Figure 3-5A). Regardless of the observed overall increasing down section trend, the significant variations in fabric strength and pole figure symmetries on a small spatial scale are consistent with individual crystallization of relatively small melt bodies.

Plagioclase pole figures with point maxima in (010) and girdle distributions in [100] in the LFG and upper LG units (i.e., low BA and BC values) indicate a compaction-induced fabric (VanTongeren et al., 2015) where shear, if present, played a minor role. Girdle distributions in [100] pole figures tend to evolve to point maxima down section in the lower LG unit and MTZ (i.e., higher value of BA and BC; Figure 3-5B and C) indicating a stronger lineation, hence likely more significant shearing of the lower crustal regions. Regardless of local variations in CPO strength and pole figure symmetries, a general increase of fabric strength and higher impact of shear strain below 3500 m was not described in previous CPO studies (e.g., VanTongeren et al., 2015; Morales et al., 2011; Figure 3-5A). Local differences are well-pronounced for instance in samples OM12Gid045 and OM12Gid044, which show weaker fabrics, different to those in the samples above and below (see pole figure compilation and microstructural data in Mock et al., 2020b). The differences in J values between earlier fabric studies and our data may be caused by different approaches in the sample selection (i.e., anorthosite in Morales et al., 2011 versus gabbroic rocks in our study) and/or calculation of the orientation distribution function (see section 4.1). They do not change the observation that a down section increasing trend in fabric strength is visible along the LG unit in our study. This trend cannot be explained by crystallizing sills alone. A process affecting the CPO strength and symmetry (development of mineral lineation) of all primary phases could be the active flow of the underlying mantle, as proposed based on the continuity of lineation trajectories in the upper mantle and gabbros above, and the inferred mechanical coupling between the mantle and the crystallizing gabbroic mush (Nicolas and Boudier, 2000; Nicolas et al., 1994; Ildefonse et al., 1995; Jousselin et al., 2012; Jousselin et al., 1998). In the lower crustal magmatic mush, shear strain imposed by the actively convecting upper mantle can produce a magmatic fabric with a lineation component being most pronounced close to the crust-mantle transition and attenuating up section where the effect of mantle-induced shear is reduced. A limited amount of melt would 1) allow crystal preferred orientation, 2) accommodate the induced shear strain and therefore 3) prevent intracrystalline deformation which would lead to higher misorientation in the grains. Misorientation in the primary phase grains is indeed low, particularly in clinopyroxene and plagioclase, along the entire reference profile (Figure 3-7). It is generally stronger for olivine than for clinopyroxene or plagioclase (Figure 3-7), because olivine is more sensitive to crystal-plastic deformation in hypersolidus conditions (Yoshinobu and Hirth, 2002). Decreasing misorientation in the lowermost 800 m of the crust (Figure 3-7), may relate to a higher melt fraction present in this region when incipient crystal-plastic deformation started to overprint the magmatic fabric. A possible explanation for higher melt proportions in the lowermost 800 m of the crust could be its vicinity to the hot upper mantle or deep melt lenses in the MTZ (e.g., Garmany, 1989; Crawford et al., 1999; Dunn et al., 2000) and correlated emplacement of melt in the MTZ horizon (e.g., Kelemen et al., 1997). Post-magmatic tectonic processes are unlikely to account for the observed misorientation for two main reasons: (1) tectonic emplacement, e.g., during obduction, would be expected to affect the entire crust, and not only the LG unit, and (2) if local regions of the crust were affected by plastic strain, e.g., in the proximity of fault zones, they might present sharply contrasting misorientation

signals. Fault zones have been described in Wadi Gideah (e.g., Zihlmann et al., 2018) indicating that local heterogeneities in plastic deformation intensity might exist. However, the sample suite used in this study did not include samples from fault zones; we therefore assume that the misorientation in our samples is not affected by late plastic deformation.

3.5.2   Comparison with previous fabric studies in the Samail ophiolite

The importance of microstructural features to understand magmatic processes during crustal formation led to several studies performed on plutonic rocks from Oman. Nicolas et al. (2009) focused on the root zone of the sheeted dyke complex and the uppermost gabbros and found clear indicators for a crystal mush subsiding from the AML and contributing to the lower crustal accretion. Morales et al. (2011) analyzed anorthosites throughout the uppermost 2000 m of the gabbros and found an increasing strain down section. Jousselin et al. (2012) investigated microstructures within gabbroic lenses in the MTZ and concluded that the convecting underlying mantle significantly contributes to the deformation of gabbros in the MTZ.

VanTongeren et al. (2015) did not observe any trend in fabric strength along the lower crust in Wadi Khafifah (Figure 3-5A), which contrasts with the increasing J trend that we observe in the LFG and LG units down to 1000 mam. We posit that the absence of such a trend in VanTongeren et al. (2015) is possibly an artifact of the lower data density with an average sample spacing of ~330 m. In order to test this hypothesis, we identified 13 data points of our sample suite that are close to the stratigraphic heights of VanTongeren's samples (symbols with thick contours Figure 3-5A). Indeed, the gaps between the selected data points and the overall distribution conceals a down section trend. This also reveals that the number of samples, hence the data density, significantly affects the measurability of trends. With an average spacing of less than two meters between adjacent samples of layered gabbros cored during the Oman Drilling Project, Mock et al. (2020a) have shown that even on the meter scale gradual changes in plagioclase fabrics occur within the lower oceanic crust. VanTongeren et al. (2015) interpret their plagioclase pole figures as representing no or only very weak lineation by the [100] girdle or weakly clustered distributions. We interpret at least the three samples from the lowermost 1000 m of the crust in VanTongeren et al. (2015) (figure 4) as revealing a more clustered distribution of [100] indicating a significant lineation component in the fabric. This interpretation would be consistent with the fabrics we observe in the LG unit of Wadi Gideah, showing stronger lineation with depth as quantified by BA and [100] pfJ increasing along the LFG and LG units. The 14 samples we analyzed in the uppermost 1500 m of the gabbro section (AML, VG/FG TZ, UFG) provide a high spatial resolution for a better discussion of accretion models, as suggested by VanTongeren et al. (2015).

Morales et al. (2011) analyzed 15 more or less monomineralic anorthosites mostly from the uppermost 1500 m of the plutonic crust. The samples correspond to anorthositic layers and lenses of different thickness, which is a significantly different approach to our study using gabbroic samples. Morales et al. (2011) found indicators for increasing strain down section below the root zone of the sheeted dyke complex in the Wadi Tayin massif. This is consistent with the plagioclase [100] point maxima, and relatively high BA we observe along the VG/FG TZ and the UFG units. Although we calculated very low J indices of plagioclase and clinopyroxene in those units (<2.03 for plagioclase, <1.97 for clinopyroxene), Morales et al. found J between 2 and 8.7 increasing down section for steeply foliated and widely scattered J between 2 and 11.9 for flat-lying anorthosites (figure 8 in Morales et al., 2011). They analyzed anorthosites arguing that they "record the evolution of textures controlled by magmatic flow, compaction and recrystallization more clearly than the enclosing gabbros" (Morales et al., 2011). Magmatic deformation textures might be weaker in our gabbros where mostly three

phases of the main crystallization (cotectic crystallization) are present, leading to the observed low J. Moreover, the formation of monomineralic anorthosite crystallized from a cotectic assemblage containing olivine, clinopyroxene and plagioclase, requires a specific sorting process in the context of layer formation, which is not known up to now, increasing the probability that these rocks are not representative of the overall gabbro section.

Nicolas et al. (2009) studied the root zone of the sheeted dyke complex with a focus on the transition from the AML to the gabbroic section. They also found evidence for a gabbro mush subsiding from the floor of the melt lens and contributing to the lower crustal accretion. The random fabrics in the uppermost 10 m below the root zone of the sheeted dyke complex is consistent with the random fabrics we see in the AML samples. They also observe increasing fabric strengths below this horizon, first showing [100] girdles, which then evolve to weak point maxima at 365 m below the root zone of the sheeted dyke complex in a way similar to our results in the VG/FG TZ.

In their microstructural investigation of gabbroic lenses within the MTZ, Jousselin et al. (2012) identified four fabric types depending on the intensity of foliation, lineation or both. We ascribe seven of our samples to the MTZ, between 16 and 157 mam. They also show different fabric symmetries from intermediate (OM15_15D_II) to foliated with a [100] girdle (e.g., OM15_13_II) to foliated and lineated with point maxima in both (010) and [100] (e.g., OM10_Gid_A31). This is consistent with the interpretation of Jousselin et al. (2012) that both compaction and magmatic shearing imposed by the convecting mantle might play a role in creating magmatic deformation of the lowermost gabbros in Oman. Olivine crystals of the lowermost gabbros in our sample suite partially display [100] point maxima, parallel to [100] lineations of plagioclase (Figure 3-5C). This likely indicates a plastic deformation component recorded by olivine and is consistent with the type 4 layering described by Jousselin et al. (2012) in the MTZ.

3.5.3   Combining the evaluated end-member processes to a hybrid model

Our results point to a hybrid model of lower crustal as explained in the following and depicted inFigure 3-8. Intermediate pole figure symmetries (BA and BC close to 0.5) along the uppermost 1500 m of the profile with point maxima in both [100](010) of plagioclase and (010)[001] of clinopyroxene indicate that the rock fabrics are not only foliated but also show significant lineation. Lineation can be explained by either subsiding crystal mush from the AML (e.g., Quick and Denlinger, 1993) or upward migrating porous melt flow (MacLeod and Yaouancq, 2000; VanTongeren et al., 2015; Morris et al., 2019) being dominant in this section. More scattered CPO strengths and significantly distinct pole figure symmetries in the section between 3500 mam and the MTZ are well-explained by in-situ crystallization of individual magma reservoirs, and do not agree with cumulates being transported by a global flow mechanism from the AML downward. In the horizon between 3500 mam and 2600 mam, both grain size and CPO (J, pfJ, BA, pole figures) significantly change. These changes occur in the same horizon as changes in geochemical and petrological data from the same sample suite do (Garbe-Schoenberg et al., 2014; Müller et al., 2014; Müller, 2016; Mueller et al., 2017; Koepke et al., 2017). We interpret them as indicators for changing formation mechanisms, calling for a hybrid crustal accretion model that combines in-situ crystallizing melt bodies in the LFG unit and the LG unit with flow-dominated transport of crystals in the UFG unit and VG/FG TZ. A two-mechanisms accretion model is consistent with the sheeted sill model of Kelemen et al. (1997), which posits that the uppermost horizon beneath the AML might form by subsiding mushes from the AML. However, we infer from previous studies (Kelemen et al., 1997; Korenaga and Kelemen, 1997; Garrido et al., 2001; VanTongeren et al., 2015) supporting a sheeted sill model that this horizon is relatively thin expanding over only a few hundred meters below the AML. Our results suggest that a change in the accretion
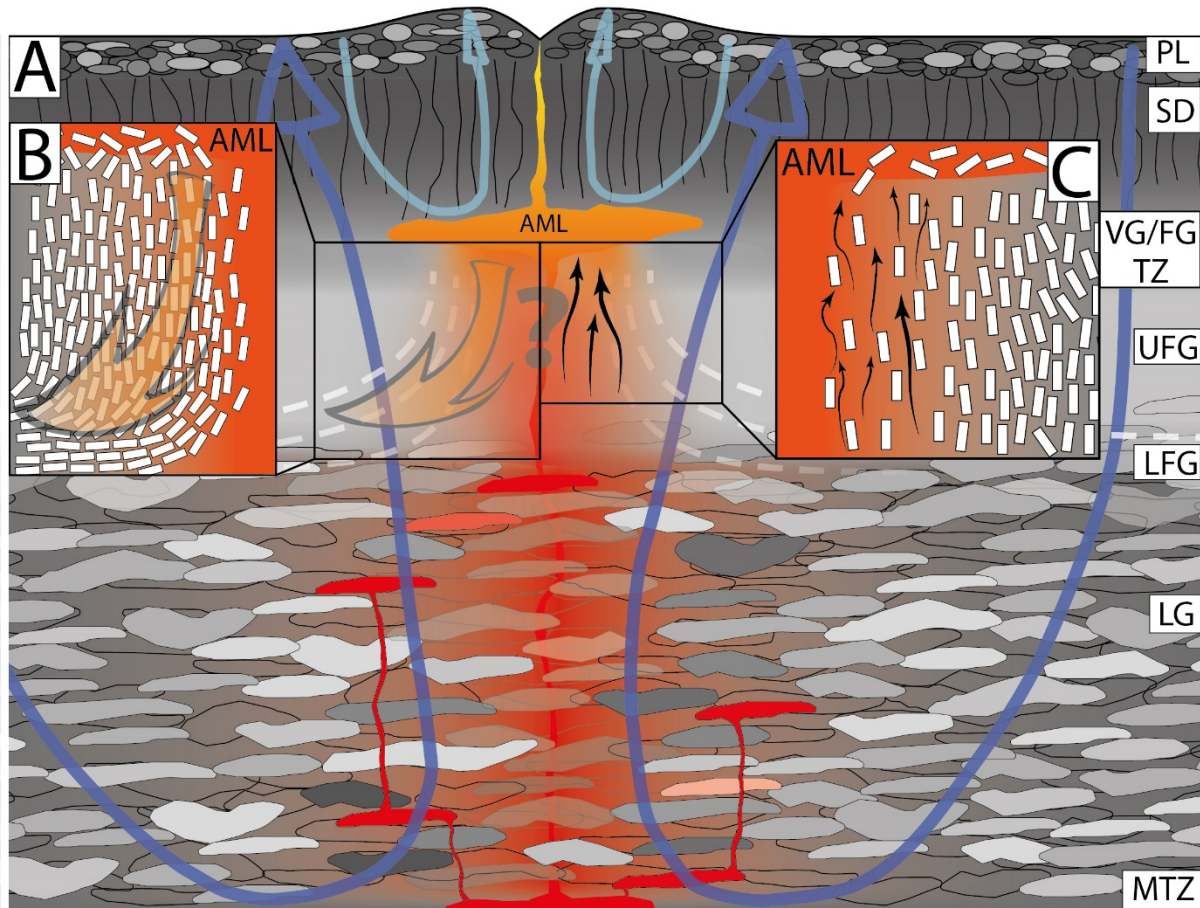
Figure 3-8   A) Schematic model of lower crustal accretion beneath fast-spreading mid-ocean ridges based on the results of this study. The data of our study support the crystallization of individual meld bodies (sills) at various depths in the lower oceanic crust (color corresponds to temperature), whereas the data from the varitextured and upper foliated gabbros are in agreement with both a subsiding crystal mush of cumulates from the axial melt lens (orange arrow; see B for details) and upward migrating crystal-carrying melt (black arrows and white rectangles; see C for details). Both mechanisms may result in the observed steep foliations with significant lineation in the varitextured/foliated gabbro transition and the upper foliated gabbros and agree with our data, symbolized by the question mark. See text for further discussion. Blue arrows represent hydrothermal activity (light blue for the shallow, and dark blue for the deep crust), the curved, dashed lines symbolize the foliations observed in the field.

mechanism occurred ~1500 m below the AML indicating that the lower two thirds of the analyzed section crystallized at depth whereas the upper third results either from subsiding mush from the AML or from upward migrating porous melt flow. We therefore suggest to describe crustal accretion by a hybrid model where several accretion mechanisms play key roles, rather than by the end-member sheeted sill (e.g., Kelemen et al., 1997) or gabbro glacier (e.g., Henstock et al., 1993) models. Boudier et al. (1996) already proposed a hybrid accretion model where sill intrusions crystallize randomly distributed within a gabbro glacier that expands over the entire lower crust. The gabbro glacier mechanism is restricted in our model to the upper 1500 m of the lower crust leading to a clear spatial separation between in-situ crystallization within the lowermost 3500 m and vertical crystal mush movement in the uppermost 1500 m of the lower crust. This is a key difference between our model and the hybrid model of Boudier et al. (1996). Increasing CPO strength accompanied by slightly higher misorientation in the LG unit can be caused by mantle flow-induced deformation (Nicolas et al., 1994; Jousselin et al., 2012) in the presence of a limited amount of melt. This (likely syn-magmatic) secondary

process is compatible with magma reservoirs crystallizing deep in the crust. The weak lineation component in plagioclase and clinopyroxene (low BA or BC, respectively) within the LFG unit could then result from the less pronounced effect of shear strain forced by mantle flow higher up in the section. Shear strain induced by the upper mantle flow is also consistent with lineated [100][010] olivine CPO that match the [100](010) lineation of plagioclase as described above. This feature indicates plastically deformed olivine in those samples (Jousselin et al., 2012), as well as increasing GOS and GAM in olivine (Figure 3-7).

Assuming that the UFG unit started to crystallize within the AML, efficient cooling of this horizon by seawater circulation within the sheeted dike complex can explain the small grain size of the UFG unit. An off-axis hydrothermal cooling system, as suggested by Garrido et al. (2001), reaching the FG unit could alternatively explain finer grain sizes from this region in a scenario of upward migrating magma crystallizing beneath the AML. To form the coarser grained LG unit, a different crystallization regime is required. Individually crystallizing magma reservoirs are consistent with scattering of the microstructural parameters and the observed differences between several adjacent samples (Table 1; e.g., from OM12_Gid_026 at 1246 mam to OM12_Gid_027 at 1237 mam, or from OM11_Gid_A26 at 945 mam to OM11_Gid_A27 at 831 mam). A requirement for in-situ crystallization is a hydrothermal cooling system removing the latent heat of crystallization. The petrological record in gabbros from high-temperature fault zones in the Wadi Gideah implies that such a system indeed exists (Koepke et al., 2014). Although several authors describe hydrothermal activity in the lower crust of the Samail ophiolite (e.g., Bosch et al., 2004; Abily et al., 2011; Zihlmann et al., 2018), cooling of these units may be less efficient and slower than within the overlying units (e.g., Garrido et al., 2001; Coogan et al., 2002a, 2007) resulting in coarser grain sizes of the primary phases. However, this is contradictory to the quantitative cooling results of VanTongeren et al. (2008) who calculated cooling rates using Ca in olivine without significant trends down section, or to the fast cooling along the crust numerically modeled by Hasenclever et al. (2014). We point out that our interpretation from plagioclase CSD that cooling is slower in the LG unit than in the FG unit and the FG/VG TZ is only qualitative. We therefore do not speculate here whether the cooling of the lowermost crust is sufficient to enable in-situ crystallization. Nonetheless, we wish to emphasize that from a microstructural point of view, magma reservoirs crystallizing at depth provide a plausible explanation for the observed trends and variabilities in fabric strength and symmetry.

3.6 Conclusions

We sampled a cross section along the Wadi Gideah in the Wadi Tayin massif of the Samail ophiolite in order to establish a reference profile through the lower crust from the AML down to the MTZ. Wadi Gideah provides an ideal opportunity for this, since all primary lithological units of the gabbroic crust (VG/FG TZ, FG, LG, MTZ) are present and observable in surface outcrops. Our results show that the VG and the UFG units (above 3500 mam) and LFG and the LG units (below 3500 mam) accreted either in different deformation regimes or by different processes or both, as indicated by differences in textural features and differences in the characteristics of CPO above and below 3500 mam. A constantly weak CPO with moderate lineation in the VG/FG TZ and the UFG unit contrasts with stronger variations in the LFG and LG units. This variability is consistent with small-scaled magmatic systems crystallizing individually at various times and depths whereas the former indicate a formation mechanism aligning formerly crystallized phases. We found that our data are in good agreement with a hybrid accretion model where the UFG and VG are either accumulated in the AML and subsiding downward (e.g., Quick and Denlinger, 1993) or crystallized from an upward migrating crystal-laden magma (e.g., MacLeod and Yaouancq, 2000). In our hybrid model, the LFG and LG units

formed by multiple sill intrusions (e.g., Kelemen et al., 1997). This hybrid model is generally consistent with the sheeted sill model proposed by Kelemen et al. (1997), where the gabbros directly beneath the AML are also formed by subsiding crystal mush. However, our data indicate a thicker portion of the upper gabbros being built by subsidence and/or upward melt migration. The LFG unit between 3500 and 2600 mam could represent a transition zone between the two mechanisms. The increasingly lineated fabric from the top of the LFG unit down section, together with a consistent trend of slightly increasing fabric strength, is consistent with shear deformation induced by mantle flow.

3.7   Data availability statement

The data obtained for this study and discussed in this paper are available on the FAIR-aligned pangaea repository under https://doi.org/10.1594/PANGAEA.924445.

4 Accretion of the layered gabbro section in Oman – insights from drill core GT1A

4.1 Drill site GT1A

The approximately 400 m long drill core from drill site GT1A crosses a section of layered gabbros from 1173 m above the base of the mantle transition zone (maM) down section. Due to the inclination of the Samail crust in the Ibra area described in chapter 2.1, a net crustal depth interval of 356 m is considered to be covered by the drill core. In the following, depth values are given in meters above the base of the mantle transition zone. Although GT1A was chosen with respect to the large hydrothermal fault zone described by Zihlmann et al. (2018) close to the drill site, the samples chosen for this study focus on fresh primary rock material and sampling hydrothermally altered rocks was omitted. Detailed descriptions on alteration of drill core GT1 is provided in the proceedings of the Oman Drilling Project by Kelemen et al. (2020) and deeper insights into hydrothermal processes having affected GT1 are provided by Greenberger et al. (2021).

With its crustal position in the layered gabbro unit and a recovery of approximately 100 %, the obtained drill core is perfectly qualified to provide detailed insights into magmatic processes from the decameter- down to the cm-scale. The coherent section was sampled for this thesis to reach a high spatial resolution, the recovery of coherent layer boundaries or even full cm- to dm-thick layers, as well as anorthositic, troctolitic, or wehrlitic lithologies that are only rarely documented at the surface of Wadi Gideah. The average spatial resolution approximates 2 m and ranges from a few centimeters to 16.31 m at maximum. Some thin sections were subdivided into several domains, based on modal or textural features, leading to distances of only a few millimeters between some adjacent data points.

Because drill site GT1A is located within the same wadi as the surface samples from chapter 3, they can be integrated into the Wadi Gideah reference profile significantly increasing its spatial resolution along a 356 m long interval. The consequent improvement in data quality allows to test the crustal accretion model suggested in chapter 3 with respect to microstructural, petrological, and geochemical features. A key aim of this chapter is, therefore, to identify indicators in the drill core data supporting or falsifying the in-situ crystallization mechanism suggested for the lowermost 3500 m of the Wadi Gideah crust from the reference profile data. The analytical methods applied for this chapter are described in chapter 2.4.

4.2 Results

4.2.1 Core description on CHIKYU

Drill core GT1A was described by the Oman Drilling Project Science Team (under participation of the author) on the Japanese drilling vessel CHIKYU from July 15th to July 31st 2017 with respect to igneous and alteration petrological features, textural and fabric observations, geochemistry, and physical properties. The results briefly presented in the chapters 4.2.1.1 to 4.2.1.4 are compiled by Kelemen et al. (2020) in detail. Here, an overview on the descriptive findings, selected with respect to their applicability to the samples of this study, is provided to set the results from the collected samples into an appropriate context.

4.2.1.1 Igneous petrology

The major rock types listed by Kelemen et al. (2020) are olivine gabbro (65.9 %), olivine-bearing gabbro (olivine abundance <5 %; 21.5 %) and olivine melagabbro (olivine and clinopyroxene total abundance >65 %; 3.9 %). Minor rock types are oxide-bearing olivine gabbro, gabbro, anorthositic gabbro, troctolitic gabbro, and dunite, each with abundances between 0.3 and 2.4 % at maximum. Seven units were identified along drill core GT1A based on textural properties and modal abundances. Some characteristics of every unit are listed in Table 4-1. The presence of decameter scale units along the drill core is an interesting feature that has to be taken into account also during detailed petrological and geochemical descriptions in the chapters 4.2.3, 4.2.5, and 4.2.6.

Table 4-1   Lithologic units in drill core GT1A identified during the core description on CHIKYU by Kelemen et al. (2020).

Unit	Top[a] [maM]	Bottom[b] [maM]	Thickness [m]	Rock types[c]	Textural properties[d]
I	1168.67	1149.50	19.18	ol gb	med, gran
II	1149.50	1095.16	54.34	ol gb, ol-b gb	med, gran
III	1095.16	1080.54	14.62	ol m-gb, ox-b gb, ol gb, ol-b gb	med
IV	1080.54	1036.99	43.55	ol gb, ol-b gb	med, gran
V	1036.99	982.97	54.02	ol gb, ol-b gb, ol m-gb, gb	med, gran; fin
VI	982.97	901.99	80.98	ol gb, ol-b gb, opx-b gb, gbn	med, gran
VII	901.99	816.85	85.14	ol gb, ol-b gb	fin - med, gran

[a] unit top height in meters above the base of the MTZ
[b] unit bottom height in meters above the base of the MTZ
[c] gb = gabbro, m-gb = melagabbro, gbn = gabbronorite, ol = olivine, ox = oxide, opx = orthopyroxene, "-b" indicates "bearing" = <5 % modal abundance
[d] med = medium-grained, fin = fine-grained, gran = granular

The modal proportions of the primary phases olivine, clinopyroxene, and plagioclase are widely scattered along the core, with a higher variation of olivine and clinopyroxene in the upper 105 m of the core compared to the lower depths (Kelemen et al., 2020). Along the entire drill core, a full number of 64 igneous contacts was defined from changes in modal abundances, grain size (lithologic contacts), or different rock types by intrusions or faulting (structural contacts). Lithologic contacts are by far more common with 91 % of the total observed.

Except for some varitextured pegmatitic lithologies within a narrow horizon of 2 m thickness at about 1105 maM, grain sizes are mostly fine to medium in clinopyroxene and plagioclase. They do not change systematically with depth. In contrast, olivine grain lengths range from <1 to 15 mm in the lowermost 270 m of the core. They are elongate to tabular in shape and are aligned subparallel to rock foliations defined by plagioclase and clinopyroxene (Kelemen et al., 2020).

Igneous layering is a common feature along the entire core. Its nature is always modal, in some cases accompanied by grain size variations. Pure grain size layering is generally absent. The thickness of a layer varies along the core from the cm- to the m-scale, which occasionally hampered a precise thickness estimation since a layer exceeded the length of a drill section, which have all been described separately (Kelemen et al., 2020). Nonetheless, the occurrence of modal layering along the core, again, emphasizes its importance for crustal accretion mechanisms, as described in more detail in chapter 6.

4.2.1.2 Alteration petrology

Rocks from GT1A are usually not fresh, but have undergone hydrothermal alteration. This did not only play a role during the magmatic emplacement of the Samail crust but water-rock reactions were present through the entire life span of the ophiolite from the emplacement until today, covering a wide range in temperature and fluid compositions (Kelemen et al., 2020). The total alteration intensity was macroscopically quantified between 10 and 100 %, with a mean of 60 %. Secondary phases replacing primary host rock minerals are mostly described as albite (replacing plagioclase) and chlorite (replacing olivine, clinopyroxene, and plagioclase). Amphibole is also present as secondary phase replacing clinopyroxene. If present, the alteration intensity in vein halos tends to be higher than the pervasive background alteration (55-100 % with a mean of 85 %). Vein halos commonly precipitate a similar range of secondary phases with albite, chlorite, and amphibole. Epidote and some other minor secondary phase (e.g., laumontite, prehnite, or zeolites) were also described. The most common vein halos are white in color and do not exceed 5 mm in width and is correlated to chlorite and prehnite veins. Associated with dark amphibole veins, the next most common halo type is gray or dark gray and only occurs in the lowermost 100 m of the core (Kelemen et al., 2020).

4.2.1.3 Structural geology

Magmatic structures described in drill core GT1A are magmatic layering, foliation, veins, and contacts. Magmatic layering is a common feature of the core: a total number of 863 layers were measured, with thicknesses between <1 cm to 3.3 m (mean: 24 cm) which agrees with the layer thickness observed in Wadi Somerah, discussed in chapter 6. However, cm-scale layering dominates in the drill core. The mean dip of the magmatic layering is 18° - 19°, i.e., subparallel to the paleo-Moho. Magmatic foliation is a ubiquitous feature of the drilled gabbros. It dips 0° to 40° with a mean of 19° which is described as slightly increasing down core (Kelemen et al., 2020). However, the variation of dip with depth does not occur continuously but appears to vary systematically with decameter thick cycles (~50 – 75 m on average) of increasing dip down core which is assumed to be a magmatic feature rather than a result of later tectonic events.

Magmatic veins or contacts are generally rare in GT1A. During the core description, only a single anorthositic and a few dioritic veins were described (Kelemen et al., 2020). The latter are very steeply dipping, therefore, discordant to the magmatic layering. Same is for the observed anorthositic vein which dips with 83°. However, as presented in chapter 4.2.2, there were a few further magmatic contacts or dykelets of wehrlite, troctolite, or anorthosite found which appear to be concordant with the magmatic layering.

Consistently with the low misorientation data reported for the lower crust in Wadi Gideah (see chapter 3.4.5), crystal-plastic deformation was not observed macroscopically in drill core GT1A. Only very narrow horizons of <35 mm thickness show such features, mostly being associated with strong cataclasis at the contact with sheared veins where plagioclase and olivine show undulose extinction, tapered twins, and subgrain development (Kelemen et al., 2020). Brittle deformation is common throughout the core, and is usually associated with strain-weakened precursors, such as veinlets or lithologic contacts.

4.2.1.4 Geochemistry

To identify differentiation of whole rock samples, Kelemen et al. (2020) used the Mg# (=Mg/(Mg+Fe) x 100; molar basis), the Ca# (Ca/(Ca+Na) x 100; molar basis), and the contents of compatible (Cr, Ni) and incompatible (Y) trace elements. They found that the most common lithology, olivine gabbro, plots over the widest range of differentiation, and that the average rock compositions

differentiate from melagabbros over olivine gabbros to olivine-bearing gabbros. They found that REE patterns (normalized to primitive mantle) show typical characteristics of differentiation from olivine gabbros to olivine-bearing gabbros. Removal of plagioclase during fractional crystallization is indicated by an Eu anomaly in all samples except for one dunite and a single altered vein halo. Partial melting of the mantle as parental melt source is indicated by depletion of light REEs (LREE) compared to primitive mantle compositions.

4.2.2 Petrographic observations of this study

The results presented in the following chapters 4.2.2 to 4.2.6 are obtained by the author from the sample suite presented in chapter 2.2.

As already macroscopically described and presented in the previous chapter, the majority of the sampled lithologies are olivine gabbros, olivine-bearing gabbros, and gabbros. The gabbroic lithologies are interlayered by a few cm-scale troctolitic, anorthositic, or wehrlitic assemblages (Figure 4-1). Those interlayers appear coherent with the host rock and do not show indicators of late-stage intrusions, such as chilled margins. Single thin sections reveal granular oxide contents of <1 %, and small amounts of magmatic amphibole were observed in some samples (Figure 4-2 A, B).

As shown in Figure 4-3, the major phase in most of the samples is plagioclase with a mean of 43.55 % (0 – 98.8 %), followed by clinopyroxene with a mean of 29.97 % (0 – 66.4 %), and olivine with a mean of 11.99 (0 – 86.8). All major primary phases show significant scattering along the core. Although alteration plays an important role in the evolution of the drilled rocks (see chapter 4.2.1.2 and below), primary textures are well recognizable in most of the thin sections. The results of the petrographic description of primary phases are listed in the electronic supplemental of this thesis.

Olivine forms granular, fine- to medium-sized grains and usually shows an anhedral, in single cases subhedral, shape, mostly with an irregular and often elongated habitus. Only in a few samples, olivine shows a prismatic shape. Some olivine grains form oikocrysts containing small plagioclase
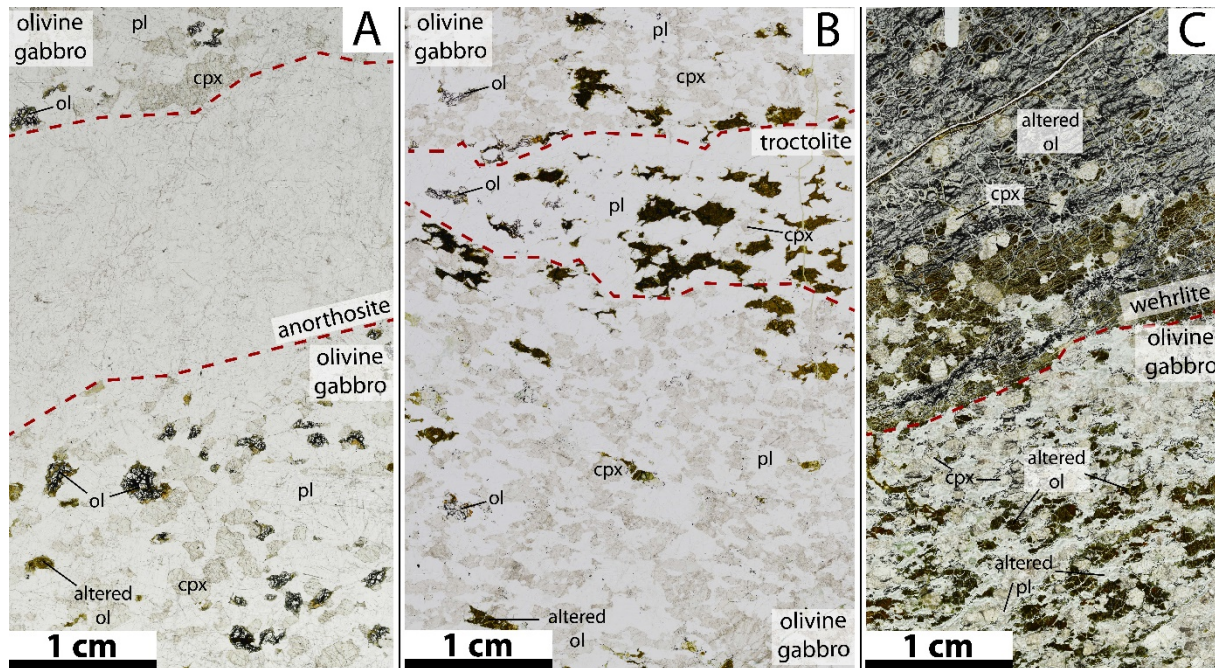
Figure 4-1   Thin section photographs of primitive lithologies discovered in drill core GT1A marked by the dashed lines. A) anorthosite, B) troctolite, and C) wehrlite in olivine gabbro. ol = olivine, cpx = clinopyroxene, pl = plagioclase. Note the scale bar of 1 cm at the bottom left corner of each image.

chadacrysts (Figure 4-2 D), or the intergrowth of olivine and plagioclase lead to a skeletal olivine grain shape. Olivine is strongly altered throughout the whole drill core with an average replacement of 82 % (15 – 100 %). Mesh serpentinization or complete serpentinization of olivine are very common (Figure 4-2 B, D, E). Occasionally, serpentinization forms a corona around a primary olivine grain relic. Indicators for crystal-plastic deformation, such as kink bending, subgrain formation, or undulose extinction are rarely documented in olivine grains from drill core GT1A (Figure 4-2 E).
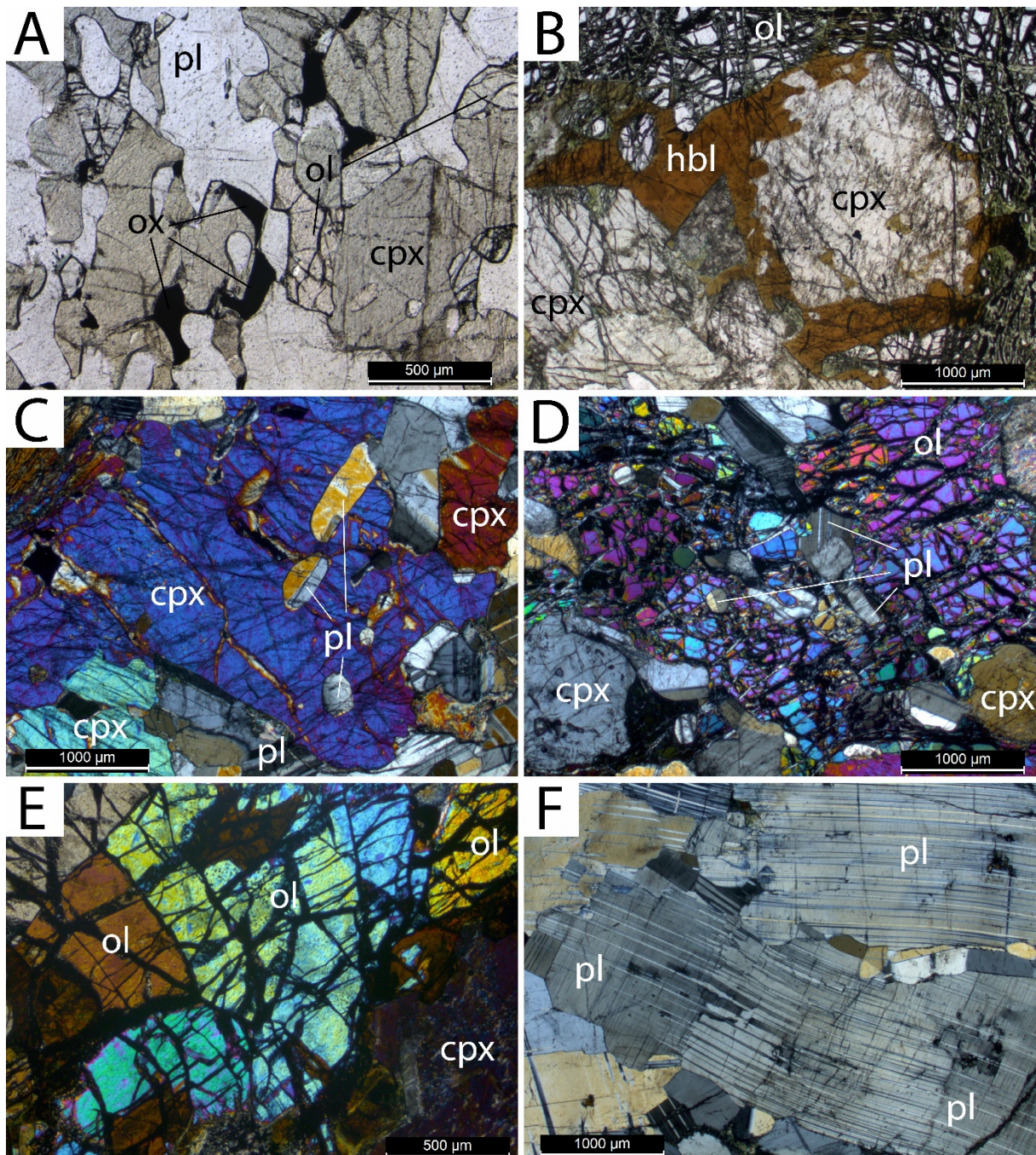
Figure 4-2   Photomicrographs of petrographic observations in drill core GT1A. A) Granular Fe-Ti-oxides in the oxide-bearing olivine gabbro of sample OM-DP-BI-15 at 1075 maM. B) Clinopyroxene with a corona of magmatic hornblende in sample 38-4-55-58. C) Clinopyroxene oikocryst containing plagioclase chadacrysts in sample 1-29-2b. D) Olivine oikocryst containing plagioclase chadacrysts samples 38-3-38-41. E) Olivine showing subgrain formation in sample 1-46-3a. F) Sheared twinning in plagioclase grains of sample 1-53-3a. cpx = clinopyroxene, hbl = hornblende, ol = olivine, ox = (Fe-Ti-)oxide, pl = plagioclase. Note that the features shown in A), B), E), and F) are not ubiquitous throughout the drill core.

75

Clinopyroxene also forms fine- to medium-size grains, however, with the occasional abundance of cm-scale megacrysts. Clinopyroxene shapes are, to a major extent, anhedral to subhedral, their habitus is mostly prismatic, only in a few cases ranging from irregular to prismatic, and in a single sample elongated. Some exsolution blebs, or lamellae in a few cases, were observed. Also clinopyroxene occasionally forms oikocrysts containing plagioclase chadacrysts (Figure 4-2 C). Twins are rare in the clinopyroxenes of drill core GT1A. Averaged over the whole drill core, clinopyroxene is replaced to an extent of 25 % (5 – 98 %). Secondary phases replacing clinopyroxene are mostly green or brown amphiboles and in some cases chlorite.

Plagioclase usually forms the smallest grains of the constituent primary phases, with fine average grain sizes of <1 mm. Plagioclase chadacrysts hosted by olivine or clinopyroxene are often very fine grained with sizes of <0.2 mm (Figure 4-2 C, D). The plagioclase shape is mostly subhedral, sometimes tending to anhedral, and only in single cases anhedral or tending to euhedral. Plagioclase shows a prismatic habitus and is often twinned. Tapered or even sheared twins are rarely documented in GT1A (Figure 4-2 F). Plagioclase alteration is relatively weak with an average replacement of 17 % ranging from 0 – 100 %.

Granular oxides were found in some samples of the upper 200 m of the drill core, most common in the uppermost 125 m, with abundances never exceeding 1 % (Figure 4-2 A). Magmatic amphibole is rare in drill core GT1A, and if present, it appears in the upper 140 m of the core with low modal abundances of <3 % replacing clinopyroxene Figure 4-2 B). Orthopyroxene was not observed in the thin sections of this study.

The whole rock alteration intensity was quantified from the replacement of the constituent phases, weighed for their modal abundance, in every sample. An average alteration intensity of 28 % (2 – 100 %) was calculated throughout the drill core, which is significantly less than the average alteration intensity of 60 % quantified macroscopically during the core description on CHIKYU (Kelemen et al., 2020). Some thin sections cover (sub-)mm-size veins, mostly containing hydrothermal secondary phases (see chapter 4.2.1.2), and it is evident that alteration of the host rock is elevated in the region of such veins.

Figure 4-3 Depth plot of primary modal proportions in drill core GT1A normalized to 100 %

4.2.3   Compositions of primary phases

Electron probe microanalyses were performed on the major primary phases olivine, clinopyroxene, and plagioclase. If possible, four grains per thin section, or domain, were analyzed, each with four measurements at the core and four measurements at the rim, i.e., 10 μm from the contact with the adjacent grain at maximum. Taking failed analyses or highly altered grains into account, the total number of measurements used for further processing ranged between 1 and 31 analyses per phase and sample or domain.

4.2.3.1   Primary phase analyses – olivine

Due to the strong alteration of olivine, in a large number of samples initial olivine grains were not analyzable anymore. A total of 83 olivine data sets were obtained for drill core GT1A. The Mg# (Mg/(Mg+Fe) x 100; molar basis) of olivine plots in the range between 69.53 and 82.7 with standard deviations from the mean of <1.6 in the core and 69.59 and 82.96 with standard deviations of <1.89 in the rim, without any clear zoning (Figure 4-4A left). The Mg# down hole trend shows a clear minimum at 1075 maM, representing the most fractionated composition of gradual differentiation trends above and below 1075 maM. Olivine compositions are variable along the core, with a distinct fractionation trend from the bottom of the core towards the minimum Mg# at 1075 maM mentioned above. The Mg# shifts up towards more primitive compositions above 1075 maM over a narrow interval of 15 m, reaching its maximum value at 1090 maM. Above, the Mg# behaves variable at relatively primitive compositions along the uppermost 80 m of the core.

The NiO content in olivine ranges between 0.12 and 0.18 wt% in both core and rim, with standard deviations from the mean of 0.03 and 0.04 wt% in core and rim, respectively. Although the variations in NiO content along the core mostly plot within the range of the errors (Figure 4-4A right), key features of the Mg# are also developed in the NiO content, such as decreasing NiO values from the bottom of the core to 1075 maM, where NiO reaches its minima values, followed up section by a narrow reverse fractionation trend towards its maximum.

4.2.3.2   Primary phase analyses – clinopyroxene

Clinopyroxene was analyzable in almost all domains resulting in a total of 197 data sets of clinopyroxene EPMA measurements for core GT1A. The Mg# of clinopyroxene ranges between 73.98 and 87.03 with standard deviations from the mean of <2 in the core and 74.7 and 86.22 with standard deviation of <2.18 in the rim (Figure 4-4B left). Standard deviations >1 are exceptional indicating a high homogeneity of the grain cores and rims in the most samples. The clinopyroxene Mg# describes a down section trend very similar to the one observed in olivine with a gradual differentiation from the bottom of the drill core to 1075 maM and a reverse fractionation trend between 1075 and 1090 maM, where the Mg# reaches its maximum. Above, the values vary in a narrow range between 82 and 87 over the upper 80 m of the drill core. The higher data density of clinopyroxene compared to olivine significantly improves the coherency of the depth plots leading to more detailed observations that are described in chapter 4.2.3.5.
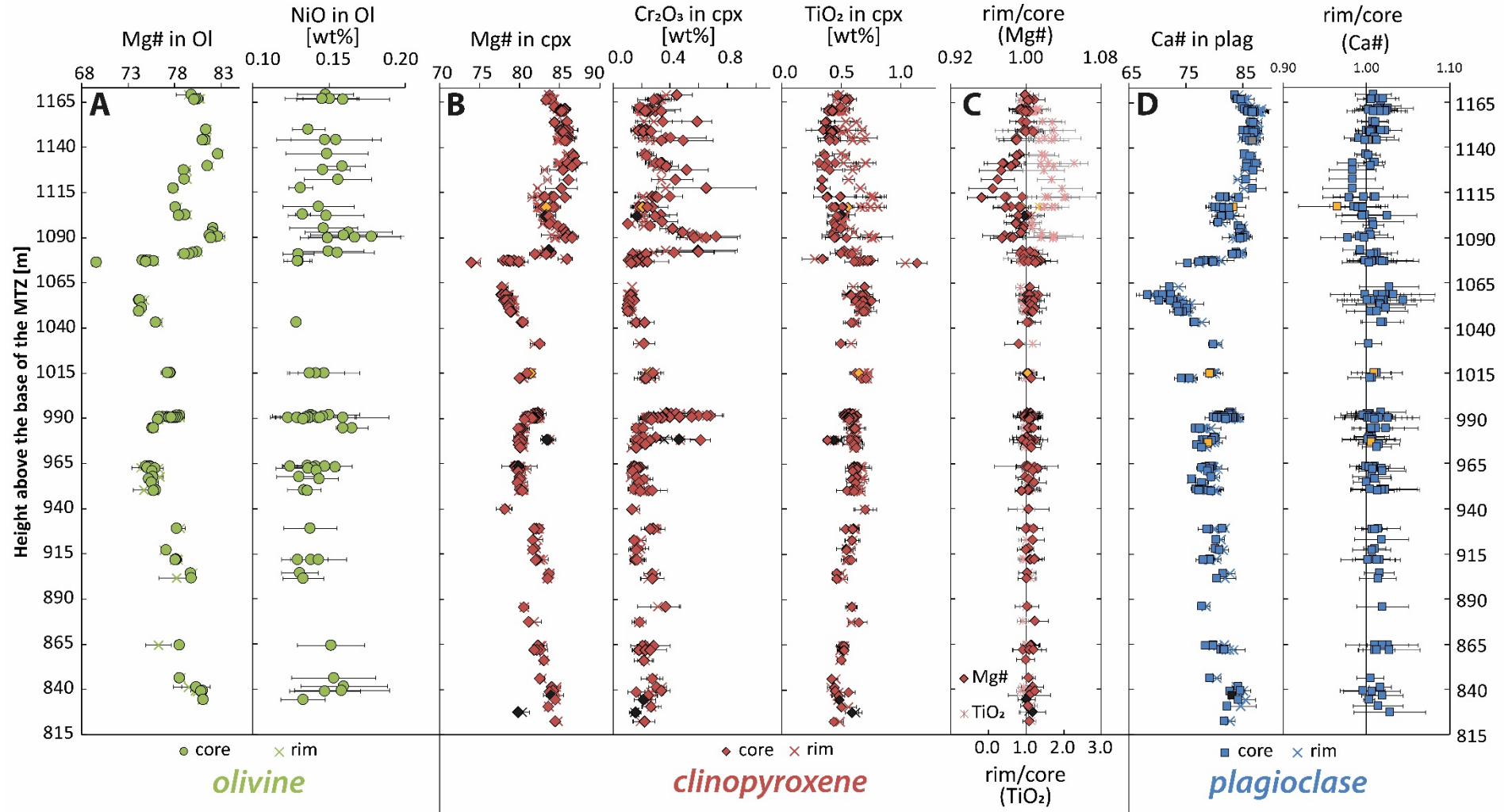
Figure 4-4 Major and minor element results of the primary phases olivine (A), clinopyroxene (B, C), and plagioclase (D) plotted versus the height above the base of the MTZ. In A, B, and D, closed symbols are core, crosses are rim analyses. In C, closed diamonds are rim/core ratios of the Mg# and stars are rim/core ratios of TiO2. Note that TiO2 is plotted on the lower x-axis. Gray symbols are anorthositic, orange are troctolitic, and black are wehrlitic samples. Error bars symbolize standard deviations from the mean or, in case of rim/core ratios, propagating errors from the standard deviations of the concerned components.

Chromium contents in clinopyroxene plot in a high range of 0.1 to 0.72 wt% with standard deviations from the mean of 0.001 to 0.35 wt% in the core and 0.1 to 0.66 wt% with standard deviations of 0.002 to 0.27 in the rim. Most values lie between 0.15 and 0.4 wt%, however, some excursions with higher values, often accompanied with higher standard deviations, are observed (Figure 4-4B mid). Except for intense scattering of Cr_2O_3 at 990 maM, the data follow a slightly decreasing trend from the bottom of the drill core to 1075 maM, following the trend observed in the Mg#. Also, the Cr_2O_3 content steeply increases above 1075 maM and behaves more variable over the upper 80 m of the core than below.

The average content of TiO_2 in clinopyroxene plots on a clearer trend than Cr_2O_3. It ranges from 0.31 to 1.14 wt% with a standard deviation from the mean of 0.02 to 0.18

Figure 4-5 Rim (crosses) and core (diamond) values of all GT1A clinopyroxene TiO_2 analyses plotted versus the Mg#. Dotted line represents the trend in core, dashed line in rim analyses. Note the two steeper trends in rim data between Mg#=84-86 and Mg#=81-83.

in the core and from 0.28 to 1.04 wt% with a standard deviation of 0.01 to 0.19 wt% in the rim. Although less clearly, the depth plot of the TiO_2 content in clinopyroxene mirrors the trend of the Mg# as expected in a fractionating magmatic system. The TiO_2 content slightly increases up section from the bottom of the core to its maximum value at 1075 maM. However, the TiO_2, the maximum value appears as outlier rather than plotting on a gradual reverse or normal fractionation trend (Figure 4-4B right). The standard deviations from the mean are higher above 1075 maM than below. A well-defined correlation between increasing Mg# and decreasing TiO_2 content is observed (Figure 4-5). Except for a few single analyses with minimum Mg# and maximum TiO_2 contents associated with the sample at 1075 maM, core analyses plot on a relatively straight trend. However, the trend described by rim values in TiO2 content is less clear than the core trend with two steeper excursions the Mg#s 86 and 84 as well as 83 and 81.

Remarkably, significant zoning in clinopyroxene is only observed in the upper 80 m of the core where rim/core ratios calculated for clinopyroxene reach 0.95 for the Mg# and up to 2.27 for TiO_2. Below 1075 maM, no significant zoning exceeding the size of the calculated error (i.e., propagating errors of the standard deviations in core and rim values) is observed (Figure 4-4C).

4.2.3.3 Primary phase analyses – plagioclase

Plagioclase was analyzed in 198 domains of drill core GT1A. The obtained Ca# (Ca/(Ca+Na) x 100; molar basis) ranges from 68.31 to 87.32 with standard deviations from the mean of 0.1 to 2.42 in the core and from 69.29 to 88.25 with standard deviations of 0.29 to 2.63 in the rim. The median of the standard deviations is 0.9 or 0.82 in core and rim, respectively. The depth plot of the Ca# agrees with the trends observed in olivine and clinopyroxene Mg#s, however, revealing slightly larger error bars indicating a higher heterogeneity in the grains. Moreover, the minimum in Ca# of plagioclase is at 1060 maM where a continuous fractionation trend starting at 1030 maM ends. The sample correlating with minima in the Mg#s of olivine and clinopyroxene at 1075 maM also represents the most evolved composition of a reverse fractionation trend from 1075 to 1090 maM. Its composition is, however,
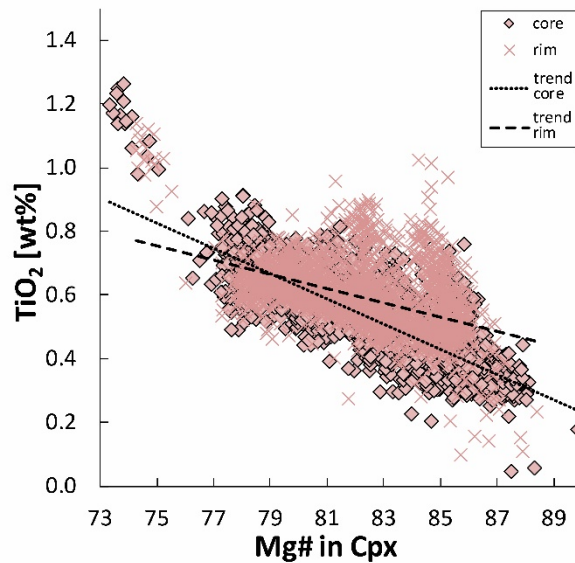
slightly more primitive than the corresponding clinopyroxene and olivine grains which requires further discussion.

Zoning is generally very weak in plagioclase and differences between core and rim always plot within the uncertainty defined by the propagating errors of the standard deviations in core and rim. However, it is remarkable that rim/core ratios represent rims being slightly enriched in Ca#, except for a horizon between 1110 and 1140 maM where a the samples show slight Ca# depletion in the rim, although still within the uncertainty (Figure 4-4D right).

4.2.3.4   *Primary phase analysis – Fe-Ti-oxides*

As presented in Figure 4-3, a small amount of opaque phases in the thin sections from GT1A were identified as Fe-Ti-oxides using the EDX system of the SEM at the Institute of Mineralogy in Hannover. Whereas magnetite is usually associated to the serpentinization olivine and, therefore, a secondary phase, ilmenite or titanomagnetite are assumed to be primary products crystallized from a relatively evolved melt in the Samail ophiolite (e.g., Pallister and Hopson, 1981). The grains which are usually smaller than 1 mm in size often reveal ilmenite-magnetite exsolutions (Figure 4-6). Their composition was analyzed also by EDX in order to obtain detailed information on the Fe-Ti ratio and also to identify minor elements within the grains, such as V. The results are listed in the electronic supplement of this thesis.

The nearly pure magnetite compositions reveal FeO contents ranging from 93.7 to 98.5 wt%. Minor elements are TiO_2 (<3.2 wt%), Al_2O_3 (<2 wt%), Mn_3O_4 (<0.6 wt%), V_2O_5 (<0.8 wt%), and in a single sample CoO (<1.6 wt%). In the ilmenite, the FeO content ranges from 42 to 56.2 wt% and TiO_2 reveals contents between 41.8 and 53.9 wt%. Minor constituents are MgO (<3.2 wt%), Al_2O_3 (<3.0 wt%), Mn_3O_4 (<2 wt%, SiO_2 (<1.6 wt%) and V_2O_5 (<0.4 wt%). Titanomagnetite was found in two samples with FeO contents ranging from 55.6 to 66.5 wt% and TiO_2 contents ranging from 30.1 to 39.2 wt%. Minor elements are Al_2O_3 (<1.7 wt%), MgO (1.6 wt%), SiO_2 (<1.2 wt%), Mn_3O_4 (<1.2 wt%), Cr_2O_3 (<0.7 wt%), and V_2O_5 (<0.8 wt%).
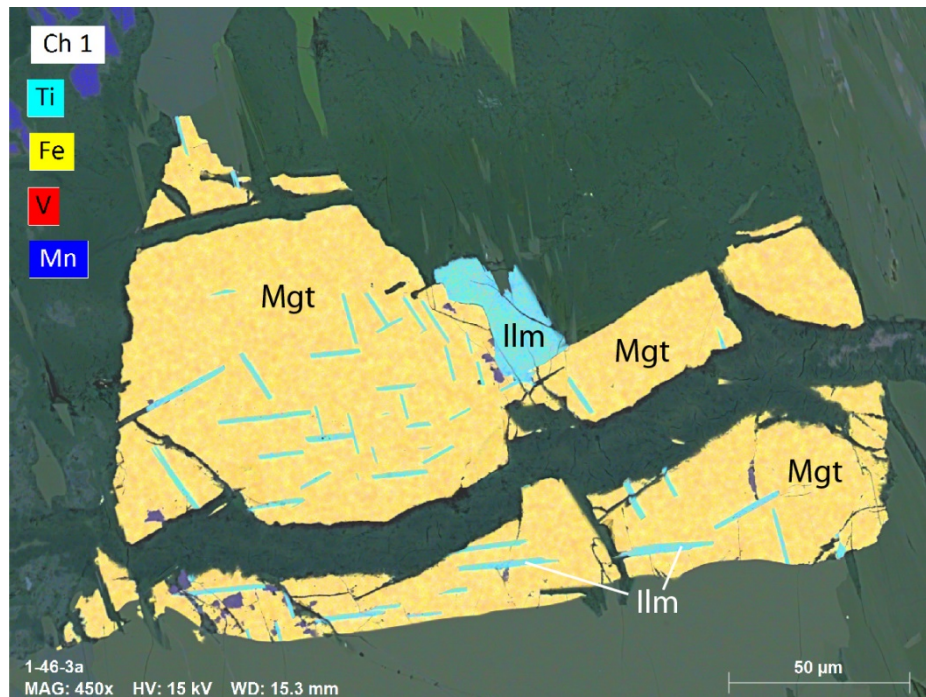
Figure 4-6   EDX map of a magnetite grain (Mgt; orange) in sample 1-46-3a containing Ti-rich ilmenite exsolutions (Ilm; turquoise). Element colors were adjusted for best visualization of the detected elements.

4.2.3.5   Decameter fractionation units in GT1A

Beside the fractionation trend from the bottom of the drill core to a height of 1075 maM described above, several smaller trends and compositional changes are observed along the drill core. They are marked as eight units in Figure 4-7A where Mg#s of olivine and clinopyroxene and Ca# of plagioclase are plotted: six units showing normal fractionation (normal fractionation units; NFU 1 – 6) and two units showing reverse fractionation up section (reverse fractionation units; RFU 1 – 2). They are listed here with respect to the direction of normal fractionation from the bottom to the top of the drill core. Since NFU 6 starts at the very bottom of the drill core, its base height above the MTZ is unknown. However, it can be followed up to a height of 886 maM, where clinopyroxene and plagioclase compositions are significantly more differentiated than in the overlying sample at 900 maM. The shift towards more primitive compositions, here, is interpreted as start of NFU 5 which then can be followed up section to 985 maM, and which is only interrupted by a couple of elevated Mg# values in clinopyroxene of a wehrlitic sample at 978 maM. Normal fractionation unit 4 then starts at 990 maM, where the major element compositions of all present primary phases are more primitive, again. This NFU appears relatively thin with its highest sample at 1015 maM. Moreover, the sampling density is not as high as in other units because large gaps between 995 and 1010 maM and between 1016 and 1028 maM have not been sampled due to intense alteration by a thick hydrothermal fault zone. Thus, the upper boundary of NFU 4 cannot be defined. The start of NFU 3 is then set at 1031 maM, where clinopyroxene and plagioclase compositions again shift towards more primitive values. Normal fractionation unit 3 ends at 1060 maM where plagioclase compositions are most evolved. This is contradictory to olivine and clinopyroxene compositions which are even more evolved at 1075 maM; the choice to set the upper boundary of NFU 3 at 1060 rather than at 1075 maM is further explained below. The evolved compositions at 1075 maM are used to constrain the base of RFU 2 which shows phase compositions steeply evolving towards primitive compositions at 1090 maM. The start of NFU 2 is set at the most primitive compositions at 1090 maM and it evolves up to 1103 maM where RFU 1 starts with the evolution of more primitive phase compositions up section until 1136 maM. Normal fractionation unit 1 is the uppermost unit recovered in drill core GT1A and starts at 1136 maM. Its upper boundary cannot be identified.

The fractionation units and their top and base heights above the base of the MTZ correlate relatively well with the lithologic units defined during the core description on CHIKYU (Table 4-1; chapter 4.2.1.1; Kelemen et al., 2020). A key difference is that on the basis of the EPMA data, unit II described in Kelemen et al. (2020) is separated into a NFU and a RFU leading to eight instead of seven units in total. The boundaries between adjacent units may vary on the meter scale which might be an artifact of the different methodical approaches of unit definition (i.e., macroscopic observations by Kelemen et al., 2020, petrological data in this study).

4.2.3.6   Phase correlations

Taking the observed fractionation units into account, compositional correlations between the most abundant primary phases clinopyroxene and plagioclase were investigated. As a useful tool to determine fractional crystallization by precipitation of both phases, the Ca# of plagioclase was plotted versus the Mg# in clinopyroxene (Figure 4-7B). It appears that all samples, except for the sample with the lowest Mg# correlating to the compositional minimum at 1075 maM, plot on the same fractionation trend. However, plotting the Ca# versus the Mg# with respect to the individual units reveals that the trends significantly vary from one unit to another (Figure 4-7C).

A key observation is that the minima in Mg#s of olivine and clinopyroxene at 1075 maM does not fit the fractionation trend in NFU 3 (see gray symbol inFigure 4-7C.5), but rather matches the reverse

fractionation trend of RFU 2 (see red framed symbol inFigure 4-7C.4) which covers a wide range in Mg# over the narrow horizon between 1075 and 1090 maM. Consequently, the question arises how such a steep reverse fractionation can be produced within the lower oceanic crust.

The phase correlations of other units plot on different trends with some cloudy distributions (e.g., NFUs 1, 4, and 5) and some clearer trends (e.g., RFU 1, NFUs 2, 3, and 6). The angles of the plotted interpolated lines vary from one unit to another indicating that the fractionation path is different within the individual units.
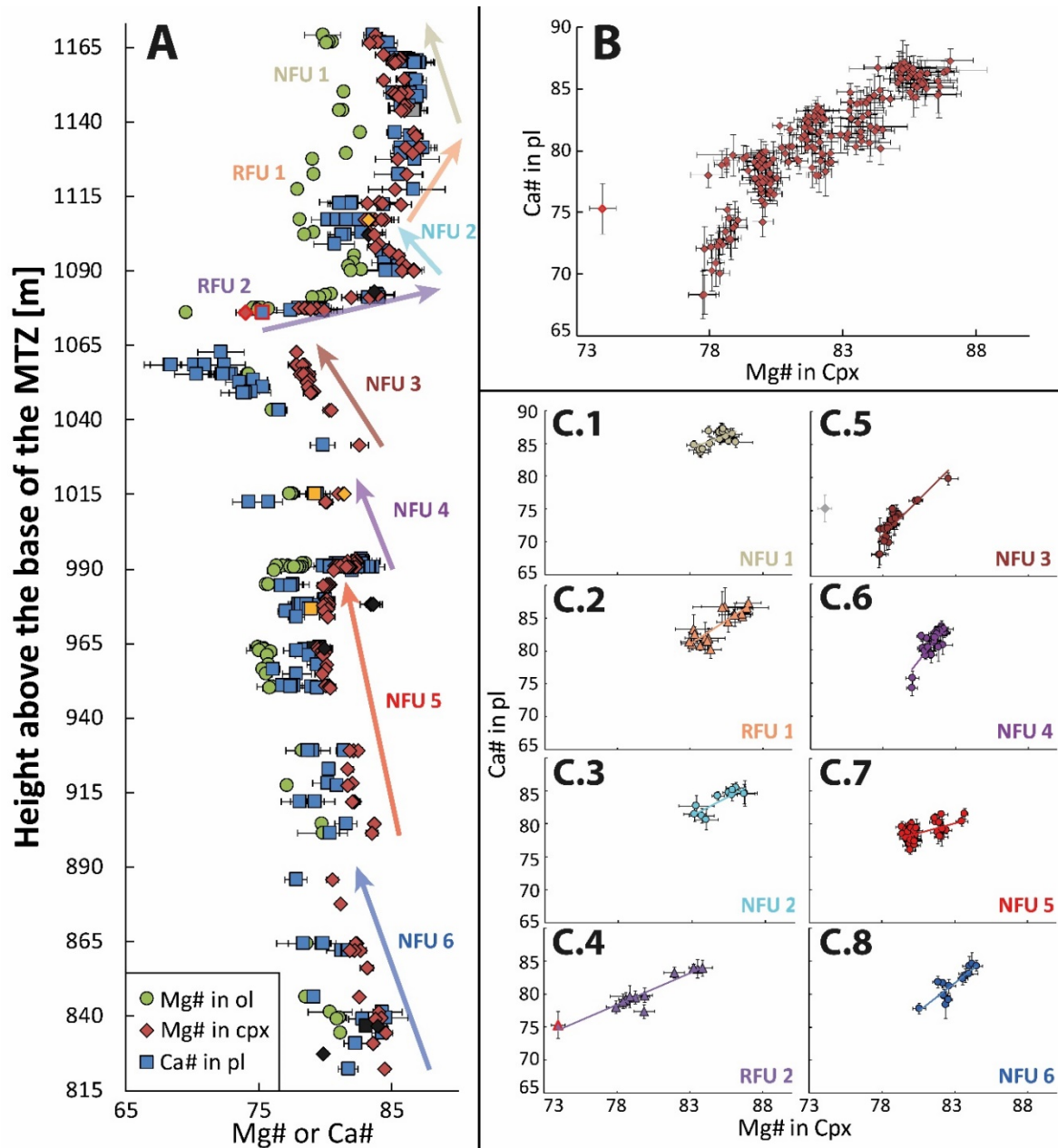
Figure 4-7 A) Average core values of the Mg#s in olivine and clinopyroxene, and the Ca# in plagioclase plotted versus the height above the base of the MTZ and errors indicating decameter scale normal (NFU) or reverse (RFU) fractionation units. Grey data points are anorthositic, orange are troctolitic, and black are wehrlitic samples. See text for details. B) Ca#s of plagioclase cores plotted versus Mg#s in clinopyroxene cores. Note the clear fractionation trend except for the outlier (red frame) corresponding to the marked data points at 1075 maM in A. C) Individual fractionation trends of each fractionation unit. Note i) the colors in C correspond to the colored arrows marking the trends in A. ii) differently dipping fractionation paths of individual cycles in C. iii) the red marked data point in C.4 corresponding to marked points in A and B clearly fits with the reverse trend in C.4 (RFU 2) rather than with the normal trend in C.5 (NFU 3; grey data point).

4.2.4 Microstructural analysis using electron backscattered diffraction

The fabric analyses on drill core GT1A reveal varying microstructural features throughout the core. The data of clinopyroxene and plagioclase fabrics were obtained using the grain methods described in chapter 3.3.2 in order to prevent overrepresentation of large crystals, as they are present in some samples. This method is not applicable to olivine because of the observed mesh serpentinization which leads to the artificial separation of a single grain into several smaller grains by the applied MTEX toolbox. Therefore, the grid data method was used for olivine. However, reliable olivine fabric data are generally rare due to the relatively low abundance of primary olivine relicts. Fabric depth plots are, thereby, presented only for plagioclase and clinopyroxene.

The J index quantifying the fabric strength of a phase ranges between 1.63 and 6.33 for plagioclase and between 1.39 and 6.45 for clinopyroxene. The J indices of both phases do not show clear trends down section but vary irregularly along the core with plagioclase data usually being a bit higher than clinopyroxene data (Figure 4-8A). As already observed in the surface samples described in chapter 3, misorientation within the analyzed grains is relatively weak with a grain orientation spread
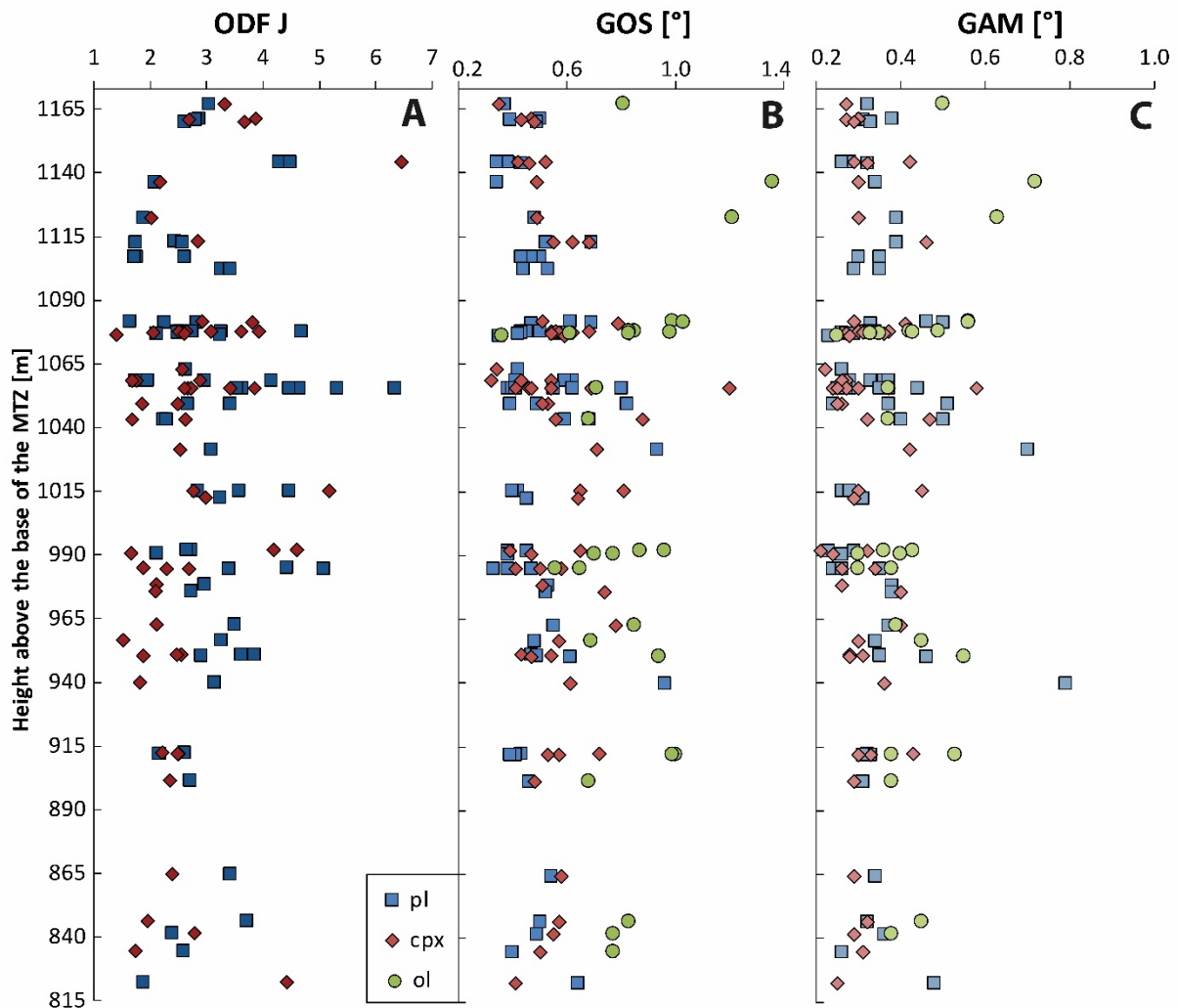
Figure 4-8   A) The J indices of the orientation distribution function (ODF J) of plagioclase (blue rectangles) and clinopyroxene (red diamonds) plotted versus height above the base of the MTZ. B) the grain orientation spread (GOS) quantifying internal misorientation within plagioclase, clinopyroxene, and olivine (green circles) plotted versus the height above the base of the MTZ. C) the grain average misorientation (GAM) as a quantitative proxy of subgrain formation in plagioclase, clinopyroxene, and olivine plotted versus the height above the base of the MTZ.

(GOS) ranging from 0.33° to 0.96° with a mean of 0.5° in plagioclase and ranging from 0.32° to 1.2° with a mean of 0.56° in clinopyroxene (Figure 4-8B). The grain average misorientation (GAM) varies from 0.23° to 0.79° with a mean of 0.34° in plagioclase and from 0.21° to 0.58° with a mean of 0.31° in clinopyroxene (Figure 4-8C). The low GAM indicates that the average misorientation within a grain per sample is very weak and the low GAM, with its sensitivity to subgrain formation, confirms the petrographic observation that subgrains are practically absent in clinopyroxenes and plagioclases of drill core GT1A. Only olivine, with elevated misorientation data of both GOS (mean: 0.84°) and GAM (mean: 0.43°), shows a slightly stronger misorientation which is consistent with data obtained from surface samples.

Although the fabric strength does not show systematic variations down sections, those are observed in the BA or BC indices of plagioclase and clinopyroxene, respectively. They plot between 0.27 and 0.9 with a mean of 0.51 for plagioclase and between 0.28 and 0.74 with a mean of 0.53 for clinopyroxene indicating that a significant lineation component of those phases is present in the drill core (Figure 4-9A). The two indices show a nice parallelism along the core with a gradually decreasing trend (i.e., toward weaker lineation) from ~0.6 at 865 to ~0.3 at 1090 maM. Above 1090 maM, both indices increase immediately to ~0.6 indicating a stronger lineation in clinopyroxene and plagioclase along the uppermost 65 m of the core. This trend describes a distinct parallelism to the down hole
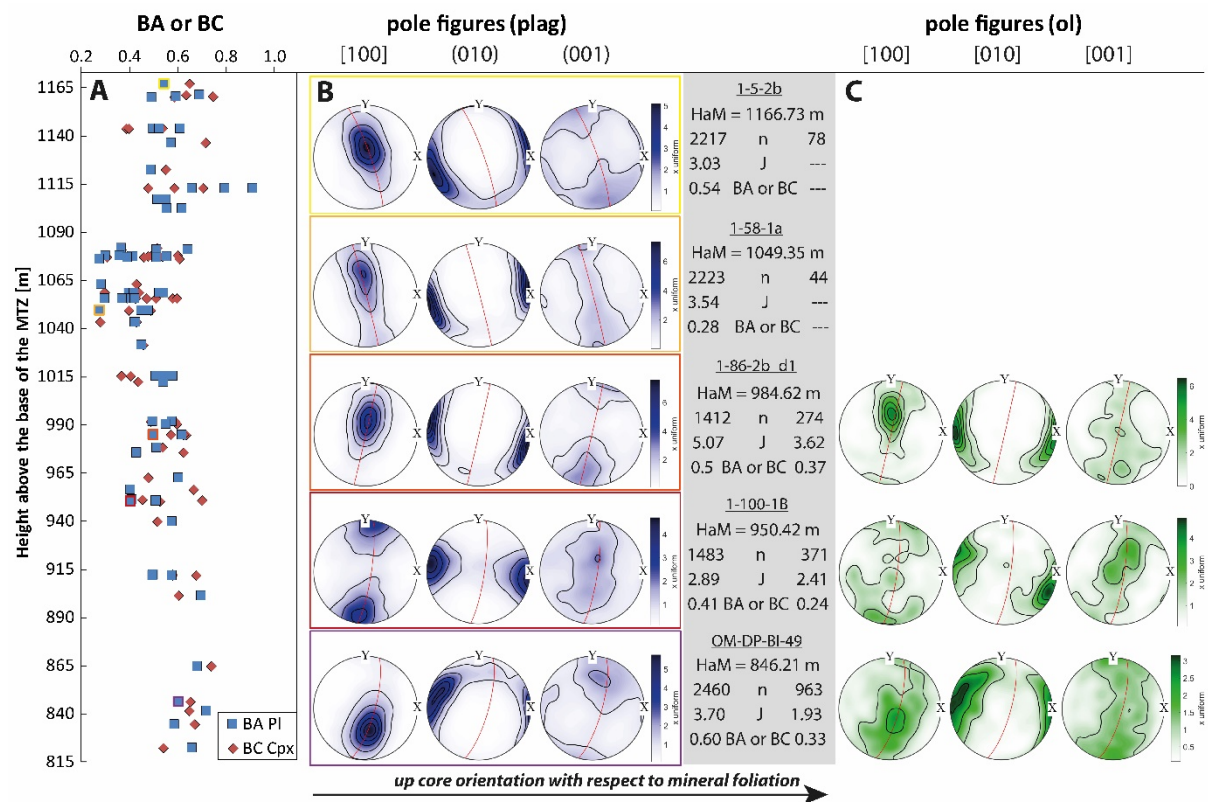
Figure 4-9   A) The BA or BC index of plagioclase and clinopyroxene, respectively, quantifying the degree of lineation (with higher values indicating stronger lineation) plotted versus the height above the base of the MTZ. Note the similarity of the plotted trend with the petrological trend shown in Figure 4-4. B) and C) representative pole figures of 100, 010, and 001 of plagioclase or olivine, respectively, arranged by height above the base of the MTZ. Values in the gray column provide some key information on the sample (name underlined) with n = number of indexed grains, J = J index of the orientation distribution function (ODF), and BA or BC indices of plagioclase and olivine, respectively. Note that the colored frames around plagioclase pole figures correspond to colored data points in A). X points towards the top of the drill core, as also indicated by the black arrow at the base. Red lines mark the foliation within the sample obtained by plagioclase (010) poles. Only pole figures of samples with >100 grains of a phase are plotted (e.g., Satsukawa et al., 2013).

trends observed in the Ca# of plagioclase and the Mg# of clinopyroxene, and provokes the question of how chemical and microstructural features in the samples can be correlated.

As BA and BC indices quantify the pole figure symmetry, the trends described above are also observed in the pole figures (see Figure 4-9B for a pole figure selection and the electronic supplement for all pole figures obtained in drill core GT1A arranged by height above the base of the MTZ): at the base of the core, pole figures with [100](010) point maxima in plagioclase and (010)[001] point maxima in clinopyroxene dominate, representing a fabric showing both foliation and lineation. Up section (010) of both phases gradually evolves from a point maximum to a girdle distribution indicating that the lineation intensity weakens up section such that at 1081 maM, the fabric is dominantly foliated. Pole figures above 1100 maM show [100](010) and (010)[001] point maxima in plagioclase and clinopyroxene, respectively, demonstrating that the fabric is again both foliated and lineated above 1100 maM. Interestingly, olivine [100] occasionally parallels plagioclase [100] (Figure 4-9) indicating a plastic shearing component in those samples (Jousselin et al., 2012).

4.2.5 Mineral geochemistry

Trace element analyses, with a focus on REE concentrations, were performed with the purpose, among others, to determine compositional differences between (olivine) gabbros and adjacent interlayers of anorthosite, troctolite, or wehrlite in terms of phase compositions. A subset of eight thin sections containing 13 domains was analyzed with an anorthositic layer adjacent to olivine gabbro in sample 16-4-20-30, a troctolitic layer adjacent to olivine-bearing gabbro in sample 1-72-4, and a wehrlite layer adjacent to mela-olivine gabbro in sample 88-3-49-55.

Zirconium in clinopyroxene and Ce in plagioclase were plotted versus depth as representative trace elements for both phases. Although the low spatial resolution hampers the determination of some down hole trends, compositional variations along the core are observed in both phases. Cer in plagioclase ranges from 0.37 to 0.62 µg/g, and Zr concentrations in clinopyroxene cores vary from 5.85 to 11.98 µg/g in the core and from 6.56 to 13.6 µg/g at the rim. Again, the zonation is significantly stronger in some samples above 1075 maM than below and reaches enrichment factors of up to 2.25 at the rim compared to the core (Figure 4-10).

Figure 4-11 shows chondrite-normalized La+REE contents in clinopyroxene of all analyzed samples. All samples plot on smooth curves from low chondrite-normalized light rare earth element (LREE) values to a magnitude higher values in the heavy rare earth elements (HREE). A negative Eu anomaly is observed in all samples. The data obtained from troctolite (orange line) and wehrlite (blue line) are plotted together with the adjacent gabbroic results separately (Figure
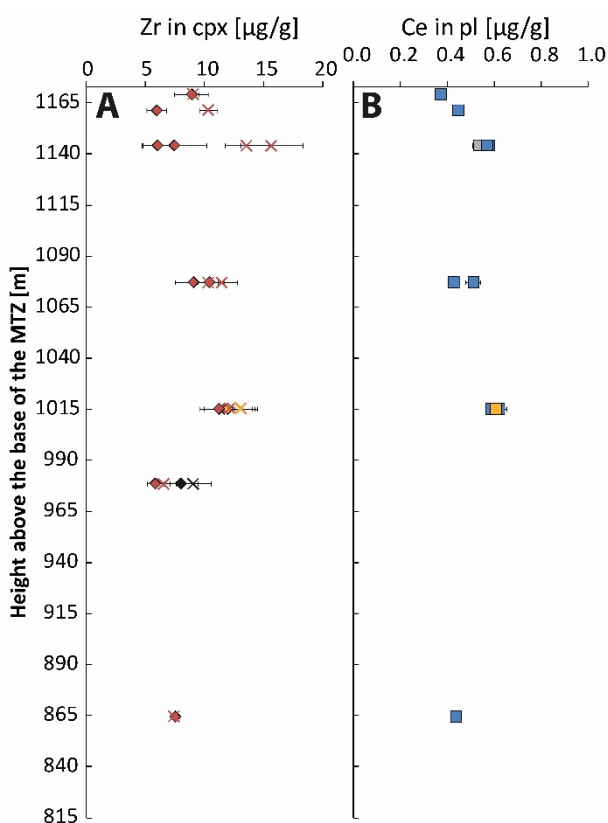
Figure 4-10 Depth plots of Zr in clinopyroxene (A) and Ce in plagioclase (B). Closed symbols are core, crosses are rim data. Grey data points represent anorthositic, orange represent troctolitic, and black represent wehrlitic samples. Error bars symbolize standard deviation from the mean.

85

4-11 A.2 and A.3) in order to emphasize potential differences with the gabbroic analyses. However, troctolite reveals the same phase composition as the adjacent olivine-bearing gabbro, although representing the most evolved composition of all samples. Wehrlite shows a slight enrichment in all La+REE data and reveals a stronger Eu anomaly than the gabbroic host rock. Clinopyroxene analyses were performed in the core and the rim separately in order to determine the degree of zonation within the grains. The rim/core ratios plotted in Figure 4-11 A.4 show that the rim is in almost every sample enriched compared to the core. Based on the observations made in Mg# and TiO_2 zoning of clinopyroxene (see chapter 4.2.3.2), the data from above 1075 maM are plotted as dashed lines, those from below as full lines. Obviously, the most intense zonation occurs in samples above 1075 maM with enrichment factors of ~1.3 (sample 1-10-2b) or ~1.65 (sample 16-4-20-30 domains 1 and 2). The zonation in Eu is weaker than in other elements in almost every sample. This might be a consequence of the generally decreased Eu concentration in the melt such that fractionation does not affect the Eu content in clinopyroxene as it does for other elements.

The depletion of Eu in the melt when clinopyroxene nucleation starts is well represented by distinct positive Eu anomalies in the plagioclase La+REE data of every analyzed sample (Figure 4-11B). Whereas the chondrite-normalized LREE values in plagioclase are as high as those in clinopyroxene, the compatibility drops towards HREEs such that their concentrations are up to 1.5 magnitudes lower than those of the LREEs. Heavy REE lines are generally slightly more scattered which is due to the very low HREE concentrations in plagioclase that are close to the detection limit of the applied method. Troctolite and anorthosite are plotted separately with the adjacent gabbroic rocks. Troctolite reveals, similar to the clinopyroxene data, the same REE concentrations as the olivine-bearing gabbro above and below (Figure 4-11 B.2). Anorthosite shows slightly decreased LREE concentrations compared to the olivine gabbro, gradually evolving to more enriched concentrations in the HREEs (Figure 4-11 B.3). Therefore, a slightly more differentiated composition of the anorthosite compared to the gabbroic host rock is indicated.
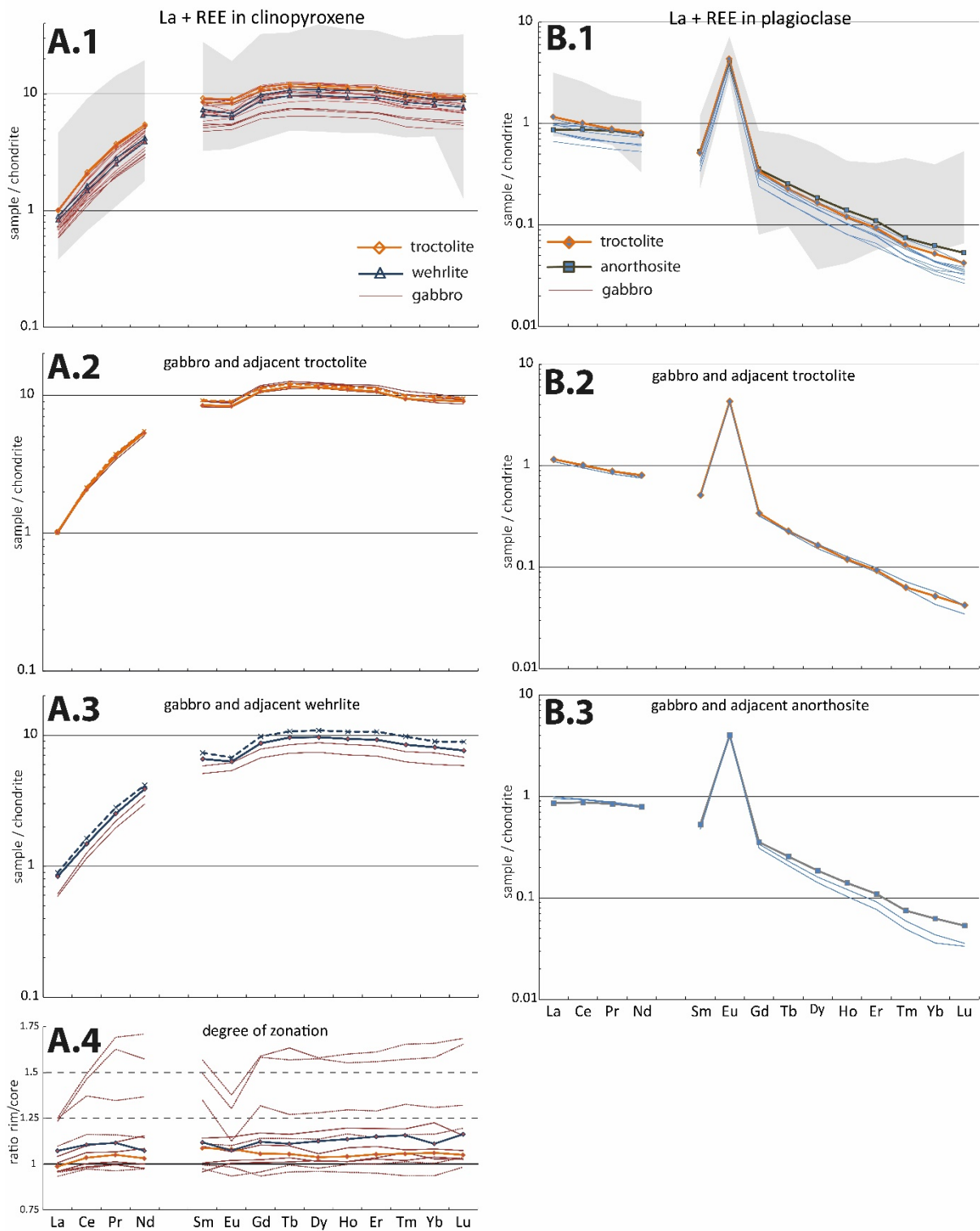
Figure 4-11 A.1-3) Chondrite-normalized La + REE data in clinopyroxene plotted with respect to sample lithology. A.4) The degree of zonation quantified by the rim/core ratio. dark red patterns are (olivine) gabbros, orange patterns are troctolitic, dark blue patterns are wehrlitic samples. Closed symbols are core, crosses are rim analyses. B) Chondrite-normalized La + REE data in plagioclase. Light blue patterns are (olivine) gabbros, grey pattern is an anorthositic sample. Grey background patterns in A.1 and B.1 mark the range measured by Lissenberg et al. (2013).

4.2.6   Bulk rock geochemistry

To increase the data density of bulk rock analyses, not only results obtained at the Institute of Geosciences at Kiel but also geochemical bulk rock data obtained during the core description on CHIKYU (Kelemen et al., 2020) are presented here. Both data sets were acquired using the same method, with XRF for major and LA-ICP-MS on pressed powder pellets for trace elements. To approach a best-possible spatial resolution, also mass balance data calculated from the modal proportions and EPMA results on olivine, clinopyroxene, and plagioclase were added. Those were corrected with respect to the analyzed phases (e.g., if olivine was found but too altered to analyze by EPMA, the sample was not used for mass balance calculations). Only major element data were used for mass balance calculation. The calculated values are only plotted as grey background values to emphasize that they are not as reliable as data obtained analytically.

The down hole variations already observed in major and trace element data from the phase analyses are undeniable also in the bulk rock data. Moreover, the compositional units defined from fractionation trends in major element mineral compositions are also observed in bulk rock data, e.g., the bulk rock Mg# or the bulk rock Cr/Zr ratio (Figure 4-12A and B). Although less pronounced and more scattered, cyclic variations do exist in the bulk rock geochemistry of the drill core.

Trace element patterns of all chondrite-normalized bulk rock compositions measured on CHIKYU (Kelemen et al., 2020) and in Kiel reveal a wide compositional range and plot in the depleted range of the layered gabbros sampled in Wadi Gideah at the surface by Garbe-Schönberg et al. (subm) (Figure 4-12C). They are presented in Figure 4-12D arranged by the fractionation units defined in chapter 4.2.3.5. It was tested whether the trace element concentration is correlated to the height in a fractionation unit, as could have been expected from both mineral and bulk rock major element data. There was no such correlation observed and for the sake of simplicity, the patterns were not color-coded with respect to their actual height in a unit. A plausible explanation for the absence of such a trend could be the decoupling of the modal proportions from the height in a fractionation unit (Figure 4-3). Since modal abundances have a strong effect on trace element distributions at the same time, it is questionable how strong the correlation between bulk rock REE concentrations and the height in a unit can be. Most of the special lithologies, where grey patterns represent anorthositic gabbro/anorthosite, green patterns are dunite, and orange and black belong to troctolitic gabbro or wehrlite, respectively, plot at low REE concentrations, with depleted HREE contents in anorthosite and depleted LREE in dunite and wehrlitic samples. The former is due to the low compatibility of HREEs in plagioclase, which is the major constituent of anorthosite, and the latter can be assumed to result from the intense alteration of the sample removing fluid-mobile LREEs.

The generally observed positive Eu anomaly is interpreted as a consequence of the high modal abundance of plagioclase throughout the core. The wehrlitic sample in NFU 5 also shows a positive Eu anomaly, although the corresponding clinopyroxenes revealed a negative one. However, it cannot be excluded that the dark mela-olivine gabbro which was also part of the concerned sample piece contaminated the sample during preparation for bulk rock analysis. The generally low REE concentrations in this sample are consistent with its primitive clinopyroxene compositions with high Mg#.
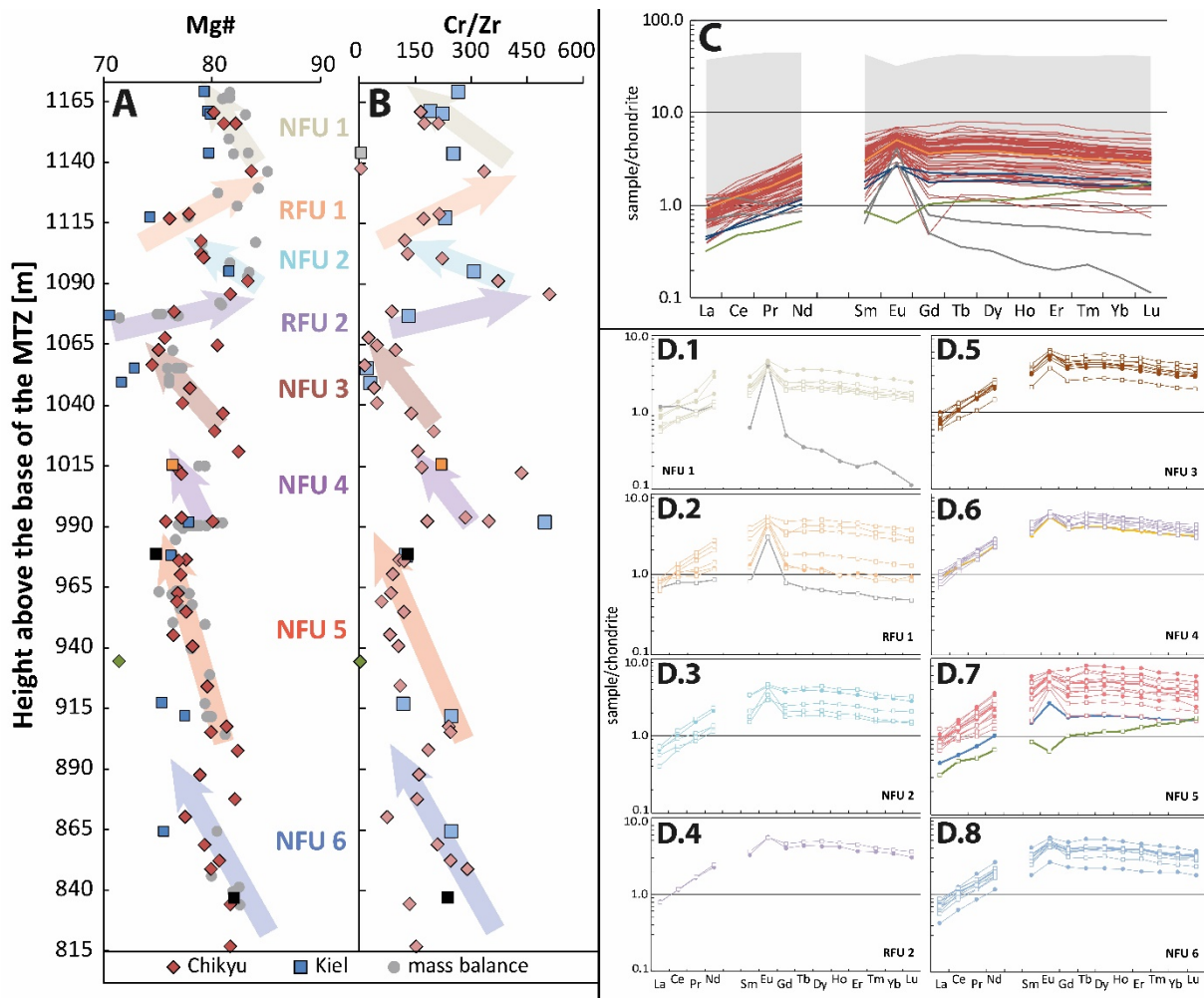
Figure 4-12 A) and B) Bulk rock Mg# or Cr/Zr ratio, respectively, plotted versus height above the base of the MTZ. Rectangle represent data obtained at the Institute of Geosciences in Kiel for this study, diamonds are data obtained during core description on CHIKYU. Grey circles are data obtained by mass balance for major elements. The light grey rectangle represents an anorthositic sample, the green diamonds are serpentinized dunites, and the orange and black symbols belong to troctolites or wehrlites, respectively. Coloured arrows represent normal (NFU) or revers (RFU) fractionation units. Note the parallelism between both depth logs and the major element mineral compositions presented in Figure 4-7A. C) Lanthanum + REE bulk rock concentrations in drill core GT1A with red = olivine gabbros, grey = anorthosite, orange = troctolite, green = dunite, and black = wehrlite. Grey pattern in the background represents the range of bulk rock data obtained from surface layered gabbro samples by Garbe-Schönberg et al. (subm.). D.1-8) Trace element patterns presented for every fractionation unit with closed circles for analyses obtained in Kiel and open rectangles for analyses obtained on CHIKYU. Colors of gabbroic samples correspond to arrow colors in A and B, other colors as defined for C.

89

4.3 Discussion

Drill core GT1A of the OmanDP reveals a huge amount of data which have never been obtained in this spatial resolution and coherency before over such a long section. The observations described above are interpreted in the following by best-possible integration of the present data into the scientific context of previous studies. The hypothesis made in chapter 3 that the lowermost 3500 m of the lower crust in Wadi Gideah accrete by in-situ crystallization is tested for consistency with the data obtained from drill core GT1A.

4.3.1 Decameter scale fractionation units

Larger scale compositional variations in the gabbroic crust of the Samail ophiolite were already reported by Pallister and Hopson (1981) in the wadis Khafifah, Kadir, and Gideah, which are all located in the Wadi Tayin massif of the Samail ophiolite. The variations they observed, with an average spacing of several 100 meters in every wadi, are mostly unsystematic. Only in Wadi Gideah, anorthite in plagioclase and enstatite in clinopyroxene show decreasing up section trends along the lower crust. The decameter scale trends observed in both mineral and bulk rock compositions from drill core GT1A are also in agreement with the findings of Browning (1984) who observed repeated mineral compositional changes along a 600 m long section from the Wadi Bani Kharus in the Rustaq massif of the Samail ophiolite. They identified three major units which contain a total of 14 individual cycles, including two "reversed" cycles where the base is more fractionated than the top of the cycle. On average, their units have a thickness of approximately 43 m being in good agreement with an average unit thickness of approximately 35 m in the samples of this study. It is remarkable that at the base of their lower reversed cycle, TiO_2 in clinopyroxene is extraordinary high, as at the base of RFU 2 in drill core GT1A. Another similarity between the data sets is the well-developed trend in the anorthite versus forsterite plot reported by Browning (1984), as it is also observed in drill core GT1A Figure 4-7 C.

Browning (1984) suggested that the units correspond to open system fractionation where primitive "resets" occur every tens or hundreds of meters. To constrain the potential dimensions of such sills, the method introduced by Browning (1984) was applied to the sample suite of drill core GT1A. Browning (1984) calculated the height of a magma sill based on the height of the crystallized cumulate pile and the distribution of NiO in olivine or Cr_2O_3 in clinopyroxene. A tabular magma lens shape and perfect Rayleigh fractionation is assumed for the calculation using the following equation

$$l = \frac{c}{1 - (C_{Xf}/C_{Xi})^{1/(D-1)}}$$

Eq. 4.1

with l = lens height, c = height of the cumulus pile, C_{Xf} = element content at beginning crystallization (i.e., the element content at the base of a unit averaged from the three lowermost analyses here), C_{Xi} = element content at the end of crystallization (i.e., the element content at the top of a unit averaged from the three uppermost analyses here), and D = distribution coefficient of the element between the concerned solid phase and the melt. Browning (1984) used the distribution coefficients calculated by Cox et al. (1979) with D_{ol}^{Ni} = 10 and D_{cpx}^{Cr} = 10. For this study, the Cr_2O_3-in-clinopyroxene calculation was applied because the coherency of reliable olivine analyses is much lower than the one of Cr_2O_3 in clinopyroxene. The results of the sill height calculation have to be handled with caution due to several uncertainties:

1) The Cr_2O_3 contents of clinopyroxene were averaged for base and top of a cumulate pile from the lower- or uppermost three gabbroic samples of a unit, respectively. Obviously, the usage

of an average composition is accompanied with a range of possible results which is given in parantheses below.

2) The distribution coefficient D of every phase was calculated as bulk D for every unit. As Browning (1984) already pointed out, calculating bulk D is not straightforward because the units show indicators of crystal sorting, i.e., their modal abundances are variable (Figure 4-3). Following the procedure of Browning (1984), bulk D was calculated from modal proportions by weight and averaged per unit. The resulting bulk D is only an approach to a mathematic range which puts further uncertainty on the resulting sill height calculation. However, the bulk D calculation is based on precise modal abundance quantifications by point counting with 500 points per domain providing some confidence for the estimated bulk D values.

3) Browning (1984) restricted the proper sill height calculation to cases where "the liquid remained homogeneous at all stages of the fractionation cycle". It is unclear, whether the liquid composition was homogeneous during the fractionation, but relatively straight phase compositional trends along the fractionation units imply that the parental melt did not experience strong heterogeneities during fractionation. However, widely scattered Cr_2O_3 contents in NFU 5 may be an indicator of heterogeneous melt compositions.

4) The exact geometry of a melt sill is unknown. A tabular shape – as assumed here – may be plausible, but other shapes like triangular with inclined walls may result in different results (Browning, 1984).

The heights of a melt lens for every NFU was calculated, except for the NFUs 1 and 6 whose top or bottom boundaries, respectively, are not covered by the drill core. From the remaining four NFUs, NFU 2 and NFU 3 provide results with sill heights of 69 m (range: 47 – 122 m) or 89 m (range: 63 – 185 m), respectively. The cumulus heights of the NFUs approximate 13 m for NFU 2 and 31 m for NFU 3, indicating that the sills were 4 – 10 times higher than the crystallized cumulate pile. For NFU 5, a sill height of 217 m (range 95 m – n.d.) was calculated, indicating with the height of the cumulus pile of 83 m that the sill was about 1.2 – 2.6 times higher than the cumulus pile. However, it was not possible to calculate a proper maximum sill height due to relatively high standard deviations from the means of bottom and top Cr_2O_3 contents. An implausible sill height of 623 m was calculated for NFU 4 being approximately 25 times higher than the cumulus thickness of 26 m. The value results from a very small difference between bottom and top Cr_2O_3 contents in the cumulus pile. Moreover, the widely scattered Cr_2O_3 content at the base NFU 4 (Figure 4-4 B) shows a very weak correlation with the Mg# covering only a narrow range in this unit, and indicating that NFU 4 is not representative for a normal Rayleigh fractionation.

The sill heights calculated from NFU 2 and NFU 3 plot in a range that overlaps with sill thicknesses imaged by seismic reflection data from the EPR of about 50 m (e.g., Marjanovic et al., 2014; Carbotte et al., 2021) which increases their trustworthiness. However, the sills imaged at EPR were found in a horizon up to 800 m below the AML which is much shallower than the horizon penetrated by GT1A. Marjanovic et al. (2014) and Carbotte et al. (2021) point out that the applied seismic reflection method might not be able to detect <50 m thick melt sills at greater depth such that they could exist, although not discovered by the most recent studies.

From the findings presented in chapter 3, it could be inferred that every fractionation unit results from the crystallization of a decameter-scaled sill. If the calculated sill heights are real, the residual melt, which then makes a portion of 70 – 90 % of the sill height, must be removed from the sill before fractionating late stage phases, which were not observed in the fractionation units used for sill height calculation. Ferrando et al. (2021) inferred from a microstructural study on gabbros from Atlantis Bank at the ultraslow-spreading Southwest-Indian Ridge that gabbros were compacted at the stage of a

crystal mush to nearly complete solidification aiding to expel melt from the mush which then migrates through the crust. Although the setting of an ultraslow-spreading ridge is significantly different from the fast-spreading setting assumed for the Samail ophiolite (e.g., Dick et al., 2006), compaction might also have played a role in the formation of the lower crust in Oman (e.g., VanTongeren et al., 2015). The crystal-plastic deformation reported by Ferrando et al. (2021), which is nearly absent in plutonic samples from the Samail ophiolite (e.g., MacLeod and Yaouancq, 2000; Jousselin et al., 2012; VanTongeren et al., 2015) and which is very weak in GT1A, could have been accommodated by the higher melt portion in the fast-spreading environment (e.g., VanTongeren et al., 2015). Another indicator of compaction is the ubiquity of a foliation along the crust, overprinted by a lineation component increasing with depth (see chapter 3; see Figure 4-9). VanTongeren et al. (2015) interpret pole figures revealing [100] girdles and (010) point maxima, as they are widely observed along the crust (see chapter 3), as results of compaction.

However, some observations are difficult to reconcile with the model that every fractionation trend results from an individual compacted and solidified sill. This hypothesis presumes that the individual sills show different properties in terms of microstructures and/or compositions. In such a system, the gradual up section trends in both phase compositional and fabric data (Figure 4-4, Figure 4-9) are not consistent with individually fractionating stacked sills which were rather expected to show larger differences between each sill. Such stronger pronounced differences are only observed from the top of NFU 3 to the base of NFU 2 over the narrow horizon of reverse fractionation in RFU 3. Also the degree of lineation significantly changes there, leading to the interpretation that possibly the boundary between two different melt sill is recovered, as discussed in more detail below.

Browning (1984) suggested that the observed trends along the fractionation units did not create in single sills, but by primitive composition resets of a single – eventually compositionally stratified – magma chamber. Indeed, it might be possible that more than one fractionation trend was created in a single melt sill which was occasionally replenished by fresh primitive melt. Such a model agrees with the relatively weak compositional differences between adjacent units. Assumed that the four NFUs identified between 1075 maM and the bottom of the drill core were formed in a single melt sill that was replenished by primitive melt several times, this sill should not only fit the sill height calculated above, but also fulfill the dimensional restrictions found at EPR (e.g., Marjanovic et al., 2014) with heights of about 50 m. A huge stratified magma chamber, where a fractionation unit corresponds to a stratified horizon as suggested by Browning (1984), must be significantly higher than 50 m to produce the cumulate pile with a height of at least 260 m from 1075 maM to the bottom of the core. Therefore, the idea of a stratified magma chamber has to be ruled out.

An environment that allows the crystallization of several fractionation units with a cumulate height of 260 m in total within a single melt sill, could be a dynamic melt sill which migrates upward when replenished by fresh melt. Such dynamics were suggested for the AML by Müller et al. (2017). If primitive melt is emplaced within the crystal mush of the lower crust close to the ridge axis, the melt can fractionate a first cumulate pile. The height of the residual melt column decreases with ongoing fractionation until an influx of primitive melt and mixing of residual and fresh melts creates a new intermediate melt melt. The changed melt composition leads to crystallization of more primitive minerals which accumulate on the previously formed cumulate pile and whose phase compositions evolve up section with ongoing fractionation. Kelemen and Aharanov (1998) modeled the emplacement of melt within the lower oceanic crust in melt-filled fractures and suggest that such fractures open and close elastically as a reaction on the influx of melt. The partial crystallization of a melt in such a fracture would then form cumulates deposited at the base of the fracture. With a new replenishment, the fracture widens again such that, if the process is repeated several times, the total

height of the cumulates can be higher than the thickness of the sill during crystallization of a single fractionation unit.

Consequently, the crustal composition reveals fractionation trends at various scales: one at the scale of hundreds of meters because the melt composition is always a mixture between a previously differentiated and a fresh melt. And one at the decameter scale, depending on the fractionated volume of minerals between two replenishments of the melt sill.

Whether the fractionation of 10 – 30 % of a tholeiitic melt is sufficient to create the fractionation trends found in the drill core and also along the reference profile in Wadi Gideah (e.g., Müller, 2016; Koepke et al., 2017; Garbe-Schoenberg et al., 2014; Koepke et al. (submitted)) has to be estimated by the application of modeling tools such as MELTS (Ghiorso and Sack, 1995) or COMAGMAT (Ariskin and Barmina, 2004; see chapter 4.4).

4.3.2   Influx and migration of evolved melt

A remarkable sample in the suite of GT1A is sample OM-DP-BI-15 at 1075 maM which shows distinctly evolved compositions in terms of the Mg# in olivine and both the Mg# and the TiO_2 content in clinopyroxene. Moreover, granular oxides are only present at this horizon (Figure 4-3) being also most abundant in sample OM-DP-BI-15. Also the Ca# in plagioclase is low, although the most evolved plagioclases were found a few meters below at 1065 maM. Figure 4-7 C.5 shows that the evolved compositions at 1065 maM result from fractional crystallization as they all plot on the same trend. Sample OM-DP-BI-15, which marks the minimum in Mg#s of olivine and clinopyroxene, clearly falls off this trend (grey data point in Figure 4-7 C.5), but fits the reverse trend in RFU 2 (red marked symbol in Figure 4-7 C.4).

Koepke et al. (2018) provide experimental support for the stabilization of oxides as liquidus phase in evolved basaltic melts by increased oxygen fugacity due to elevated water contents. Abily et al. (2011) suggested that water can penetrate deep crustal levels leading to the interaction of seawater with melt or crystal mushes. If this was the case, a suddenly increased water activity in the melt could explain the stabilization of oxides, and explains at the same time why plagioclase Ca#s are elevated compared to Mg#s in olivine and clinopyroxene of the same sample, since the anorthite content in plagioclase is elevated in presence of water (e.g., Sisson and Grove, 1993; Berndt et al., 2005; Feig et al., 2006). However, petrographic indicators suggest that olivine was on the liquidus rather than oxides which are only rarely observed as inclusions in olivine. Furthermore, as Koepke et al. (2018) have shown, the Mg# in clinopyroxene is also sensitive to the water activity such that it should also be elevated which appears not to be the case. Another problem with the suggested mechanism is that it cannot explain the gradually increasing values of Ca# and Mg#s through the overlying 15 m of the drill core, which clearly plot on a common reversed fractionation trend (Figure 4-7 C.4). Also the spinel-orthopyroxene coronae around olivine described by Abily et al. (2011) as indicating high-temperature reactions between seawater and crystal mush were not observed in this sample.

A consequence of the accretion model supported in chapter 3 with in-situ crystallization in the layered gabbros and of the decameter fractionation trends presented above is that evolved residual melt from fractional crystallization deep in the crust can migrate through the crust and potentially enters overlying magmatic systems. A possible explanation for the evolved phase compositions, the presence of oxides, and the gradual up section trend toward more primitive compositions over a narrow horizon between 1075 and 1090 maM is the influx of an evolved residual melt migrating upwards after significant fractionation in a deeper magmatic system. Cumulates crystallizing from such a melt will show evolved compositions and – depending on the degree of melt fractionation – Fe-Ti oxides can precipitate, whereas the successive mixing of the evolved with a more primitive melt leads

to a successive up section trend back to more primitive phase compositions. The unzoned minerals at this horizon (1075 – 1090 maM; see Figure 4-4) must have nucleated in the mixed melt rather than already existing when the evolved melt entered the system.

The TiO_2 content in clinopyroxene of sample OM-DP-BI-15 at 1075 maM is extraordinary high, which is remarkable taking the high abundance of oxides into account. Pure (Ti-free) magnetite was found in the Samail ophiolite as a secondary product of serpentinization of olivine, while primary oxides form not only magnetite but also Ti-rich ilmenite or titanomagnetite (e.g., Pallister and Hopson, 1981; MacLeod and Yaouancq, 2000). In the concerned sample, oxides are titanomagnetites with Ti-rich (~52 wt% TiO_2) ilmenite exsolutions (Figure 4-6). The high TiO_2 content in clinopyroxene indicates that it crystallized before ilmenite was stabilized, whereas small oxides included into clinopyroxene imply that they crystallized simultaneously. Both is consistent with the stability fields reported by Feig et al. (2006) for tholeiitic melts at variable oxygen fugacities and water contents, where clinopyroxene starts crystallizing earlier than magnetite, but with overlapping stability fields of both phases. How the high TiO_2 content in clinopyroxene can be reconciled with the presence of Fe-Ti-oxides requires further investigation.

Distinct changes in both rock fabrics and mineral zonations are observed at 1110 maM with the development of significant lineation in plagioclase and clinopyroxene (Figure 4-9 A) and of normal zonation in clinopyroxene (Figure 4-4 C). These changes are accompanied by an abrupt steepening of the foliation dip reported by Kelemen et al. (2020) and indicate that melt, possibly the residue of the evolved melt replenished at 1075 maM, with a relatively evolved composition migrated upwards through cumulates being previously precipitated from more primitive melt. The steeper foliation, an increased mineral lineation, and normal zonation in clinopyroxene are consistent with pervasive porous melt flow migrating upwards through the crystal mush (Figure 4-13 D). Such a process was described for the plutonics beneath the AML in the southern Samail ophiolite (MacLeod and Yaouancq, 2000; Morris et al., 2019), but was also found to have occurred in the lower crust at Hess Deep (Lissenberg et al., 2013). The absence of clinopyroxene zonation between 1090 and 1110 maM indicates that melt/rock interaction did not occur at this horizon. It is rather an indicator that melt flow was focused, here (e.g., Korenaga and Kelemen, 1998). Combined with the melt/rock interactions described above in the horizon between 1110 and 1040 maM, these features can be reconciled by the migration of evolved melt by focused flow through the primitive cumulates at the base of a melt sill, which changed to porous melt flow toward the middle of the sill where the cumulates are less dense and the pore space between the precipitates is wider (Figure 4-13 D).

The general absence of systematic mineral zoning throughout the core, except for the horizon from 1110 to 1140 maM, indicates that pervasive melt migration is not the major process of melt transport. Even at the abovementioned horizon, zoning in clinopyroxene is weak, with enrichment factors of <2 between rim and core for TiO_2 and some trace elements (Figure 4-4 C and Figure 4-11 A.4), compared to the samples from Hess Deep, where Lissenberg et al. (2013) found enrichment factors of up to 15 between rim and core for some trace elements. Nevertheless, the abovementioned fabric indicators and the weak zonation are in good agreement with melt migration through the pores of a crystal mush at the narrow horizon between 1110 and 1140 maM, which is consistent with the findings of Korenaga and Kelemen (1998) who suggested that pervasive melt flow makes up to a few percent of the melt flow within the lower crust.

Zoning with rims being slightly depleted in Ca# is also observed in plagioclase grains between 1110 and 1140 maM (Figure 4-4 D). It is much weaker than in clinopyroxene (plotting within the range of uncertainty defined by the error bars in Figure 4-4) which is contradictory to the very slow CaAl/NaSi diffusion in plagioclase (e.g., Morse, 1984) compared to relatively fast Mg/Fe diffusion in clinopyroxene

(e.g., Dimanov and Sautter, 2000) or to the much faster Mg/Fe diffusion in olivine (e.g., Buening and Buseck, 1973; Chakraborty, 1997), where no zoning is observed. An explanation for the weak plagioclase zoning could be the generally more heterogeneous composition indicated by the standard deviations from the mean of core and rim analyses which are always higher than in other phases (Figure 4-4), hence concealing a distinct core/rim zonation.
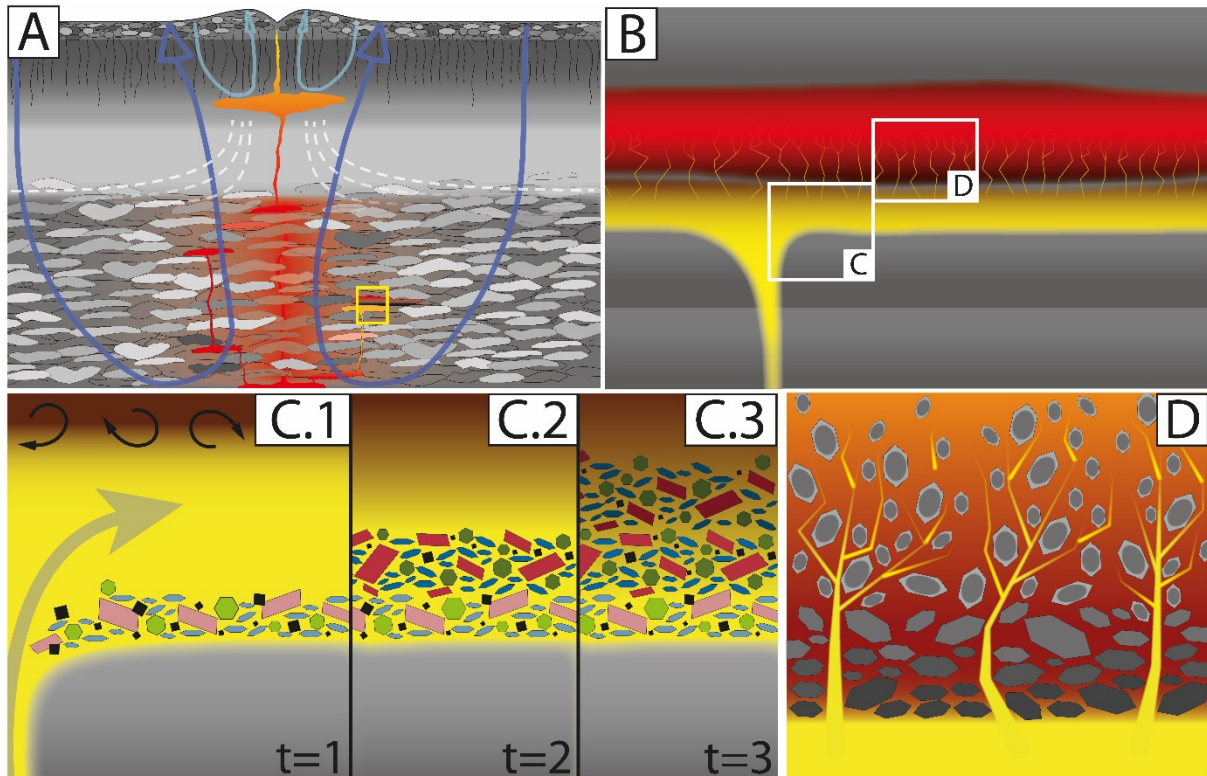
Figure 4-13 Synthesis model reconciling chemical and microstructural data between 1075 and 1140 maM. A) Entire lower crust as found to accrete in chapter 3; note the yellow rectangle indicating the position of (B) and the different colors of the melt sills in there. B) Close-up of the rectangle from (A) showing focused flow and intrusion of an evolved melt (yellow) below a still hot primitive sill filled with cumulates (red). Yellow lines represent channels of upward melt migration from the evolved into the primitive sill. White rectangles indicate the positions of (C) and (D), respectively. C) Close-up on the intrusion (grey arrow) of evolved melt from which relatively differentiated oxide-bearing olivine gabbro crystallizes. C.1-C.3 show the evolvement of the crystallization with time (t). Green hexagons are olivine, red rectangles are clinopyroxene, blue elongate polygons are plagioclase, and black squares are oxides. Black arrows indicate mixing of evolved melt and the primitive melt from the incompletely crystallized sill above. Note (1) ongoing mixing from t=1 to t=3 symbolized by yellow-to-red shadowing which smoothes from t=1 to t=3, (2) that mineral compositions become more primitive from C.1 to C.3 symbolized by darker colors for more primitive compositions, and (3) that oxide content decreases from C.1 to C.3. D) Evolved melt migrates through focused channels in the dense, lower cumulates of the overlying sill, without initiating melt/rock interaction. Were cumulates become less dense, melt migration evolves to porous flow initiating melt rock interaction, i.e., core/rim zonation, steepening of the foliation, increasing the degree of lineation. Darker colors generally represent more primitive melt or mineral compositions.

4.3.3 Formation of anorthositic, troctolitic, and wehrlitic layers

Investigating primitive lithologies adjacent to the gabbros or olivine gabbros in drill core GT1A can provide insights into the formation mechanisms of those cm-scale units which only form a minor proportion of the drilled samples (Figure 4-1). The primitive lithologies discovered within the investigated samples suite cross the drill core slightly inclined, which is consistent with the layering dip angle of 18° on average (0 – 40°) reported for the drill core (Kelemen et al., 2020). The grain size distribution within the interlayers does not show significant coarsening with distance from the contacts. The absence of such chilled margins discards an emplacement of the primitive lithologies by late stage intrusions of melt crystallizing them within much cooler host rock. These indicators suggest that the emplacement of the primitive lithologies already occurred at the magmatic stage of the crustal accretion and that they are possibly concordant with the surrounding magmatic stratigraphy.

Anorthosite

An anorthosite layer was found in sample 16-4-20-30_d2 where it is enclosed between olivine-bearing gabbro above and below (Figure 4-1 A). From a petrologic and a microstructural perspective, the data obtained from the anorthosite do not significantly differ from the surrounding gabbro. However, trace elements in both whole rock and plagioclase reveal significant differences: as the compatibility of REEs in plagioclase decreases with their mass, REEs heavier than Nd (except for Eu) are depleted in the anorthosite with decreasing sample/chondrite ratios toward the HREEs. This effect is due to the absence of clinopyroxene in the anorthosite which hosts the very majority of HREEs in a gabbro. It can therefore not be considered as indicator for magmatic processes forming the anorthosite.

That HREEs of the anorthositic plagioclase is enriched compared to the plagioclases within the adjacent gabbro might indicate that the anorthositic plagioclase crystallized solely without clinopyroxene. Otherwise, HREEs would have occupied positions within the clinopyroxene such that the plagioclase would show a stronger HREE depletion as the plagioclases analyzed in the gabbroic samples do. Following the crystallization sequence ol > pl > cpx assumed for olivine gabbros from the Samail ophiolite (e.g., Browning, 1984), plagioclase could have been separated from the melt prior to the stabilization of clinopyroxene. Nicolas and Boudier (2011) suggested that anorthosite bodies in the root zone of the sheeted dyke complex of the Samail ophiolite could have formed by the deposition of early crystallized plagioclases at the bottom of the AML. In chapter 6.5.2.2 it is shown that plagioclase can be expected to be buoyant or even floating in a basaltic magma rather than sinking. Nonetheless, a density-controlled process could lead to the segregation of more or less pure plagioclase before clinopyroxene crystallizes. This cannot explain, however, what kind of process could have created the sharp upper and lower contacts of the anorthosite to the surrounding gabbro. One could argue that the anorthosite was transported through the crust and then pressed into the olivine gabbro at the stage of a crystal mush, such that plastic deformation remained week, as indicated by the low moisorientation data shown in Figure 4-8 B and C. However, the pole figure symmetries of the gabbroic host rock and the anorthosite both show point maxima in [100] and (010) pointing to the same direction (see pole figure compilation in the electronic supplement) which indicates a present lineation with the same orientation in both lithologies. Consequently, they were deformed the same way. A possible mechanism creating the sharp contact (or emphasizing previous heterogeneities) is the formation of modal layering by ductile deformation suggested by Jousselin et al. (2012). In this scenario, a batch of anorthositic crystal mush became sheared, as it is suggested to occur by upper mantle convection within the gabbro unit (see chapter 3; e.g., Ildefonse et al., 1995; Jousselin et al., 2012) and was sheared in the gabbroic host rock. Shearing as a reaction of the external force of mantle convection is then recorded by both lithologies leading to the observed parallel lineation, and the

primary chemical differences between anorthositic and gabbroic plagioclases observed in their REE patterns might survive such an event.

Troctolite

As introduced in chapter 1.3.1, Arai and Matsukage (1996) suggest for the troctolite units being a major constituent to the modal layering at Hess Deep that they formed by a reaction of primitive melt with mantle harzburgite. As a relict of the mantle harzburgite, they found Cr-spinel in the regions of olivine-rich troctolite supporting their hypothesis that they formed by the interaction of basaltic melt with mantle rock. Furthermore, they reported high heterogeneities in modal proportions and phase compositions of both troctolite and olivine gabbro which is not observed in the troctolitic sample 1-72-d_d2 from this study (Figure 4-1 B). Bulk rock REE data reveal a depleted REE concentration in the troctolitic sample which is, similar to anorthosite, due to the low REE concentrations in the contained phases olivine and plagioclase. That the pattern generally parallels the patterns of gabbros from the same unit might be an artifact of contamination with the adjacent gabbro, because an appropriate separation of the troctolite from the gabbroic host rock was not possible. In terms of mineral geochemistry of plagioclase and small clinopyroxenes in the troctolite, they plot in between the values of the same phases in the adjacent olivine gabbro without strong differences. Arai and Matsukage (1996) reported distinct differences in clinopyroxene minor and major element composition between troctolite and olivine gabbro in their sample suite, which cannot be observed in the samples of this study. Therefore, the results of this study are inconsistent with the model suggested by Arai and Matsukage (1996), at least if it is assumed that troctolite and adjacent olivine gabbro resulted from the same melt/harzburgite reaction event. The alternative − that troctolite and gabbro formed independently of each other and the troctolite was transported into the olivine gabbro − can explain the similarities in chemical composition of both lithologies only by a very unlikely coincidence.

Leuthold et al. (2018) found indicators that partial melting of lower crustal olivine gabbros from Hess Deep and the Kane Megamullion at the Mid-Atlantic Ridge lead to the formation clinopyroxene-poor olivine gabbros or even troctolites. They provide geochemical and textural data which suggest the partial melting and subsequent overgrowth of clinopyroxene cores by a second clinopyroxene stabilization with significantly different composition. Such features were not observed in the troctolitic sample from drill core GT1A. A potential explanation including partial melting could be that the clinopyroxene was almost completely molten and the resulting melt was extracted from the system. The remaining restite of olivine and plagioclase would then be free of overgrown clinopyroxenes. However, a partial melting event is generally difficult to reconcile with the very localized presence of troctolite with <2 cm thick layers in drill core GT1A. If such an event counts for their occurrence, they could have been transported to their actual positions. But this is − again taking the similar geochemical signatures to the adjacent gabbroic rocks into account − not very likely.

If troctolite and adjacent olivine gabbro crystallized from the same melt, as indicated by their geochemical similarities, one would expect that troctolite crystallized earlier than olivine gabbro, i.e., before clinopyroxene stabilized. If the calculation in chapter 6.5.2.2 is correct, again, a mechanism is required to let plagioclase sink in the liquid together with olivine. Such a process, i.e., density currents slumping from the magma chamber wall, is discussed by Irvine (1980) and in chapter 6.5.2.3. If troctolite crystallized for a certain period at the margins of a melt lens and slumped down before clinopyroxene stabilization, they can erode underlying layers or may be eroded themselves by following (olivine gabbroic) currents. The limited spatial extent of the troctolite layers is easy to reconcile with such a mechanism, as is the wavy contact and irregular thickness of the troctolite layers (Figure 4-1 B).

Wehrlite

Wehrlite was analyzed in detail in sample 88-3-49-55 of the present sample suite where is consumes half of a normal thin section adjacent to mela-olivine gabbro being poor in altered plagioclase (Figure 4-1 C). Both wehrlite and olivine gabbro reveal more primitive compositions with higher Mg# and Cr_2O_3 content and lower TiO_2 and bulk rock REE contents than the other gabbroic samples from the same unit. The REE patterns of clinopyroxenes in the wehrlite and the adjacent olivine gabbro reveal a slightly enriched composition of the former compared to the latter with normal clinopyroxene zoning in both lithologies. It is remarkable that wehrlite, although free of plagioclase, reveals a distinct negative Eu anomaly in clinopyroxene indicating that the melt crystallizing wehrlite was already depleted in Eu by former plagioclase precipitation.

Koepke et al. (2009) explain the petrogenesis of wehrlite in the Samail ophiolite by the subduction-related origin of the ophiolite, and the correlated elevated water contents in the parental melts (e.g., Juteau et al., 1988; MacLeod et al., 2013; Müller et al., 2017) leading to the suppression of plagioclase nucleation (e.g., Gaetani et al., 1993; Feig et al., 2006). Hydrating the melt of a magma chamber for a certain amount of time would, consequently, lead to the temporary formation of wehrlite, instead of olivine gabbro, which then settles down either directly from the melt or by density currents as suggested for troctolite above. A mechanism to hydrate a melt could either be a replenishment by fresh pre-hydrated melt or the interaction of melt with seawater, as suggested by Abily et al. (2011)). The elevated Mg# in wehrlite and the underlying mela-olivine gabbro is consistent with the findings of Koepke et al. (2018) who showed that an increased water activity not only increases the anorthite content in plagioclase but also the Mg# in clinopyroxene. That the Mg# is elevated in both wehrlite and mela-olivine gabbro indicates that the latter also crystallized from a hydrated melt, implying that plagioclase possibly already existed when the melt became hydrated. If that was the case, a deposition by density currents appears more likely to explain the occurrence of presumably buoyant or floating plagioclase in the cumulates rather than the settling from a stagnant melt.

4.3.4 Implications for lower crustal accretion

In chapter 3, it is suggested that the lower two thirds of the gabbros from Wadi Gideah, where drill core GT1A is located covering the interval from 1173 to 815 maM, accrete by in-situ crystallizing melt sills as proposed by, e.g., Korenaga and Kelemen (1997) in the sheeted sill model. This hypothesis was tested in terms of consistency with the data obtained in drill core GT1A. The decameter scale fractionation trends discussed above might also have formed when the entire lower crust was accreted from subsiding cumulates of the AML, as suggested by, e.g., Henstock et al. (1993)) in the gabbro glacier model: cyclic replenishments with primitive melt in the AML could reset the compositions of the precipitated minerals leading to the observed fractionation cycles, as Browning (1984) already proposed.

However, the reverse trend between 1075 and 1090 maM is interpreted as mixing of entering evolved melt with primitive one, and a model where crystallization, i.e., fractionation of the melt, only occurs within the AML cannot explain the replenishment with a more evolved melt from depth. The differentiation creating an evolved melt composition must have occurred somewhere below the lens that is replenished with the evolved melt, implying that crystallization already occurred within the lower crust. Furthermore, the gradual changes in fabric symmetry along the drill core are difficult to reconcile with a mechanism where cumulates subside from the AML down to deeper regions of the crust (e.g., Quick and Denlinger, 1993) which is assumed to create a continuously increasing strain down section consequently being reflected by a fabric with continuously increasing lineation

component down section (e.g., Gillis et al., 2014a; VanTongeren et al., 2015). Drill core GT1A reveals an abrupt shift from both foliated and lineated symmetries to almost purely foliated symmetries below 1110 maM followed by gradual strengthening of the lineation component down section (Figure 4-9 A). These variations are inconsistent with the continuously increasing strain expected in a gabbro glacier model (e.g., Quick and Denlinger, 1993; VanTongeren et al., 2015; Gillis et al., 2014a).

The occurrence of cm-scaled layers of wehrlite in the drill core is discussed above. They are assumed to have formed due to the suppressed plagioclase nucleation as a result of increased water activity (e.g., Koepke et al., 2009). As it was reported by Gaetani et al. (1993) and Feig et al. (2006), the size and shape of the plagioclase stability field in a water-containing melt strongly depends on the pressure with decreasing plagioclase stability when increasing pressure results in decreasing water activities. Assumed that the wehrlite layers are concordant with the gabbros, as described above, they cannot have formed within the AML: a pressure not significantly higher than 100 MPa can be assumed for the AML deviated from the thickness of the sheeted dyke complex (~1 km; e.g., Pallister and Hopson, 1981) and the pillow lavas (0.5 – 2 km; e.g., Godard et al., 2003) of the Samail ophiolite. At these pressures, Feig et al. (2006) reported plagioclase stabilization before clinopyroxene at all water contents, such that wehrlite does not form.

For the abovementioned reasons, the detailed drill core study supports the hypothesis stated in chapter 3 and provides further evidence that fractional crystallization has taken place the lower oceanic crust cropped out in Wadi Gideah. As already stated in chapter 3, this interpretation is only based on the chemical and microstructural findings described above. A quantitative analysis of cooling rates with depth does not exist, yet, for drill core GT1A or Wadi Gideah in general. As described in chapter 1.2, constraints on cooling rate within the lower oceanic crust are heterogeneous and in parts contradictory. Coogan et al. (2002a, 2007) and Faak et al., 2015 reported decreasing cooling rates with depth in the Samail ophiolite or at Hess Deep, respectively, suggesting that the resulting dominantly conductive cooling is not sufficient to remove latent crystallization heat from the lower crust such that crystallization is hampered. VanTongeren et al. (2008) estimated faster cooling without a down section trend in the Samail ophiolite, supported by numerical modeling results by Hasenclever et al. (2014) and Cherkaoui et al. (2003) who stated that the modeled cooling mechanisms are sufficient to remove the crystallization heat of the system, enabling in-situ crystallization at greater depth. It is very unlikely that heat removal from the lower oceanic crust occurs homogeneously over large crustal volumes, taking the existence of both high- and low-temperature fluid fault zones at different scales into account (e.g., Coogan et al., 2006). As it is stated in chapter 6.5.3, cooling in lower horizons of the crust can occur faster than in shallower regions under certain conditions. It is, therefore, questionable whether the crustal profiles on cooling rates existing so far can rule out distinct thermic heterogeneities along the crust. Those could, in turn, enable magma sills to crystallize in-situ within the lower crust providing a key requirement for the abovementioned model including lower crustal crystallizing melt sills.

4.4   Conclusions and outlook

Drill core GT1A provides extraordinary insights into magmatic processes in lower oceanic crust at the cm- to decameter-scale. Compositional units revealing normal fractionation in six and reverse fractionation in two cases were defined from major element distributions along the core and their co-variations between clinopyroxene and plagioclase. They can be explained by melt sills which crystallize to an extent of 10 to 30 % (based on the cumulus/sill height ratio calculated after Browning, 1984) before a replenishment of more primitive melt resets the melt composition. The absence of late-stage magmatic phases being indicative for evolved melt compositions implies that such sills cannot have crystallized completely within the layered gabbros.

A distinct reverse fractionation trend from the most evolved to the most primitive mineral compositions of the drill core could is best-explainable by an influx of evolved melt that mixes with the melt from the crystal mush above, such that the composition of the precipitated phases gradually becomes more primitive with height over a narrow horizon of 12 m in height. The residue of the entered and mixed melt most-likely moved upwards over several meters by focused flow which evolved into a pervasive flow mechanism above, as suggested by the presence of normal clinopyroxene zoning in major, minor, and trace elements. A porous melt migration is, moreover, supported by a steepening of the rock foliation at this height, accompanied by a higher degree of lineation in the rock fabrics. These features were used as indicators for porous melt flow in past (e.g., MacLeod and Yaouancq, 2000; Lissenberg et al., 2013). However, it is striking that only the horizon between 1110 and 1140 maM reveals those features, supporting the findings of Korenaga and Kelemen (1998) that porous melt migration makes only a portion of a few percent of the melt transport within the lower crust of the Samail ophiolite.

Primitive lithologies (such as anorthosite, troctolite, and wehrlite) coherent with the layering of the gabbros require different formation mechanisms. Anortosite layers can have formed from plagioclase-rich or pure plagioclase batches that crystallized before clinopyroxene (as indicated by elevated HREE concentrations in plagioclases from the anorthosite compared to adjacent gabbro) and were separated from olivine by distinct density contrasts. The identical lineation in both anorthosite and adjacent gabbro suggests that both have been deformed simultaneously. Mantle-induced shearing, as suggested by Jousselin et al. (2012) as layer-forming process, could have emphasized the initial modal heterogeneity leading to sharp contacts of the anorthosite with the gabbro. Troctolites discovered in drill core GT1A are identical with the adjacent gabbro in terms of mineral compositions. Their emplacement can be explained by troctolitic density currents which slumped down from the margin of a melt lens before clinopyroxene was stabilized. The settling of (olivine) gabbro before and afterwards limits the extent of troctolite to cm-thick layers. With wehrlite, it could have been similar when the water content of a melt temporarily suppressed plagioclase nucleation and wehrlite slumps down and deposits on the gabbro.

The findings of fractionation units combined with indicators for an influx of evolved melt support the conclusions made in chapter 3 that the layered gabbros accrete by in-situ crystallization as suggested by, e.g., Korenaga and Kelemen (1997) (i.e., sheeted sill model) rather than by subsiding cumulates of the AML (i.e., gabbro glacier model; e.g., Henstock et al., 1993). The latter cannot explain why the degree of lineation within the layered gabbros gradually changes with depth along the drill core, since the subsidence mechanism inherent in the gabbro glacier model is expected to form a constant strengthening of lineation with depth (e.g., VanTongeren et al., 2015; Gillis et al., 2014a). However, this study lacks a quantification of cooling rates which are assumed to be critical to distinguish between the gabbro glacier and the sheeted sill model (e.g., Coogan et al., 2002a Maclennan et al., 2005). Modeling diffusion profiles of Mg in plagioclase (Faak et al., 2014) or of Ca in olivine (Coogan et al., 2002a) can provide quantitative information on the cooling and, therefore, on the efficiency of heat removal out of the system to constrain the extent of crystallization occurring in-situ in the lower gabbroic crust.

Further tools can be applied, such as the Ti-in-amphibole thermobarometer of Ernst and Liu (1998), although magmatic amphibole was only rarely observed in the drill core, or the thermometer based on element exchange between magnetite and ilmenite of Sauerzapf et al. (2008). The latter might help to estimate crystallization temperatures of the most evolved oxide gabbros in the horizon above 1075 maM. These can support further application of modeling software such as MELTS (Ghiorso and Sack, 1995) or COMAGMAT (Ariskin, 1999). Thermodynamic modeling of fractional crystallization helps to improve the reliability of the interpretations only drawn from analytical data, yet. It can be

tested, whether the fractionation trends along the decameter scale throughout the drill core are reproducible with the modeling software potentially providing further support that fractional crystallization occurred within the lower crust in Wadi Gideah.

5 The foliated/layered gabbro transition – a data report from drill core GT2A

5.1 Drill site GT2A

The location of drill site GT2A was chosen to cover the transition between the foliated and the layered gabbros in Wadi Gideah which is difficult to detect in the field (Kelemen et al., 2020). GT2A approximates 400 m in length with a top height of 2695 maM. In order to drill a large steeply dipping greenschist fault zone, thee drill hole was inclined by 30° from the vertical trending to the northeast. Similar to GT1A, a drilled meter of drill core GT2A does not exactly correspond to a meter in the crustal context due to the inclination of the Samail crust in the Ibra area described in chapter 2.1. However, the inclination of the drill hole compensates the tilt of the ophiolite to a wide extent such that a depth recalculation for every sample in the crustal height context was omitted, here.

The drilled lithologies are mainly olivine gabbros to gabbros with a few hornblende-gabbro veinlets (Kelemen et al., 2020). More detailed information on the drill site and results of the detailed core description on CHIKYU are provided in the proceedings of the Oman Drilling Project by Kelemen et al. (2020).

The average spatial resolution approximates 2.5 m and ranges from a few centimeters to 16.82 m at maximum. Some thin sections were subdivided into several domains, based on modal or textural features, leading to distances of only a few millimeters between some adjacent data points.

Because drill site GT2A is located within the same wadi as the surface samples from chapter 3, they can be integrated into the Wadi Gideah reference profile significantly increasing its spatial resolution along the 400 m long drilled interval. During the preparation of this thesis, detailed analytical data from drill core GT2A were only obtained for phase compositional information by EPMA and for the quantification of microstructural features by EBSD. The analytical methods applied for this chapter are described in chapter 2.4.

Foliated and layered gabbros in drill core GT2A are visually distinguished by their grain sizes. Primitive lithologies (i.e., anorthosite, pyroxenite, wehrlite) were contributed to the crustal unit they are surrounded of, although their textural features occasionally differ from those of the gabbroic lithologies. 45 % of the collected samples are defined as foliated gabbros, 55 % are defined as layered gabbros. The presented plots of the results are color-coded with respect to the crustal unit the data belong to.

5.2 Results

5.2.1 Phase compositions measured by electron probe micro analysis

As for drill core GT1A, the samples of the drill core presented here were analyzed with four grains per phase and sample or domain, each with four core and four rim measurements. After removing low quality data (i.e., total beyond 100 wt% ± 2, strongly altered grains), the present mean values were calculated from a number of 2 – 29 single measurements per sample or domain.

5.2.1.1 Primary phase analyses – olivine

Primary olivine grains are often too altered for a proper EPMA analysis such that olivine data were obtained only from 23 samples. In those samples ascribed to the FG unit, the Mg# in olivine cores ranges from 71.79 to 74.6 with standard deviations from the mean of <0.51. Olivine rims of the FG unit

reveal Mg#s ranging from 72.01 to 74.74 with standard deviations of <0.71. The Mg#s of olivine cores in the LG unit range from 71.97 to 76.31 with standard deviations of <0.69, and those of olivine rims in the LG unit range from 72.01 to 76.27 with standard deviations of <0.59. A single wehrlite sample at 2316 maM was analyzed in terms of olivine composition and reveals Mg#s of 72.1 ±0.16 and 72.26 ±0.38 in core and rim, respectively. The down hole trends reveal a maximum in Mg# at 2460 maM and minima at 2375 and 2575 maM (Figure 5-1 A). The low spatial resolution of the data points conceals any trend along the core, and the absence of analyzable olivine gabbro adjacent to the wehrlite hampers an assessment whether the latter is more primitive than the former, or not.

The NiO content in olivine is only above the detection limit in a few samples. It ranges in both olivine cores and rims of the FG from 0.12 to 0.17 wt% with a standard deviation of <0.03 wt%. Olivine from the LG unit reveal NiO contents of 0.12 to 0.14 wt% with standard deviations <0.01 wt% and with an outlier containing 0.31 wt% NiO in the rim at 2461 maM. The highest NiO contents (expect for the outlier) were measured in the wehrlite at 2316 maM.

5.2.1.2 *Primary phase analyses – clinopyroxene*

A total of 154 samples or domains contained analyzable clinopyroxene in drill core GT2A. Clinopyroxene cores of the FG unit reveal Mg#s between 74.35 and 83.27 with standard deviations of <1.92 and their rims reveal Mg#s ranging from 74.38 to 83.4 with standard deviations of <1.76. In the LG unit, clinopyroxene cores reveal Mg#s ranging from 72.53 to 84.76 with standard deviations of <2.61 and their rims have Mg#s between 72.91 and 83.81 with standard deviations of <2.13. The wide majority of the analyses reveal standard deviations <1, indicating that only a small proportion shows internal compositional heterogeneity within a sample or a grain. As the overlapping ranges in Mg# already suggested, the compositional variations are not correlated with the crustal units of the samples; FG and LG samples both plot on a curvy trend that starts with low values (~75) at the bottom of the drill core and gradually increases to up to 80.51 from 2280 to 2320 maM. After another decrease back to ~75 over 40 m, a steep trend toward the most primitive compositions with up to 84.76 at 2437 maM follows, which is only interrupted by a single sample plotting at the minimum value of the drill core with 72.91 at 2400 maM. From the maximum at 2437 maM, the Mg# gradually decreases over 50 m and then remains constant (within the range of the statistical error) at 78.61 along the drill core interval from 2488 to 2589 maM. Above 2600 maM, the Mg# increases again to up to 80.91 at 2650 maM, followed by a gradual decrease from 80.91 to 74.85 over the uppermost 40 m of the drill core (Figure 5-1 B).

The content of Cr_2O_3 in the clinopyroxene cores of the FG unit plots between 0.1 and 0.29 wt% with standard deviations of <0.21 wt% and three samples with significantly elevated contents of up to 0.46 wt%. Clinopyroxene rims of the FG unit reveal Cr_2O_3 contents between 0.1 and 0.28 wt% with standard deviations of <0.12 wt% and two samples beyond this range with 0.34 or 0.41 wt%, respectively. The LG unit clinopyroxenes show similar contents in the cores ranging from 0.1 to 0.26 wt% with standard deviations of <0.1 wt% and with an increased Cr_2O_3 content of 0.55 ±0.26 within a single sample. Rim values range from 0.1 to 0.23 wt% with standard deviations of <0.07 wt%. The down hole plot of Cr_2O_3 in clinopyroxene reveals an intense scattering over the lowermost 110 m of the drill core, whereas the trend remains relatively constant at contents between 0.1 and 0.2 wt% above. The parallelism with the Mg# in clinopyroxene is weak; only the scattering being more intense between 2400 and 2290 maM connects both values (Figure 5-1 B). Cr_2O_3 contents above 0.3 wt% do not correlate with a lithology or crustal unit, it is only remarkable that both wehrlite and pyroxenite near the bottom of the core plot at ~0.4 wt%, i.e., higher than most of the other values. However, olivine gabbros of both FG and LG units also plot at higher contents in single samples below 2400 maM.
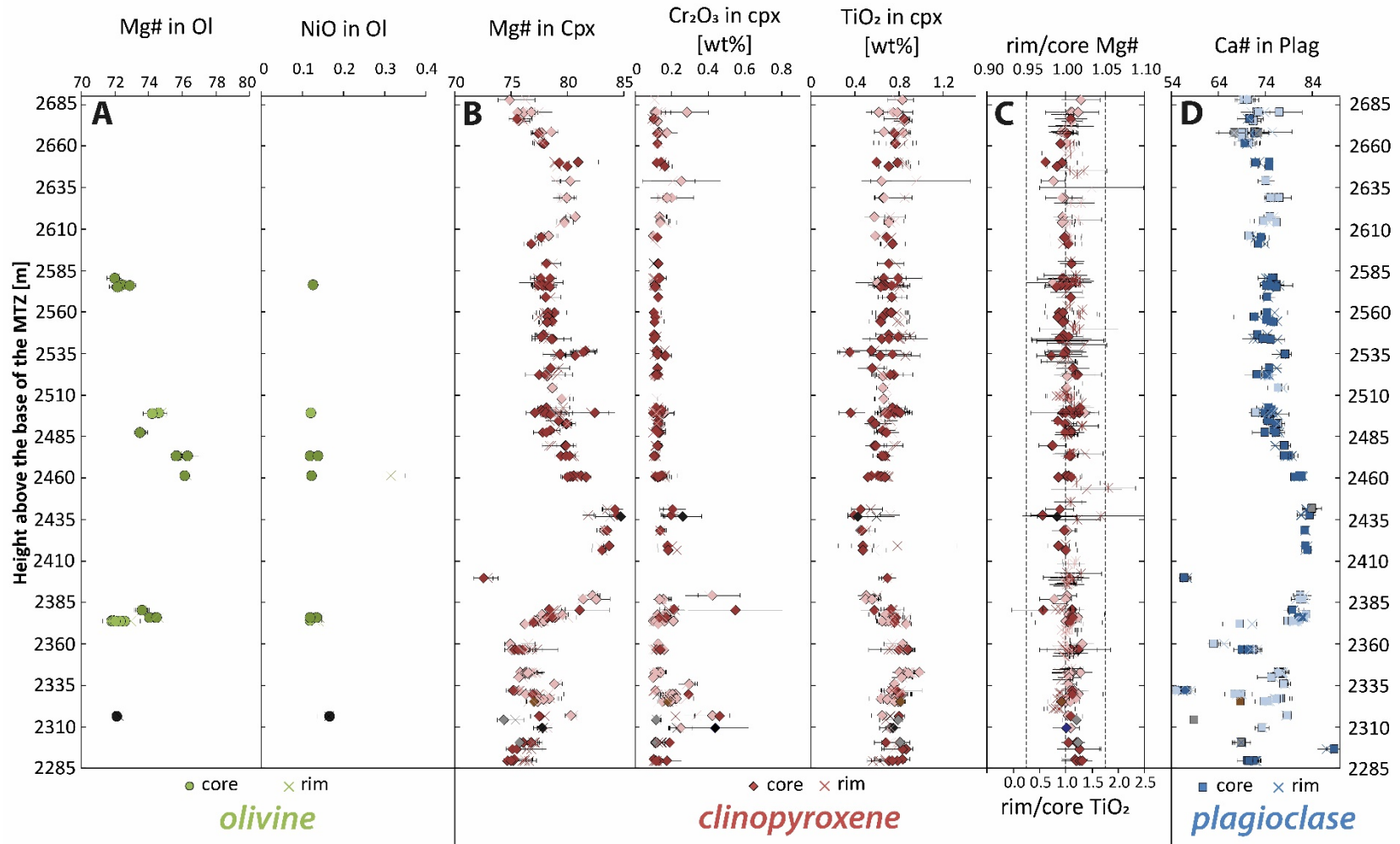
Figure 5-1   Major and minor element results of the primary phases olivine (A), clinopyroxene (B, C), and plagioclase (D) plotted versus the height above the base of the MTZ. In A, B, and D, closed symbols are core, crosses are rim analyses. In C, closed diamonds are rim/core ratios of the Mg# and stars are rim/core ratios of TiO_2. Note that TiO_2 is plotted on the lower x-axis. Light colored data points are foliated, dark colored data points are layered gabbros. Gray symbols are anorthositic, brown are pyroxenitic, and black are wehrlitic samples. Error bars symbolize standard deviations from the mean or, in case of rim/core ratios, propagating errors from the standard deviations of the concerned components.

The TiO$_2$ contents in clinopyroxene cores from the FG unit plot in the range of 0.45 and 0.98 wt% with standard deviations of <0.15 wt%. Clinopyroxene rims in the FG unit reveal TiO$_2$ contents between 0.48 and 0.96 wt% with standard deviations of <0.19 wt% (except for a single sample with a standard deviation of 0.5 wt%). In the LG unit, the clinopyroxene cores contain between 0.36 and 0.88 wt% TiO$_2$ with standard deviations of <0.22 wt% and the rims contain between 0.34 and 0.99 wt% with standard deviations of <0.26 wt% (except for a single sample with a standard deviation of 0.54 wt%). The down hole trend of TiO$_2$ in clinopyroxene mirrors the curvy trend of the Mg#, however, revealing a bit stronger scattering relative to the absolute values between 2690 and 2400 maM, where the trend in Mg# is clearer (Figure 5-1 B). As already observed in the trends described above, there is not compositional difference between FG and LG units; even wehrlitic of pyroxenitic samples plot in the same range of TiO$_2$ content as the adjacent gabbroic samples. The plot of TiO$_2$ versus Mg# in clinopyroxene (Figure 5-2 A) reveals a good correlation between them, with similar fractionation trends for both core and rim. It is striking, however, that the range of the core data extends to more primitive compositions with higher Mg#s and lower TiO$_2$ contents than the rim data which indicates the presence of normal zoning in the samples.

Indeed, the depth plot of rim/core ratios in Mg# and TiO$_2$ of clinopyroxene indicates that the grains are zoned along the core. Although zoning appears to be weak with respect to the propagating errors of the standard deviations of the concerned components, a change in the type of zoning throughout the drill core is observed: from 2400 maM down to the bottom of the drill core, reverse zoning with rim/core ratios of up to 1.2 or down to 0.75 in Mg# and TiO$_2$ content, respectively, is observed. Above 2400 maM, normal zoning with rim/core ratios of down to 0.97 or up to 1.5 in Mg# and TiO$_2$ content, respectively, dominates (Figure 5-1 C). The reverse zoning horizon correlates with the interval that reveals more scattered phase compositions in both olivine and clinopyroxene.

5.2.1.3 Primary phase analyses – plagioclase

Plagioclase was analyzed in 142 domains of drill core GT2A. In the FG unit, plagioclase cores reveal Ca#s in the wide range of 55.2 to 82.83 with standard deviations of <5.25. In the plagioclase rims the FG unit, the Ca# ranges from 55.72 to 82.68 with standard deviations of <4.52. High standard
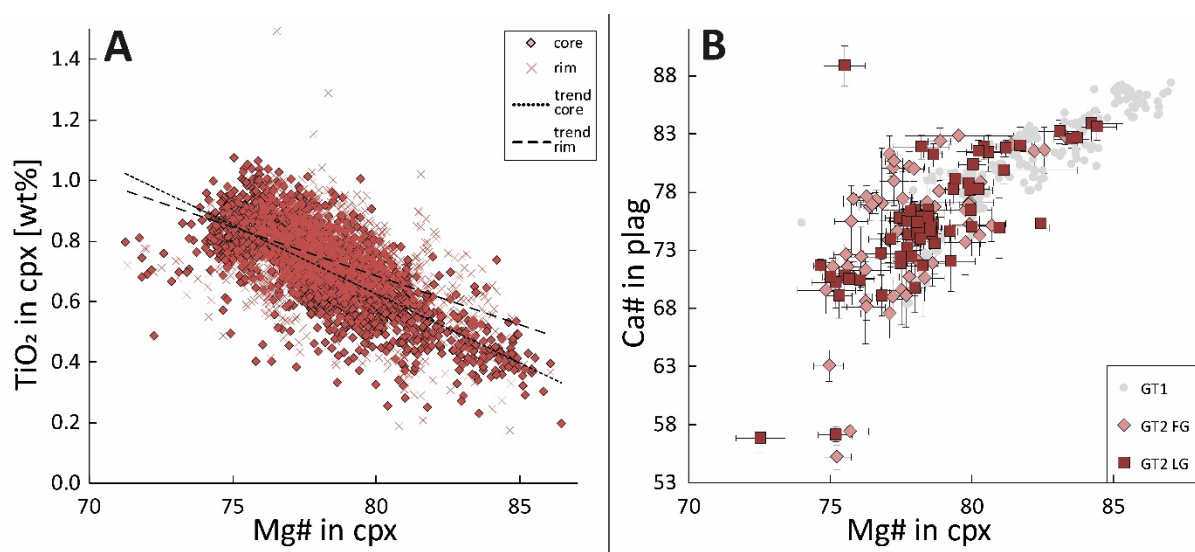
Figure 5-2 A) Rim (crosses) and core (diamond) values of all GT2A clinopyroxene TiO$_2$ analyses plotted versus the Mg#. Dotted line represents the trend in core, dashed line in rim analyses. B) Ca# in plagioclase plotted versus the Mg# in clinopyroxene of GT2A (red symbols with light diamonds = foliated gabbro, dark rectangles = layered gabbro) and GT1A (grey circles) for comparison. Error bars symbolize standard deviation from the mean.

deviations above 2 in 21 domains indicates a strong heterogeneity within the grains. In the LG unit, plagioclase cores reveal Ca#s between 56.84 and 88.85 with a standard deviation of <4.44. The rims of plagioclase in the LG unit reveal Ca#s in the range of 56.46 to 87.1 with a standard deviation of <3.26. A standard deviation of 2 was exceeded by 15 core and 14 rim analyses, indicating heterogeneous plagioclase compositions also in the LG unit. Regardless of the partially high standard deviations, a trend in good agreement with the trend observed in clinopyroxene Mg#s is observed (Figure 5-1 D). However, whereas the clinopyroxene data reveal some gradual changes below 2400 maM, the data of plagioclase in both FG and LG units are widely scattered here, obscuring a potential trend. Above 2400 maM, the Ca# in plagioclase of all lithologies decreases smoothly up core with a plateau of a constant Ca# between 2500 and 2580 maM as observed in clinopyroxene. Core and rim data in plagioclase always plot in the same range of the standard deviation indicating that no significant zoning is present in the plagioclase grains of drill core GT2A.

Figure 5-2 B shows the Ca# in plagioclase plotted versus the Mg# in clinopyroxene of both FG and LG units. For comparison, GT1A data are also plotted, revealing that the majority of the data from GT2A plot at more evolved compositions. Moreover, Figure 5-2 B makes clear that no significant compositional differences between the crustal unit FG and LG exist.

5.2.2 Microstructural analysis using electron backscattered diffraction

Microstructural data were obtained for a subset of 66 samples or domains, representing an average spacing of 8.5 m (0.06 – 27.3 m) between the data points. The data acquisition and processing were performed in the same way as for GT1A samples, however using the MTEX version 5.2.7. Olivine data are rare also in drill core GT2A – only seven data sets reveal reliable olivine data after filtering out those with <100 grains (e.g., Ismaıl and Mainprice, 1998) – such that the microstructural investigations are mostly based on plagioclase and clinopyroxene.

The J indices of plagioclase range from 1.86 to 6.87 or 1.69 to 6.63 in the FG unit and LG unit, respectively. However, values >5 are often related to analyses of only slightly more than 100 grains, suggesting that the relatively high values might be an artifact of the relatively low number of analyzed grains (Ismaıl and Mainprice, 1998; Satsukawa et al., 2013). On the down hole plot, the plagioclase J index gradually increases with depth, with values between 2 and 3 in the uppermost 100 m of the drill core and values between 2.5 and 5 in the lowermost 120 m of the drill core, however, revealing a wider scattering in the samples below 2400 maM (Figure 5-3 A). This describes a slight parallelism to the Ca# in plagioclase (see above). It is no difference in the data from the FG or the LG unit observed.

Clinopyroxene J indices plot in the range from 1.38 to 3.22 or 1.52 to 6.41 in the FG unit and the LG unit, respectively. They do not show a down hole trend with constantly low values between 1.5 and 2.5 in the samples of the FG unit along the drill core, whereas samples from the LG unit plot on a widely and unsystematically scattered range between 2 and 6 (Figure 5-3 B). The differences between FG and LG unit samples are shortly discussed below. The misorientation per phase quantified using GOS and GAM reveal a low internal misorientation in all phases with a GOS of up to 1.5° and a GAM of up to 0.7° (with the exception of two outliers, where both plagioclase and clinopyroxene reveal elevated values of up to 2.4 in the GOS and up to 1.4 in the GAM). A slight trend is observed with the highest values plotting in the upper- or lowermost 80 m of the drill core, and with a zone of weaker misorientation between 2450 and 2590 maM (Figure 5-3 C and D).

The BA indices of plagioclase plot between 0.23 and 0.51 (mean: 0.41) in the FG unit and between 0.25 and 0.71 (mean: 0.42) in the LG unit. Clinopyroxene BC indices range from 0.27 to 0.73 in the FG unit and from 0.26 to 0.73 in the LG unit (mean in both: 0.5). Although the mean values are similar, the samples from the FG unit by trend reveal lower BA values of plagioclase indicating a weaker
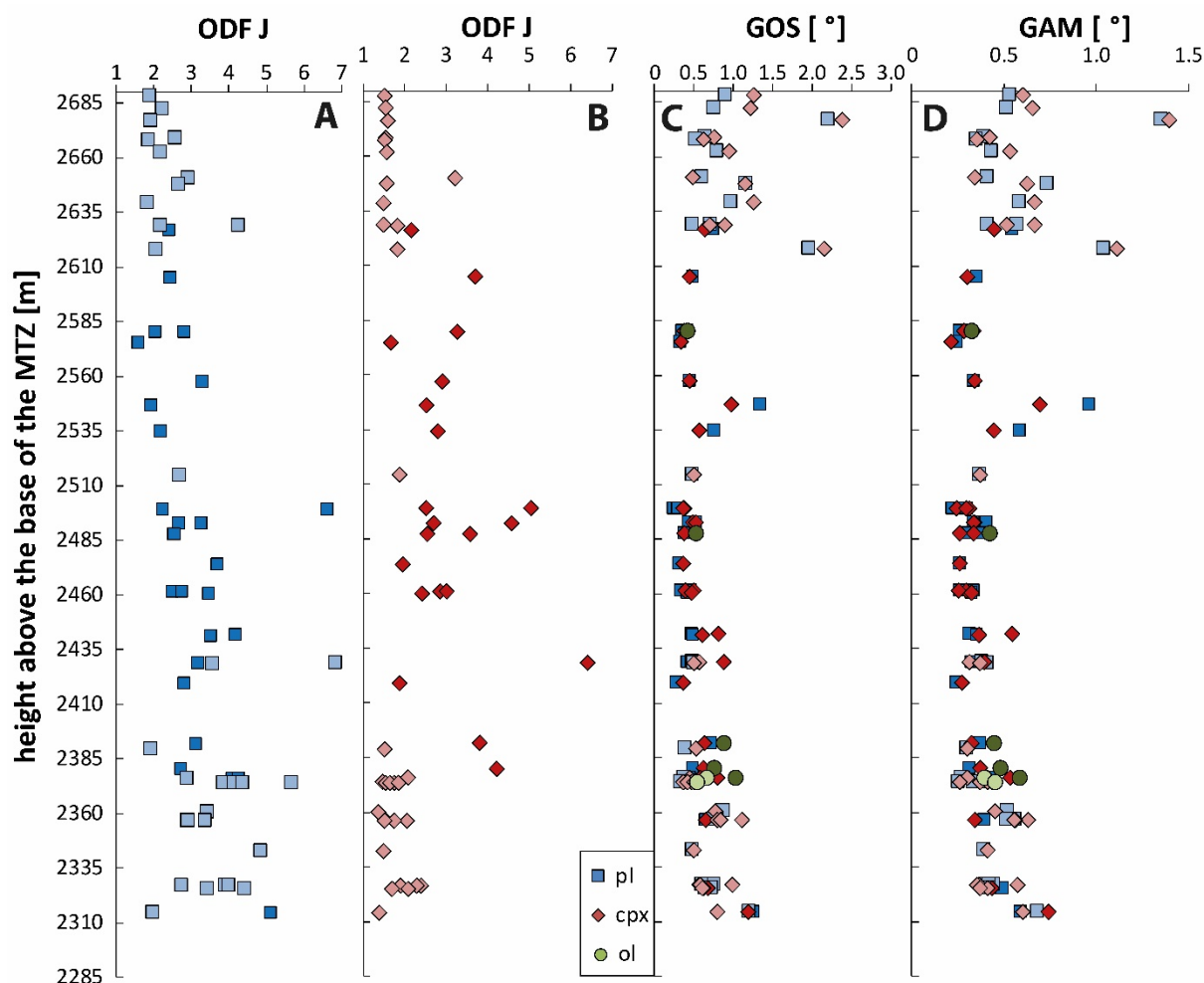
Figure 5-3   The J indices of the orientation distribution function (ODF J) of plagioclase (A); blue rectangles) and clinopyroxene (B); red diamonds) plotted versus height above the base of the MTZ. C) the grain orientation spread (GOS) quantifying internal misorientation within plagioclase, clinopyroxene, and olivine (green circles) plotted versus the height above the base of the MTZ. D) the grain average misorientation (GAM) as a quantitative proxy of subgrain formation in plagioclase, clinopyroxene, and olivine plotted versus the height above the base of the MTZ.

lineation component within those samples compared to LG unit samples. The BC index of clinopyroxene lacks any down hole trend but scatters irregularly over the ranges mentioned above. In contrast, the BA indices of plagioclase gradually increase from 0.3 at 2515 maM to up to 0.5 at 2430 maM followed by a more scattered gradual down section decrease to 0.23 at the bottom of the drill core (Figure 5-4 A). These trends are similarly observed in the Ca# in plagioclase and the Mg# in clinopyroxene, indicating a similar correlation between the fabric symmetry as already found in drill core GT1A.

The pole figures of drill core GT2A generally reveal a parallelism between the plagioclase [100](010) and the clinopyroxene [001](010) pole figures, which is only weak in some samples as indicated by the absence of parallel BA indices in plagioclase and BC indices in clinopyroxene (Figure 5-4 A and B). Only the sample 2-20-3 at 2651 maM, respectively, shows a parallelism between the plagioclase [100](010) and the clinopyroxene (100)(010) pole figures which was not observed in the other samples. Remarkably, this sample is the uppermost of three samples between 2651 and 2639 maM where the foliation marked by plagioclase is rotated by about 80° compared to the samples above or below (Figure 5-4 C and D; see pole figure compilation in the electronic supplement).
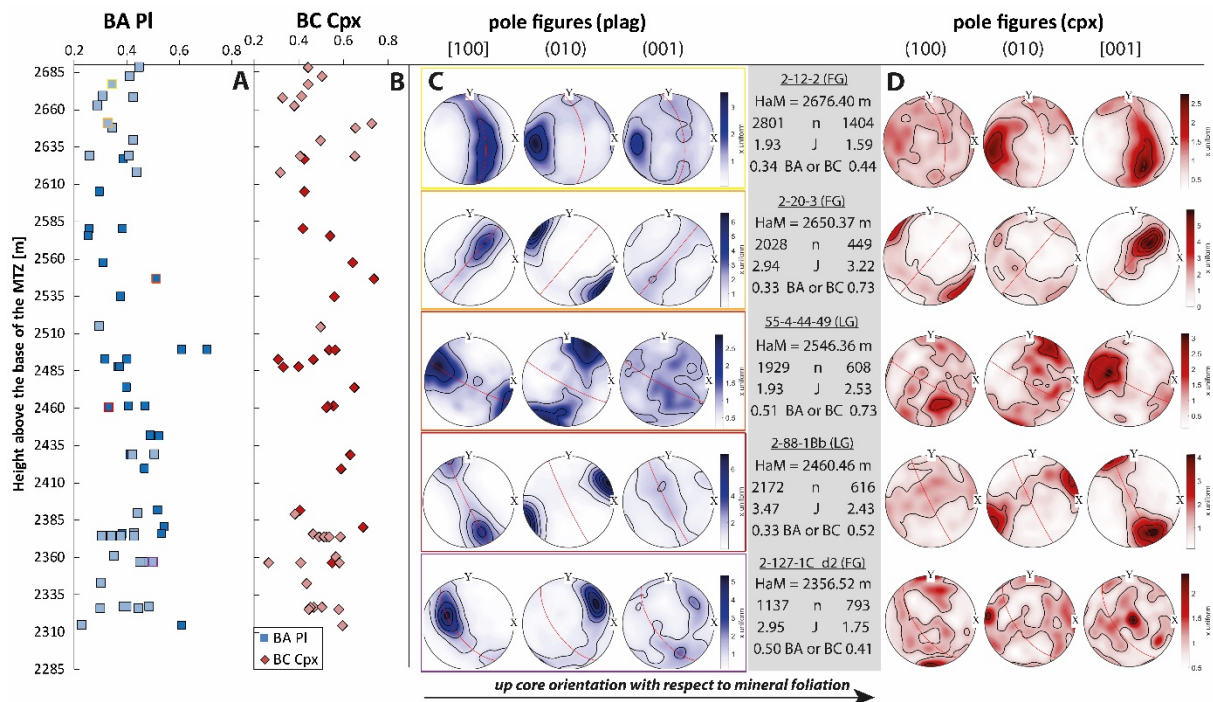
Figure 5-4   The BA or BC index of plagioclase (A) and clinopyroxene (B), respectively, quantifying the degree of lineation (with higher values indicating stronger lineation) plotted versus the height above the base of the MTZ. Note the similarity of the plotted plagioclase trend with the petrological trend shown in Figure 5-1 D. C) and D) representative pole figures of 100, 010, and 001 of plagioclase and clinopyroxene, arranged by height above the base of the MTZ. Values in the gray column provide some key information on the sample (name underlined, FG = foliated gabbro, LG = layered gabbro) with n = number of indexed grains, J = J index of the orientation distribution function (ODF), and BA or BC indices of plagioclase and clinopyroxene, respectively. Note that the colored frames around plagioclase pole figures correspond to colored data points in A). X points towards the top of the drill core, as also indicated by the black arrow at the base. Red lines mark the foliation within the sample obtained by plagioclase (010) poles. Only pole figures of samples with >100 grains of a phase are plotted (e.g., Satsukawa et al., 2013).

5.3   Preliminary interpretations

It is clear now that the transition from coarse- to fine-grained, i.e., from layered to foliated gabbros in the lower crust is not necessarily as sharp as indicated by the grain size distributions reported in chapter 3 (Figure 3-3 B). Layered and foliated gabbros change several times along the drill core and the sharp appearance of their contact in chapter 3 might be an effect of the much lower spatial resolution in the surface profile compared to the drill core. However, the data obtained during this study from drill core GT2A are not sufficient, yet, to explain the textural differences between both crustal units, or to explain, how the fine-grained foliated gabbros where emplaced within the coarser layered gabbros. The question arises, whether the units crystallized separately from each other and the FGs where transported into the pre-existing LG unit or vice versa. However, such a mechanism would be expected to be traced by some microstructural features, since one unit would experience a different mechanical emplacement than the other. Indeed, J indices of clinopyroxene are elevated in samples from the LG unit compared to those from the FG unit. The clinopyroxene J indices were compared to the clinopyroxene M indices (Skemer et al., 2005), which is also used by some researchers as quantifier of the fabric strength, but with a lower sensitivity to the number of analyzed grains.

Indeed, differences between FG and LG units are weaker in the M index, indicating that the elevated values of the J index in the LG unit are most likely an artifact of the lower number of analyzed grains due to the generally coarser grain sizes in the LG unit (Ismaıl and Mainprice, 1998) rather than providing reliable evidence of stronger fabrics in the LG unit. This is in agreement with the J index of plagioclase which gives almost identical results for samples from the FG and LG unit.

A transport over long distances is, furthermore, inconsistent with the smooth compositional trends along the core, which are independent from the crustal units. If sections, that are adjacent in the drill core, initially crystallized in different regimes or at different locations of the crust, compositional differences would be expected rather than smooth gradual variations over several decameters.

The presence of hornblende, orthopyroxene, and oxides in some gabbros or gabbronorites from drill core GT1A (Kelemen et al., 2020) reflects a more evolved parental melt composition of those rocks compared to gabbros from deeper crustal sections, as from drill core GT1A. This is also reflected by phase compositions which tend towards a more evolved composition with some variations along the drill core. Although abrupt changes at the decameter scale, as observed in drill core GT1A, were not identified in GT2A, the phase compositions gradually change in both major and minor element contents throughout the core. The gradual decreases in Ca# of plagioclase of Mg# of clinopyroxene are indicative of ongoing fractional crystallization in the horizons between 2440 and 2500 maM as well as between 2650 and the top of the drill core. A steep reverse fractionation trend is observed from 2360 to 2385 maM which underlain by an interval of strongly scattered results in the Ca# of plagioclase. Those are potentially a secondary effect of localized albitization of plagioclase (e.g., Agrinier et al., 1995; Gillis et al., 1992); however, it is not clear why this effect should be observed only in the samples below 2360 maM, which do not show different alteration features than the samples above.

The described normal and reverse trends agree with the findings from drill core GT1A where similar observations are described in more detail. They emphasize again the importance of high sampling resolutions along coherent sample suites to discover fine-scale differences.

5.4 Outlook

Although a wide range of petrological and microstructural data is already obtained from drill core GT2A, some more detailed analyses and further methods could complete the data set. That both drill cores GT1A and GT2A were both obtained in the same wadi which is already sampled and described in detail from the surface (see chapter 3; Garbe-Schönberg et al.; Koepke et al.; Müller et al., all submitted) provides the opportunity to perform studies from the hundreds of meters scale down to the cm-scale on a single crustal section. A key to distinguish between the crustal accretion models described in chapter 1.2 is the evolution of rock properties with depth, such that the data obtained from drill core GT1A ideally become obtained from GT2A, too, such that rock properties can be best-possible described as a function of height above the crust/mantle boundary. A selection of the samples from GT2A should also be investigated by application of geochemical tools to the phases and the whole rock, as it was done in GT1A in order to get closer information on their degree of fractionation with respect to MORB or in comparison to the gabbros geochemically investigated in chapter 4 or at the surface (Garbe-Schönberg et al., submitted).

Quantitative major and minor analyses using EPMA were also obtained from a few up to cm-schale magmatic hornblende grains in drill core GT2A. They might provide semi-quantitative information on their crystallization temperatures (Ernst and Liu, 1998) which provide, combined with Cl contents as indicator for a seawater-derived fluid in the melt (Currin et al., 2018b), helpful information on cooling mechanisms and its temperature regime within the lower oceanic crust from

Wadi Gideah. Further information on crystallization temperatures can be obtained by quantitative analysis of titanomagnetite and ilmenite in the same samples following the method presented by Sauerzapf et al. (2008).

As already described in chapter 4.4, a quantification of the cooling history of the crust provides key insights into the thermodynamic processes within the lower crust after its solidification which can then be used as indicator for the possible crustal accretion mechanisms (e.g., Coogan et al., 2002a; VanTongeren et al., 2008; Faak et al., 2014). Studying cooling rates applying the Mg-in-plagioclase speedometer of Faak et al. (2014) as a function of depth provides detailed insights into the subsolidus cooling history on the meter scale within the drill core and in combination with similar data obtained in drill core GT1A makes differences in the cooling rate with depth on the lower crustal scale visible.

Beside the question of how the entire lower crust accreted, the transition from foliated to layered gabbros is still mysterious. First insights from major element distributions do not reveal clear differences between both units. Trace element distributions in both minerals and whole rock may provide more detailed information on the source of both units.

6 Formation of igneous layering in the lower oceanic crust from the Samail Ophiolite, Sultanate of Oman

D. Mock[1,2]*, D.A. Neave[1,3], S. Müller[4], D. Garbe-Schönberg[4], O. Namur[5], B. Ildefonse[2], J. Koepke[1]

[1] Institut für Mineralogie, Leibniz Universität Hannover, Germany
[2] Géosciences Montpellier, Université de Montpellier, CNRS, Université des Antilles, Montpellier, France
[3] Department of Earth and Environmental Sciences, The University of Manchester, UK
[4] Institut für Geowissenschaften, Christian-Albrechts-Universität zu Kiel, Kiel, Germany
[5] Department of Earth and Environmental Sciences, KU Leuven, Belgium

Abstract

As the largest and best exposed example of paleo fast-spreading oceanic crust on land, the Samail ophiolite in the Sultanate of Oman represents an ideal natural laboratory for investigating deep crustal processes at fast-spreading mid-ocean ridges. We studied two layered gabbro sequences from different stratigraphic depths: one from the middle of the plutonic crust showing decimeter-scale modal layering (i.e., varying phase proportions) with olivine abundances gradually decreasing from layer bases to tops (Wadi Somerah, Sumail block) and one located near the crust-mantle boundary showing millimeter-scale olivine-rich layers (Wadi Wariyah, Wadi Tayin block). Our multimethod approach of field, petrographic, geochemical, and microstructural observations focuses on documenting layered textures that are widely observed within the lower oceanic crust as well as understanding their formation mechanisms within the context of small scale crustal accretion processes beneath fast-spreading mid-ocean ridges. Results from the mid-crustal sequence indicate moderate cooling rates (Ca-in-olivine: log $[dT/dt$; °Cyr$^{-1}] = -2.21 \pm 0.7$) and correlated variations in mineral compositions and microstructures. We infer that decimeter-scale layers in Wadi Somerah were deposited by density currents of crystal-laden magma within a sill environment that potentially experienced occasional magma replenishment. The millimeter layering in Wadi Wariyah is best explained by Ostwald ripening emphasizing initial heterogeneities possibly being provoked by cyclical nucleation of olivine through the competing effects of element diffusion and rapid cooling. Fast cooling is recorded for the crustal base (Ca-in-olivine: log $[dT/dt$; °Cyr$^{-1}] = -1.19 \pm 0.5$, Mg-in-plagioclase: log $[dT/dt$; °Cyr$^{-1}] = -1.35$°C ± 0.6) demonstrating that heat locally can be lost very efficiently from the lowermost crust.

6.1 Introduction

Oceanic crust represents more than two thirds of Earth's surface. It is formed at mid-ocean ridges (MOR), where ~75% of Earth's volcanism takes place. The 60,000 km long global mid-ocean ridge system is the planet's most effective environment for exchanging mass and heat between interior of the Earth and the hydrosphere, which has major implications for global geochemical cycles. In spite of numerous ship-based sampling campaigns performed over recent decades aimed at investigating the modern oceanic crust, coherent sample series from the deep crust beneath fast-spreading ridges are rare. Therefore, it remains important to perform complementary studies on ophiolites, in particular on the Samail ophiolite in the Sultanate of Oman, which is regarded as the best example of fast-spreading oceanic crust on land. This ophiolite has played a pivotal role in developing crucial paradigms for understanding sea floor spreading and ocean crust formation (e.g., Boudier et al., 1996; France et al., 2009; Henstock et al., 1993; Kelemen et al., 1997; Nicolas et al., 2000; Pallister and Hopson, 1981; Phipps Morgan and Chen, 1993; Quick and Denlinger, 1993). Since modal layering is a ubiquitous feature of the lower crust, not only in Oman (e.g., Browning, 1984; Pallister and Hopson, 1981) but also at the recent East Pacific Rise (EPR; Gillis et al., 2014b), its understanding is essential to approach the still unsolved question, how the crust accretes.

Many studies on ophiolite complexes performed in the 1980s and 1990s reported distinct rhythmic variations in modal proportions within the lower oceanic crust forming layered gabbros (e.g., Samail ophiolite in Oman, Troodos ophiolite on Cyprus, and Bay of Island ophiolite in Newfoundland; for a review see Nicolas, 1989). Their similarity to well-studied mafic layered intrusions, such as Bushveld (South Africa), Skaergaard (Greenland), or Rum (Scotland), led to the hypothesis that cumulate formation and the layer-forming processes occurring during crustal accretion at mid-ocean ridges are similar to those taking place in layered intrusions.

Multichannel seismic experiments at the EPR in the late 1980s, however, ruled out the presence of large magma chambers of the kind implied by early models of ridge crust architecture (Detrick et al., 1987; Vera et al., 1990). Instead, these authors detected only small volume "chambers" about 100 m in height and <4–6 km in width at a crustal depth of 1.2–1.4 km (i.e., beneath the sheeted dyke complex) by their low seismic velocity. These have been interpreted as axial melt lenses (AMLs) residing on top of wider and thicker regions of anomalously low velocity material that have in turn been interpreted as partially molten crystal mushes and/or solidified (but still hot) plutonic sequences of the lower crust (e.g., Detrick et al., 1987; Vera et al., 1990).

Although many studies were performed in order to align these findings with crustal accretion models at fast-spreading ridges—without yet establishing a scientific consensus—only a few of them address the question of how layering formed within lower oceanic crust (e.g., Buck, 2000; Jousselin et al., 2012). In contrast, large continental layered intrusions are of scientific interest for many decades leading to numerous studies and detailed descriptions of different types of layering, that is, cyclic variations in textural, mineralogical, or chemical features of a rock. These variations can create grain size layering (e.g., Duke Island, USA; Irvine, 1974), textural layering (e.g., Rum Layered Suite, Scotland; Brown, 1956), cryptic layering (i.e., chemical variation; e.g., Skaergaard, Greenland; Wager and Brown, 1968; Sept Iles, Canada; Namur et al., 2010), or modal layering (i.e., variation in phase proportions) as it is observed in the lower oceanic crust. Layering varies in terms of layer thickness, regularity, or lateral continuity, and layer contacts can be sharp or gradational, or asymmetric. So far, there is only a consensus that no single process can account for all these types of layering but rather that many processes may play a role in creating different types of layering. Potential layer-forming processes have been described in several reviews (e.g., Namur et al., 2015; Naslund and McBirney, 1996) and can be divided into dynamic and non-dynamic processes. During dynamic processes, layering is formed within a magma chamber by movement of melt, mush, and/or crystals. This can include gravity-controlled

settling, magma currents, convective-related processes, metasomatism, or magma replenishment and mixing. Non-dynamic layer-forming processes reflect conditional changes during crystallization or occur by self-organization of the mineral assemblage in a crystal mush. Layer formation by non-dynamic processes can include magmatic or tectonic deformation of a crystal mush, fluctuations of magma chamber conditions, diffusive exchange, or coarsening of grains.

The complexity of layer formation makes clear that both cumulus and post-cumulus processes have to be taken into account, especially when considering an oceanic spreading center where magmatic processes are continuously accompanied by tectonic and also hydrothermal processes. We approach this challenging situation by combining petrographic, petrological, geochemical, and microstructural data in order to constrain the layer-forming processes at different stratigraphic depths of the lower oceanic crust. As we point out in the next section, and as suggested by many groups before (e.g., Nicolas and Rabinowicz, 1988; Pallister and Hopson, 1981), we assume that the Oman ophiolite is a good analogue for recent fast-spread oceanic crust where, for example, modal layering was recently discovered by IODP Expedition 345 at Hess Deep (Gillis et al., 2014b). Moreover, layered textures similar to those observed in the Oman ophiolite have also been found at Pito Deep at EPR (Gess et al., 2018; Perk et al., 2007). Understanding how layers form in the deep oceanic crust is thus crucial for constraining the dynamics and mechanisms of crustal accretion at fast-spreading ridges. Here we present observations on layered gabbros from two sites in the Samail ophiolite with contrasting modes of layer appearance, and we provide insights based on multi-method observations into the mechanisms that led to the formation of the studied layering.

6.2 Geological Setting

The Samail ophiolite in the Sultanate of Oman, a ~400 km long mountain chain of oceanic lithosphere obducted onto the Arabic continental margin during the Cretaceous, is regarded as the best example of fast-spreading oceanic crust on land (e.g., Nicolas et al., 2000). The mountain chain is located on the north-eastern coast of Oman and covers an area of more than 20,000 km^2 (Pallister and Hopson, 1981). It is made up of twelve massifs that represent a complete crustal transect from the Moho transition zone (MTZ) via the gabbros of the lower oceanic crust up to the volcanic layer consisting of sheeted dikes and erupted basalts. The paleo oceanic crust formed ~95 Ma ago (Rioux et al., 2013) and is thought to have formed at a fast-spreading center with a paleo half-spreading rate of 50–100 mm/yr (Rioux et al., 2012a).

Geochemical investigations and field relations suggest a polygenetic origin for the Oman ophiolite (e.g., Alabaster et al., 1982; Goodenough et al., 2014; Koepke et al., 2009; Pearce et al., 1981; Yamasaki et al., 2006). A first phase produced the so-called V1 lavas and the majority of the gabbroic crust which is very similar to the modern EPR crust in terms of structure, lithology, petrography, and bulk crustal thickness. However, in contrast with the EPR, the parental basalts which formed the crust during the first magmatic stage in the Wadi Gideah (Oman) are thought to have contained elevated water contents of 0.4 to 0.8 wt% due to their formation in a subduction-influenced setting (MacLeod et al., 2013; Müller et al., 2017; Pearce et al., 1981). A second magmatic phase (V2) probably related to flux-induced peridotite melting subsequently intruded the first magmatic phase and consists of boninites in the upper crust and wehrlites, gabbronorites, and larger plagiogranite bodies in the lower and mid-crust (e.g., Goodenough et al., 2014; Juteau et al., 1988; Koepke et al., 2009; Yamasaki et al., 2006). The second magmatic stage is more voluminous in the northern blocks than in the southern segments of the ophiolite (e.g., Goodenough et al., 2014; MacLeod et al., 2013). Therefore, many studies that focused on understanding primary magmatic processes at mid-ocean ridges have been performed in

the southern massif of the ophiolite (e.g., Garrido et al., 2001; Koga et al., 2001; VanTongeren et al., 2008).

In spite of the inferred location of the ophiolite in a region of subduction zone initiation, the following observations related to the first magmatic event demonstrate a close similarity with the modern, fast-spreading EPR: a continuous, typically layered crustal architecture with an average crustal thickness of 6–7km (Lippard et al., 1986; Nicolas, 1989); an absence of amagmatic spreading that is common at slow-spreading ridges (e.g., Cannat and Casey, 1995); a very narrow range from 96.40 ± 0.17 to 94.18 ± 0.54 Ma of zircon crystallization ages across the width of the ophiolite (maximum ~100 km) sampled normal to the ridge direction (Rioux et al., 2012a; Tilton et al., 1981; Warren et al., 2005); spinel Cr/Al versus Mg# (= MgO/(MgO + FeO); molar) ratios that overlap those for peridotites from modern fast-spreading ridges (Le Mee et al., 2004); the lengthscale of segmentation and absence of transform faults indicating a weaker impact of tectonic processes due to high magma supply (MacLeod and Rothery, 1992; Nicolas et al., 2000); and the orientation of a well-developed sheeted dike sequence perpendicular to the Moho which implies frequent magma ascent from the lower to the upper crust (MacLeod and Rothery, 1992). These features make clear that a detailed understanding of the magmatic processes which have formed the Oman paleo-crust provides insights into those taking place beneath recent fast-spreading centers. Our study focuses on outcrops in the southernmost blocks of the ophiolite at Wadi Somerah (Sumail block) and Wadi Wariyah (Wadi Tayin block), where the record of the second-stage magmatism is minor and comparisons with the modern EPR are well founded.
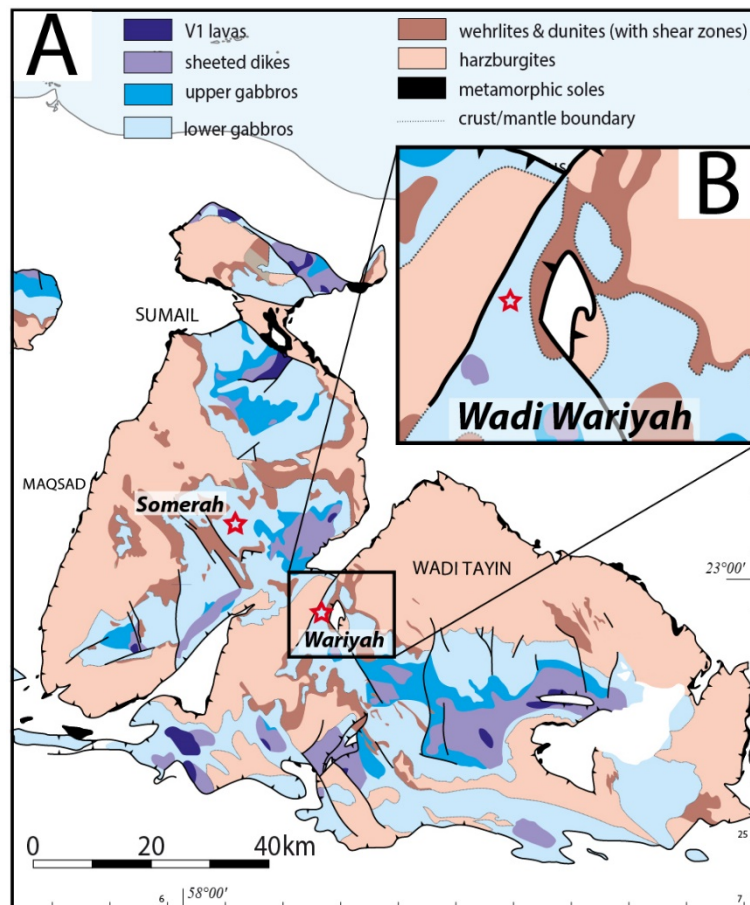
Figure 6-1   A) Geological map of the southernmost massifs of the Oman Ophiolite "Sumail" and "Wadi Tayin". B) crop of the geologically complex area of the Wadi Wariyah outcrop. The red stars give the positions of the two sampled outcrops in Wadi Somerah and in Wadi Wariyah. Map modified after Nicolas et al., 2000.

6.3 Materials and Methods

6.3.1 Sample Materials

We collected two types of samples from adjacent massifs of the Oman ophiolite (Sumail block for the material from Wadi Somerah, Wadi Tayin block for the material from Wadi Wariyah). They are consequently not representative of the same crustal section but were instead selected to represent two contrasting styles of layering. First, a suite of samples was taken from an outcrop in the central part of the layered gabbro section in the Wadi Somerah (N 23°5'34.66", E 58°6'14.62";Figure 6-1) that shows decimeter-scale modal layering (Figure 6-2A and B). This is representative of the average thickness of layering in the lower crust of the Oman ophiolite (Browning, 1984; Pallister and Hopson, 1981). The outcrop is about 30 m tall and 100 m wide. The modal layers are nearly horizontal at the southern face of the outcrop and can be followed over several tens of meters (Figure 6-2A). The layering is crossed by bright and dark centimeter-scale veins that usually propagate sub-perpendicular to the layering. As previously observed in Oman (e.g., Nicolas et al., 2000), olivine crystals are lineated. The much smaller western flank of the outcrop reveals the layering to be strongly sheared and folded (Figure 6-11A). We sampled a coherent profile of six consecutive layers. Each layer (except for layer 6 where we sampled only the layer base) consists of a melanocratic olivine-rich base that grades up section into a leucocratic top that is significantly depleted in, or free from, olivine but strongly enriched in plagioclase. Twenty-nine thin sections were prepared with a vertical distance of 1 to 42 cm between two stratigraphically successive samples.

Second, a single angular block was investigated which we collected just below an outcrop at the mouth of the Wadi Wariyah (N 22°59'0.42", E 58°15'54.68";Figure 6-1). This outcrop represents deep layered gabbro at a crustal height of about 0.1 km above the MTZ (Bosch et al., 2004). The layering occurs as millimeter- or centimeter-thick layers with significantly differing olivine contents (Figure 6-2D). The locality where we collected the sample is located 300 m north to a well-studied outcrop of layered gabbro that preserves magmatic and hydrothermal veins ranging in formation temperature from very high (magmatic regime) to low temperatures which cut perpendicularly across the layering (Figure 6-2C; Bosch et al., 2004; Currin et al., 2018b; Nicolas, 2003; Wolff, 2013). Foliation in plagioclase and olivine is here parallel to the igneous layering. Layering as thin as we observe in the investigated sample (millimeter-scale) has been rarely documented in the Oman ophiolite (Jousselin et al., 2012). Nonetheless, the analyzed sample allows new insights into magmatic processes operating in the lowermost oceanic crust. From this block, we prepared two thin sections that cover 111 coherent olivine-rich layers of the sample. Depth information given in the following chapters are estimated from the top of each sequence.

Although the sample from Wadi Wariyah originates from a locality with a complex geological evolution (Figure 6-1B), detailed mapping by Nicolas et al. (2000) and others (e.g., Bosch et al., 2004; Nicolas, 2003) substantiates our interpretation that the sample originates from the lowermost layered gabbros close to the MTZ. Our samples were not collected as oriented samples. Therefore, we cannot comment on orientations of the measured foliations and lineations in a crustal context. Nevertheless, since thin sections from Wadi Wariyah have been prepared from the same piece of rock, the measured orientations are consistent along the profile. The samples from Wadi Somerah have been cut from one hand piece per melanocratic or leucocratic sub-layer, respectively, such that all thin sections of one sub-layer are oriented the same way providing consistency at the sub-layer scale.
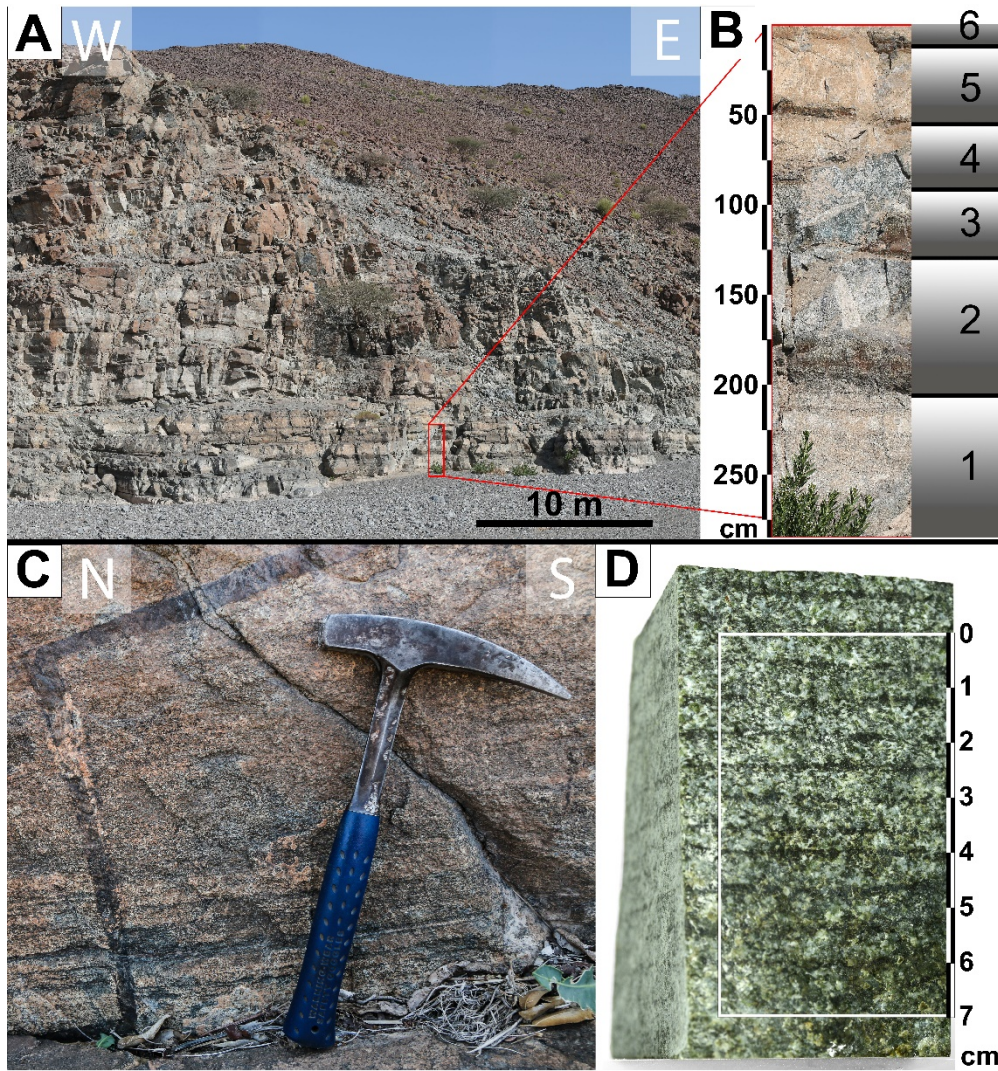
Figure 6-2   A) Photograph of the outcrop in Wadi Somerah exposing dm-scale modal layering. B) shows the sequence sampled for this study, given by the red rectangle, in detail. Numbers 1 – 6 are the layer numbers, grey shaded fields represent melanocratic layer bases and leucocratic tops, demonstrating decreasing olivine content within each layer. Height of the sequence: 285 cm. C) Photograph taken at an outcrop in Wadi Wariyah 300 m south of the locality where the sample in D) was collected. It representatively shows mm-scale layering and a late stage magmatic vein perpendicularly cutting across the fine layering. Note the mm-scale modal layering at the base and the gabbroic late-stage vein cross-cutting the layered host rock. D) Detailed photograph of the hand piece from the mouth of the Wadi Wariyah which was investigated in this study. Thin dark layers are olivine-rich. Rectangle symbolizes the region where two thin-sections were prepared covering 11 layers. Note scale bars aside of B and D giving sequence heights in cm and which correspond to the depth intervals given in text and figures of this paper. Orientation directions given in white in A and C. Photographs by D. Mock

6.3.2   Analytical Techniques

Petrographic analysis was performed using a binocular optical microscope. Modal proportions were estimated visually by comparison of thin section photographs with charts for estimating mineral percentages. Grain sizes have been measured along their long axis. The average grain size of a phase per thin section was calculated by measuring 10 grains: two of the smallest, two of the largest, and six

medium-sized grains. Grains where chosen with respect to their habit, that is, poikilitic crystals were excluded from measurement. With respect to best possible consistency along both sections, we decided to obtain phase pro-portions and grain sizes by visual estimation rather than EBSD analysis since the latter was for the Wadi Somerah only applied to a subset of samples. Nonetheless, we compared the results of our visual approach with those obtained by EBSD and found that both phase proportions and relative grain size differences between the samples are consistent between both methods.

Major and minor element compositions of olivine, clinopyroxene, and plagioclase were determined in the cores and rims of crystals in thin sections with a Cameca SX 100 electron microprobe at the Institute of Mineralogy in Hannover. The electron probe was operated through the Peaksight software. We used an accelerating voltage of 15 kV and a beam current of 15 nA. The beam was focused to 2 μm for olivine and plagioclase analyses; for clinopyroxene analysis the beam was defocused to 20 μm in order to integrate potential exsolution lamellae. Measurement times were 10 s on peak and 5 s on each background for all elements. Diffusion profile analyses of Ca in olivine were performed in order to estimate cooling rates (see below). For those analyses, we used a focused beam with an accelerating voltage of 15 kV and a beam current of 100 nA. Calcium was measured on a large pentaerythritol (LPET) crystal with a peak time of 240 s and 120 s on each background. High-precision analyses of Mg in plagioclase were also performed with an accelerating voltage of 15 kV and a high beam current of 100 nA. Magnesium was analyzed on a thallium acid phthalate (TAP) crystal with 240 s on peak and 120 s on each background. A matrix correction was applied following the PAP scheme (Pouchou and Pichoir, 1991).

In situ analyses of trace elements, and in particular of rare earth elements (REE), in plagioclase and clinopyroxene were performed at the Institute of Geosciences in Kiel using a 193 nm ArF excimer laser ablation system (GeoLasPro HD, Coherent) coupled to an Agilent 7,900-s inductively coupled plasma mass spectrometry (ICP-MS). Analyses were performed as point measurements with 16 Hz pulse rate, 18 Jcm^{-2} fluence, and a crater diameter of 120 μm on plagioclase, and 10 Hz, 12 Jcm^{-2}, and a crater diameter of 32 μm on clinopyroxene. Helium was used as carrier gas with addition of 14 ml H$_2$. Initial data processing and setting of integration intervals were performed with the GLITTER software package, applying the method of internal standardization with CaO as determined from electron probe measurements as internal standard and using NIST SRM612 for initial calibration. A second matrix matched calibration step was applied using micro-analytical reference materials BIR-1P, BHVO-2P, JGb-1P, and JF-1P prepared as nano-particulate pellets (Garbe-Schönberg and Müller, 2014; see calibration data in Mock et al., 2020e). Precision of replicate measurements was <2% relative standard deviation for most elements with an accuracy of ~5% RMSD (root-mean-square deviation) on BCR-2G at >10*LOD (limit of detection; see accuracy data in Mock et al., 2020e).

Electron backscatter diffraction (EBSD) mapping was performed at Géosciences Montpellier with a JEOL JSM 5600 scanning electron microscope equipped with an Oxford/Nordlys EBSD detector and using the Aztec software. We used an accelerating voltage of 15 kV. Analyses were performed for each crystal along a grid with a step size of 16.5 to 30.0 μm depending on grain size.

6.3.3   Estimation of Cooling Rates and Crystallization Temperatures

Cooling rates were estimated using the Ca-in-olivine speedometer (Coogan et al., 2005) and the Mg-in-plagioclase speedometer (Faak et al., 2014). Both methods use diffusion profiles in crystals to estimate how fast the rocks cooled in the sub-solidus down to their closure temperatures. Following the arguments of Coogan et al. (2007), we modeled the Ca diffusion in olivine at a fixed fO$_2$ of 10−12 bar. Both methods, Ca-in-olivine and Mg-in-plagioclase, are based on high spatial resolution rim-core-

rim electron microprobe profiles in olivine or plagioclase crystals, respectively, that are adjacent to clinopyroxene crystals which serve as semi-infinite reservoirs for both Ca and Mg. Using the geothermometers of Shejwalkar and Coogan (2013) for Ca-in-olivine and Faak et al. (2013) for Mg-in-plagioclase allows the closure temperature (T_c)—the temperature at which diffusion in the crystal becomes too inefficient for significant changes in element distribution to occur—to be estimated for every measurement point along a rim-core-rim profile. T_c depends on the distance from the interface (Dodson, 1986; Onorato et al., 1981) such that the shape of profile, that is, the absolute values for T_c and the relative difference between core and rim data, can be used to estimate the sub-solidus cooling rate.

Modeling diffusion profiles and using them for geospeedometry involves several sources of uncertainty which we tried to minimize or eliminate. As shown by Dalton and Lane (1996), rim analyses of Ca as a trace element in olivine adjacent to a Ca-rich phase are highly sensitive to secondary fluorescence. The profiles started and ended always ~5 µm from the rim. Following Coogan et al. (2002a), secondary fluorescence potentially affects the outermost 100 µm of a profile. However, the profiles used for the modeling have very similar shapes with only small differences between core and rim composition, regardless of the adjacent phases at the start and end of the profile. Since we would expect secondary fluorescence to affect every profile in a different way (i.e., depending on adjacent phases; Coogan et al., 2002a), the similarities between the profiles appear unlikely to result from secondary fluorescence. Moreover, taking the small number of clear outliers in the measured profiles on many different samples into account, it is improbable that secondary fluorescence significantly affected our results. Uncertainties may also arise from grain shapes (i.e., cutting effects; e.g., Coogan et al., 2007) which we tried to minimize by analyses of several grains per sample. Occasionally, we performed measurements of two perpendicular profiles per grain in order to eliminate erroneous impact from crystal shapes. The similarity of results obtained by applying independent methods (i.e., Ca-in-olivine and Mg-in-plagioclase) in Wadi Wariyah suggests that both methods are reliable. All profile data are collected in Mock et al. (2020d). Crystallization temperatures were estimated using the thermometer of Sun and Liang (2017) that exploits the temperature-dependent partitioning of REE between plagioclase and clinopyroxene.

6.3.4   Processing EBSD Data

The first steps of post-processing and refining EBSD data were performed with the Channel5 Tango application. Grain statistics, maps, eigenvalue analyses, and pole figures were calculated using the MTEX toolbox for Matlab® (e.g., Mainprice et al., 2015). Very small grains with a size of less than 10 pixels were deleted since they are assumed to be results of analytical errors. Twins in plagioclase and clinopyroxene were defined assuming a misorientation angle of 180° ± 2 to the neighbored grain of the same phase. Crystallographic preferred orientations (CPO) were quantified using the J index of the orientation distribution function (called ODF J index here) after Bunge and Esling (1982), which varies between 1 for a random fabric and ∞ for a single crystal. The pole figure symmetry was quantified using the BA index for plagioclase and the BC indices for clinopyroxene and olivine, respectively (Satsukawa et al., 2013). These indices vary between 0 for a foliated symmetry (axial B-type) and 1 for a lineated symmetry (axial A-type or axial C-type, respectively). The intermediate P-type symmetry corresponds to an index of ~0.5. Using the orientation of each pixel, it is possible to calculate the misorientation of a single pixel from the average orientation of the corresponding grain and, therefore, to quantify the internal misorientation of a grain. The grain orientation spread (GOS) is the average internal misorientation of all grains per phase in a sample. Hence, the GOS provides a quantification of the intracrystalline deformation intensity per mineral phase within the samples. We

present and interpret the GOS for plagioclase and clinopyroxene only. Due to intense mesh serpentinization, olivine grain boundaries obtained by EBSD were determined incorrectly, meaning that the GOS cannot be calculated for whole primary grains and is therefore probably underestimated. Pole figures and fabric indices of plagioclase and clinopyroxene were calculated using a randomly chosen pixel per grain (grain data) instead of all indexed pixels (grid data; e.g., Satsukawa et al., 2013) in order to avoid that data from large grains become overestimated. Due to the potentially incorrect identification of olivine grain boundaries, olivine fabrics have been calculated using the grid data. This may lead to an increased ODF J index.

6.4   Results

6.4.1   Wadi Somerah

The primary lithologies of the decimeter-scale layering in Wadi Somerah are gabbros or olivine gabbros with the main phases being plagioclase, clinopyroxene, and olivine. Modal layering is mostly expressed by variability in olivine contents of up to 23% in melanocratic layer bases and less than 10% in leucocratic tops (Figure 6-4). Complex mesh serpentinization of olivine leads to the dark appearance of the layer bases observed in the field. Olivine-enriched layer bases and olivine-depleted layer tops are represented by EBSD phase maps in Figure 6-3A and B. Plagioclase usually forms the smallest grains with grain sizes of 0.2–0.7 mm long axis length. Olivine and clinopyroxene grain sizes are larger, with average grain sizes of 1–2.5 mm. Clinopyroxene grains are the largest at the base of layer 2, which has significantly larger grains than the top of layer 1 (see layer details in Figure 6-4). An increasing trend in grain size toward the layer base is only observed in layers 1 and 2; other layers show either no trend or even a trend of grain size coarsening upward. On a thin-section scale, grain size variation is small for every phase (see representative phase maps in Figure 6-3A and B). The grain shape of all phases is anhedral to subhedral with prismatic and occasionally elongated habits. Plagioclase occasionally forms chadacrysts in poikilitic clinopyroxene or olivine, indicating that plagioclase partially crystallized simultaneously with olivine and clinopyroxene. Olivine shows strong alteration to mesh serpentine, often related to alteration veins and their halos, implying that olivine alteration was triggered by hydrothermal activity. An alignment of elongated olivine crystals is well preserved in leucocratic samples with small amounts of olivine. The majority of olivine grains in the melanocratic samples shows a round shape and no clear lineation. All petrographic results are summarized in Table 1.

Mineral compositions (see Mock et al., 2020d, for compositional data) from the Wadi Somerah sequence show that there is no general correlation with position in different modal layers (Figure 6-4). The core Mg# ([Mg/(Mg + Fe)] × 100; molar basis) in olivine varies between 78.1 and 80.6. From the base of the sequence up section, the Mg# is nearly constant in the depth interval between 225 and 275 cm. It significantly decreases from 80.5 to 78 toward the base of layer 2 at a depth in the sequence of 200 cm. Above this minimum, the Mg# increases up section to 175 cm, reaching its maximum of 80.6. The following trend up section is relatively homogeneous, showing a slight decrease which is most pronounced between the base and top of layer 5. NiO in olivine follows the Mg# trend of olivine except for layer 2 and layer 5, where NiO is decoupled from the Mg# value.

The Mg# in clinopyroxene cores shows nearly constant values throughout the stratigraphy with only limited variability between 83.7 and 85.9, showing small shifts within the natural variability along the whole sequence. These shifts seem not to correlate with the Mg# in olivine. The most distinct shift in clinopyroxene Mg# occurs in layer 5, where it varies from 84 to 85.8 in a single sample, while the
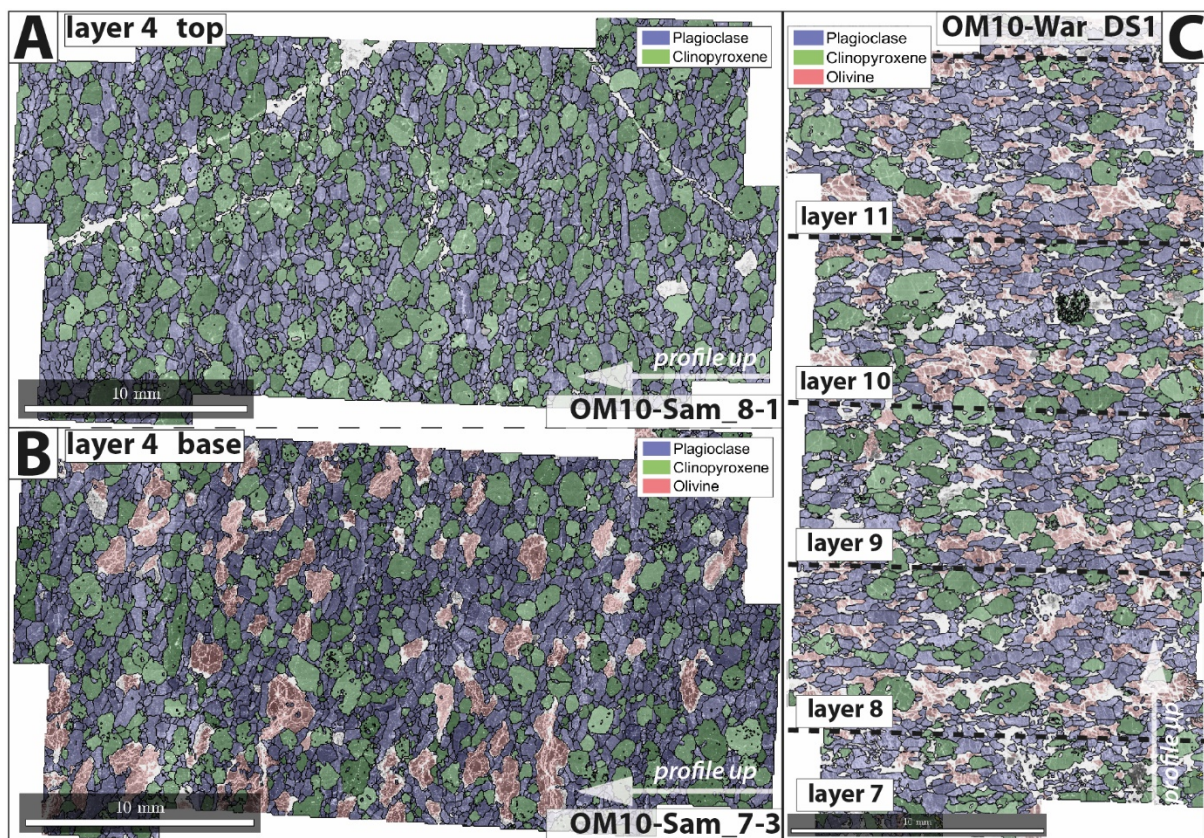
Figure 6-3   Phase maps of three thin-sections from our study. A) Sample OM10-Sam_8-1 representing the leucocratic, olivine-poor top of layer 4. B) Sample OM10-Sam_7-3 representing the melanocratic, olivine-rich base of layer 4. Both A and B correspond to the dm-scaled layering in Wadi Somerah. C) Sample OM10-War_DS1 covering layers 1-5 from the mm-layering in Wadi Wariyah. Note the legend of every image. The bars at the image bases are 10 mm. White arrows give direction profile up.

corresponding olivine in the same horizon does not show this anomaly to more primitive compositions, neither with respect to the Mg# nor to NiO. In contrast to olivine and plagioclase, clinopyroxene crystals are slightly zoned, with higher Mg# values in the core. Rim Mg#s generally vary between 81.8 and 85.9. The degree of zoning differs significantly (up to 2 Mg# units between core and rim at the base of layer 2) but does not show any evolution in the whole sequence or within individual layers. We also observed zoning in TiO_2 with concentrations being increased in the rims by an average enrichment factor of 1.18 (with 1.74 at maximum). Incompatible trace elements (represented by Zr in Figure 6-4) reflect this trend consistently, with higher values in the rims enriched by a factor of up to 2.4 in the case of Zr. All trace element data are collected in Mock et al. (2020e).

Ca# ([Ca/(Ca + Na)] × 100, molar basis) in plagioclase covers a range between 79.8 and 84.1 with a distinct minimum at a depth of 200 cm (base of layer 2), clearly correlating with the minimum in Mg# of olivine in that horizon. The Ca# increases above and below this point from 79.8 to 82.9 and 82.6, respectively. The evolution of the Ce content (representing a proxy for plagioclase trace element content) inversely correlates with the trends of the Ca# within layers 2 and 3 (i.e., increasing Ce with decreasing Ca# and vice versa) but behaves differently within layer 1 and at the transition between layers 5 and 6 where Ce shows a consider-able scattering at constant Ca#.
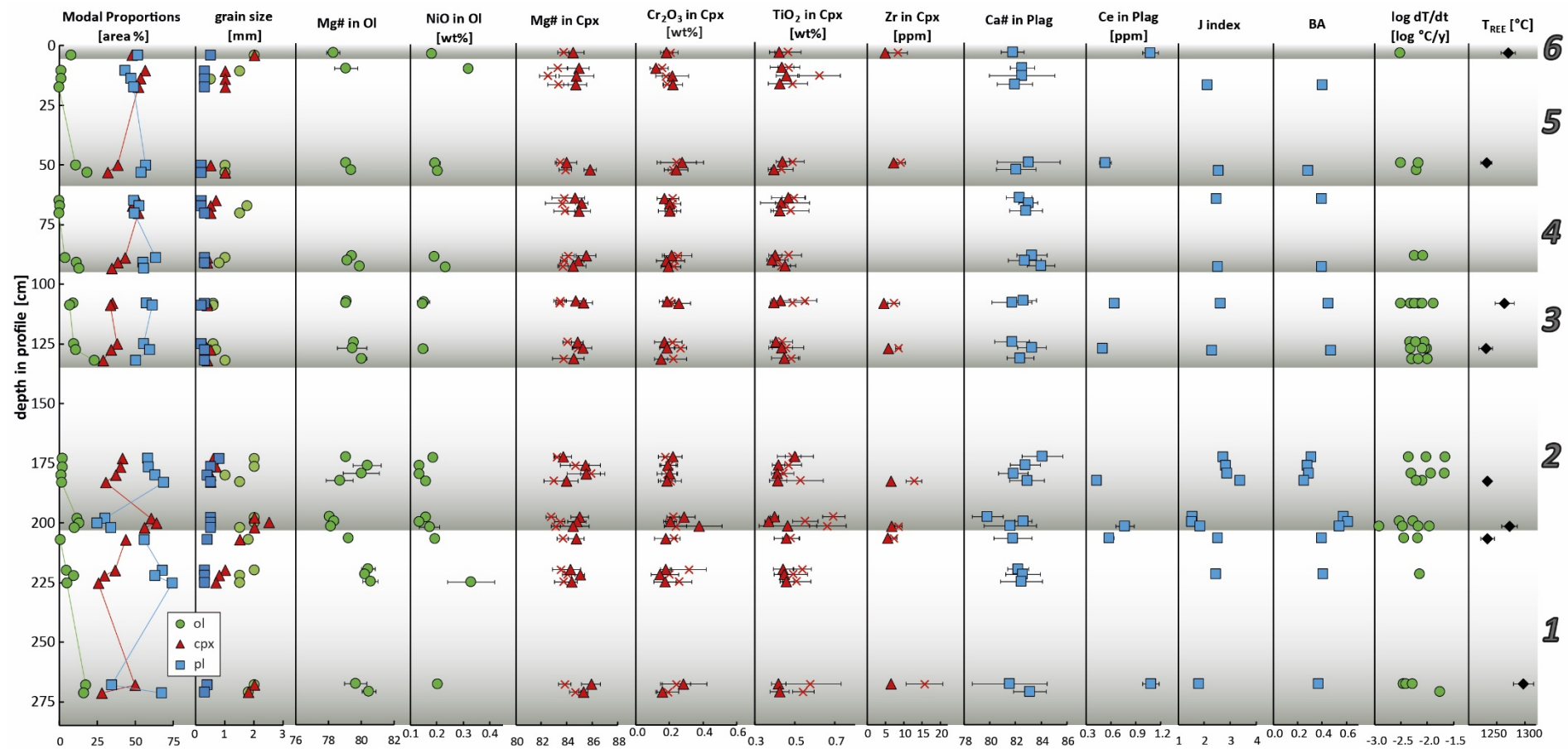
Figure 6-4 Summarized results of analyses on the dm-scale layered gabbro sequence from Wadi Somerah. Grey numbers on the right give the layer number; gradational grey background symbolizes the layer color, most pronounced by olivine content. Closed symbols are core, crosses are rim analyses. Black bars in element plots give 1 sigma standard deviation from the mean. Black bars in T_{REE} plot give standard error of the regression line provided by the Sun and Liang (2017) excel sheet. Mg# = Mg/(Mg+Fe)x100; molar basis, Ca# = Ca/(Ca+Na)x100; molar basis. Note correlating trends with respect to several data sets within a given layer, most pronounced in layer 2. See text for further interpretation.

Table 6-1   Table 1 Petrographic observations and phase properties for sample sets from Wadi Somerah (OM10-Sam) and Wadi Wariyah (OM10-War)

Sample	DiS [cm] [a]	Litho-logy [b]	grain size mode [c]	Olivine mode [%] [d]	GS [mm] [e]	shape [f]	habit [g]	com [h]	Plagioclase mode [%] [d]	GS [mm] [e]	shape [f]	habit [g]	com [h]	Clinopyroxene mode [%] [d]	GS [mm] [e]	shape [f]	habit [g]	com [h]
OM10-Sam_11	4	ol gb	med	7	2.0	shd	prm	oc, rrm	48	0.5	shd	elg	cc	45	2.0	shd	prm	oc
OM10-Sam_10-1	10.5	ol-b gb	fin	1	1.5	shd	prm	oc, rrm	43	0.3	shd	elg	cc	56	1.0	shd	prm	oc
OM10-Sam_10-2	13.85	ol-b gb	fin	1	0.5	shd	prm	oc, rrm	47	0.3	shd	elg	cc	52	1.0	shd	prm	oc
OM10-Sam_10-3	17.35	gb	fin	-					49	0.3	shd	elg	cc	51	1.0	shd	prm	oc
OM10-Sam_9-1	49.95	ol gb	fin	10	1.0	shd	prm	oc, rrm	54	0.2	shd	elg	cc	36	0.5	shd	prm	oc
OM10-Sam_9-2	53.05	ol gb	fin	18	1.0	shd	prm	oc, rrm	52	0.2	shd	elg	cc	30	1.0	shd	prm	oc
OM10-Sam_8-1	64.9	gb	fin	-					49	0.2	shd	elg	cc	51	0.7	shd	prm	oc
OM10-Sam_8-2	67.1	ol-b gb	fin	1	1.8	shd	prm	rrm	52	0.2	shd	elg	cc	47	0.5	shd	prm	oc
OM10-Sam_8-3	70.2	ol-b gb	fin	1	1.5	shd	prm		49	0.3	shd	elg	cc	50	0.5	shd	prm, elg	oic
OM10-Sam_7-1	88.9	ol gb	med	3	1.0	shd	prm, elg		57	0.3	shd	elg, prm	cc	40	0.4	shd	prm	oc
OM10-Sam_7-2	90.95	ol gb	med	11	0.8	shd	prm		52	0.3	shd	elg, prm	cc	37	0.4	shd	prm, elg	oc
OM10-Sam_7-3	93.4	ol gb	med	13	0.6	shd	prm, elg	rrm	53	0.3	shd	elg, prm	cc	34	0.4	shd	prm	oc
OM10-Sam_6-1	107.9	ol gb	med	9	0.6	shd	prm, elg	rrm	57	0.3	shd	elg	cc	34	0.4	shd	prm	oc
OM10-Sam_6-2	108.7	ol gb	med	7	0.6	shd	prm	rrm	60	0.2	shd	prm, elg	cc	33	0.4	shd	prm, elg	oc
OM10-Sam_5-1	125	ol gb	med	9	0.6	shd	prm, elg	rrm	54	0.2	shd	prm, elg	cc	37	0.3	shd	prm	oc
OM10-Sam_5-2	127.5	ol gb	med	11	0.7	shd	prm	rrm	56	0.3	shd	prm, elg	cc	33	0.5	shd	prm, irg	oc
OM10-Sam_5-3	131.9	ol gb	med	23	1.0	shd	prm	oc, rrm	49	0.3	shd	prm, elg	cc	28	0.4	shd	prm	oc
OM10-Sam_4-1	173	ol-b gb	fin	2	2.0	shd	prm, elg	oc, rrm	57	0.8	shd	prm, elg	cc	41	0.6	shd	prm	oc
OM10-Sam_4-2	176.5	ol-b gb	med	2	2.0	shd	prm, elg	oc, rrm	58	0.5	shd	prm, elg	cc	40	0.7	shd	prm	oc
OM10-Sam_4-3	180	ol-b gb	fin	1	1.0	shd	prm, elg	oc, rrm	62	0.4	shd	prm, elg	cc	37	0.5	shd	prm	oc
OM10-Sam_4-4	183	ol-b gb	med	2	1.5	shd	prm, elg	oc, rrm	68	0.5	shd	prm, elg	cc	30	0.5	shd	prm	oc
OM10-Sam_3-1	198	ol gb	med	12	2.0	shd	prm, irg	oc, rrm	29	0.5	shd	prm, elg	cc	59	2.0	shd	prm	oc
OM10-Sam_3-2	200	ol gb	med	13	2.0	shd	prm, irg	oc, rrm	24	0.5	shd	prm, elg	cc	63	2.5	shd	prm	oc

Table 6-1 continued

Sample	depth[a]	rock[b]	size[c]	%[d]	size[e]	shape[f]	habit[g]	feat[h]	%[d]	size[e]	shape[f]	habit[g]	feat[h]	%[d]	size[e]	shape[f]	habit[g]	feat[h]
OM10-Sam_3-3a	202	ol gb	med	10	1.5	shd	prm, irg	oc, rrm	34	0.5	shd	prm, elg	cc	56	2.0	shd	prm	oc
OM10-Sam_3-3b	207	ol-b gb	med	1	1.8	shd to ehd	prm	oc, rrm	56	0.4	shd	elg	cc	43	1.5	shd	prm	oc
OM10-Sam_2-1	220	ol-b gb	fin	4	2.0	shd	prm, elg	oc, rrm	62	0.3	shd	prm, elg	cc	34	1.0	shd	prm	oc
OM10-Sam_2-2	222.1	ol-b gb	fin	9	1.5	shd	prm	oc, rrm,	62	0.3	shd	prm, elg	cc	29	0.8	shd	prm	oc
OM10-Sam_2-3	225.1	ol-b gb	fin	5	1.5	shd	prm	oc, rrm	71	0.3	shd	prm, elg	cc	24	0.7	shd	prm	oc
OM10-Sam_1-1	267.9	ol gb	med	17	2.0	shd	prm, irg	oc, rrm	34	0.4	shd	prm, elg	cc	49	2.0	shd	prm	oc
OM10-Sam_1-2	271.2	ol gb	med	14	1.8	shd	prm, irg, elg	oc, rrm	61	0.3	shd	prm, elg	cc	25	1.8	shd	prm	oc
OM10_War_DS1-11	0.5	ol gb	med	15	1.5	shd	prm, elg	oc	65	0.4	shd	prm, elg	cc	20	1.5	shd	prm	rare oc
OM10_War_DS1-10	1.2	ol gb	med	15	1.5	shd	prm, irg	oc	55	0.7	shd	prm, elg	cc	30	1.5	shd	prm	
OM10_War_DS1-9	1.9	ol gb	med	12	1.5	shd	prm, irg	oc	58	0.5	shd	prm, elg	cc	30	1.2	shd	prm	
OM10_War_DS1-8	2.5	ol gb	med	18	1.0	shd	prm, irg	oc	62	0.5	shd	prm, elg	cc	20	1.0	shd	prm	rare oc
OM10_War_DS1-7	3.1	ol gb	med	10	1.0	shd	prm, irg	oc	60	0.6	shd	prm, elg	cc	30	0.8	shd	prm	
OM10_War_DS2-6	3.8	ol gb	med	16	1.2	shd	prm, irg		57	0.6	shd	prm, elg		27	0.7	shd	prm	
OM10_War_DS2-5	4.1	ol gb	med	18	1.2	shd	prm, irg		55	0.5	shd	prm, elg		27	0.5	shd	prm	
OM10_War_DS2-4	4.8	ol gb	med	15	1.3	shd	prm, irg		50	0.5	shd	prm, elg		35	0.6	shd	prm	
OM10_War_DS2-3	5.6	ol gb	med	20	1.3	shd	prm, irg		50	0.5	shd	prm, elg		30	0.6	shd	prm	
OM10_War_DS2-2	6.2	ol gb	med	7	1.0	shd	prm, irg		62	0.5	shd	prm, elg		30	0.6	shd	prm	
OM10_War_DS2-1	7	ol-b gb	fin	3	1.5	shd	irg, elg	skl	55	0.4	shd	prm, elg	cc	42	0.5	shd	prm	

[a] depth of the sample within the sequence

[b] gb = gabbro, ol-b gb = olivine-bearing gabbro (<5% olivine), ol gb = olivine gabbro (>5% olivine)

[c] grain size range of the entire thin-section domain with med = medium grained (>1 - 5 mm) and fin = fine grained (>0.2 - 1 mm)

[d] modal proportions per phase in area % by visual estimation

[e] diameter or long-axis length for elongated grains averaged by the long axis measurements of ten grains per sample

[f] grain shape with shd = subhedral, ehd = euhedral

[g] grain habit with prm = prismatic, elg = elongated, irg = irregular

[h] observed special features with oc = oikocrysts, rrm = reaction rim, skl = skeletal, cc = chadacrysts

horizontal lines mark layer boundaries, dashed horizontal lines mark the transition from leucocratic layer top to melanocratic layer base

A high spatial resolution microprobe profile with a step size of 27 μm throughout the transition between layer1 and layer 2 reveals slight differences in clinopyroxene composition, indicating that clinopyroxene at the base of layer 2 is more primitive than at the top of layer 1 (Figure 6-5). The profile also reveals a slightly lower Mg# in olivine, which is consistent with core and rim analyses but does not fit the observed difference of more primitive clinopyroxene composition in layer 2. In contrast, the mean plagioclase Ca# is similar in both layers but shows significant intergranular heterogeneities. Crystallization temperatures estimated using the Sun and Liang (2017) REE-in-plagioclase-and-clinopyroxene thermometer range between 1230°C and 1300°C, with a mean of 1254°C and a one sigma standard deviation of 24°C. Considering the data and model uncertainties, which lead to uncertainties of about 50°C, we assess the crystallization temperatures as being more or less constant along the profile.
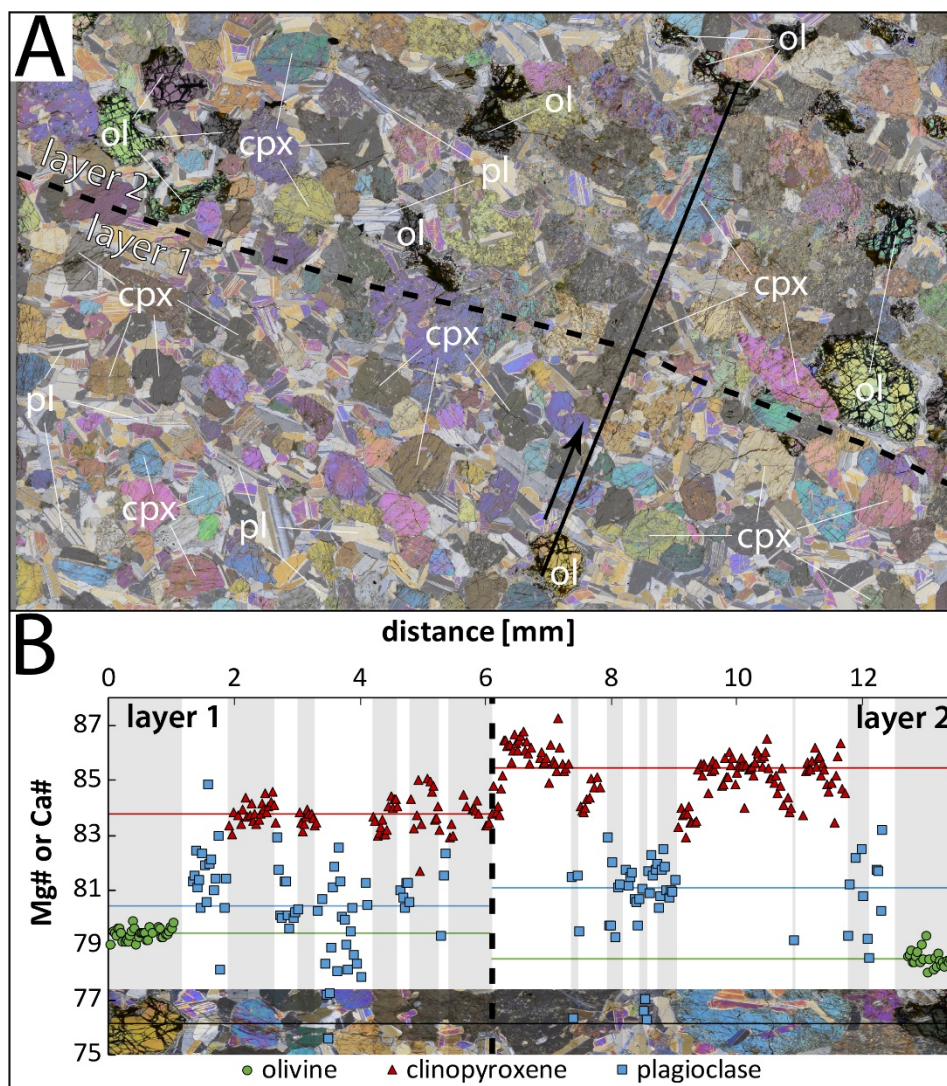
Figure 6-5   A) cross-polarized thin-section photograph of the layer boundary between layers 1 and 2 from Wadi Somerah. ol = olivine, cpx = clinopyroxene, pl = plagioclase. Black line gives the position of the EPMA profile, the black arrow marks its direction. Dashed black line marks the layer boundary deviated from modal proportions. Note the significantly increased olivine content at layer 2. Image width = 2 cm. B) Mg#s of clinopyroxene and olivine and Ca# of plagioclase plotted along the profile given in A). Green circles give olivine, red triangles clinopyroxene and blue rectangles plagioclase data. The image at the bottom shows the profile position, cropped and rotated from A). The grey and white bars symbolize individual grains. Horizontal colored lines give median for layer 1 or layer 2, respectively, with green = Mg# in ol, red = Mg# in cpx, and blue = Ca# in pl. Note its changes at 6 mm coinciding with the layer boundary in A).

A) Olivine

Wadi Somerah

B) Plagioclase

5 base   OM10-Sam_9-2
profile depth [cm] = 53.05
   n = 161
   ODF J = 3.42
   BC = 0.343
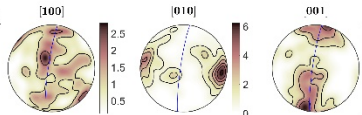
4 base   OM10-Sam_7-3
profile depth [cm] = 93.40
   n = 139
   ODF J = 8.72
   BC = 0.14
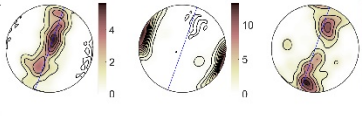
3 base   OM10-Sam_5-2
profile depth [cm] = 128.5
   n = 133
   ODF J = 6.02
   BC = 0.278
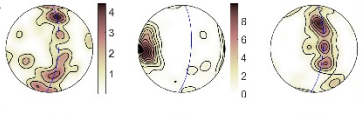
2 top *   OM10-Sam_4-3
profile depth [cm] = 180
   n = 16
   ODF J = 26.83
   BC = 0.312
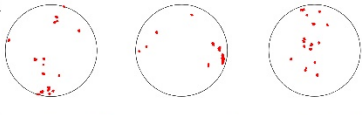
2 base   OM10-Sam_3-2
profile depth [cm] = 200
   n = 108
   ODF J = 9.32
   BC = 0.314
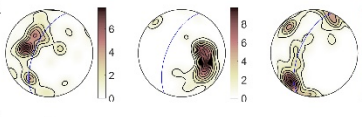
1 top *   OM10-Sam_2-2
profile depth [cm] = 221.1
   n = 24
   ODF J = 6.39
   BC = 0.266

5 base   OM10-Sam_9-2
profile depth [cm] = 53.05
   n = 1843
   ODF J = 2.55
   BA = 0.283
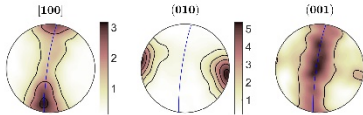
4 base   OM10-Sam_7-3
profile depth [cm] = 93.40
   n = 2639
   ODF J = 2.52
   BA = 0.394
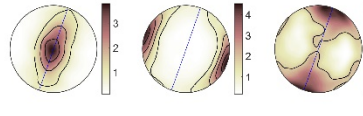
3 base   OM10-Sam_5-2
profile depth [cm] = 128.5
   n = 3692
   ODF J = 2.29
   BA = 0.472
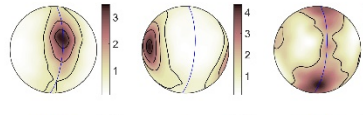
2 top   OM10-Sam_4-3
profile depth [cm] = 180
   n = 2879
   ODF J = 2.89
   BA = 0.288
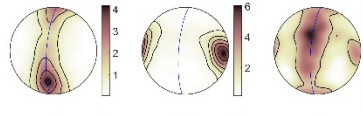
2 base   OM10-Sam_3-2
profile depth [cm] = 200
   n = 1696
   ODF J = 1.52
   BA = 0.610
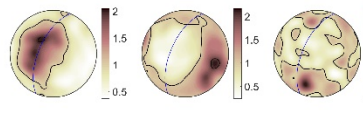
1 top   OM10-Sam_2-2
profile depth [cm] = 222.1
   n = 3804
   ODF J = 2.46
   BA = 0.406
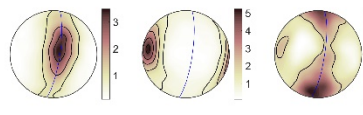
Figure 6-6   Representative pole figures for crystallographic axes [100], [010] and [001] of olivine (A) and the crystallographic axes or poles [100], (010) and (001) of plagioclase (B) in Wadi Somerah. The pole figures are arranged by their height in the sequence, text block aside gives the layer number and the sample position within the layer (base/top), the depth in the layered sequence, the corresponding BA or BC index, and the ODF J index of the sample. n is the number of analyzed grains. The blue line gives the foliation estimated from (010) of plagioclase. The star behind a layer number indicates a low number of analyzed grains (< 70). Patterns with a point of every analyzed pixel are plotted for samples with <70 analyzed grains because contoured pole figures are not significant, here. Note the differently scaled color bars.

The cooling rates obtained by Ca-in-olivine calculations using the thermometer of Shejwalkar and Coogan (2013) result in slow cooling rates between 1.2°C/kyr and 22°C/kyr with an average of 7°C/kyr (log[dT/dt]=−2.21°C ± 0.7°C yr^{-1}) and closure temperatures of 910°C to 965°C in the core. Using Mg-in-plagioclase after Faak et al., 2014 for an estimate of the cooling rate does not provide reliable results for Wadi Somerah samples due to Mg contents in plagioclase falling below the detection limit of about 0.005 wt%. The very low closure temperature of 550°C modeled for a putative MgO content of 0.005 wt% is far below the closure temperatures calculated using Ca-in-olivine and indicates much slower cooling. Before the background of the misfit between the two applied methods, and taking indicators for hydrothermal alteration of the sampled material into account, we interpret the low MgO contents in plagioclase from Wadi Somerah as result of secondary reactions (e.g., dissolution-reprecipitation) rather than solid-state diffusion as it was already observed in samples in recent lower oceanic crust by Faak et al. (2015).

The orientation of our samples was not documented during collection. Therefore, the pole figures and indicated orientations of fabric features can only be interpreted on the thin-section scale and not at outcrop or crustal scales. Nonetheless, the pole figures of olivine and plagioclase obtained by EBSD reveal remarkable observations (see Figure 6-6; all pole figures are compiled in Mock et al., 2020d). Except for the base of layer 2, which is described in more detail below, the pole figures show relatively similar features. Plagioclase shows distinct maxima in (010) coupled with weak maxima of [100]. Maxima in plagioclase [100] are most dominant at layer 5 top, layer 4 base, and layer 3, therefore indicating a slightly more linear fabric in these layers. Most olivine fabrics of this section also shows

125

well-pronounced [010] maxima and more modest [001] maxima. Olivine [100] maxima at layer 4 base, layer 2 top, and layer 1 top correlating with plagioclase [100] lineation possibly indicate some plastic deformation overprint (although layer 2 top and layer 1 top should be read with caution due to the low number of measured olivine grains). At the bases of layer 5 and layer 3, olivine [001] correlates with plagioclase [100], suggesting a weak (010) [001] olivine fabric, which can be ascribed to magmatic flow (e.g., Jousselin et al., 2012). In contrast to these more or less well-pronounced fabrics, the layer 2 base has at most only a very weak plagioclase fabric. The number of analyzed olivine grains is very low here, such that the results cannot be as representative as those of plagioclase; the pole figures show maxima in all crystallographic axes.

The nearly absent fabric at the base of layer 2 is reflected by a low plagioclase ODF J index of 1.52 (Figure 6-4 and Figure 6-6). Importantly, the minimum ODF J here correlates with the minimum in olivine Mg# and plagioclase Ca#. Furthermore, the corresponding samples are the only ones in the entire profile where the modal abundance of clinopyroxene is significantly higher than that of plagioclase and clinopyroxene grain sizes are clearly higher when compared with the surrounding tops of layers 1 and 2. Very low internal misorientations in plagioclase and clinopyroxene (GOS < 0.5° in both phases) imply that samples from Wadi Somerah did not experience significant intracrystalline deformation.

6.4.2 Wadi Wariyah

Due to the millimeter-scale layering in the sample from Wadi Wariyah, it is not possible to clearly assign crystals to either the melanocratic base of a layer or its leucocratic top. Thus, only average values are given for individual layers. The millimeter-scale layers from Wadi Wariyah contain between 3% (layer 1) and 20% (layer 3) olivine, 50% (layer 3 and 4) to 65% (layer 11) plagioclase, and 20% (layers 8 and 11) to 40% (layer 1) clinopyroxene (see Table 1 for modal proportions of every layer). Olivine is enriched in diffuse, millimeter-scaled bands defining the observed layering. All layers in the sample from Wadi Wariyah are classified as olivine gabbro (>5 modal % olivine) except for layer 1 which is classified as olivine-bearing gabbro. The EBSD phase map in Figure 6-3C shows the sample OM10-War_DS1 which covers the upper five millimeter layers from Wadi Wariyah. Note the fine differences in olivine abundance from base to top of every layer. Plagioclase shows a homogeneous, sub-millimeter, crystal long-axis length along the sequence whereas olivine grains are larger (1–1.5 mm on average). Clinopyroxene shows the largest grains in layer 1 with a 1.5-mm average size, but the grain size gradually decreases down section to a minimum of 0.5 in layer 5. Clinopyroxene size is then constant from layer 1 to layer 5. As for the Wadi Somerah samples, grain shape is commonly subhedral, olivine is irregular, whereas plagioclase occasionally forms elongated laths. Poikilitic or skeletal olivine and clinopyroxene crystals containing plagioclase indicate a similar crystallization sequence to that inferred from Wadi Somerah. The petrographic results from Wadi Wariyah are summarized in Table 1.

The microprobe data from Wadi Wariyah (see collected data in Mock et al., 2020d) reveal Mg# values of olivine and clinopyroxene ranging between 85.0 and 86.5, and 86.3 and 89.0, respectively (Figure 6-7). The Mg# of olivine slightly decreases up section with a significantly outlier at layer 6. The NiO content ranges between 0.1 and 0.2 wt%. The Mg# of clinopyroxene shows an evolution similar to that of the Mg# in olivine with nearly constant values along the sequence and with a distinct maximum of 89.0 at layer 6. The evolution of Cr_2O_3 is correlated with that of the Mg#. We observe clear trends in the TiO_2 content in clinopyroxene, which is positively correlated with Mg# in layer 6. Both Cr_2O_3 and TiO_2 show significant differences in core and rim compositions which do not, however, represent systematic zonation. The Ca# varies within a small range between 86.7 and 87.9, thus generally higher than in Wadi Somerah, with a slight increase up section from layer 2 to 11 and a marked decrease to
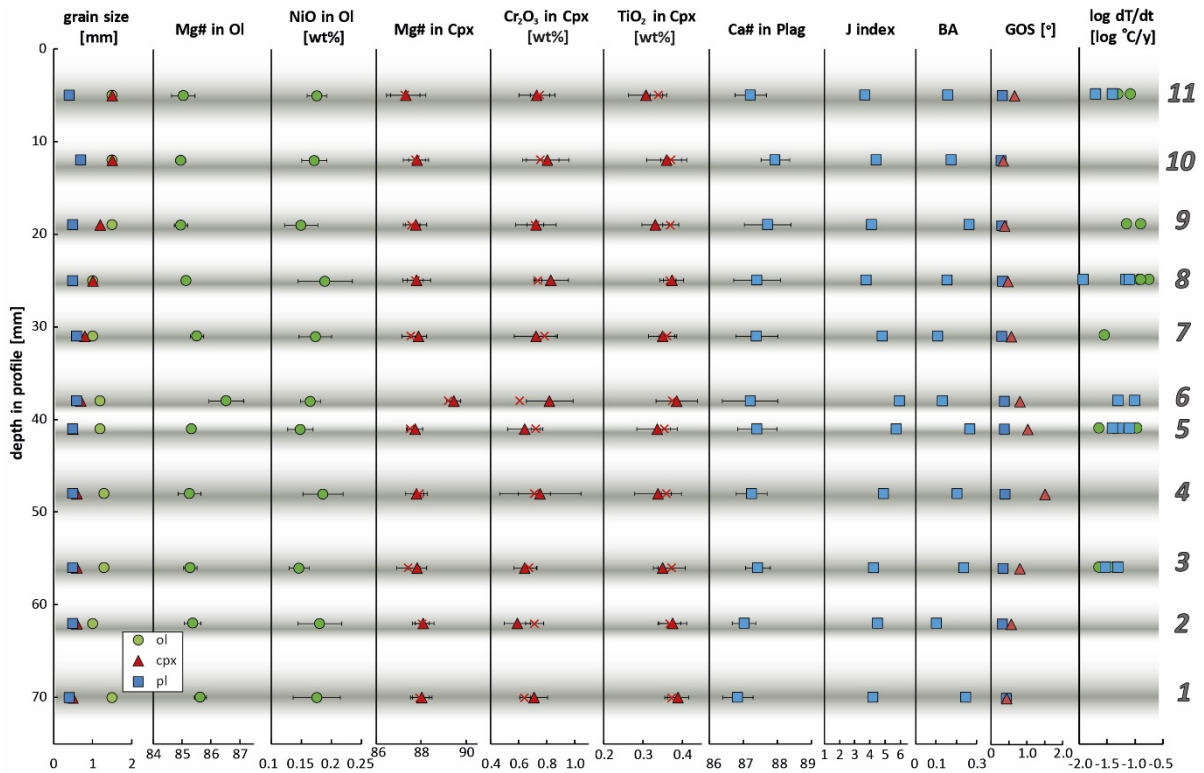
Figure 6-7 Summarized results of analyses on the mm-scale layered gabbro sequence from Wadi Wariyah. Grey numbers on the right give the layer number; gradational grey background symbolizes the layer color, most pronounced by olivine content. Closed symbols are core, crosses are rim analyses. Black bars give 1 sigma standard deviation from the mean. Mg# = Mg/(Mg+Fe)x100; molar basis, Ca# = Ca/(Ca+Na)x100; molar basis. GOS = grain orientation spread. See text for further interpretation.

layer 1. However, the Ca# does not show its maximum in layer 6, as may be expected from elevated Mg# in olivine and clinopyroxene, here.

Cooling rates in Wadi Wariyah were estimated using both Ca-in-olivine and Mg-in-plagioclase speedometers. Both methods reveal broadly similar cooling rates within a wide range of 12 to 180°C/kyr, with an average of 81°C/kyr (log[dT/dt]= −1.19 ± 0.5°C yr^{-1} using Ca in olivine) and 51°C/kyr (log[dT/dt]=−1.35°C ± 0.6°Cyr^{-1} using Mg in plagioclase) (see Mock et al., 2020d). Compared to Wadi Somerah, subsolidus cooling in Wadi Wariyah was up to one and a half orders of magnitude faster. The closure temperatures calculated for plagioclase rims vary from 850 to 930°C.

The pole figures obtained for every layer of the Wadi Wariyah profile are very similar (Figure 6-8; see compiled pole figures for Wadi Wariyah Mock et al., 2020d) with a consistent distinct maximum of plagioclase (010) and well-pronounced girdle with weak point maxima of [100]. This dominantly planar plagioclase fabric is reflected by olivine with maxima of [010] and girdles with weak point maxima of both [100] and [001] of every layer, therefore suggesting a compaction-dominated regime. Magmatic lineation, as we found indicated by olivine fabrics in Wadi Somerah, are less distinct in Wadi Wariyah, and only suggested by the correlating weak point maxima in [100] and [001] in plagioclase and olivine, respectively. These findings are well-represented by low values for the BA and the BC indices in plagioclase and olivine, respectively, of up to 0.28. Only the BC of olivine, being calculated from a relatively small number of grains, reaches 0.6 in layer 6. The ODF J index of 3.71 to 6.01 for plagioclase is slightly higher than the one from Wadi Somerah. Calculating the ODF J index for only 300 randomly chosen plagioclase grains of every sample from both locations confirmed that the increased ODF J
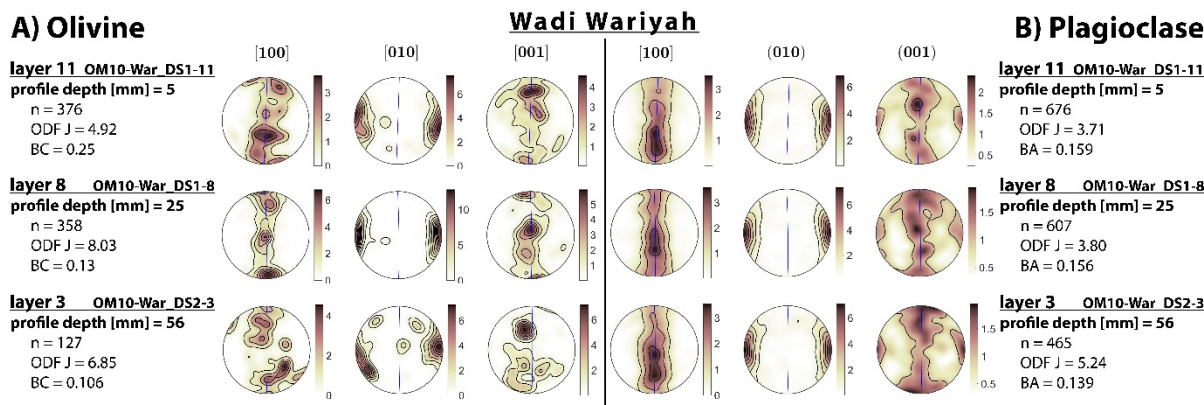
Figure 6-8   Representative pole figures for crystallographic axes [100], [010] and [001] of olivine (A) and axes or poles [100], (010) and (001) of plagioclase (B) in Wadi Wariyah. The pole figures are arranged by their height in the sequence, text block aside gives the layer number, the depth in the layered sequence, the corresponding BA or BC index, and the ODF J index of the sample. n is the number of analyzed grains. The blue line gives the foliation estimated from (010) of plagioclase. Note the differently scaled color bars.

index in Wadi Wariyah is not a mathematical artifact resulting from analyzing a smaller number of analyzed grains. Misorientation is low—similar to Wadi Somerah—with only clinopyroxene revealing slightly elevated values (GOS < 1.5°). Nevertheless, the low values also suggest weak or no impact of intracrystalline deformation in Wadi Wariyah.

6.5   Discussion

6.5.1   Our Data in the Context of Previous Studies

Data from this study can be interpreted in the context of many previous works on Oman. The layering of the oceanic crust as observed in Wadi Somerah is well-known from Oman gabbros and has already been described by many authors (e.g., Browning, 1984; Pallister and Hopson, 1981). These authors observed large-scale correlating variations in major and minor element distributions of the three near-liquidus phases olivine, plagioclase, and clinopyroxene in the crust. In contrast to these studies, our spacing is very fine with a maximum of 42 cm between two thin sections. As Pallister and Hopson (1981) and Browning (1984) already noted, we see general inter-phase correlations in terms of major element composition at the base of layer 2 in our profile from Wadi Somerah where Mg# in olivine, Ca# in plagioclase, and Mg# in clinopyroxene rims follow the same fractionation trend. A simple explanation for this behavior could be an increased amount of trapped melt within this region. A longer time to equilibrate the minerals with the trapped melt leads to more fractionated melt- and therefore evolved mineral compositions. This scenario is consistent with fast Mg/Fe diffusion in olivine (Chakraborty, 1997) equilibrating initial core-rim zonation which is hence no longer observed in our samples. In clinopyroxene, a core-rim zonation can still be observed due to slower Mg/Fe interdiffusion (e.g., Dimanov and Sautter, 2000). Simultaneous Ti enrichment in the rim is consistent with Ti diffusion being 1–3 orders of magnitude slower in pyroxenes than the diffusion of Mg and Fe (Cherniak and Liang, 2012). However, the coupled Na + Si/Ca + Al diffusion in plagioclase is very slow (e.g., Morse, 1984) implying that the observed lack of zoning is primary and plagioclase crystallization did not occur within a trapped liquid. Apart from at the base of layer 2 base, our data do not show significant trends, and no further inter-phase correlations are observed, in part due to analytical uncertainties being large with respect to the very limited compositional variation present at Wadi Somerah (Figure 6-9). It can be argued that inter-phase correlations are overprinted by post-cumulus percolation of evolved melt

interacting with the cumulates (e.g., Jansen et al., 2018; Lissenberg et al., 2013), but indicators for such processes, for example, strong enrichment of trace elements from core to rims in clinopyroxene, are only weakly developed in our samples. We found a maxi-mum enrichment of Zr in the rim by a factor of 2.4 compared to its core in a single sample. Other trace elements show weaker rim/core enrichments, with observed factors reaching a maximum of 1.6. Also, the rim/core ratios of Zr/Nd and Ce/Y give relatively homogeneous element distributions with values up to 1.6 and down to 0.8, respectively. In contrast, rim/core enrichment factors of up to 15 were reported for deep gabbros from Hess Deep where melt percolation is assumed to have taken place (Lissenberg et al., 2013). However, interpreting these data needs consideration of diffusivity of these elements which tends to balance differences and therefore could weaken the initial degree of zonation. As Sun and Liang

Figure 6-9 Ca# ((Ca/Ca+Na)x100; molar basis) in plagioclase and Mg# ((Mg/Mg#Fe)x100; molar basis) in olivine plotted versus Mg# in clinopyroxene. Blue rectangles are plagioclase data, green circles are olivine data. lighter colors belong to samples from Wadi Somerah, darker to Wadi Wariyah. Error bars symbolize one sigma standard deviation from the mean.

(2017) point out, diffusion of REEs in clinopyroxene and plagioclase is significantly slower than Mg diffusion in both minerals. This first explains why REE zonation in clinopyroxene is more systematic than the zonation of Mg (Figure 6-10) and second indicates that initial zonation was not much stronger than the zonation we observed in our samples. Taking the cooling rate of up to 22°C/kyr into account which limits the efficient equilibration of REEs due to their low diffusivities (e.g., Sun and Liang, 2017), enrichment factors of ~15 as found by Lissenberg et al. (2013) at Hess Deep are absent in our profile from Wadi Somerah. Therefore, we assume that the influence of percolating porous melt was very limited in our samples.

Values of differentiation indices in Wadi Wariyah close to the MTZ are lower than typical numbers from mantle olivines in Oman (Fo > 90; e.g., Tamura and Arai, 2006), indicating that the melt has undergone some crystallization since leaving the mantle. Defining the crustal region where differentiation of the melt occurred is, however, beyond the scope of this study. Our data are in good agreement with most of the fractionation indices obtained by Korenaga and Kelemen, 1997 who sampled modally layered gabbros from the MTZ. However, in contrast with our results, they also found that phase compositions correlated with modal proportions. Since these variations occur on a millimeter to centimeter scale, they conclude that the modal layering they observed cannot have formed by crystal settling as this would have led to relatively high porosities eliminating fine chemical variations by equilibration with interstitial melt.
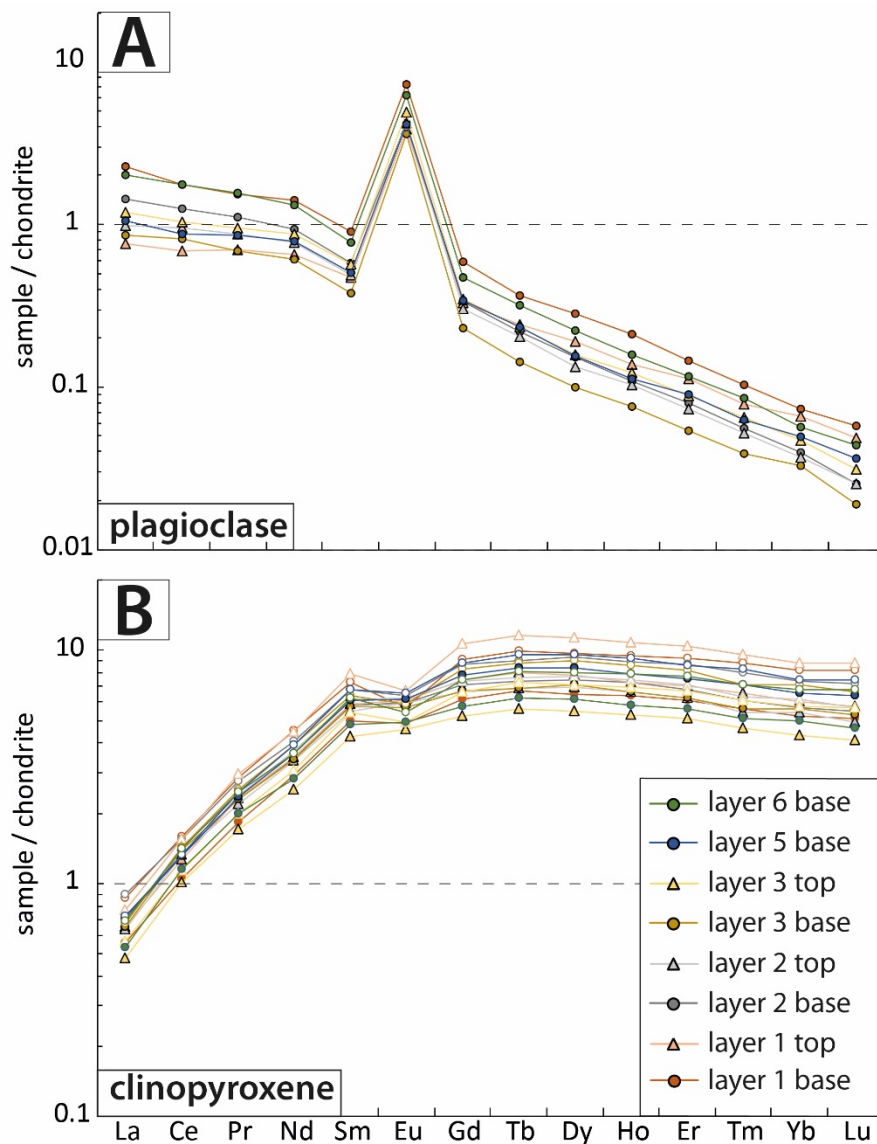
*Figure 6-10 Chondrite-normalized rare earth element data in plagioclase (A) and clinopyroxene (B). Chondrite values from **McDonough and Sun (1995)**. Circles symbolize data from layer bases, triangles from the tops. Closed symbols are core, open symbols are rim data.*

6.5.2 The Formation of Igneous Layering in Profiles From Wadi Somerah and Wadi Wariyah

Layer-forming processes have been reviewed in detail byNaslund and McBirney (1996) and more recently Namur et al. (2015) who also argued that they can generally be separated into dynamic (i.e., occur during filling or crystallization of a magma chamber) and non-dynamic (i.e., rapid changes in intensive conditions of crystallization) layer-forming processes and that they range from physical processes (e.g., gravitational sorting) to tectonic (e.g., seismic shocks) and chemical ones (e.g., dissolution-precipitation). Many of these processes can occur in any given magmatic system, and none of them are thought to be exclusively responsible for any distinct type of layering. We provide a compilation and brief evaluation of 31 layer-forming processes (according to Namur et al., 2015) that are potentially relevant to our samples in the electronic supplement, and we discuss the processes which find at least partial support in our data in detail below. Providing a full overview of all layer-forming processes is, however, beyond the scope of this work.

6.5.2.1 Magma Injection

Correlated changes in major mineral compositions and crystallographic preferred orientations (Figure 6-4) in layer 2 from Wadi Somerah indicate that the formation of this particular section of the profile was accompanied by processes affecting the mechanical and chemical properties of the rock. One explanation considered above invokes an increased amount of trapped melt at the base of layer 2 leading to more fractionated minerals. An alternative explanation for a compositional shift toward more primitive phase compositions at the top of layer 2 could be the influx of more primitive melt, provoked by a replenishment process. We see evidence for such an event in the different phase compositions between the base and the top of layer 2: while the compositions follow a clear fractionating trend from layer 1 top to the base of layer 2, with decreasing Mg# correlating with decreasing NiO in olivine, decreasing Ca# correlating with increasing Ce in plagioclase, and decreasing Mg# correlating with increasing TiO_2 and Cr_2O_3 contents at the rim of clinopyroxene, the compositions at the top of layer 2 show more primitive signals. The Mg# of olivine is increased compared to the base of layer 2, the Ca# of plagioclase as well which correlates with a decreased Ce content. Also, the rim values of TiO_2 and Cr_2O_3 in clinopyroxene decreased from the base of layer 2 toward its top, indicating that the top of layer 2 crystallized from a more primitive melt than the base of this layer.

A remarkable change in rock fabric occurring between the base and the top of layer 2 (i.e., no fabric at the base, plagioclase (010) maximum with [100] girdle, copied by [010] and [001] of small amounts of analyzed olivine; Figure 6-6A, see pole figure compilation in Mock et al., 2020d) coincides with the shifts in mineral compositions described above. Although an increased amount of trapped melt at the base of layer 2 can explain most of the observed variation in phase compositions, the absence of a clear rock fabric appears more consistent with the hypothesis that the base of layer 2 crystallized in a system with only limited amounts of melt where solid phase mobility was reduced. However, the magmatic fabric at the top of the same layer indicates a higher liquid/solid ratio, which would in turn result in higher crystal mobility enabling crystals to orient and form the observed foliation. We therefore argue that the shift toward more primitive phase compositions at the top of layer 2 could also be interpreted as indicators for a magma replenishment affecting both chemical and textural features of the sample. If this interpretation is correct, we infer that localized melt injections are possible within the lower crust.

If magma replenishment occurs within the lower oceanic crust, is it able to trigger modal layering formation by resetting the crystallization sequence? Correlating every layer with an individual pulse of fresh magma would create correlations between phase compositions and the layer height and

therefore, in case of modal layering, also between phase compositions and mineral abundances. This was observed by Korenaga and Kelemen (1997) who found that olivine-rich sections were more primitive in terms of Fo in olivine and partially also Cr in clinopyroxene. They concluded that the melt lens composition could be reset by expulsion of melt through hydrofractures and repetitious expulsion and replenishment could create modal layering. While this interpretation is relevant to their data, it is inconsistent with the absence of layer-correlated compositional trends from our profiles. Although magma replenishment can cause chemical and textural variability within the lower crust, it does not seem to have driven the formation of modal layering in the samples we have studied.

6.5.2.2 *Gravitational Sorting by Crystal Settling*

The concentration of the denser phases—olivine and clinopyroxene—and the deficit of plagioclase at the base of each layer lead to the intuitive suggestion that gravitational sorting plays a key role in the formation of the modal layering in the Wadi Somerah sequence. Theoretically, an increased water activity expected for Oman paleo-magmatism (e.g., MacLeod et al., 2013; Müller et al., 2017; Pearce et al., 1981) could restrict plagioclase nucleation and therefore result in layers being depleted in plagioclase (or even wehrlitic layers which we do not observe in our profiles; e.g., Feig et al., 2006). However, the water content of 0.4–0.8 wt% estimated for the melt beneath the Oman spreading center by Müller et al., 2017 is insufficient to fully suppress plagioclase nucleation in basaltic melts (Feig et al., 2006; Gaetani et al., 1993). Furthermore, poikilitic olivine and clinopyroxene hosting plagioclase chadacrysts makes it clear that plagioclase crystallization occurred—at least in part—simultaneously with olivine and clinopyroxene.

Korenaga and Kelemen, 1997 conclude that crystal settling could not have formed modal layering in the Maqsad area since the large porosity in a cumulate formed by crystal settling was inconsistent with the millimeter-scale modal variation they observed in their samples. However, such systematic small-scale correlations between modal proportions and phase compositions have not been observed in our samples. Nonetheless, if a magmatic system contains enough melt to mobilize solid particles, density-controlled phase segregation and therefore modal layering may be formed. However, if density-controlled phase segregation occurs, a process is required to explain the rhythmic layer sequence that we observe. Possibly, every layer could represent a completely crystallized individual sill (cf., the sheeted sills model; e.g., Kelemen et al., 1997). However, the crystallization from individual sills would be expected to result in greater chemical differences between the layers, demanding a physical barrier between layers of sill intrusion into already solidified hence colder surrounding gabbro. The limited variation in our petrological and chemical data does not agree with every layer having formed from a different sill. Sparks et al. (1993) instead suggested that intermittent convection could form cyclic layering in a magma chamber: At a high convection velocity, crystals can be kept in suspension and will settle down as soon as the convection velocity decreases or stops. Following Stoke's law, denser crystals will settle faster and are therefore accumulated at the base of the convective subunit. Repeated changes in convection velocity would lead to rhythmic deposition of several layers.

In order to evaluate the potential role of gravitational sorting on layer formation, we modeled the settling velocities of olivine, plagioclase, and clinopyroxene. As parental melt composition, we considered the average Samail melt composition estimated by Pallister and Gregory (1983) with water contents between 0.4 and 0.8 wt% (MacLeod et al., 2013; Müller et al., 2017). We used the models of Giordano et al. (2008) and of Ueki and Iwamori (2016) to estimate the viscosity and the density of the melt, respectively, at a pressure of 0.2 GPa and in a temperature range of 1230°C–1300°C, according to the calculated crystallization temperatures given by the Sun and Liang, 2017 REE thermometer. The resulting liquid parameters were applied to the Stoke's law equation, taking into account the densities

of olivine, plagioclase, and clinopyroxene as well as their estimated grain sizes. The results show that plagioclase would float (or "rise" with a velocity in the range of 10^{-6} to 10^{-7} ms^{-1}) in the liquid, while olivine and clinopyroxene would sink with a velocity in the range of 10^{-3} to 10^{-5} ms^{-1}. Similar results are given considering a normal mid-ocean ridge basalt (NMORB) melt composition of Gale et al. (2013). This shows that intermittent convection could provoke the formation of cyclic layers by gravity settling. However, floating of plagioclase would then lead to cumulates only containing olivine and clinopyroxene with small amounts of interstitial plagioclase. The floating plagioclase would be expected to form anorthositic layers at the top of a magma reservoir which, as the olivine-clinopyroxene layers mentioned before, we do not observe in our sections. Moreover, taking grain size as a key parameter in Stoke's law into account leads to the assumption that clear coarsening of all phases toward the layer bases should be observed if the crystals uniformly settled down in a magma chamber. This is not the case (except for layer 2), which further suggests that crystal settling from a melt-rich magma is not the dominant layer-forming process.

6.5.2.3   Gravitational Sorting by Density Currents

As described in the previous section, crystal settling would lead to clear trends in both the modal proportions and the grain size distribution of each layer. Those could, however, be obscured during layer formation if the gravitational forces are overprinted by dynamic processes. Considering that a given magma lens crystallizes first at its margins and roof, highly crystalline parts from the roof or margins of the magma reservoir may become unstable and slump downward (Figure 6-13A). The concept of density currents resulting from this mechanism and forming modal layers was first proposed by Irvine (1980). Irvine et al. (1998) then applied the same concept to modal layer formation in the Skaergaard intrusion in Greenland, and Vukmanovic et al. (2018) recently illustrated it in details. Since evidence for density currents is mostly observed in dykes and sills (Namur et al., 2015), they may also occur in the lower oceanic crust. Similar to submarine turbidites, crystals will be sorted in such a current by density and grain size (Irvine et al., 1998), leading to both modal and grain size layering (Figure 6-13A, t = 1). As shown above, plagioclase should float in a basaltic magma and is therefore expected to be expelled from the olivine-plagioclase-pyroxene-liquid system. However, consideration of other processes proposed by Irvine et al. (1998) makes clear that the mobility of plagioclase in a mafic magma—and even more in a current of crystal-laden magma—is not only controlled by density:

(1) Before or during slumping of such a current, crystals might form aggregates or plagioclase can be enclosed in poikilitic clinopyroxene. Both aggregates and poikilitic grains are able to carry plagioclase downward, independently of the negative buoyancy of pure plagioclase in mafic melt. (2) Crystallization of the interstitial liquid will decrease its porosity and, therefore, can be expected to limit plagioclase buoyancy.(3) Once deposited, the yield strength of the residual liquid in the deposited layer will rapidly increase during stagnation (Murase and McBIRNEY, 1973), hampering crystal movement within the current. (4) In case that plagioclase buoyancy overcomes the yield strength, ongoing deposition of density currents will also prevent plagioclase floatation. Additionally, it remains possible that granular plagioclase crystallized in situ after deposition of a density current.

The structure of the outcrop in Wadi Somerah (Figure 6-11) indicates that layers formed by a dynamic process: Although the layering appears nearly horizontal and sub-parallel from the southern point of view (Figure 6-11C), looking onto the western flank of the outcrop reveals highly disturbed layers with sedimentary structures (Figure 6-11A). This appearance can be explained by post-cumulus shear strain deforming the cumulates. Structural maps of the Oman ophiolite (Nicolas et al., 2000) reveal E-W oriented lineations in the gabbros of this region, meaning that the lineation would be perpendicular to the western outcrop face. However, field measurements would be required to develop these ideas further. Discordant layers cross-cutting each other (Figure 6-11B) may, however,

be an indicator for slumping currents of crystal-laden magma, eroding underlying layers while moving downward.

Our petrological data suggest (except for the base of layer 2) only weak inter-phase compositional correlations (Figure 6-4and Figure 6-9) and are consistent with a scenario where crystals of slightly different compositions become re-sorted and form a cumulate with limited homogeneity in terms of major and minor element distributions. Trace elements also imply that there are no internal systematics whether or not the top of a layer is more fractionated than its base (Figure 6-10). Korenaga and Kelemen (1997) argue that density currents (or other concepts for layer formation requiring thermal gradients, such as oscillatory nucleation or double-diffusive convection) are not applicable to
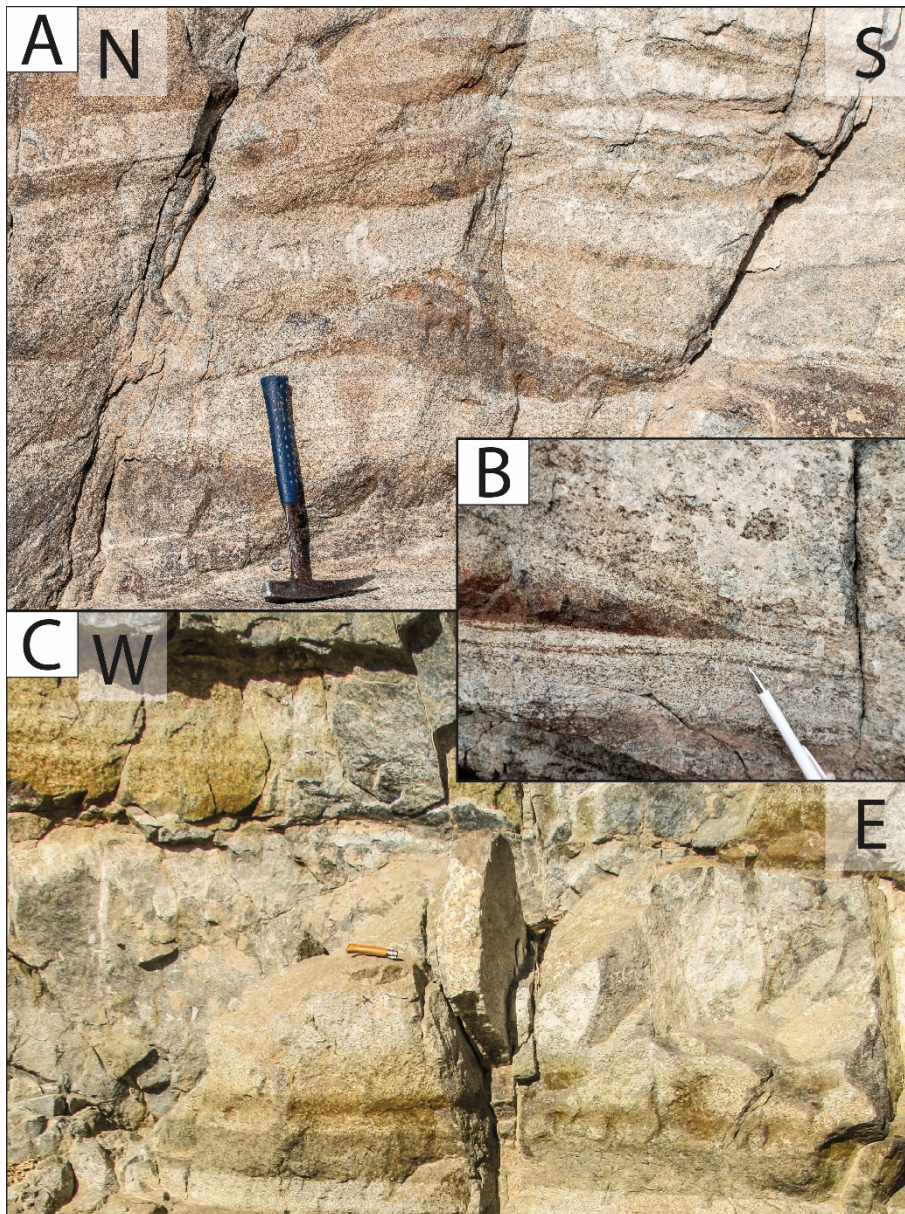
Figure 6-11 A) cm- to dm-scaled disturbed modal layering at the western flank of the Wadi Somerah outcrop. B) cm-scaled layer cross-cutting a layer deposited before at the southern front of the outcrop in Wadi Somerah. C) dm-scaled laminar horizontal modal layering at the southern front of the Wadi Somerah outcrop. Knife as scale bar with a length of about 10 cm. Orientation directions given in black in A and C. Note the significant difference in the appearance between A) and B), and C).
Photographs by D. Mock and P. E. Wolff

the modal layers in their samples due to the temperature of the system being buffered by the large-scale thermal evolution beneath the ridge. In this kind of thermally buffered system, they assume slow cooling of <1°C/kyr and thermal gradients of less than 1°C from the margin to the core of a melt sill, which raises the question whether crystallization occurs preferentially at the margins of a lens. These conditions may indeed be applicable to the gabbroic sills of the MTZ. However, the outcrop in Wadi Somerah is located in the middle of the layered gabbro sequence. Maclennan et al. (2005) modeled the thermal evolution beneath a ridge for the scenarios of both a gabbro glacier and a hybrid model combining features of subsiding crystal mush and in situ crystallization. They have shown that in both cases the middle of the lower crust is cooler than the MTZ on-axis. Applied to our samples from the mid-lower crust in Wadi Somerah, we therefore assume that they might have been subjected to lower temperatures and less thermal buffering than the samples from the MTZ investigated by Kelemen et al., 1997. The sub-solidus cooling rates estimated for Wadi Somerah indicate cooling of about $\log[dT/dt]= -2.21 \pm 0.7°\mathrm{Cyr}^{-1}$, being also faster than the very slow cooling assumed by Korenaga and Kelemen (1997), at least in the sub-solidus. It might therefore be possible that crystallization preferentially occurred at the margins of a melt lens.

Once the crystals have formed along the margins of a magma chamber, a topographic gradient is required for the crystal mush to slump down. Pallister and Hopson (1981), who already observed cross bedding and slump structures, found rare evidence for steep floor slopes during crystal accumulation. However, they cite Brown (1956) among others, who considered an angle of 15° being the maximum angle of repose for ultra-mafic cumulates of the Rum intrusion. We do not know the geometry of the magma reservoir where the samples from Wadi Somerah crystallized. Nonetheless, from the floor to the wall of such a reservoir, the increasing slope must have exceeded a critical angle of repose at some point where slumping of previously crystallized material might have been initialized. Slumping crystal-laden magma currents could benefit from slightly dipping chamber floors that might extend their run out distances.

In terms of rock fabrics, density currents would align minerals along a linear fabric parallel to the magmatic flow. Although indicators such as aligned and elongated olivine crystals are observed in the field, the degree of lineation obtained by EBSD is relatively weak in Wadi Somerah and is in some cases superimposed by planar fabrics, possibly caused by compaction in response to deposition by a current. Interpreting these fabrics, however, requires consideration of dynamic conditions in an assumed density current. If an already relatively solidified crystal-laden current slumps down, it is unclear whether crystal alignment occurs efficiently or is hampered due to an absence of grain mobility. Therefore, the presence of different degrees of linear fabrics does not necessarily rule out a role for density currents. Considering that field lineations are relatively homogeneous over large scales (e.g., Nicolas et al., 2000; Nicolas et al., 1988) leads to the question of whether their homogeneity is consistent with magmatic currents. In a melt lens, they are assumed to move from all sides which in turn would lead to variable lineations. However, depending on the shape of the magma lens, there might be a preferred flow direction. Assuming an elongated chamber being aligned sub-parallel to the spreading axis would be consistent with lineations being sub-perpendicular to the ridge axis at the global ophiolite scale (Nicolas et al., 2000). These workers moreover point out that on a smaller scale "a given outcrop often yields opposite shear directions" which could be formed by internal shear within magma currents slumping from opposite chamber walls.

6.5.2.4   Simple Shear

Beside internal shear induced by the movement of a magma current, simple shear induced by external forces (e.g., mantle movement) may occur and deform the cumulate material. Simple shear as a post-cumulus process is able to develop weak heterogeneities in a massive rock into lenticular

bands (Ramsay and Graham, 1970). By studying layered gabbros in the MTZ of the Oman ophiolite, Jousselin et al. (2012) identified simple shearing, induced by lateral movement of the asthenospheric mantle, as a potentially important process for the formation of modal layering in lower oceanic crust. As Nicolas (1992) already suggested, shearing is able to affect not only the lowermost crustal section near the MTZ but also the overlying layered gabbro sequence where they also found indicators for simple shearing. Although in some layers from Wadi Somerah olivine reveals a magmatic fabric, possibly formed by slumping currents (e.g., base of layer 5), a lineation defined by [100](010) in olivine (e.g., at the bases of layers 1 and 4) suggests a plastic deformation overprint of the highly solidified crystal mush consistent with post-cumulus shearing. Also, the deformation of layering as observed at the western flank of the outcrop in Wadi Somerah (Figure 6-11A) is likely to have occurred as a result of simple shear (e.g., Jousselin et al., 2012; Nicolas, 1992). Moreover, the paucity of crystal-plastic deformation cannot be seen as indicator for the absence of shear, since the presence of a small amount of interstitial melt may prevent crystal-plastic deformation (e.g., Nicolas and Ildefonse, 1996). Nonetheless, the asymmetric appearance of sharp layer bases and gradational tops in Wadi Somerah appears unlikely to have formed by externally induced simple shear, which would be expected to create olivine-rich bands without systematically gradual or sharp boundaries between neighboring layers. We therefore conclude that simple shear emphasizes heterogeneities that are already present within lower crustal rocks but that it cannot have created much of the modal layering in Wadi Somerah.

In contrast with Wadi Somerah, the contacts between millimeter-thick layers in Wadi Wariyah are symmetric with fine layers being enriched in olivine. Its proximity to the MTZ also suggests that mantle-induced shearing could have deformed the material. Moreover, olivine crystals are partially elongated, indicating significant shearing that has deformed the rocks. It is unclear, however, whether the shearing was sufficient to form the well-defined millimeter layers. According to the study of Jousselin et al. (2012), the fabrics of our sample with (010) maxima in both olivine and plagioclase, and girdles in [001] and [100], respectively, belong to the type 2 samples which represent the beginning stage of deformation. Their description of type 2 layers, "Type 2 shows weakly defined layers which can be followed over few centimeters.", however, is inconsistent with the appearance of the layering in Wadi Wariyah. From a macroscopic perspective, the layering observed here fits better the type 4 deformation in Jousselin et al.: "[…] type 4 correspond to the presence of very well-defined layers with sharp and straight limits." (Compare Figure 6-2C and D of this study with Figure 2 in Jousselin et al., 2012). However, the linear fabrics defined by Jousselin et al. (2012) for type 4 gabbros are defined by well-pronounced maxima in both [100] and (010) of olivine and plagioclase which are less clearly pronounced in our case. The less pronounced lineations in our samples could be an effect of the sample preparation which was not always performed along the X-Z plane of the sample. If this is the case, simple shear might have been a major process to drive the formation of layering in Wadi Wariyah.

6.5.2.5 Diffusion-Controlled Nucleation and Ostwald Ripening

Millimeter-scale modal bands like those observed in Wadi Wariyah can be formed under specific conditions at crystallization fronts in a cooling system, that is, at the top of a crystal mush (McBirney and Noyes, 1979): Elements diffuse through the melt toward growing crystals, and the diffusion timescale therefore increases with increasing distance from the interface, that is, the crystallization front. This may lead to a trend of increasing compatible element concentration with distance from the interface, which can ultimately provoke mineral supersaturation a certain distance ahead of the crystallization front. A new layer of crystals thus nucleates in this region of supersaturation that is separated from the underlying crystallization front, and the diffusive exchange between solid and liquid starts again (see Figure 6-13B, t = 2 for details). The potential of this process to form rhythmic layering, compare Liesegang banding, was experimentally demonstrated in saline solutions by
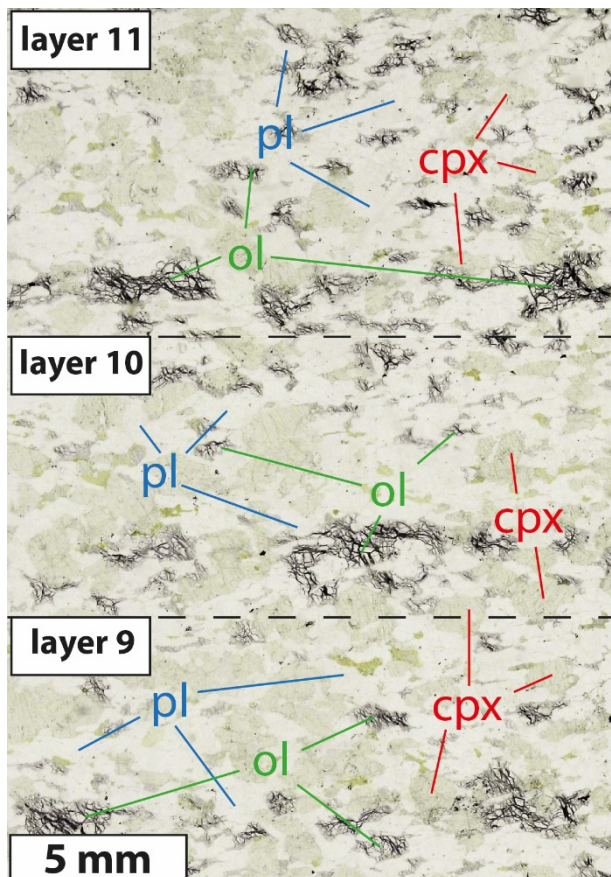
Figure 6-12 Thin-section photograph of sample OM10-War_DS1 from Wadi Wariyah covering the upper three fine layers. Note diffuse bands with increased olivine abundance and the olivine grains being coarser within these bands than in the regions depleted in olivine. See text for further discussion.

McBirney and Noyes (1979) and Fisher and Lasaga (1981). They concluded that their experimental results could be applied to any crystallizing system and therefore could be a plausible explanation for millimeter-scale Liesegang bands. McBirney and Noyes (1979) pointed out that this process is also able to take place in magmatic systems when cooling and crystallization are faster than diffusion and thereby enable the cyclical formation of new layers. The cooling rates estimated here are calculated for a sub-solidus regime. Therefore, we cannot state whether cooling in the supersolidus also occurred atypically fast. If that was the case, mass diffusion potentially was not able to keep pace with heat diffusion leading to cyclic nucleation of olivine. This is contradictory to conclusions of Korenaga and Kelemen (1997) who excluded cyclical nucleation as layer-forming process within the MTZ due to the very slow cooling of less than 1°C/kyr buffered by the large-scale mid-ocean ridge thermal evolution. Our data which show mineral compositions with only small variations—except for layer 6—could be consistent with the cyclical nucleation model. However, the observed outlier in terms of Mg#s in olivine and clinopyroxene in layer 6 is difficult to integrate into the proposed model. There is no textural evidence for a late stage intrusion observed. Potentially, the best explanation is a change in melt composition by a small melt influx, although it is unclear why surrounding layers are unaffected. While our data can only give indirect evidence for the possibility of cyclical nucleation, we found evidence for the process of Ostwald ripening that was proposed by Boudreau (1995) to explain fine layering in silicate rocks: Due to their greater reactive surface in relation to their volume, smaller crystals have a higher solubility than larger ones (e.g., Boudreau, 1995). Larger crystals, that is, crystals that nucleated earlier, will therefore grow faster on the expense of smaller grains in their proximity (Figure 6-13C). In the sample from Wadi Wariyah we see that the olivines in the olivine-rich bands are significantly larger than those in the olivine-poor bands (Figure 6-12). If initial nucleation of olivine was heterogeneous (e.g., cyclical nucleation as suggested above), the heterogeneous grain size distribution between olivine-rich and olivine-poor bands indicates that Ostwald ripening occurred and emphasized initial heterogeneities in olivine nucleation forming significant millimeter-scaled differences in olivine abundance and its grain size.
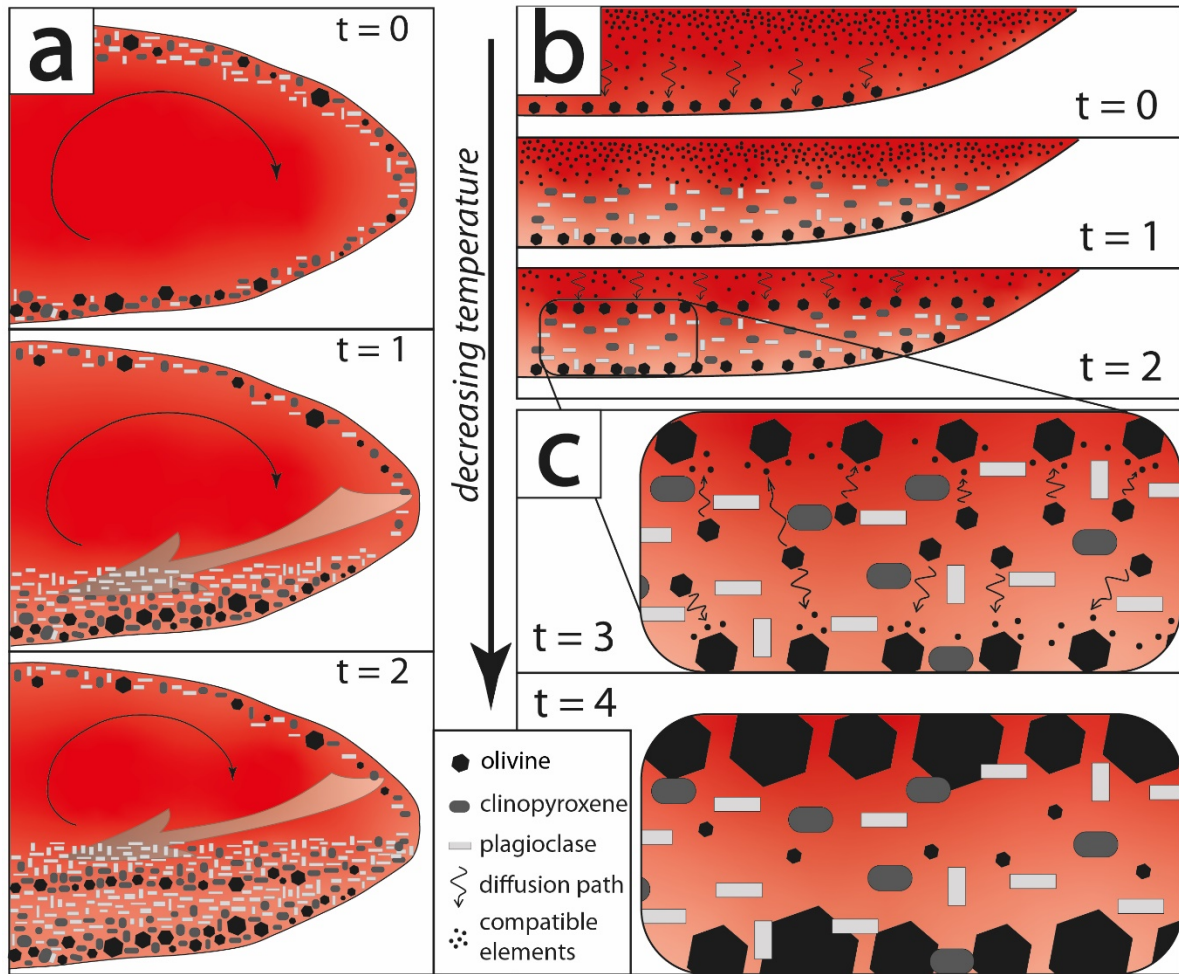
Figure 6-13 Igneous layer-forming processes being in agreement with our data from Wadi Somerah and Wadi Wariyah. a) close-up into an active melt sill showing schematically the process of density currents forming modal layering as we propose for Wadi Somerah resulting in dm-scale layering. Black thin arrows indicate possible convection cells, grey arrows mark slumping path of a density current. See text for details. b) close-up into a fast-cooled melt sill where mm-scale layers form due to oscillatory nucleation. Small black dots symbolize the abundance of compatible elements, thin black arrows mark their diffusion paths towards the crystallization front. See text for details. c) zoom into mm-layer formed by the process in b). Ostwald ripening leads to coarsening of larger crystals, smaller crystals dissolve in the melt due to their higher reactive surface emphasizing modal heterogeneities. Small black dots symbolize the abundance of compatible elements diffusing from small to larger grains, as indicated by the black arrows. See text for details. Black polygones represent olivine, dark grey ellipses clinopyroxene, and light grey bars plagioclase grains. t = x in every figure gives relative point in time of the sequence.

6.5.3 Cooling Rates—Implications for Deep Hydrothermal Cooling

Both the Ca-in-olivine and the Mg-in-plagioclase geospeedometers indicate that the material from Wadi Wariyah, which formed near the MTZ, cooled up to 100 times faster in the sub-solidus regime than the mid lower crustal gabbros from Wadi Somerah. This is a counterintuitive and remarkable observation which strongly contrasts with the decreasing cooling rates down section calculated by Coogan et al. (2002a) in the Nakhl-Rustaq massif of the Samail ophiolite and by Faak et al. (2015) at the EPR. The fast cooling of up to 120°C/kyr in Wadi Wariyah appears to be consistent with results from VanTongeren et al. (2008) who also calculated cooling rates in the range of up to 50°C/kyr close to the MTZ. We estimated much slower cooling ($\log[dT/dt]= -2.21°C \pm 0.7°C\ yr^{-1}$) in the mid-level gabbros from Wadi Somerah where VanTongeren et al. found the cooling being faster than

at the MTZ. However, significant differences in the approach (i.e., high resolution rim-core-rim diffusion profiles in our study, core/rim analyses averaged per thin-section in VanTongeren et al.) make the comparability of the two studies difficult.

Unexpected features of the cooling rates from Wadi Wariyah indicate that these results have to be handled with caution. Mg-in-plagioclase and Ca-in-olivine give similar and consistent results. However, it is questionable whether these reflect an undisturbed sub-solidus cooling or if the cooling has undergone late stage perturbations. Several processes appear plausible to explain the fast cooling close to the MTZ and in our sample from Wadi Wariyah in particular. Nicolas et al. (1994) and Ildefonse et al. (1995) have shown that active mantle upwelling has also affected the lowermost gabbros from the Samail ophiolite. If the upwelling leads to an efficient transport of the MTZ gabbros away from the ridge axis, gabbros from Wadi Wariyah, that is, close to the MTZ, can be assumed to cross isotherms and therefore cool faster than the mid-level gabbros from Wadi Somerah which might be less affected by active mantle upwelling.

Deep hydrothermal circulation that can efficiently transport heat away from the system (e.g., Zihlmann et al., 2018) could also be a potential explanation for the fast cooling of the lowermost gabbros. Hydrothermal circulation at high temperatures in Wadi Wariyah is supported by observations in a well-studied outcrop ~300 m south of the locality where our fine-layered sample was taken: This outcrop of layered gabbros is characterized by a complex system of hydrothermal veins containing brown pargasitic amphibole and green magnesio-hornblende which have formed under high to very high temperatures (850°C and 1030°C; Bosch et al., 2004; Wolff, 2013). Very high Cl contents in hastingsites and pargasites within these veins (up to 5 wt%, Currin et al., 2018b) provide evidence for the presence of highly saline, seawater-derived fluids at depth. Evidence for deep hydrothermal activity at high and very high temperatures in layered gabbros from fast-spreading systems has been reported in several studies (Bosch et al., 2004; Garrido et al., 2001; Koepke et al., 2014; Nozaka et al., 2016). Coogan et al. (2006) outlined that hydrothermal activity is channeled to focused fluid flow zones, hence not affecting the entire crust homogeneously. It seems plausible that the sample from Wadi Wariyah represents a horizon where efficient hydrothermal cooling was enhanced, leading to higher cooling rates. In contrast, other stratigraphically higher regions were possibly less affected by focused cooling, as recorded in the Wadi Somerah section.

Further observations from the Wadi Wariyah indicate that the gabbros have been affected not only by hydrothermal fluids but also by some late stage intrusive events. A large wehrlite intrusion regarded as typical late stage event close to the locality where our sample was taken could have re-heated the surrounding solidified gabbro. Further evidence for a re-heating event are late stage gabbroic veins in the outcrop where also high-temperature hydrothermal activity was described (e.g., Bosch et al., 2004; Wolff, 2013). The angular shape of those veins indicates that the host rock they intruded was already highly solidified. Re-heating, either by a wehrlite intrusion or by gabbroic veins, could have led to a temporarily increased Ca or Mg solubility in olivine and plagioclase, respectively. Fast cooling, as expected after the re-heating of a relatively small volume, would record the very high Ca and Mg concentrations in both phases. Alternatively, our sample could represent a part of a large late-stage intrusion that itself cooled very quickly after entering the host rock and therefore preserved high Ca and Mg contents in olivine and plagioclase, respectively. The latter alternatives appear the most plausible, taking the presence of late stage intrusions and the generally very complex geological environment in Wadi Wariyah into account (Figure 6-1B). The hypothesis mentioned above clearly reflect scenarios which are untypical for "normal" lower gabbros in the Oman ophiolite, implying that the investigated sample is not representative for typical lower, layered gabbros in Oman. However, validating these models is impossible with the data we obtained. Nonetheless, we would like to emphasize that while the high cooling rates estimated for Wadi Wariyah may not be representative

for the lowermost oceanic crust as a whole, they do demonstrate that lower crustal rocks locally can cool very rapidly in some circumstances.

6.6   Conclusions

We sampled two short sequences of layered gabbros from the plutonic oceanic crust of the Oman ophiolite with a high spatial resolution. One sequence from Wadi Somerah sampled layered gabbros with decimeter-scale modal layering from the mid of the lower crust, while another from Wadi Wariyah sampled gabbros from about 100 m above the MTZ representing millimeter-scale modal layering at the base of the crust. The two sequences show significant differences in terms of layer properties, mineral compositions, microstructural features, and cooling rates. While layering in the mid-lower crustal sequence (285 cm total length) is characterized by decimeter-scale modal layers with sharp base contacts and gradually decreasing olivine contents up section, the sample from the base of the crust (70-mm total length) shows alternating millimeter-scale layers with highly variable olivine contents.

Comparisons with layered intrusions suggest that the formation of the decimeter-scale layering in the mid-lower oceanic crust from Wadi Somerah could have initially formed by deposition from density currents of crystal-laden magma that had previously crystallized at the margins of a magma reservoir before slumping downward to its floor. In this model, density-triggered phase segregation occurs during the slumping, leading to an enrichment of dense olivine and clinopyroxene at layer bases and an enrichment of more buoyant plagioclase above (Figure 6-13A). The dynamics within such a current might prevent clear trends in grain size and phase density within a layer, as would be expected in an environment of undisturbed crystal settling (cf., Stoke's law). The millimeter-scale layering at the crustal base from Wadi Wariyah is unlikely to have formed in a similar environment. Although it is difficult to find clear evidence for any specific layer-forming process, a possible explanation could be the formation of Liesegang bands during relatively fast cooling and periodic supersaturation of compatible elements at the distance from the crystallization front at which diffusive transport cannot keep pace with the cooling (Figure 6-13B). Growth of large crystals at the expense of smaller ones during crystal aging is indicated by the larger size of olivine grains within the olivine-enriched layers and could have emphasized initial heterogeneity associated with Liesegang banding (Figure 6-13C). Alternatively, the millimeter-scale layering could have formed by simple shear, possibly induced by the convecting upper mantle close to the MTZ. Post-cumulus deformation might have affected both profiles, as it is a global feature of the Oman ophiolite, and potentially accentuated previously formed modal layering. Indicators of plastic deformation in Wadi Somerah support this assumption.

Cooling rates up to 100 times higher close to the MTZ than in the mid-layered gabbros appear not to be representative for the lowermost oceanic crust as a whole but most likely are a result of late stage re-heating events followed by relatively fast cooling and leading to local anomalies in the cooling of the oceanic crust.

6.7   Data Availability Statement

The data obtained for this study are available on the FAIR-aligned PANGAEA repository (https://doi.org/ 10.1594/PANGAEA.914266 for EPMA, cooling rates, and EBSD results and https://doi.org/10.1594/PANGAEA.914260 for LA-ICP-MS results and https://doi.org/10.1594/PANGAEA.914257 for petrographic results).

Concluding Remarks

During this PhD project, gabbroic rocks from the lower oceanic crust of the Samail ophiolite in the Sultanate of Oman were analyzed from the crustal down to the mm-scale. The key objective was an understanding of the magmatic processes taking place on or close to the axis of a fast-spread mid-ocean ridge, which is assumed to be well-represented by the Samail ophiolite (e.g., Nicolas, 1989). Processes at the crustal scale were investigated by application of microstructural methods to a complete lower crustal section from Wadi Gideah in the Samail ophiolite in order to discover deformation mechanisms playing a role during or shortly after the emplacement of magma beneath the spreading center. Processes at the decameter scale were investigated by the highly resolved petrological, geochemical, and microstructural analyses of two drill cores obtained in the frame of the Oman Drilling Project (Kelemen et al., 2020) which each cover an approximately 400 m long section of the layered gabbro section and of the transition from layered to foliated gabbros, respectively. Two short profiles showing dm- and mm-scale cyclic variations in mineral proportions (i.e., modal layering) were sampled and also analyzed by petrological, geochemical, and microstructural methods in order to explain layer formation in lower oceanic crust.

The microstructural features along the entire crustal profile indicate that not a single mechanism led to the accretion of lower oceanic crust in Wadi Gideah, as suggested by the crustal accretion end-member models sheeted sill (e.g., Kelemen et al., 1997) and gabbro glacier (e.g., Henstock et al., 1993). Instead, a hybrid model where the upper third of the lower crust accretes from vertical magmatic flow and the lower two thirds crystallize in-situ within relatively small melt sills in the lower crust is consistent with the obtained data. The hypothesis that in-situ crystallization can take place in lower crustal gabbros close to the ridge axis was tested by high resolution sampling along the drill core from the layered gabbros. The high sample density revealed fractionation trends at the decameter scale. Moreover, a steep reverse fractionation trend over only a few meters is interpreted as resulting from relatively evolved melt which interacted with primitive melt from the crystal mush. Consequently, the occurrence of fractional crystallization within the lower oceanic crust is suggested to explain both fractionation trends and the presence of evolved melts. This supports the previous finding that the layered gabbros in Wadi Gideah accreted in a complex environment where sills with heights of only a few decameters crystallize individually and residual melt with different compositions migrates through the crust.

The modal layering with graded upper boundaries between two adjacent layers sampled in Wadi Somerah of the Samail ophiolite during this study can be explained by deposition of crystal-laden density currents slumping downward from the margins of such melt sills. Density-controlled phase segregation leads to the concentration of the denser olivine at the layer bases, whereas less dense plagioclase concentrates at the top of each layer. Millimeter scale bands of olivine enrichment in the sample from Wadi Wariyah of the Samail ophiolite can be explained by Liesegang banding, where mineral-forming elements become supersaturated at a certain distance from the crystallization front as a result of increasing distance and decreasing diffusion velocities during relatively fast cooling of the melt. A new band of early phases crystallizes in the region of supersaturation. The resulting modal heterogeneity may be emphasized by Ostwald ripening where larger grains grow on the expense of smaller ones. Both layer-forming mechanisms are potentially supported by mantle-induced shearing as suggested to form modal layering by Jousselin et al. (2012).

References

Abily, B., & Ceuleneer, G. (2013). The dunitic mantle-crust transition zone in the Oman ophiolite: Residue of melt-rock interaction, cumulates from high-MgO melts, or both? Geology, 41(1), 67-70. doi:10.1130/g33351.1

Abily, B., Ceuleneer, G., & Launeau, P. (2011). Synmagmatic normal faulting in the lower oceanic crust: Evidence from the Oman ophiolite. Geology, 39(4), 391-394. doi:10.1130/g31652.1

Agrinier, P., Hékinian, R., Bideau, D., & Javoy, M. (1995). O and H stable isotope compositions of oceanic crust and upper mantle rocks exposed in the Hess Deep near the Galapagos Triple Junction. Earth and Planetary Science Letters, 136(3), 183-196. doi:https://doi.org/10.1016/0012-821X(95)00159-A

Alabaster, T., Pearce, J. A., & Malpas, J. (1982). The volcanic stratigraphy and petrogenesis of the Oman ophiolite complex. Contributions to Mineralogy and Petrology, 81(3), 168-183.

Anonymous. (1972). Penrose Field Conference: Ophiolites. Geotimes, 17, 24–25.

Arai, S., & Matsukage, K. (1996). Petrology of gabbro-troctolite-peridotite complex from Hess Deep, equatorial Pacific: implications for mantle-melt interaction within the oceanic lithosphere. Proc. ODP, Sci. Results, 147, 135-155.

Ariskin, A., & Barmina, G. (2004). COMAGMAT: Development of a Magma Crystallization Model and Its Petrological Applications. Geochem. Int., 42.

Ariskin, A. A. (1999). Phase equilibria modeling in igneous petrology: use of COMAGMAT model for simulating fractionation of ferro-basaltic magmas and the genesis of high-alumina basalt. Journal of Volcanology and Geothermal Research, 90, 115-162.

Bachmann, F., Hielscher, R., & Schaeben, H. (2010). Texture analysis with MTEX–free and open source software toolbox. Paper presented at the Solid State Phenomena.

Bedard, J. H. (1999). Petrogenesis of boninites from the Betts Cove Ophiolite, Newfoundland, Canada: Identification of subducted source components. Journal of Petrology, 40(12), 1853-1889.

Bedard, J. H., Sparks, R. S. J., Renner, R., Cheadle, M. J., & Hallworth, M. A. (1988). Peridotite Sills and Metasomatic Gabbros in the Eastern Layered Series of the Rhum Complex. Journal of the Geological Society, 145, 207-224.

Bell, D. R., & Rossman, G. R. (1992). Water in Earth's mantle: the role of nominally anhydrous minerals. Science, 255(5050), 1391-1397.

Bemis, K., Lowell, R. P., & Farough, A. (2012). Diffuse flow: On and around hydrothermal vents at Mid-Ocean Ridges. Oceanography, 25(1), 182-191.

Benn, K., & Allard, B. (1989). Preferred mineral orientations related to magmatic flow in ophiolite layered gabbros. Journal of Petrology, 30(4), 925-946.

Berndt, J., Koepke, J., & Holtz, F. (2005). An experimental investigation of the influence of water and oxygen fugacity on differentiation of MORB at 200 MPa. Journal of Petrology, 46(1), 135-167.

Boddupalli, B., & Canales, J. P. (2019). Distribution of Crustal Melt Bodies at the Hot Spot-Influenced Section of the Galápagos Spreading Centre From Seismic Reflection Images. Geophysical Research Letters, 46(9), 4664-4673. doi:10.1029/2019gl082201

Bosch, D., Jamais, M., Boudier, F., Nicolas, A., Dautria, J.-M., & Agrinier, P. (2004). Deep and high-temperature hydrothermal circulation in the Oman ophiolite - Petrological and isotopic evidence. Journal of Petrology, 45, 1181-1208.

Boudier, F., Ceuleneer, G., & Nicolas, A. (1988). Shear zones, thrusts and related magmatism in the Oman ophiolite: initiation of thrusting on an oceanic ridge. Tectonophysics, 151(1-4), 275-296.

Boudier, F., Godard, M., & Armbruster, C. (2000). Significance of gabbronorite occurrence in the crustal section of the Semail ophiolite. Marine Geophysical Researches, 21(3-4), 307-326. doi:10.1023/a:1026726232402

Boudier, F., Nicolas, A., & Ildefonse, B. (1996). Magma chambers in the Oman ophiolite: Fed from the top and the bottom. Earth and Planetary Science Letters, 144(1-2), 239-250.

Boudreau, A. (1987). Pattern formation during crystallization and the formation of fine-scale layering. In Origins of igneous layering (pp. 453-471): Springer, Dordrecht.

Boudreau, A. (1995). Crystal aging and the formation of fine-scale igneous layering. Mineralogy and Petrology, 54(1-2), 55-69.

Boudreau, A. (1999). Fluid fluxing of cumulates: the JM reef and associated rocks of the Stillwater Complex, Montana. Journal of Petrology, 40(5), 755-772.

Boudreau, A., & McCallum, I. (1992). Infiltration metasomatism in layered intrusions—an example from the Stillwater Complex, Montana. Journal of Volcanology and Geothermal Research, 52(1-3), 171-183.

Boudreau, A. E., & McBirney, A. R. (1997). The Skaergaard layered series. Part III. Non-dynamic layering. Journal of Petrology, 38(8), 1003-1020.

Bown, J. W., & White, R. S. (1994). Variation with spreading rate of oceanic crustal thickness and geochemistry. Earth and Planetary Science Letters, 121(3-4), 435-449.

Brey, G. P., & Koehler, T. (1990). Geothermobarometry in four-phase lherzolites; II, New thermobarometers, and practical assessment of existing thermobarometers. Journal of Petrology, 311, 353-1378.

Brown, G. M. (1956). The layered ultrabasic rocks of Rhum, Inner Hebrides. Philosophical Transactions of the

Royal Society of London. Series B, Biological Sciences, 1-53.

Brown, T., Cheadle, M., John, B., Coogan, L., Gee, J., Karson, J. A., & Swapp, S. (2019). Textural Character of Gabbroic Rocks from Pito Deep: a Record of Magmatic Processes and the Genesis of the Upper Plutonic Crust at Fast-Spreading Mid-Ocean Ridges. Journal of Petrology, 60(5), 997-1026.

Browning, P. (1984). Cryptic variation within the Cumulate Sequence of the Oman ophiolite: magma chamber depth and petrological implications. Journl Geological Society, London, Special Publications, 13, 71-92.

Buck, W. R. (2000). Can downward flow of dense cumulate slurry through mushy upper gabbros produce lower gabbros at a fast-spreading center? SPECIAL PAPERS-GEOLOGICAL SOCIETY OF AMERICA, 121-128.

Buening, D. K., & Buseck, P. R. (1973). Fe-Mg lattice diffusion in olivine. Journal of Geophysical Research, 78(29), 6852-6862. doi:10.1029/JB078i029p06852

Bunge, H. J. (1982). Texture analysis in materials science : mathematical methods. Mathematische Methoden der Texturanalyse <engl.>. London [u.a.]: Butterworths;.

Bunge, H. J., & Esling, C. (1982). Quantitative texture analysis. Deutsche Gesellschaft fur Metallkunde, v+ 551, 24 x 17 cm, illustrated(DM 168. 00.

Canales, J. P., Carton, H., Carbotte, S. M., Mutter, J. C., Nedimovic, M. R., Xu, M., . . . Newman, K. (2012). Network of off-axis melt bodies at the East Pacific Rise. Nature Geoscience, 5(4), 279-283. doi:10.1038/ngeo1377

Canales, J. P., Detrick, R. S., Toomey, D. R., & Wilcock, W. S. D. (2003). Segment-scale variations in the crustal structure of 150-300 kyr old fast spreading oceanic crust (East Pacific Rise, 8 degrees 15 ' N-10 degrees 5 ' N) from wide-angle seismic refraction profiles. Geophys. J. Int., 152, 766-794.

Canales, J. P., Nedimovic, M. R., Kent, G. M., Carbotte, S. M., & Detrick, R. S. (2009). Seismic reflection images of a near-axis melt sill within the lower crust at the Juan de Fuca ridge. Nature, 460(7251), 89-U100. doi:10.1038/nature08095

Cann, J. R. (1974). MODEL FOR OCEANIC CRUSTAL STRUCTURE DEVELOPED. Geophysical Journal of the Royal Astronomical Society, 39(1), 169-187. doi:10.1111/j.1365-246X.1974.tb05446.x

Cannat, M., & Casey, J. F. (1995). An ultramafic lift at the Mid-Atlantic Ridge: successive stages of magmatism in serpentinized peridotites from the 15°N region. In R. L. M. Vissers & A. Nicolas (Eds.), Mantle and lower crust exposed in oceanic ridges and in ophiolites (pp. 5-34). Dordrecht: Kluwer Academic.

Cannat, M., Manatschal, G., Sauter, D., & Peron-Pinvidic, G. (2009). Assessing the conditions of continental breakup at magma-poor rifted margins: what can we learn from slow spreading mid-ocean ridges? Comptes Rendus Geoscience, 341(5), 406-427.

Carbotte, S. M., Marjanović, M., Arnulf, A. F., Nedimović, M. R., Canales, J. P., & Arnoux, G. M. (2021). Stacked Magma Lenses Beneath Mid-Ocean Ridges: Insights From New Seismic Observations and Synthesis With Prior Geophysical and Geologic Findings. Journal of Geophysical Research: Solid Earth, 126(4), e2020JB021434.

Caress, D. W., Burnett, M. S., & Orcutt, J. A. (1992). Tomographic image of the axial low-velocity zone at 12° 50′ N on the East Pacific Rise. Journal of Geophysical Research: Solid Earth, 97(B6), 9243-9263.

Cawthorn, R. G. (1996). Re-evaluation of magma compositions and processes in the uppermost Critical Zone of the Bushveld Complex. Mineralogical Magazine, 60(398), 131-148.

Cawthorn, R. G., & Ashwal, L. D. (2009). Origin of anorthosite and magnetitite layers in the Bushveld Complex, constrained by major element compositions of plagioclase. Journal of Petrology, 50(9), 1607-1637.

Chakraborty, S. (1997). Rates and mechanisms of Fe-Mg interdiffusion in olivine at 980°–1300° C. Journal of Geophysical Research: Solid Earth, 102(B6), 12317-12331.

Charlier, B., Namur, O., & Grove, T. L. (2013). Compositional and kinetic controls on liquid immiscibility in ferrobasalt–rhyolite volcanic and plutonic series. Geochimica et Cosmochimica Acta, 113, 79-93.

Charlier, B., Namur, O., Toplis, M. J., Schiano, P., Cluzel, N., Higgins, M. D., & Auwera, J. V. (2011). Large-scale silicate liquid immiscibility during differentiation of tholeiitic basalt to granite and the origin of the Daly gap. Geology, 39(10), 907-910.

Chen, Y. J. (1992). Oceanic crustal thickness versus spreading rate. Geophysical Research Letters, 19(8), 753-756.

Cherkaoui, A. S. M., Wilcock, W. S. D., Dunn, R. A., & Toomey, D. R. (2003). A numerical model of hydrothermal cooling and crustal accretion at a fast spreading mid-ocean ridge. Geochemistry, Geophysics, Geosystems, 4(9), n/a-n/a. doi:10.1029/2001gc000215

Cherniak, D. J., & Liang, Y. (2012). Ti diffusion in natural pyroxene. Geochimica et Cosmochimica Acta, 98, 31-47. doi:10.1016/j.gca.2012.09.021

Cloos, M. (1993). Lithospheric buoyancy and collisional orogenesis: Subduction of oceanic plateaus, continental margins, island arcs, spreading ridges, and seamounts. Geological Society of America Bulletin, 105(6), 715-737.

Coats, R. R. (1936). Primary banding in basic plutonic rocks. The Journal of Geology, 44(3), 407-419.

Coogan, L. A., Hain, A., Stahl, S., & Chakraborty, S. (2005). Experimental determination of the diffusion coefficient for calcium in olivine between 900°C and 1500°C. Geochimica et Cosmochimica Acta, 69(14), 3683-3694. doi:10.1016/j.gca.2005.03.002

Coogan, L. A., Howard, K. A., Gillis, K. M., Bickle, M. J., Chapman, H., Boyce, A. J., . . . Wilson, R. N. (2006). Chemical and thermal constraints on focussed fluid flow in the lower oceanic crust. American Journal of Science, 306(6), 389-427. doi:10.2475/06.2006.01

Coogan, L. A., Jenkin, G. R. T., & Wilson, R. N. (2002a). Constraining the cooling rate of the lower oceanic crust: a new approach applied to the Oman ophiolite. Earth and Planetary Science Letters, 199(1-2), 127-146.

Coogan, L. A., Jenkin, G. R. T., & Wilson, R. N. (2007). Contrasting Cooling Rates in the Lower Oceanic Crust at Fast- and Slow-spreading Ridges Revealed by Geospeedometry. Journal of Petrology, 48(11), 2211-2231. doi:10.1093/petrology/egm057

Coogan, L. A., Thompson, G., & MacLeod, C. J. (2002b). A textural and geochemical investigation of high level gabbros from the Oman ophiolite: implications for the role of the axial magma chamber at fast-spreading ridges. Lithos, 63(1-2), 67-82.

Cox, K. G., Bell, J., & Pankhurst, R. (1979). The interpretation of igneous rocks (004552016X). Retrieved from

Crawford, W. C., Webb, S. C., & Hildebrand, J. A. (1999). Constraints on melt in the lower crust and Moho at the East Pacific Rise, 9 48′ N, using seafloor compliance measurements. Journal of Geophysical Research: Solid Earth, 104(B2), 2923-2939.

Currin, A., Koepke, J., Almeev, R., & Beermann, O. (2018a). Interaction of highly saline fluid and olivine gabbro: experimental simulation of deep hydrothermal processes involving amphibole at the base of the oceanic crust. Lithos, https://doi.org/10.1016/j.lithos.2018.09.017.

Currin, A., Wolff, E. P., Koepke, J., Almeev, R., Zhang, C., Zihlmann, B., . . . Teagle, D. A. H. (2018b). Chlorine-rich amphibole in deep layered gabbros as evidence for brine/rock interaction in the lower oceanic crust: a case study from the Wadi Wariyah, Samail Ophiolite, Sultanate of Oman. Lithos, https://doi.org/10.1016/j.lithos.2018.09.015.

Dalton, J. A., & Lane, S. J. (1996). Electron microprobe analysis of Ca in olivine close to grain boundaries: the problem of secondary X-ray fluorescence. American Mineralogist, 81(1-2), 194-201.

de Graaff, S., Goodenough, K., Klaver, M., Lissenberg, C., Jansen, M., Millar, I., & Davies, G. (2019). Evidence for a moist to wet source transition throughout the Oman-UAE ophiolite, and implications for the geodynamic history. Geochemistry, Geophysics, Geosystems, 20(2), 651-672.

Detrick, R. S., Buhl, P., Vera, E., Mutter, J., Orcutt, J., Madsen, J., & Brocher, T. (1987). Multichannel seismic imaging of a crustal magma chamber along the East Pacific Rise. Nature, 326, 35-41.

Dick, H. J., & Sinton, J. M. (1979). Compositional layering in alpine peridotites: evidence for pressure solution creep in the mantle. The Journal of Geology, 87(4), 403-416.

Dick, H. J. B., Lin, J., & Schouten, H. (2003). An ultraslow-spreading class of ocean ridge. Nature, 426(6965), 405-412. doi:10.1038/nature02128

Dick, H. J. B., Natland, J. H., & Ildefonse, B. (2006). Deep drilling in the oceanic crust and mantle. Oceanography, 19, 74-82.

Dimanov, A., & Sautter, V. (2000). "Average" interdiffusion of (Fe, Mn)-Mg in natural diopside. European Journal of Mineralogy, 12(4), 749-760.

Dodson, M. (1986). Closure profiles in cooling systems. Paper presented at the Materials Science Forum.

Dunn, R. A., Toomey, D. R., & Solomon, S. C. (2000). Three-dimensional seismic structure and physical properties of the crust and shallow mantle beneath the East Pacific Rise at 9 degrees 30'N. Journal of Geophysical Research-Solid Earth, 105(B10), 23537-23555. Retrieved from <Go to ISI>://000089895700013

Dygert, N., Kelemen, P. B., & Liang, Y. (2017). Spatial variations in cooling rate in the mantle section of the Samail ophiolite in Oman: Implications for formation of lithosphere at mid-ocean ridges. Earth and Planetary Science Letters, 465, 134-144. doi:10.1016/j.epsl.2017.02.038

El-Shazly, A., & Lanphere, M. (1992). Two high-pressure metamorphic events in NE Oman: Evidence from 40Ar/39Ar dating and petrological data. The Journal of Geology, 100(6), 731-751.

El-Shazly, A., Bröcker, M., Hacker, B., & Calvert, A. (2001). Formation and exhumation of blueschists and eclogites from NE Oman: new perspectives from Rb–Sr and 40Ar/39Ar dating. Journal of Metamorphic Geology, 19(3), 233-248.

Ernewein, M., Pflumio, C., & Whitechurch, H. (1988). The death of a accretion zone as evidenced by the magmatic history of the Sumail ophiolite (Oman). Tectonophysics, 151, 247-274.

Ernst, W. G., & Liu, J. (1998). Experimental phase-equilibrium study of Al- and Ti-contents of calcic amphibole in MORB - a semiquantitative thermobarometer. American Mineralogist, 83, 952-969.

Faak, K., Chakraborty, S., & Coogan, L. A. (2013). Mg in plagioclase: Experimental calibration of a new geothermometer and diffusion coefficients. Geochimica et Cosmochimica Acta, 123, 195-217. doi:10.1016/j.gca.2013.05.009

Faak, K., Coogan, L. A., & Chakraborty, S. (2014). A new Mg-in-plagioclase geospeedometer for the determination of cooling rates of mafic rocks. Geochimica et Cosmochimica Acta, 140, 691-707. doi:10.1016/j.gca.2014.06.005

Faak, K., Coogan, L. A., & Chakraborty, S. (2015). Near conductive cooling rates in the upper-plutonic section of crust formed at the East Pacific Rise. Earth and Planetary Science Letters, 423, 36-47. doi:10.1016/j.epsl.2015.04.025

Feig, S., Koepke, J., & Snow, J. (2006). Effect of water on tholeiitic basalt phase equilibria: An experimental study under oxidizing conditions. Contributions to Mineralogy and Petrology, 152, 611-638.

Ferrando, C., Basch, V., Ildefonse, B., Deans, J., Sanfilippo, A., Barou, F., & France, L. (2021). Role of compaction in melt extraction and accumulation at a slow spreading center: Microstructures of olivine gabbros from the Atlantis Bank (IODP Hole U1473A, SWIR). Tectonophysics, 815, 229001. doi:https://doi.org/10.1016/j.tecto.2021.229001

Fisher, G. W., & Lasaga, A. C. (1981). Irreversible thermodynamics in petrology. Rev. Mineral.;(United States), 8.

France, L., Ildefonse, B., & Koepke, J. (2009). Interactions between magma and the hydrothermal system in the Oman ophiolite and in IODP hole 1256D: fossilisation of a dynamic melt lens at fast spreading ridges. Geochemistry Geophysics Geosystems, 10, doi:10.1029/2009GC002652.

Gaetani, G. A., Grove, T. L., & Bryan, W. B. (1993). The influence of water on the petrogenesis of subductionrelated igneous rocks. Nature, 365(6444), 332-334.

Gale, A., Dalton, C. A., Langmuir, C. H., Su, Y., & Schiling, J. (2013). The mean composition of ocean ridge basalts. Geochemistry Geophysics Geosystems, 14(3), doi 10.1029/2012GC004334. Retrieved from <Go to ISI>://WOS:000326242700003

Ganino, C., Arndt, N. T., Zhou, M.-F., Gaillard, F., & Chauvel, C. (2008). Interaction of magma with sedimentary wall rock and magnetite ore genesis in the Panzhihua mafic intrusion, SW China. Mineralium Deposita, 43(6), 677-694.

Garbe-Schönberg, D., Koepke J., Müller, S., Mock D., & Müller, T. A reference section through fast-spread lower oceanic crust, Wadi Gideah, Samail Ophiolite (Sultanate of Oman): Whole rock geochemistry. submitted to Journal of Geophysical Research: Solid Earth

Garbe-Schoenberg, C.-D., Koepke, J., Mueller, T., Wolff, P. E., & Strauss, H. (2014). Trace element systematics in the plutonic section of fast-spread oceanic crust-evidence from the Wadi Gideah reference profile (Wadi Tayin Massif, Oman ophiolite). AGUFM, 2014, V31B-4728.

Garbe-Schönberg, D., & Müller, S. (2014). Nano-particulate pressed powder tablets for LA-ICP-MS. Journal of Analytical Atomic Spectrometry, 29(6), 990-1000. doi:10.1039/c4ja00007b

Garmany, J. (1989). Accumulations of melt at the base of young oceanic crust. Nature, 340(6235), 628-632.

Garrido, C. J., Kelemen, P. B., & Hirth, G. (2001). Variation of cooling rate with depth in lower crust formed at an oceanic spreading ridge: Plagioclase crystal size distributions in gabbros from the Oman ophiolite. Geochemistry Geophysics Geosystems, 2, 2000GC000136.

German, C., Baker, E., Mevel, C., & Tamaki, K. (1998). Hydrothermal activity along the southwest Indian ridge. Nature, 395(6701), 490-493.

Gess, M., John, B. E., Cheadle, M. J., Brown, T. C., Swapp, S., & Gee, J. S. (2018). Questioning the Penrose Paradigm: Insights from in-situ gabbroic lower ocean crust at Pito Deep. Paper presented at the AGU Fall Meeting Abstracts.

Ghiorso, M. S., & Sack, R. O. (1995). Chemical mass transfer in magmatic processes. IV. A revised and internally consistent thermodynamic model for the interpolation and extrapolation of liquid-solid equilibria in magmatic systems at elevated temperatures and pressures.

Contributions to Mineralogy and Petrology, 84, 107-145.

Gillis, K., Snow, J., Klaus, A., Guerin, G., Abe, N., Akizawa, N., . . . Faak, K. (2014a). Expedition 345 summary. Paper presented at the Proceedings of the Integrated Ocean Drilling Program.

Gillis, K. M., Ludden, J. N., Plank, T., & Hoy, L. D. (1992). Low-temperature alteration and subsequent reheating of shallow oceanic crust at Hole 765D, Argo Abyssal Plain. Paper presented at the Gradstein, FM, Ludden, JN, et al., Proc. ODP, Sci. Results.

Gillis, K. M., Snow, J. E., Klaus, A., Abe, N., Adriao, A. B., Akizawa, N., . . . Wintsch, R. P. (2014b). Primitive layered gabbros from fast-spreading lower oceanic crust. Nature, 505(7482), 204-207. doi:10.1038/nature12778

Gillis, K. M., Snow, J. E., Klaus, A., Guerin, G., Abe, N., Akizawa, N., . . . Wintsch, R. P. (2014c). Methods. In.

Giordano, D., Potuzak, M., Romano, C., Dingwell, D., & Nowak, M. (2008). Viscosity and glass transition temperature of hydrous melts in the system CaAl2Si2O8–CaMgSi2O6. Chemical Geology, 256(3-4), 203-215.

Godard, M., Dautria, J.-M., & Perrin, M. (2003). Geochemical variability of the Oman ophiolite lavas: Relationship with spatial distribution and paleomagnetic directions. Geochemistry, Geophysics, Geosystems, 4(6), n/a-n/a. doi:10.1029/2002gc000452

Goodenough, K. M., Styles, M. T., Schofield, D., Thomas, R. J., Crowley, Q. C., Lilly, R. M., . . . Carney, J. N. (2010). Architecture of the Oman-UAE ophiolite: evidence for a multi-phase magmatic history. Arabian Journal of Geosciences, 3(4), 439-458. doi:10.1007/s12517-010-0177-3

Goodenough, K. M., Thomas, R. J., Styles, M. T., Schofield, D. I., & MacLeod, C. J. (2014). Records of Ocean Growth and Destruction in the Oman-UAE Ophiolite. Elements, 10(2), 109-114. doi:10.2113/gselements.10.2.109

Gray, D. R., & Gregory, R. T. (2000). Implications of the structure of the Wadi Tayin metamorphic sole, the Ibra-Dasir block of the Samail ophiolite, and the Saih Hatat window for late stage extensional ophiolite emplacement, Oman. Marine Geophysical Researches, 21(3), 211-227. doi:10.1023/A:1026772717865

Gray, D. R., Hand, M., Mawby, J., Armstrong, R. A., Miller, J. M., & Gregory, R. T. (2004a). Sm–Nd and zircon U–Pb ages from garnet-bearing eclogites, NE Oman: constraints on high-P metamorphism. Earth and Planetary Science Letters, 222(2), 407-422.

Gray, D. R., Miller, J. M., Foster, D. A., & Gregory, R. T. (2004b). Transition from subduction-to exhumation-related fabrics in glaucophane-bearing eclogites, Oman: evidence from relative fabric chronology and 40Ar/39Ar ages. Tectonophysics, 389(1-2), 35-64.

Greenberger, R. N., Harris, M., Ehlmann, B. L., Crotteau, M., Kelemen, P. B., Manning, C. E., & Teagle, D. A. (2021). Hydrothermal Alteration of the Ocean Crust and Patterns in Mineralization with Depth as Measured

by Micro-Imaging Infrared Spectroscopy. Journal of Geophysical Research. Solid Earth.

Gregory, R., Gray, D., & Miller, J. M. (1998). Tectonics of the Arabian margin associated with the emplacement of the Oman margin along the Ibra transect: new evidence from northeast Saih Hatat. Tectonics, 17, 657-670.

Guilmette, C., Smit, M. A., van Hinsbergen, D. J., Gürer, D., Corfu, F., Charette, B., . . . Savard, D. (2018). Forced subduction initiation recorded in the sole and crust of the Semail Ophiolite of Oman. Nature Geoscience, 11(9), 688-695.

Haase, K. M., Freund, S., Koepke, J., Hauff, F., & Erdmann, M. (2015). Melts of sediments in the mantle wedge of the Oman ophiolite. Geology, 43(4), 275-278. doi:10.1130/g36451.1

Hacker, B. R., Mosenfelder, J. L., & Gnos, E. (1997). Rapid emplacement of the Oman ophiolite: Thermal and geochronologic constraints. Tectonics, 15, 1230-1247.

Hale, L. D., Morton, C. J., & Sleep, N. H. (1982). Reinterpretation of seismic reflection data over the East Pacific Rise. Journal of Geophysical Research: Solid Earth, 87(B9), 7707-7717.

Harding, A., Orcutt, J., Kappus, M., Vera, E., Mutter, J., Buhl, P., . . . Brocher, T. (1989). Structure of young oceanic crust at 13 N on the East Pacific Rise from expanding spread profiles. Journal of Geophysical Research: Solid Earth, 94(B9), 12163-12196.

Harney, D. M., Merkle, R. K., & Von Gruenewaldt, G. (1990). Platinum-group element behavior in the lower part of the upper zone, eastern Bushveld Complex; implications for the formation of the main magnetite layer. Economic Geology, 85(8), 1777-1789.

Hasenclever, J., Theissen-Krah, S., Rupke, L. H., Morgan, J. P., Iyer, K., Petersen, S., & Devey, C. W. (2014). Hybrid shallow on-axis and deep off-axis hydrothermal circulation at fast-spreading ridges. Nature, 508(7497), 508-512. doi:10.1038/nature13174

Henstock, T. J., Woods, A. W., & White, R. S. (1993). The accretion of oceanic crust by episodic sill intrusion. Journal of Geophysical Research: Solid Earth, 98(B3), 4143-4161. doi:10.1029/92jb02661

Herron, T. J., Stoffa, P. L., & Buhl, P. (1980). Magma chamber and mantle reflections–East Pacific Rise. Geophysical Research Letters, 7(11), 989-992.

Hess, H. H., & Smith, J. R. (1960). Stillwater igneous complex, Montana a quantitative mineralogical study (Vol. 80): Geological Society of America.

Hielscher, R., & Schaeben, H. (2008). A novel pole figure inversion method: specification of the MTEX algorithm. Journal of Applied Crystallography, 41(6), 1024-1037.

Higgins, M. D. (1991). The origin of laminated and massive anorthosite, Sept Iles layered intrusion, Quebec, Canada. Contributions to Mineralogy and Petrology, 106(3), 340-354.

Higgins, M. D. (1994). Numerical modeling of crystal shapes in thin sections: estimation of crystal habit and true size. American Mineralogist, 79(1-2), 113-119.

Higgins, M. D. (2000). Measurement of crystal size distributions. American Mineralogist, 85(9), 1105-1116.

Hort, M., Marsh, B. D., & Spohn, T. (1993). Igneous layering through oscillatory nucleation and crystal settling in well-mixed magmas. Contributions to Mineralogy and Petrology, 114(4), 425-440.

Ildefonse, B., Abe, N., Blackman, D. K., Canales, J. P., Isozaki, Y., Kodaira, S., . . . Skinner, A. C. (2010). The MoHole: a crustal journey and mantle quest, workshop in Kanazawa, Japan, 3–5 June 2010. Sci. Drill, 10, 56-63.

Ildefonse, B., Abe, N., Godard, M., Morris, A., Teagle, D. A., & Umino, S. (2014). Formation and evolution of oceanic lithosphere: new insights on crustal structure and igneous geochemistry from ODP/IODP Sites 1256, U1309, and U1415. In Developments in Marine Geology (Vol. 7, pp. 449-505): Elsevier.

Ildefonse, B., Billiau, S., & Nicolas, A. (1995). A detailed study of mantle flow away from diapirs in the Oman ophiolite. In Mantle and Lower Crust Exposed in Oceanic Ridges and in Ophiolites (pp. 163-177): Springer.

Irvine, T. (1975). Crystallization sequences in the Muskox Intrusion and other layered complexes-origin of chromitite layers and similar deposits of other magmatic ores. Geochimica et Cosmochimica Acta, 39, 921-1020.

Irvine, T. (1977). Origin of chromitite layers in the Muskox intrusion and other stratiform intrusions: A new interpretation. Geology, 5(5), 273-277.

Irvine, T. (1980). Magmatic density currents and cumulus processes. American Journal of Science, 280(Jackson Volume), 1-58.

Irvine, T. (1982). Terminology for layered intrusions. Journal of Petrology, 23(2), 127-162.

Irvine, T. (1987). Layering and related structures in the Duke Island and Skaergaard intrusions: similarities, differences, and origins. In Origins of igneous layering (pp. 185-245): Springer.

Irvine, T., & Smith, C. (1967). The ultrarnafic rocks of the Muskox intrusion. IN: Ultramafic and Related Pocks, PJ Wyllie. In: J. Wiley & Sons, New York.

Irvine, T. N. (1974). Petrology of the Duke Island ultramafic complex, southeastern Alaska (Vol. 138): Geological Society of America.

Irvine, T. N., Andersen, J. C. Ø., & Brooks, C. K. (1998). Included blocks (and blocks within blocks) in the Skaergaard intrusion: Geologic relations and the origins of rhythmic modally graded layers. Geological Society of America Bulletin, 110(11), 1398-1447.

Ismaıl, W. B., & Mainprice, D. (1998). An olivine fabric database: an overview of upper mantle fabrics and seismic anisotropy. Tectonophysics, 296(1-2), 145-157.

Jakobsen, J. K., Veksler, I. V., Tegner, C., & Brooks, C. K. (2005). Immiscible iron- and silica-rich melts in basalt petrogenesis documented in the Skaergaard intrusion. Geology, 33, 885-888.

Jansen, M., Lissenberg, C., Klaver, M., de Graaff, S., Koornneef, J., Smeets, R., . . . Davies, G. R. (2018). Isotopic variation in Semail Ophiolite lower crust reveals crustal-level melt aggregatio. Geochemical Perspectives Letters, 8, 37-42.

Jousselin, D., Morales, L. F. G., Nicolle, M., & Stephant, A. (2012). Gabbro layering induced by simple shear in the Oman ophiolite Moho transition zone. Earth and Planetary Science Letters, 331-332, 55-66. doi:10.1016/j.epsl.2012.02.022

Jousselin, D., Nicolas, A., & Boudier, F. (1998). Detailed mapping of a mantle diapir below a paleo-spreading center in the Oman ophiolite. Journal of Geophysical Research: Solid Earth, 103(B8), 18153-18170.

Juteau, T., Ernewein, M., Reuber, I., Whitechurch, H., & Dahl, R. (1988). Duality of magmatism in the plutonic sequence of the Sumail Nappe, Oman. Tectonophysics, 151, 107-135.

Karson, J. A., Kelley, D. S., Fornari, D. J., Perfit, M. R., & Shank, T. M. (2015). Discovering the Deep: A Photographic Atlas of the Seafloor and Ocean Crust: Cambridge University Press.

Keith, M., Häckel, F., Haase, K. M., Schwarz-Schampera, U., & Klemd, R. (2016). Trace element systematics of pyrite from submarine hydrothermal vents. Ore Geology Reviews, 72, 728-745. doi:https://doi.org/10.1016/j.oregeorev.2015.07.012

Kelemen, P., Matter, J., Teagle, D., Coggon, J., & OmanDrillingProjectScienceTeam. (2020). Proceedings of the Oman Drilling Project: College Station, TX (International Ocean Discovery Program). doi:https://doi.org/10.14379/OmanDP.proc.2020

Kelemen, P. B., & Aharanov, E. (1998). Periodic formation of magma fractures and generation of layered gabbros in the lower crust beneath oceanic spreading ridges. GEOPHYSICAL MONOGRAPH-AMERICAN GEOPHYSICAL UNION, 106, 267-290.

Kelemen, P. B., Koga, K., & Shimizu, N. (1997). Geochemistry of gabbro sills in the crust-mantle transition zone of the Oman ophiolite: Implications for the origin of the oceanic lower crust. Earth and Planetary Science Letters, 146(3-4), 475-488.

Koepke, J., Botcharnikov, R., & Natland, J. (2018). Crystallization of late-stage MORB under varying water activities and redox conditions: Implications for the formation of highly evolved lavas and oxide gabbro in the ocean crust. Lithos, 323, 58-77.

Koepke, J., France, L., Müller, T., Faure, F., Goetze, N., Dziony, W., & Ildefonse, B. (2011). Gabbros from IODP Site 1256 (Equatorial Pacific): Insight into axial magma chamber processes at fast-spreading ocean ridges Geochemistry Geophysics Geosystems, 12, doi:10.1029/2011GC003655.

Koepke, J., Garbe-Schoenberg, D., Mueller, T., Mueller, S., Mock, D., Strauss, H., . . . Ildefonse, B. (2017). A Reference Section through the Lower Fast-spreading Oceanic Crust in the Wadi Gideah (Sumail ophiolite, Sultanate Oman): Drill Sites GT1A and GT2A within the ICDP Oman Drilling Project Abstract V43G-2957, presented at 2017 Fall Meeting, AGU, New Orleans, 11-15 Dec.

Koepke J., Müller, S., Garbe-Schönberg, D., Müller, T., Mock D., & Nasir, S. A reference section through fast-spreading lower oceanic crust, Wadi Gideah, Samail Ophiolite: petrography and petrology. submitted to Journal of Geophysical Research: Solid Earth

Koepke, J., Mueller, T., Linsler, S., Schuth, S., Garbe-Schoenberg, D., & McCaig, A. M. (2014). Invasion of seawater-derived fluids at very high temperatures in the Oman Ophiolite – a key for cooling the deep crust at fast-spreading ridges. Abstract V23E-03, presented at 2014 Fall Meeting, AGU, San Francisco, Calif., 15-19 Dec.

Koepke, J., Schoenborn, S., Oelze, M., Wittmann, H., Feig, S., Hellebrand, E., . . . Schoenberg, R. (2009). Petrogenesis of crustal wehrlites in the Oman ophiolite: Experiments and natural rocks. Geochemistry Geophysics Geosystems, 10, doi:10.1029/2009GC002488.

Koga, K. T., Kelemen, P. B., & Shimizu, N. (2001). Petrogenesis of the crust-mantle transition zone and the origin of lower crustal wehrlite in the Oman ophiolite. Geochemistry Geophysics Geosystems, 2, 2000GC000132.

Kogarko, L., & Khapaev, V. (1987). The modelling of formation of apatite deposits of the Khibina massif (Kola Peninsula). In Origins of igneous layering (pp. 589-611): Springer.

Köhler, T., & Brey, G. (1990a). Calcium exchange between olivine and clinopyroxene calibrated as a geothermobarometer for natural peridotites from 2 to 60 kb with applications. Geochimica et Cosmochimica Acta, 54(9), 2375-2388.

Köhler, T., & Brey, G. (1990b). Geothermobarometry in 4-phase lherzolites. 2. New thermobarometers, and practical assessment of existing thermobarometers. J. Petrol., 31, 1353-1378.

König, S., Münker, C., Schuth, S., Luguet, A., Hoffmann, J. E., & Kuduon, J. (2010). Boninites as windows into trace element mobility in subduction zones. Geochimica et Cosmochimica Acta, 74(2), 684-704.

Korenaga, J., & Kelemen, P. B. (1997). Origin of gabbro sills in the Moho transition zone of the Oman ophiolite: Implications for magma transport in the oceanic lower crust. Journal of Geophysical Research: Solid Earth, 102(B12), 27729-27749.

Korenaga, J., & Kelemen, P. B. (1998). Melt migration through the oceanic lower crust: a constraint from melt percolation modeling with finite solid diffusion. Earth and Planetary Science Letters, 156, 1-11.

Le Mee, L., Girardeau, J., & Monnier, C. (2004). Mantle segmentation along the Oman ophiolite fossil mid-ocean ridge. Nature, 432, 167-172.

Leuthold, J., Lissenberg, C. J., O'Driscoll, B., Karakas, O., Falloon, T., Klimentyeva, D. N., & Ulmer, P. (2018). Partial Melting of Lower Oceanic Crust Gabbro: Constraints From Poikilitic Clinopyroxene Primocrysts. Frontiers in Earth Science, 6(15). doi:10.3389/feart.2018.00015

Liang, Y., Sun, C., & Yao, L. (2013). A REE-in-two-pyroxene thermometer for mafic and ultramafic rocks. Geochimica et Cosmochimica Acta, 102, 246-260.

Liesegang, R. (1896). Ueber einige eigenschaften von gallerten. Naturwissenschaftliche Wochenschrift, 10(30), 353-362.

Lipin, B. R. (1993). Pressure increases, the formation of chromite seams, and the development of the ultramafic series in the Stillwater Complex, Montana. Journal of Petrology, 34(5), 955-976.

Lippard, S. J., Shelton, A. W., & Gass, I. G. (1986). The ophiolite of Northern Oman (Vol. 11). Oxford: Blackwell Scientific Publ.

Lissenberg, C. J., MacLeod, C. J., Howard, K. A., & Godard, M. (2013). Pervasive reactive melt migration through fast-spreading lower oceanic crust (Hess Deep, equatorial Pacific Ocean). Earth and Planetary Science Letters, 361, 436-447. doi:10.1016/j.epsl.2012.11.012

Maclennan, J., Hulme, T., & Singh, S. C. (2005). Cooling of the lower oceanic crust. Geology, 33, 357-360.

MacLeod, C. J., Lissenberg, C. J., & Bibby, L. E. (2013). "Moist MORB" axial magmatism in the Oman ophiolite: The evidence against a mid-ocean ridge origin. Geology, 41(4), 459-462. doi:10.1130/g33904.1

MacLeod, C. J., & Rothery, D. A. (1992). Ridge axial segmentation in the Oman ophiolite: evidence from along-strike variations in the sheeted dyke complex. In L. M. Parson, B. J. Murton, & P. Browning (Eds.), Ophiolites and their modern oceanic analogues (pp. 39-63): Geol. Soc. Spec. Publ. 60.

MacLeod, C. J., & Yaouancq, G. (2000). A fossil melt lens in the Oman ophiolite: Implications for magma chamber processes at fast spreading ridges. Earth and Planetary Science Letters, 176(3-4), 357-373.

Mainprice, D., Bachmann, F., Hielscher, R., & Schaeben, H. (2015). Descriptive tools for the analysis of texture projects with large datasets using MTEX: strength, symmetry and components. Geological Society, London, Special Publications, 409(1), 251-271. doi:10.1144/sp409.8

Mainprice, D., & Silver, P. G. (1993). Interpretation of SKS-waves using samples from the subcontinental lithosphere. Physics of the Earth and Planetary Interiors, 78(3-4), 257-280.

Marjanovic, M., Carbotte, S. M., Carton, H., Nedimovic, M. R., Mutter, J. C., & Canales, J. P. (2014). A multi-sill magma plumbing system beneath the axis of the East Pacific Rise. Nature Geoscience, 7(11), 825-829. doi:10.1038/ngeo2272

Marjanović, M., Carton, H., Carbotte, S. M., Nedimović, M. R., Mutter, J. C., & Canales, J. P. (2015). Distribution of melt along the East Pacific Rise from 9°30′ to 10°N from an amplitude variation with angle of incidence (AVA) technique. Geophysical Journal International, 203(1), 1-21. doi:10.1093/gji/ggv251

Marsh, B. D. (1988). Crystal size distribution (CSD) in rocks and the kinetics and dynamics of crystallization. Contributions to Mineralogy and Petrology, 99(3), 277-291.

Marsh, B. D. (1989). On convective style and vigor in sheet-like magma chambers. Journal of Petrology, 30(3), 479-530.

McBirney, A. R., & Noyes, R. M. (1979). Crystallization and layering of the Skaergaard intrusion. Journal of Petrology, 20(3), 487-554.

McBirney, A. R., White, C. M., & Boudreau, A. (1990). Spontaneous development of concentric layering in a solidified siliceous dike, East Greenland. Earth-Science Reviews, 29(1-4), 321-330.

McDonough, W. F., & Sun, S.-S. (1995). The composition of the Earth. Chemical Geology, 120(3-4), 223-253.

Meurer, W. P., & Boudreau, A. E. (1998). Compaction of Igneous Cumulates Part Ii: Compaction and the Development of Igneous Foliations. The Journal of Geology, 106(3), 293-304. doi:10.1086/516023

Meurer, W. P., Klaber, S., & Boudreau, A. E. (1997). Discordant bodies from olivine-bearing zones III and IV of the Stillwater Complex, Montana–evidence for postcumulus fluid migration and reaction in layered intrusions. Contributions to Mineralogy and Petrology, 130(1), 81-92.

Mock, D., Ildefonse, B., Müller, T., & Koepke, J. (2020a). Crystallographic preferred orientations in Wadi Gideah (Oman)–refining a reference profile along lower oceanic crust. Paper presented at the AGU Fall Meeting 2020.

Mock, D., Ildefonse, B., Müller, T., & Koepke, J. (2020b). Electron Backscatter Diffraction (EBSD) analysis through fast-spread lower oceanic crust of Wadi Gideah in the Oman ophiolite. Retrieved from: https://doi.org/10.1594/PANGAEA.924445

Mock, D., Neave, D., Müller, S., Garbe-Schönberg, D., Namur, O., Ildefonse, B., & Koepke, J. (2020c). Formation of igneous layering in the lower oceanic crust from the Samail Ophiolite, Sultanate of Oman. Journal of Geophysical Research: Solid Earth, e2020JB019573.

Mock, D., Neave, D. A., Müller, S., Garbe-Schönberg, C.-D., Namur, O., Ildefonse, B., & Koepke, J. (2020d). Major element compositions of olivine, clinopyroxene and plagioclase, cooling rates and corresponding closure temperatures calculated by Ca in olivine and Mg in plagioclase, and textural properties from Wadi Somerah and Wadi Wariyah, Oman. Retrieved from: https://doi.org/10.1594/PANGAEA.914266

Mock, D., Neave, D. A., Müller, S., Garbe-Schönberg, C.-D., Namur, O., Ildefonse, B., & Koepke, J. (2020e). Trace element compositions in clinopyroxene and plagioclase, and crystallization temperature estimated after Sun and Liang (2017) for Wadi Somerah, Oman. Retrieved from: https://doi.org/10.1594/PANGAEA.914260

Morales, L. F. G., Boudier, F., & Nicolas, A. (2011). Microstructures and crystallographic preferred orientation of anorthosites from Oman ophiolite and the dynamics of melt lenses. Tectonics, 30(2), n/a-n/a. doi:10.1029/2010tc002697

Morris, A., Meyer, M., Anderson, M. W., & MacLeod, C. J. (2019). What do variable magnetic fabrics in gabbros

of the Oman ophiolite reveal about lower oceanic crustal magmatism at fast spreading ridges? Geology, 47(3), 275-278.

Morse, S. (1984). Cation diffusion in plagioclase feldspar. Science, 225(4661), 504-505.

Morton, J. L., & Sleep, N. H. (1985). Seismic reflections from a Lau Basin magma chamber. Geology and offshore resources of Pacific Island Arcs-Tonga region, 451-453.

Müller, S., Garbe-Schönberg, D., Koepke, J., Hoernle, K. A reference section through fast-spread lower oceanic crust, Wadi Gideah, Samail Ophiolite (Sultanate of Oman): crystallization temperatures and trace element systematics. *submitted* to Journal of Geophysical Research: Solid Earth

Mueller, S., Koepke, J., Garbe-Schoenberg, C., Müller, T., Mock, D., Strauss, H., . . . Ildefonse, B. (2017). A Reference Section through the Lower Fast-spreading Oceanic Crust in the Wadi Gideah (Sumail ophiolite, Sultanate Oman): Drill Sites GT1A and GT2A within the ICDP Oman Drilling Project. AGUFM, 2017, V43G-2957.

Müller, T. (2016). A petrological and geochemical cross section of lower crust at the Wadi Gideah (Samail ophiolite): Implications for the crustal accretion at fast-spreading mid-ocean ridges. (PhD). University of Hannover,

Müller, T., Koepke, J., Garbe-Schoenberg, C.-D., Schuth, S., & Wolff, P. E. (2014). Oman ophiolite: petrological and geochemical investigation of fast-spreading crust formation processes. AGUFM, 2014, V31B-4727.

Müller, T., Koepke, J., Garbe-Schönberg, C. D., Dietrich, M., Bauer, U., & Wolff, P. E. (2017). Anatomy of a frozen axial melt lens from a fast-spreading paleo-ridge (Wadi Gideah, Oman ophiolite). Lithos, 272-273, 31-45. doi:10.1016/j.lithos.2016.11.022

Murase, T., & McBIRNEY, A. R. (1973). Properties of some common igneous rocks and their melts at high temperatures. Geological Society of America Bulletin, 84(11), 3563-3592.

Naldrett, A. J., Gasparrini, E., Barnes, S. J., Von Gruenewaldt, G., & Sharpe, M. (1986). The Upper Critical Zone of the Bushveld Complex and the origin of Merensky-type ores. Economic Geology, 81(5), 1105-1117.

Namur, O., Abily, B., Boudreau, A. E., Blanchette, F., Bush, J. W. M., Ceuleneer, G., . . . Veksler, I. V. (2015). Igneous Layering in Basaltic Magma Chambers. In Layered Intrusions (pp. 75-152).

Namur, O., Charlier, B., & Holness, M. B. (2012). Dual origin of Fe–Ti–P gabbros by immiscibility and fractional crystallization of evolved tholeiitic basalts in the Sept Iles layered intrusion. Lithos, 154, 100-114.

Namur, O., Charlier, B., Toplis, M. J., Higgins, M. D., Hounsell, V., Liégeois, J.-P., & Vander Auwera, J. (2011). Differentiation of tholeiitic basalt to A-type granite in the Sept Iles layered intrusion, Canada. Journal of Petrology, 52(3), 487-539.

Namur, O., Charlier, B., Toplis, M. J., Higgins, M. D., Liégeois, J.-P., & Vander Auwera, J. (2010).

Crystallization sequence and magma chamber processes in the ferrobasaltic Sept Iles layered intrusion, Canada. Journal of Petrology, 51(6), 1203-1236.

Namur, O., Humphreys, M. C., & Holness, M. B. (2013). Lateral reactive infiltration in a vertical gabbroic crystal mush, Skaergaard intrusion, East Greenland. Journal of Petrology, 54(5), 985-1016.

Naslund, H., Turner, P., & Keith, D. (1991). Crystallization and layer formation in the middle zone of the Skaergaard Intrusion.

Naslund, H. R., & McBirney, A. R. (1996). Mechanisms of formation of igenous layering. In R. G. Cawthorn (Ed.), Layered intrusions (pp. 1-43). Amsterdam: Elsevier.

Nicolas, A. (1989). Structures of ophiolites and dynamics of oceanic lithosphere. Dordrecht: Kluwer.

Nicolas, A. (1992). Kinematics in magmatic rocks with special reference to gabbros. Journal of Petrology, 33(4), 891-915.

Nicolas, A. (2003). High-temperature seawater circulation throughout crust of oceanic ridges: A model derived from the Oman ophiolites. Journal of Geophysical Research, 108(B8). doi:10.1029/2002jb002094

Nicolas, A., & Boudier, F. (2000). Large mantle upwellings and related variations in crustal thickness in the Oman ophiolite.

Nicolas, A., & Boudier, F. (2011). Structure and dynamics of ridge axial melt lenses in the Oman ophiolite. Journal of Geophysical Research: Solid Earth, 116(B3).

Nicolas, A., Boudier, F., & France, L. (2009). Subsidence in magma chamber and the development of magmatic foliation in Oman ophiolite gabbros. Earth and Planetary Science Letters, 284(1), 76-87. doi:https://doi.org/10.1016/j.epsl.2009.04.012

Nicolas, A., Boudier, F., & Ildefonse, B. (1994). Evidence from the Oman Ophiolite for Active Mantle Upwelling beneath a Fast-Spreading Ridge. Nature, 370(6484), 51-53.

Nicolas, A., Boudier, F., & Ildefonse, B. (1996). Variable crustal thickness in the Oman ophiolite: Implication for oceanic crust. Journal of Geophysical Research: Solid Earth, 101(B8), 17941-17950. doi:10.1029/96jb00195

Nicolas, A., Boudier, F., Ildefonse, B., & Ball, E. (2000). Accretion of Oman and United Arab Emirates ophiolite - Discussion of a new structural map. Marine Geophysical Researches, 21(3-4), 147-179.

Nicolas, A., & Ildefonse, B. (1996). Flow mechanism and viscosity in basaltic magma chambers. Geophysical Research Letters, 23(16), 2013-2016.

Nicolas, A., & Rabinowicz, M. (1988). Mantle flow pattern at oceanic spreading centres: relation with ophiolitic and oceanic structures. In I. G. Gass, S. J. Lippard, & A. W. Shelton (Eds.), Ophiolites and oceeanic lithosphere. Spec. Publ. Geol. Soc. London, Vol. 14 (pp. 147-151).

Nicolas, A., Reuber, I., & Benn, K. (1988). A new magma chamber model based on structural studies in the Oman ophiolite. Tectonophysics, 151(1-4), 87-105.

Nozaka, T., Meyer, R., Wintsch, R. P., & Wathen, B. (2016). Hydrothermal spinel, corundum and diaspore in lower oceanic crustal troctolites from the Hess Deep Rift. Contributions to Mineralogy and Petrology, 171(6), 53.

Oeser, M., Strauss, H., Wolff, P. E., Koepke, J., Peters, M., Garbe-Schönberg, D., & Dietrich, M. (2012). A profile of multiple sulfur isotopes through the Oman ophiolite. Chemical Geology, 312, 27-46.

Onorato, P., Hopper, R., Yinnon, H., Uhlmann, D. R., Taylor, L., Garrison, J., & Hunter, R. (1981). Solute partitioning under continuous cooling conditions as a cooling rate indicator. Journal of Geophysical Research: Solid Earth, 86(B10), 9511-9518.

Orcutt, J. A., Kennett, B. L., & Dorman, L. M. (1976). Structure of the East Pacific Rise from an ocean bottom seismometer survey. Geophysical Journal International, 45(2), 305-320.

Osborn, E. (1978). Change in phase relations in response to change in pressure from I atm to 10 kbar for the system Mg2SiO4-iron oxide-CaAl2SieO8-SiOe: Carnegie Inst. Washington. Year Book, 77, 784-790.

Pallister, J. S., & Gregory, R. T. (1983). Composition of the Samail ocean crust. Geology, 11(11), 638-642.

Pallister, J. S., & Hopson, C. A. (1981). Samail Ophiolite plutonic suite: Field relations, phase variation, cryptic variation and layering, and a model of a spreading ridge magma chamber. Journal of Geophysical Research, 86, B4, 2593-2644.

Pang, K.-N., Li, C., Zhou, M.-F., & Ripley, E. M. (2009). Mineral compositional constraints on petrogenesis and oxide ore genesis of the late Permian Panzhihua layered gabbroic intrusion, SW China. Lithos, 110(1-4), 199-214.

Pang, K.-N., Zhou, M.-F., Lindsley, D., Zhao, D., & Malpas, J. (2008). Origin of Fe–Ti oxide ores in mafic intrusions: evidence from the Panzhihua intrusion, SW China. Journal of Petrology, 49(2), 295-313.

Pearce, J. A., Alabaster, T., Shelton, A., & Searle, M. P. (1981). The Oman ophiolite as a Cretaceous arc-basin complex: evidence and implications. Philosophical Transactions of the Royal Society of London. Series A, Mathematical and Physical Sciences, 300(1454), 299-317.

Perk, N. W., Coogan, L. A., Karson, J. A., Klein, E. M., & Hanna, H. D. (2007). Petrology and geochemistry of primitive lower oceanic crust from Pito Deep: implications for the accretion of the lower crust at the Southern East Pacific Rise. Contributions to Mineralogy and Petrology, 154(5), 575-590. doi:10.1007/s00410-007-0210-z

Phipps Morgan, J. P., & Chen, Y. J. (1993). The genesis of oceanic-crust - magma injection, hydrothermal circulation, and crustal rlow. Journal of Geophysical Research-Solid Earth, 98(B4), 6283-6297.

Pirajno, F. (1992). Hydrothermal Processes in Oceanic Crust and Related Mineral Deposits. In Hydrothermal Mineral Deposits: Principles and Fundamental Concepts for the Exploration Geologist (pp. 450-506). Berlin, Heidelberg: Springer Berlin Heidelberg.

Pouchou, J. L., & Pichoir, F. (1991). Quantitative analysis of homogeneous or stratified microvolumes applying the model "PAP". In K. F. J. Heinrich & D. E. Newbury (Eds.), Electron probe quantification (pp. 31-75). New York: Plenum Press.

Prior, D. J., Mariani, E., & Wheeler, J. (2009). EBSD in the earth sciences: applications, common practice, and challenges. In Electron backscatter diffraction in materials science (pp. 345-360): Springer.

Quick, J. E., & Denlinger, R. P. (1993). Ductile deformation and the origin of layered gabbro in ophiolites. Journal of Geophysical Research: Solid Earth, 98(B8), 14015-14027. doi:10.1029/93jb00698

Raedeke, L., & McCallum, I. (1984). Investigations in the Stillwater complex: Part II. Petrology and petrogenesis of the ultramafic series. Journal of Petrology, 25(2), 395-420.

Ramsay, J., & Graham, R. (1970). Strain variation in shear belts. Canadian Journal of Earth Sciences, 7(3), 786-813.

Rioux, M., Bowring, S., Kelemen, P., Gordon, S., Dudas, F., & Miller, R. (2012a). Rapid crustal accretion and magma assimilation in the Oman-UAE ophiolite: High precision U-Pb zircon geochronology of the gabbroic crust. Journal of Geophysical Research-Solid Earth, 117. doi:B0720110.1029/2012jb009273

Rioux, M., Bowring, S., Kelemen, P., Gordon, S., Miller, R., & Dudas, F. (2013). Tectonic development of the Samail ophiolite: High-precision U-Pb zircon geochronology and Sm-Nd isotopic constraints on crustal growth and emplacement. Journal of Geophysical Research-Solid Earth, 118(5), 2085-2101. doi:10.1002/jgrb.50139

Rioux, M., Lissenberg, C. J., McLean, N. M., Bowring, S. A., MacLeod, C. J., Hellebrand, E., & Shimizu, N. (2012b). Protracted timescales of lower crustal growth at the fast-spreading East Pacific Rise. Nature Geoscience, 5(4), 275-278. doi:10.1038/ngeo1378

Rospabe, M., Benoit, M., Ceuleneer, G., Kaczmarek, M. A., & Hodel, F. (2019). Melt hybridization and metasomatism triggered by syn-magmatic faults within the Oman ophiolite: A clue to understand the genesis of the dunitic mantle-crust transition zone. Earth and Planetary Science Letters, 516, 108-121. doi:10.1016/j.epsl.2019.04.004

Rospabe, M., Ceuleneer, G., Benoit, M., Abily, B., & Pinet, P. (2017). Origin of the dunitic mantle-crust transition zone in the Oman ophiolite: The interplay between percolating magmas and high-temperature hydrous fluids. Geology, 45(5), 471-474. doi:10.1130/g38778.1

Satsukawa, T., Ildefonse, B., Mainprice, D., Morales, L. F. G., Michibayashi, K., & Barou, F. (2013). A database of plagioclase crystal preferred orientations (CPO) and microstructures - implications for CPO origin, strength, symmetry and seismic anisotropy in gabbroic rocks. Solid Earth, 4(2), 511-542. doi:10.5194/se-4-511-2013

Sauerzapf, U., Lattard, D., Burchard, M., & Engelmann, R. (2008). The titanomagnetite–ilmenite equilibrium: new experimental data and thermo-oxybarometric application to the crystallization of basic to

intermediate rocks. Journal of Petrology, 49(6), 1161-1185.

Schaeben, H. (1999). The de la Vallée Poussin standard orientation density function. Texture, Stress, and Microstructure, 33(1-4), 365-373.

Searle, R. (2013). Mid-ocean ridges: Cambridge University Press.

Shejwalkar, A., & Coogan, L. A. (2013). Experimental calibration of the roles of temperature and composition in the Ca-in-olivine geothermometer at 0.1MPa. Lithos, 177, 54-60. doi:10.1016/j.lithos.2013.06.013

Sisson, T. W., & Grove, T. L. (1993). Experimental investigations of the role of H2O in calc-alkaline differentiation and subduction zone magmatism. Contributions to Mineralogy and Petrology, 113, 143-166.

Skemer, P., Katayama, I., Jiang, Z., & Karato, S.-i. (2005). The misorientation index: Development of a new method for calculating the strength of lattice-preferred orientation. Tectonophysics, 411(1-4), 157-167.

Sleep, N. H. (1975). Formation of oceanic crust: Some thermal constraints. Journal of Geophysical Research, 80(29), 4037-4042. doi:10.1029/JB080i029p04037

Sørensen, H., & Larsen, L. M. (1987). Layering in the Ilímaussaq alkaline intrusion, South Greenland. In Origins of igneous layering (pp. 1-28): Springer.

Sparks, R. S., Huppert, H. E., Koyaguchi, T., & Hallworth, M. A. (1993). Origin of modal and rhythmic igneous layering by sedimentation in a convecting magma chamber. Nature, 361(6409), 246.

Sun, C., & Liang, Y. (2017). A REE-in-plagioclase–clinopyroxene thermometer for crustal rocks. Contributions to Mineralogy and Petrology, 172(4). doi:10.1007/s00410-016-1326-9

Tamura, A., & Arai, S. (2006). Harzburgite–dunite–orthopyroxenite suite as a record of supra-subduction zone setting for the Oman ophiolite mantle. Lithos, 90(1-2), 43-56.

Teagle, D. A., Ildefonse, B., & Blum, P. (2012). IODP expedition 335: deep sampling in ODP hole 1256D. Scientific Drilling, 13, 28-34.

Tegner, C., & Wilson, R. (1991). Late intrusive ultramafic suite in the Taco Point area of the Kap Edward Holm layered gabbro complex, East Greenland.

Tilton, G. R., Hopson, C. A., & Wright, J. E. (1981). Uranium-lead isotopic ages of the Samail Ophiolite, Oman, with applications to tethyan ocean ridge tectonics. Journal of Geophysical Research, 86, B4, 2763-2775.

Toplis, M., & Carroll, M. (1995). An experimental study of the influence of oxygen fugacity on Fe-Ti oxide stability, phase relations, and mineral—melt equilibria in ferro-basaltic systems. Journal of Petrology, 36(5), 1137-1170.

Ueki, K., & Iwamori, H. (2016). Density and seismic velocity of hydrous melts under crustal and upper mantle conditions. Geochemistry, Geophysics, Geosystems, 17(5), 1799-1814.

VanTongeren, J. A., Hirth, G., & Kelemen, P. B. (2015). Constraints on the accretion of the gabbroic lower oceanic crust from plagioclase lattice preferred orientation in the Samail ophiolite. Earth and Planetary Science Letters, 427, 249-261. doi:10.1016/j.epsl.2015.07.001

VanTongeren, J. A., Kelemen, P. B., & Hanghøj, K. (2008). Cooling rates in the lower crust of the Oman ophiolite: Ca in olivine, revisited. Earth and Planetary Science Letters, 267(1-2), 69-82. doi:10.1016/j.epsl.2007.11.034

Vera, E. E., Mutter, J. C., Buhl, P., Orcutt, J. A., Harding, A. J., Kappus, M. E., . . . Brocher, T. M. (1990). The structure of 0-my to 0.2-my old oceanic crust at 9° N on the East Pacific Rise from expanded spread profiles. Journal of Geophysical Research-Solid Earth and Planets, 95(B10), 15529-15556. doi:10.1029/JB095iB10p15529

Vernon, R. H. (2000). Review of Microstructural Evidence of Magmatic and Solid-State Flow. Visual Geosciences, 5(2), 1-23. doi:10.1007/s10069-000-0002-3

Vollmer, F. W. (1990). An application of eigenvalue methods to structural domain analysis. Geological Society of America Bulletin, 102(6), 786-791.

Vukmanovic, Z., Holness, M., Monks, K., & Andersen, J. Ø. (2018). The Skaergaard trough layering: sedimentation in a convecting magma chamber. Contributions to Mineralogy and Petrology, 173(5), 43.

Wager, L. (1959). Differing powers of crystal nucleation as a factor producing diversity in layered igneous intrusions. Geological Magazine, 96(1), 75-80.

Wager, L. R., & Brown, G. M. (1968). Layered igneous rocks. Edinburgh and London: Oliver and Boyd.

Warren, C. J., Parrish, R. R., Searle, M. P., & Waters, D. J. (2003). Dating the subduction of the Arabian continental margin beneath the Semail ophiolite, Oman. Geology, 31(10), 889-892.

Warren, C. J., Parrish, R. R., Waters, D. J., & Searle, M. P. (2005). Dating the geologic history of Oman's Semail ophiolite: insights from U-Pb geochronology. Contributions to Mineralogy and Petrology, 150(4), 403-422. doi:10.1007/s00410-005-0028-5

Wolff, P. E. (2013). Hydrothermal circulation from very high to low temperatures in the lower oceanic crust - Evidence from layered gabbros from the Oman Ophiolite and from partial melting experiments on oceanic gabbros. (PhD). University of Hannover,

Wright, S. I., Nowell, M. M., & Field, D. P. (2011). A review of strain analysis using electron backscatter diffraction. Microscopy and microanalysis, 17(3), 316-329.

Yamasaki, T., Maeda, J., & Mizuta, T. (2006). Geochemical evidence in clinopyroxenes from gabbroic sequence for two distinct magmatisms in the Oman ophiolite. Earth and Planetary Science Letters, 251, 52-65.

Yoshinobu, A. S., & Hirth, G. (2002). Microstructural and experimental constraints on the rheology of partially molten gabbro beneath oceanic spreading centers. Journal of Structural Geology, 24(6), 1101-1107. doi:https://doi.org/10.1016/S0191-8141(01)00094-3

Zhang, Y., Ni, H., & Chen, Y. (2010). Diffusion data in silicate melts. Reviews in Mineralogy and Geochemistry, 72(1), 311-408.

Zhao, J.-H., & Asimow, P. D. (2014). Neoproterozoic boninite-series rocks in South China: A depleted mantle source modified by sediment-derived melt. Chemical Geology, 388, 98-111.

Zhou, M.-f., Robinson, P. T., Lesher, C. M., Keays, R. R., Zhang, C.-J., & Malpas, J. (2005). Geochemistry, petrogenesis and metallogenesis of the Panzhihua gabbroic layered intrusion and associated Fe–Ti–V oxide deposits, Sichuan Province, SW China. Journal of Petrology, 46(11), 2253-2280.

Zihlmann, B., Müller, S., Coggon, R. M., Koepke, J., Garbe-Schönberg, D., & Teagle, D. A. H. (2018). Hydrothermal fault zones in the lower oceanic crust: An example from Wadi Gideah, Samail ophiolite, Oman. Lithos, 323, 103-124. doi:10.1016/j.lithos.2018.09.008

References from the Supplemental Material

Abily, B., Ceuleneer, G., & Launeau, P. (2011). Synmagmatic normal faulting in the lower oceanic crust: Evidence from the Oman ophiolite. Geology, 39(4), 391–394. https://doi.org/10.1130/g31652.1

Boudreau, A. (1987). Pattern formation during crystallization and the formation of fine-scale layering. In Origins of Igneous Layering (pp. 453–471). Dordrecht: Springer.

Boudreau, A. (1999). Fluid fluxing of cumulates: The JM reef and associated rocks of the Stillwater Complex, Montana. Journal of Petrology, 40(5),755–772. https://doi.org/10.1093/petroj/40.5.755

Boycott, A. (1920). Sedimentation of blood corpuscles. Nature, 104(2621), 532–532. https://doi.org/10.1038/104532b0

Brown, P., & Farmer, D. (1971). Size-graded layering in the Imilik gabbro, East Greenland. Geological Magazine, 108(6), 465–476. https://doi.org/10.1017/S0016756800056661

Dick, H. J., & Sinton, J. M. (1979). Compositional layering in alpine peridotites: Evidence for pressure solution creep in the mantle. The Journal of Geology, 87(4), 403–416. https://doi.org/10.1086/628428

Feig, S., Koepke, J., & Snow, J. (2006). Effect of water on tholeiitic basalt phase equilibria: An experimental study under oxidizing conditions. Contributions to Mineralogy and Petrology, 152, 611–638. https://doi.org/10.1007/s00410-006-0123-2

Ferguson, J., & Pulvertaft, T. (1963). Contrasted styles of igneous layering in the Gardar province of South Greenland. Special Papers - Mineralogical Society of America, 1, 10–21.

Gaetani, G. A., Grove, T. L., & Bryan, W. B. (1993). The influence of water on the petrogenesis of subductionrelated igneous rocks. Nature, 365(6444), 332–334. https://doi.org/10.1038/365332a0

Gorring, M. L., & Naslund, H. (1995). Geochemical reversals within the lower 100 m of the Palisades sill, New Jersey. Contributions to Mineralogy and Petrology, 119(2–3), 263–276. https://doi.org/10.1007/BF00307286

Hawkes, D. (1967). Order of abundant crystal nucleation in a natural magma. Geological Magazine, 104(5), 473–486. https://doi.org/10.1017/S0016756800049219

Higgins, M. D. (1991). The origin of laminated and massive anorthosite, Sept Iles layered intrusion, Quebec, Canada. Contributions to Mineralogy and Petrology, 106(3), 340–354. https://doi.org/10.1007/BF00324562

Higgins, M. D. (2011). Textural coarsening in igneous rocks. International Geology Review, 53(3–4), 354–376. https://doi.org/10.1080/00206814.2010.496177

Hoffer, A. (1965). Seismic control of layering in intrusions. American Mineralogist: Journal of Earth and Planetary Materials, 50(7–8), 1125–1128.

Huppert, H. E., & Sparks, R. S. J. (1981). The fluid dynamics of a basaltic magma chamber replenished by influx of hot, dense ultrabasic magma. Contributions to Mineralogy and Petrology, 75(3), 279–289. https://doi.org/10.1007/BF01166768

Irvine, N. (1980a). Magmatic infiltration metasomatism, double diffusive fractional crystallization, and adcumulus growth in the Muskox intrusion and other layered intrusions. In *Physics of Magmatic Processes*. https://doi.org/10.1515/9781400854493.325 (325–384). Princeton, New Jersey: Princeton University Press.

Irvine, T. N. (1974). *Petrology of the Duke Island Ultramafic Complex, Southeastern Alaska* (Vol. 138, Boulder, Colorado:). Geological Society of America.

Jackson, E. (1961). Primary Textures and Mineral Associations in the Ultramafic Zone of the Stillwater Complex, Montana: US Geol. Survey Prof. Paper 358, 106 p. 1963, Chromium. *23rd Session*, Sec, 1, 135–140.

Jousselin, D., Morales, L. F. G., Nicolle, M., & Stephant, A. (2012). Gabbro layering induced by simple shear in the Oman ophiolite Moho transition zone. Earth and Planetary Science Letters, 331–332, 55–66. https://doi.org/10.1016/j.epsl.2012.02.022

Korzhinskii, D. (1968). The theory of metasomatic zoning. Mineralium Deposita, 3(3), 222–231. https://doi.org/10.1007/bf00207435

Lesher, C., & Walker, D. (1988). Cumulate maturation and melt migration in a temperature gradient. Journal of Geophysical Research, 93(B9), 10,295–10,311. https://doi.org/10.1029/JB093iB09p10295

Liesegang, R. (1896). Ueber einige eigenschaften von gallerten. Naturwissenschaftliche Wochenschrift, 10(30), 353–362.

Lipin, B. R. (1993). Pressure increases, the formation of chromite seams, and the development of the ultramafic series in the Stillwater Complex, Montana. Journal of Petrology, 34(5), 955–976. https://doi.org/10.1093/petrology/34.5.955

Marsh, B. D. (1989). On convective style and vigor in sheet-like magma chambers. Journal of Petrology, 30(3), 479–530. https://doi.org/10.1093/petrology/30.3.479

McBirney, A. R. (1987). Constitutional zone refining of layered intrusions. In *Origins of Igneous Layering* (pp. 437–452). Dordrecht: Springer.

McBirney, A. R., & Nakamura, Y. (1974). Immiscibility in late-stage magmas of the Skaergaard intrusion. Carnegie Institution of Washington Yearbook, 73, 348–352.

McBirney, A. R., & Noyes, R. M. (1979). Crystallization and layering of the Skaergaard intrusion. Journal of Petrology, 20(3), 487–554. https://doi.org/10.1093/petrology/20.3.487

Moore, A. C. (1973). Studies of igneous and tectonic textures and layering in the rocks of the Gosse Pile intrusion, Central Australia. Journal of Petrology, 14(1), 49–79. https://doi.org/10.1093/petrology/14.1.49

Müller, T., Koepke, J., Garbe-Schonberg, C. D., Dietrich, M., Bauer, U., & Wolff, P. B. (2017). Anatomy of a frozen axial melt lens from a fast-spreading paleo-ridge (Wadi Gideah, Oman ophiolite). Lithos, 272–273, 31–45. https://doi.org/10.1016/j.lithos.2016.11.022

Namur, O., Abily, B., Boudreau, A. E., Blanchette, F., Bush, J. W. M., Ceuleneer, G., Charlier, B., Donaldson, C. H., Duchesne, J. C., Higgins, M. D., Morata, D., & Veksler, I. V. (2015). Igneous layering in basaltic magma chambers. In *Layered Intrusions* (pp. 75–152). Dordrecht: Springer.

Naslund, H., Turner, P., & Keith, D. (1991). Crystallization and Layer Formation in the Middle Zone of the Skaergaard Intrusion.

Naslund, H. R., & McBirney, A. R. (1996). Mechanisms of formation of igenous layering. In R. G. Cawthorn (Ed.), Layered Intrusions (pp. 1–43). Amsterdam: Elsevier. https://doi.org/10.1016/S0167-2894(96)80003-0

Petersen, J. S. (1987). Solidification contraction: Another approach to cumulus processes and the origin of igneous layering. In *Origins of Igneous Layering* (pp. 505–526). Dordrecht: Springer.

Sparks, R. S. J., Huppert, H. E., Kerr, R., McKenzie, D., & Tait, S. R. (1985). Postcumulus processes in layered intrusions. Geological Magazine, 122(5), 555–568. https://doi.org/10.1017/S0016756800035470

Ulmer, G. (1969). Experimental investigations of chromite spinels. Magmatic Ore Deposits. Symp. Econ. Geol. Monograph, 4, 114–131). Michigan: Economic Geology Publishing Company...

Wilson, J. R., Menuge, J. F., Pedersen, S., & Engell-Sørensen, O. (1987). The southern part of the Fongen-Hyllingen layered mafic complex, Norway: Emplacement and crystallization of compositionally stratified magma. In *Origins of Igneous Layering* (pp. 145–184). Dordrecht: Springer.

Supplemental Tables

Supplemental Table S-1   Layer-forming processes compiled after Naslund and McBirney (1996) and Namur et al. (2015) and evaluated in the context of the layered gabbro sequences from our study

#	process	reference	argumentation
1	crystal settling [a,b]	**Brown and Farmer (1971)**	Concentration of olivine and mostly clinopyroxene at layer bases implies gravity-triggered phase segregation in Wadi Somerah. The absence of systematic grain size grading within layers and the high abundance of buoyant plagioclase in melanocratic layer bases is however not consistent with simple crystal settling. If crystal settling plays a role, it moreover requires a process (e.g., #4) driving cyclic layer formation.
2	density currents [a,b]	**Irvine (1974)**	Gravity-triggered phase and grain size segregation, as expected for #1, could by superimposed by several kinetic processes in a magma current. Currents would result in graded modal layer with occasionally disturbed phase separation by density and grain size, weak or absent compositional interphase correlation, lineation of elongated grains, and sedimentary deposition structures (e.g., discordant cross-cutting layer contacts) which we can find more or less well pronounced in the profile from Wadi Somerah.
3	continuous convection [a,b]	**Jackson (1961)**	Changes in liquidus phase assemblage due to P-T conditions at top and base of a convection cell are suggested to be significant in large magma chambers with a vertical extent of about 4 km (Naslund and McBirney, 1996). Such dimensions are discarded by seismic studies beneath MORs.
4	intermittent convection [a,b]	**Naslund et al. (1991)**	If the temperature gradient is sufficient within a magma chamber, (intermittent) convection may occur. Intermittent convection may serve as creator of cyclic layering, combined with, e.g., process #1; Plagioclase being buoyant - even in a stagnant magma - as shown by modeling in our study, is not consistent with high plagioclase abundance in melanocratic olivine-rich layer bases at Wadi Somerah and Wadi Wariyah.
5	double diffusive convection [a,b]	**McBirney and Noyes (1979)**	Liesegang banding could be seen as a double-diffusive process where mass and heat diffuse and their coupling leads to oscillatory nucleation as is further described in process #24.
6	magma injection / magma mixing [a,b]	**Huppert and Sparks (1981); Lipin (1993)**	A magmatic recharge event could possibly have been recorded by compositional and textural changes within layer 2 at Wadi Somerah. Magmatic recharge may occur in a crustal magma chamber, however does not necessarily drive the formation of modal layering by resetting the crystallization sequence. Layer formation by magma injection would create systematic cryptic layering with layer bases being more primitive than layer tops.
7	Liquid hybridization and hydration [a]	**Abily et al. (2011)**	If hydration of a magma is sufficient to suppress plagioclase nucleation (e.g., Gaetani et al., 1993; Feig et al., 2006), olivine and clinopyroxene crystallize and form ultramafic wehrlite cumulates. Repeating this process results in rhythmic modal layering. However, even the olivine-rich parts of our profiles are far from wehrlitic phase assemblage. Therefore, this process is not applicable to the layering of our study.
8	Magma migration during crystal mush contraction [a]	**Peterson (1987)**	Shrinkage of a magma body during solidification leads to a pressure gradient in the body and as a result, the liquid migrates from crystal-poor zones into the crystal mush. Thermo- and chemical disequilibrium between solids from the mush and the infiltrating liquid leads to partial dissolution of preferentially mafic phases and hence the formation of layering. Core-rim analyses in the clinopyroxenes of our samples reveal only weak zonation being inconsistent with the significant chemical disequilibrium expected between evolved liquid and primitive solids.
9	Hydrous fluid fluxing through cumulate rock [a]	**Boudreau (1999)**	Flux of a volatile-rich liquid into the solidifying gabbroic crystal mush affects cotectic crystallization with clinopyroxene being favored over plagioclase and dissolution of plagioclase leads to a pyroxene-rich residual. Our rocks however, contain large amounts of plagioclase usually being the major component.

10	immiscibility [a,b]	McBirney and Nakamura (1974)	In order to separate a mafic magma into two immiscible liquids that crystallize and form different layers, an "extreme degree of iron-enrichment" (Naslund and McBirney, 1996) is required. High differentiation indices as well as similar mineral compositions in all layers are inconsistent with the model of two immiscible melts having separated from a common magma.
11	nucleation and crystals growth rate fluctuations [a,b]	Hawkes (1967)	Different nucleation rates in an undercooled magma are assumed for different phases, depending on their structural complexity. In order to create rhythmic layering by such a mechanism, undisturbed and stable undercooling of an intrusive body is required which is not expected in an environment of high melt flux, like a fast-spreading MOR.
12	pressure fluctuations [a,b]	Ferguson and Pulvertaft (1963)	Significantly changing overall or vapour pressure may provoke different phase assemblages. Experimental results (Feig et al., 2006) have shown, however, that the crystallization sequence of olivine - plagioclase - clinopyroxene is resistent against the small pressure fluctuations that could occur, e.g., in the dynamic axial melt lens (Müller et al., 2017).
13	oxygen fugacity fluctuations [a,b]	Ulmer (1969)	Changes in oxygen fugacity potentially control the phases crystallized. If oxygen fugacity significantly changes, layers poor of oxides and some rich of oxides are expected to crystallize. In our profiles, we do not find significant amounts of primary oxides, neither in melanocratic nor in leucocratic layer regions, indicating that there was no significant oxygen fugacity fluctuation during crystallization of the profiles.
14	compaction [a,b]	Higgins (1991)	Layers of compositionally different phases/lithologies may form if liquid is expelled from a magma by compaction. In our profiles, we do not observe different lithologies or compositional variations being consistent with significantly different melt compositions. Intracrystalline deformation, as expected to be produced by strong compaction, is not observed.
15	dissolution-precipitation [a]	Dick and Sinton (1979)	In the environment of alternating high- and low-strain domains of a solidified crystal mush, minerals tend to dissolve in regions of high stress. Pressure-sensitive phases become dissolved in high-stress levels and may reprecipitate in low-stress levels, leaving regions depleted in that phase behind. Grains in the low-stress domains will grow at the expense of minerals from high-stress domains leading also to grain size layering which we do not observe in Wadi Somerah. The coarser olivine grains in olivine-rich bands from Wadi Wariyah are discussed in #30.
16	layering by grain coarsening and changing liquid composition [a]	Higgins (2011)	Coarsening of a phase in a multi-saturared magma is expected when this phase starts crystallizing just below the liquidus of the other phases. Small grains of the last crystallizing phase will dissolve in the interstitial liquid while larger ones will grow replacing the liquid and forming oikocrysts. If all three phases crystallize at the same liquidus temperature, or the liquidus of the third phase is significantly lower than that of the first previously crystallizing ones, the texture will not be poikilitic but granular and textural layering may occur. We do not observe textural layering in our samples.
17	chemical diffusion in the crystal mush [a]	Korzhinskii (1968)	Redox gradients at lithological contacts may result in Na diffusion in interstitial provoking isothermal partial melting and dissolution of a phase (Namur et al., 2015). The remainder may form monomineralic layers with sharp contacts. The profiles we investigated show neither sharp contacts nor monomineralic layers, but alway plagioclase and clinopyroxene ± olivine assemblages.
18	crystallization along inclined surface [a]	Wilson et al. (1987)	Particles settling from an inclined wall leave behind a layer of clear fluid ("Boycott effect"; Boycott, 1920) which is buoyant and rises along the wall until it reaches neutral buoyancy. Here, it intrudes horizontally into the crystal mush leading to the formation of layering. If olivine-poor leucocratic layer tops in Wadi Somerah were assumed to have crystallized from that clear fluid, which in that case is the residual melt from the mafic layer base, systematically more fractionated layer tops could be expected. We do not observe systematic compositional differences between layer bases and their tops which discards this process as having formed the analyzed layering.
19	crystals carried in suspension [b]	Marsh (1989)	Phenocrysts carried in suspension can form well-defined layering when large and dense phases sink from suspension to the accumulation front. The clear lack of large phenocrysts and limited grain size variation between the layers of this study discard this process; however, other gravity-driven processes are discussed in #1 and #2.
20	flow segregation [b]	Gorring and Naslund (1995)	In a phenocryst-rich magma, the Bagnold effect results in solid particles migrating towards regions with the minimum shear. Their accumulation and the flow segregation may lead to layer formation. Similar to process #19, the lack of phenocrysts and only weak grain size differences between the layers discard this mechanism for our profiles.

#	Process	Reference	Description
21	simple shear by magmatic deformation [b]	Jousselin et al. (2012)	Simple shear induced by deformation, as it is described by many studies as a post-cumulus process in Oman, can emphasize initial cumulate heterogeneities, or even create them. Mineral lineations observed in the field are consistent not only with process #2, but also with post-cumulate deformation. Planar plagioclase and olivine fabrics in Wadi Wariyah are however not consistent with simple shear being the only layer-forming process.
22	seismic shocks [b]	Hoffer (1965)	In a supersaturated liquid, seismic shocks are assumed to drive crystallization. In our profiles, we did not find evidence for rapid crystallization in response to periodic seismic events.
23	tectonic deformation [b]	Moore (1973)	Changes from magmatic to tectonic deformation may occur gradually and indicators for both can be observed in some localities. Since we consider the magmatic deformation (see #21) in our samples being induced by spreading and/or active mantle flow, a tectonic component into this deformation may be involved, even if the observed foliation and lineation are essentially magmatic.
24	diffusion-controlled nucleation and growth [b]	McBirney and Noyes (1979)	Compatible elements diffusing from the melt towards a crystallization front leave a zone of depletion adjacent to the crystallization front, and hence a zone free of nucleation. Decreasing temperature can stabilize a second crystallization front at a certain distance from the first one, which is not concerned by depletion of compatible elements. This mechanism, the Liesegang banding (Liesegang, 1896), could explain mm-scale bands of olivine abundance in Wadi Wariyah, although it cannot be proved by our data.
25	crystal growth in thermal gradients [b]	Lesher and Walker (1988)	Thermal differences in a magma body drive mass transport promoting crystal growth in cooler and melt migration towards warmer regions (Naslund and McBirney, 1996). Lesher and Walker (1988) estimate that mass re-organization of tens of centimeters can be a result from heat migration in a magma body with a height of about 1 km. This dimension is inconsistent with the relatively small melt lens(es) found by seismic studies beneath recent fast-spread MORs.
26	interstitial crystal growth [b]	Sparks et al. (1985)	Interstitial crystal growth can form monomineralic layers if the interstitial liquid in an adcumulus is efficiently exchanged at the crystal-melt interface (if solidification rate is very low) or within the mush by convective transfer (Naslund and McBirney, 1996). The expected monomineralic layers are not observed in our profiles.
27	metasomatism [b]	Irvine (1980)	Metasomatism of cumulates could re-equilibrate cumulus minerals with intercumulus liquid which migrate upwards and solidify forming coarse to pegmatoid layers with mineral assemblages being significantly different from the host rock. These features do not fit the petrographic features of the sampled profiles in Wadi Somerah and Wadi Wariyah.
28	constitutional zone refining [b]	McBirney (1987)	Water percolating along grain boundaries could locally lead to decreased melting temperatures and therefore provoke partial melting leading to modally significantly different layers compared to their surroundings. Evidence for partial melting, however, is not observed in our profiles.
29	solidification contraction [b]	Peterson (1987)	This process - interstitial liquid being drawn into partially solidified crystal mushes - results in zones which appear to have large amounts of trapped liquid. Although there is a dm-thick region in Wadi Somerah that could have formed under the influence of increased amounts of trapped melt, there is generally no evidence for "large contents of trapped liquid" (Naslund and McBirney, 1996) being drawn into the crystal mush. Interstitial melt trapped in the mush during accumulation is expected to be a general result of processes #1 and #2 and should therefore not be able to form different layers.
30	ostwald ripening [b]	Boudreau (1987)	Due to their larger reactive surface, small grains are more sensitive to dissolution in a melt. Therefore, larger crystals which have nucleated earlier, can growth at the expense of dissolving smaller ones leading to zones being depleted or free of a phase and an enriched zone where grains are larger. The olivine grains in olivine-enriched bands from Wadi Wariyah are larger than those in the depleted zones indicating that such a process could have taken place. For layering formation, as it is observed in our sample from Wadi Wariyah, initial heterogeneity is required, possibly provided by process #24.
31	contact metamorphism [b]	Naslund et al. (1986)	In order to drive layer formation, contact metamorphism needs to drive partial melting as shown at the example of the Basistoppen sill in Skaergaard (Naslund et al., 1986). The layered gabbros from our profiles do not show evidence for partial melting (e.g., strong zoning of plagioclase, as it can be observed in the varitextured gabbros in Oman).

[a] process presented in Namur et al. (2015)
[b] process presented in Naslund and McBirney (1996)
red: process discarded; orange: process possible, however not provable by our data; green: process in agreement with our data

Supporting information to Supplemental Table S-1

The Samail ophiolite at the northeastern coast of the Sultanate of Oman is regarded as best-exposed analogue of fast-spreading mid-oceanic crust on land (e.g., Nicolas et al., 2000). Its crustal sequence covers the upper mantle, the lower and the upper crust, and marine sediments. The lower crust is composed of varitextured, foliated, and layered gabbros. The latter show prominent modal layering from mm- to dm-scales along wide areas of the ophiolite complex (e.g., Pallister and Hopson, 1981). Drilling performed at the recent East Pacific Rise recovered layered features similar to those observed in Oman indicating that layering in the lower oceanic crust is a common feature and an understanding of its formation is therefore crucial to understand magmatic processes beneath oceanic spreading centers. Our study was performed on two small scaled gabbro profiles, one with a height of approximately 3 m showing dm-scale modal layering with olivine being enriched at the layer bases and gradually decreasing upwards, and one with a height of 7 cm covering 11 mm-scale olivine-enriched diffuse bands. We applied petrographic, petrological, geochemical, and microstructural methods on the samples creating an interdisciplinary data set in order to find constraints for the formation of the observed modal layering. The supporting table 1 of this study lists layer-forming processes which have been compiled by Namur et al. (2015) reflecting the scientific effort in the past decades to understand igneous layer formation. Most of the cited studies focused on large continental intrusions. Nonetheless, we assume most of the suggested mechanisms being applicable also to smaller magmatic systems as we expect them within the lower oceanic crust (e.g., Detrick et al., 1987; Vera et al., 1990; Marjanovic et al., 2014). We evaluated the processes taking the parameters 1) geological setting of the Oman ophiolite, 2) field observations, 3) our data into account and tested their consistency with our findings. Processes being inconsistent with one or more of the parameters mentioned before are discarded (marked in red in the table), processes being generally consistent with all parameters but without clear indication by our study potentially play a role in layer formation (marked in yellow), and those processes which are consistent with the geological setting and field observations and which – at least in parts – find support by our data are assumed to play a key role in the formation of the observed layering (marked in green). We do not expect one of these processes being exclusively responsible for layer formation, but assume a – potentially subsequent – combination of several processes as it is pointed out in the discussion of our study.

Table S-2   Samples obtained from drill core GT1A and analytical methods applied to the samples.

#	thin section	D[a]	D[b] [m]	HaM[c] [m]	lithology[d]	PC	EPMA	EBSD	BRC	MTEC
1	3-3-27-40		4.38	1169.14	ol gb	x	x		x	x
2	1-5-2a		7.06	1166.77	ol gb	x	x	x		
3	1-5-2b		7.10	1166.73	ol gb	x	x	x		
4	5-3-34-46		7.58	1166.31	ol gb	x	x			
5	10-1-13-23		11.98	1162.42	ol-b gb	x	x			
6	1-10-2a		13.14	1161.40	ol-b gb	x	x			
7	1-10-2b		13.21	1161.33	ol gb	x	x		x	x
8	1-10-2c		13.30	1161.26	ox-b ol gb	x	x	x		
9	10-3-15-20		13.49	1161.09	ol gb	x	x			
10	10-3-52-60		13.86	1160.76	ol gb	x	x			
11	1-10-4A		14.11	1160.54	ol gb	x	x	x		
12	1-10-4Ba		14.61	1160.10	gb	x	x			
13	1-10-4Bb		14.66	1160.06	ol-ox-b gb	x	x	x		
14	1-10-4Bc	1	14.69	1160.03	ox-b ol gb	x	x			
		2	14.71	1160.01	gb	x	x		x	
15	1-10-4Bd	1	14.73	1160.00	ol-b gb	x	x			
		2	14.75	1159.98	ox-b ol gb	x	x			
		3	14.77	1159.96	ol-ox-b gb	x	x			
16	13-1-10-20		21.10	1154.37	ol gb	x	x			
17	13-1-43-55		21.43	1154.08	ol gb	x	x			
18	14-3-45-55		26.17	1149.89	ol gb	x	x			
19	1-14-4a	1	26.49	1149.61	ol gb	x	x			
		2	26.51	1149.60	gb	n/a	x			
		3	26.53	1149.58	ox-b ol gb	x	x			
20	1-14-4b		26.61	1149.51	ox-b ol gb	x	x			
21	1-14-4c		26.74	1149.39	ox-b gb	x	x			
22	15-1-46-51	1	27.54	1148.68	ol gb	x	x			
		2	27.56	1148.67	ol gb	x	x			
		3	27.58	1148.65	ol-b gb	x	x			
23	1-16-2a		31.24	1145.42	ox-b ol gb	x	x			
24	1-16-2b		31.32	1145.34	ox-b ol gb	x	x			
25	16-4-20-30	1	32.91	1143.94	ol-b gb	x	x	x	x	x
		2	32.92	1143.93	an	x	x	x	x	x
		3	32.94	1143.92	ol gb	x	x	x	x	x
26	OM-DP-BI-7		41.48	1136.38	ol gb	x	x	x		
27	20-1-25-35		42.60	1135.39	ol gb	x	x			
28	21-2-74-84	1	47.04	1131.47	ol gb	x	x			
		2	47.06	1131.45	ol gb	x	x			
		3	47.07	1131.44	ol gb	x	x			
29	22-2-5-15		49.15	1129.61	ol gb	x	x			
30	23-1-10-20		51.60	1127.44	ol gb	x	x			
31	OM-DP-BI-9		57.46	1122.27	ol gb	x	x	x		
32	26-3-55-65		62.87	1117.49	ol gb	x	x		x	

#	Sample	#			Lith						
33	1-29-2a	1	68.12	1112.86	ol-ox-am-b gb	x	x	x			
		2	68.16	1112.82	ox-b ol gb	x	x	x			
34	1-29-2b		68.23	1112.76	ox-b ol gb	x	x	x			
35	29-3-20-30		68.68	1112.36	ol gb	x	x				
36	1-31-3a	1	74.60	1107.14	gb	x	x				
		2	74.61	1107.13	tr	x	x				
		3	74.63	1107.11	ol-am-b gb	x	x				
37	1-31-3b		74.66	1107.08	ol-ox-am-b gb	x	x	x			
38	1-31-3c	1	74.72	1107.03	ox-b gb	x	x	x			
		2	74.74	1107.01	ox-b ol gb	x	x	x			
39	33-1-62-72		79.57	1102.74	ol gb	x	x				
40	1-33-2	1	80.26	1102.13	ol gb	x	x	x			
		2	80.28	1102.12	ol-b gb	x	x	x			
41	OM-DP-BI-12		83.99	1098.84	gb	x	x				
42	35-1-10-20	1	85.14	1097.83	gb	n/a	n/a				
		2	85.15	1097.82	we	x	x				
		3	85.17	1097.80	gb	n/a	n/a				
43	36-2-40-50	1	86.44	1096.68	gb	x	x				
		2	86.48	1096.65	gb	x	n/a				
44	37-1-10-20		88.20	1095.12	ol gb	x	x			x	
45	37-4-30-40		90.65	1092.96	ol gb	x	x				
46	38-2-30-38		92.32	1091.49	ox-am-b ol gb	x	x				
47	38-3-38-41		93.33	1090.60	ol gb	x	x				
48	38-4-36-40		94.00	1090.01	ol gb	x	x				
49	38-4-55-58		94.16	1089.87	ol gb	x	x				
50	44-2-2-12		101.72	1083.19	we	x	x				
51	44-3-17-24		102.69	1082.33	ol gb	x	x				
52	45-1-6-14		103.41	1081.69	ol gb	x	x	x			
53	1-45-1	1	104.13	1081.06	ol gb	x	x	x			
		2	104.15	1081.04	ol-b gb	x	x	x			
54	46-1-74-78		107.14	1078.40	gb	x	x				
55	1-46-2a	1	108.03	1077.62	ol-ox-b gb	x	x	x			
		2	108.06	1077.59	ox-b ol gb	x	x	x			
56	1-46-2b	1	108.09	1077.57	ol gb	x	x	x			
		2	108.12	1077.54	ol-b gb	x	x	x			
57	1-46-2c		108.17	1077.49	ox-b ol gb	x	x	x			
58	1-46-3a		108.73	1076.99	ox-b ol gb	x	x	x			x
59	1-46-3b		108.80	1076.94	ox-b ol gb	x	x	x		x	
60	1-46-3c		108.87	1076.87	ox-b ol gb	x	x				x
61	OM-DP-BI-15		109.64	1076.19	ox-b ol gb	x	x	x			
62	OM-DP-BI-17		124.75	1062.85	ox-b gb	x	x	x			
63	53-2-62-68		128.95	1059.14	gb	x	x				
64	1-53-3a	1	129.63	1058.54	ol gb	x	x	x			
		2	129.65	1058.52	ol gb	x	x	x			

No.	Sample	n								
65	1-53-3b	1	129.71	1058.47	gb	x	x	x		
		2	129.73	1058.45	ol gb	x	x	x		
		3	129.75	1058.44	ol gb	x	x	x		
66	1-54-4a	1	133.20	1055.39	ol-b gb	x	x	x		
		2	133.22	1055.38	ol gb	x	x	x	x	
		3	133.23	1055.37	ol-b gb	x	x	x		
67	1-54-4b	1	133.28	1055.32	ol gb	x	x	x		
		2	133.29	1055.31	ol-b gb	x	x	x		
		3	133.30	1055.30	ol gb	x	x	x	x	
		4	133.31	1055.29	gb	x	x	x		
		5	133.32	1055.28	ol gb	x	x	x		
68	55-3-3-12		135.46	1053.40	ol gb	x	x			
69	55-4-28-34		136.48	1052.49	ol gb	x	x			
70	57-1-9-15		137.99	1051.16	ol gb	x	x			
71	1-58-1a		140.05	1049.35	ol gb	x	x	x		
72	1-58-1b	1	140.15	1049.25	ol gb	x	x	x	x	
		2	140.17	1049.24	ol gb	x	x	x		
73	1-61-2	1	146.93	1043.27	ol gb	x	x	x		
		2	146.95	1043.25	ol-b gb	x	x	x		
74	OM-DP-BI-23		160.32	1031.44	ol gb	x	x	x		
75	1-72-4	1	178.79	1015.14	ol gb	x	x	x	x	x
		2	178.80	1015.13	tr	x	x	x	x	x
		3	178.82	1015.11	ol gb	x	x	x	x	x
76	1-73-4a		181.92	1012.37	ol gb	x	x	x		
77	1-73-4b		181.98	1012.32	ol gb	x	x			
78	OM-DP-BI-27		194.88	1000.93	gb	x	x			
79	82-1-28-32		203.48	993.34	ol gb	x	x			
80	82-2-18-21	1	204.18	992.72	ol-b gb	x	x			
		2	204.18	992.72	ol gb	x	x			
		3	204.19	992.71	gb	x	x			
		4	204.19	992.71	ol gb	x	x			
		5	204.21	992.69	ol-b gb	x	x			
81	1-82-3a		205.18	991.83	ox-b ol gb	x	x	x		
82	1-82-3b		205.25	991.78	ox-b ol gb	x	x	x	x	
83	1-82-3c		205.31	991.72	ox-b ol gb	x	x			
84	1-82-4a		206.08	991.04	ol gb	x	x			
85	1-82-4b	1	206.15	990.98	ol gb	x	x			
		2	206.16	990.97	gb	x	x			
		3	206.17	990.96	ol gb	x	x			
		4	206.18	990.95	ol gb	x	x			

		1	206.68	990.51	ol gb	x	x	x		
		2	206.70	990.49	gb	x	x	x		
		3	206.70	990.49	ol gb	x	x	x		
		4	206.71	990.49	ol-b gb	x	x	x		
		5	206.71	990.48	ol gb	x	x	x		
86	1-83-1	6	206.72	990.48	ol-b gb	x	x	x		
		7	206.72	990.47	ol gb	x	x	x		
		8	206.73	990.47	ol-b gb	x	x	x		
		9	206.73	990.47	ol gb	x	x	x		
		10	206.74	990.46	ol-b gb	x	x	x		
		11	206.74	990.46	ol gb	x	x	x		
		12	206.74	990.46	ol gb	x	x	x		
87	83-3-36-42		207.86	989.47	ol gb	x	x			
88	1-86-2a		213.30	984.67	ol gb	x	x	x		
89	1-86-2b	1	213.36	984.62	ol gb	x	x	x		
		2	213.38	984.60	ol gb	x	x	x		
90	1-86-2c	1	213.40	984.58	ol gb	x	x			
		2	213.42	984.56	ol-b gb	x	x			
91	88-1-64-72		218.84	979.78	ol-b gb	x	x			
92	88-1-92-97		219.12	979.53	ol gb	x	x			
93	88-3-49-55	1	220.50	978.31	we	x	x		x	x
		2	220.52	978.29	ol gb	x	x		x	x
94	1-88-3a		220.59	978.23	ol gb	x	x			
95	1-88-3b		220.65	978.17	gb	x	x		x	
96	1-88-3c		220.69	978.14	ol-ox-b gb	x	x	x		
97	88-4-20-26		221.07	977.81	ol gb	x	x			
98	89-2-41-46	1	222.39	976.64	tr	x	x			
		2	222.42	976.61	ol gb	x	x			
99	1-90-1		223.47	975.69	ol gb	x	x	x		
100	91-2-55-60		225.49	973.90	ol gb	x	x			
102	95-2-32-35		237.12	963.63	ol gb	x	x			
101	95-2-57-61	1	237.36	963.42	ol gb	x	x			
		2	237.38	963.41	we	x	x			
		3	237.39	963.40	ol gb	x	x			
103	95-3-12-23		237.75	963.08	ol gb	x	x			
104	OM-DP-BI-33		238.24	962.64	ol-b gb	x	x	x		
105	95-4-21-27		238.81	962.14	ol gb	x	x			
106	96-2-31-36		240.21	960.90	ol gb	x	x			
107	97-3-38-45		243.80	957.74	ol-b gb	x	x			
108	OM-DP-BI-35		245.23	956.48	ol gb	x	x	x		
109	98-3-76-85		247.36	954.60	ol gb	x	x			
110	1-100-1Aa		251.51	950.93	ol gb	x	x	x		
111	1-100-1Ab		251.57	950.88	ol-ox-b gb	x	x			
112	1-100-1Ac		251.62	950.83	ol gb	x	x	x		
113	1-100-1B		252.08	950.42	ol gb	x	x	x		

114	100-2-10-16		252.22	950.30	ol gb	x	x			
115	100-2-46-57		252.61	949.96	ol-b gb	x	x			
116	OM-DP-BI-38		264.12	939.80	gb	x	x	x		
117	109-3-44-57		276.09	929.23	ol gb	x	x			
118	1-110-1	1	276.44	928.92	ol gb	x	x			
		2	276.46	928.90	ol gb	x	x			
119	113-4-67-71		283.27	922.89	ol gb	x	x			
120	115-4-8.5-13		288.78	918.02	ol gb	x	x			
121	116-1-55-60		289.65	917.25	ol gb	x	x		x	
122	118-1-2-7		295.52	912.07	ol gb	x	x	x		
123	1-118-1a		295.74	911.87	ox-b ol gb	x	x	x		
124	1-118-1b		295.80	911.82	ol gb	x	x	x	x	
125	1-118-1c		295.86	911.77	ol gb	x	x			
126	120-4-38-42.5		304.25	904.36	ol gb	x	x			
127	OM-DP-BI-42		307.56	901.44	ol-b gb	x	x	x		
128	129-4-29-34		325.26	885.82	gb	x	x			
129	OM-DP-BI-45		334.55	877.61	gb	x	x			
130	134-1-52-56		338.72	873.93	gb	x	x			
131	1-137-3a		349.48	864.43	ol gb	x	x	x	x	x
132	1-137-3b	1	349.55	864.37	ol gb	x	x			
		2	349.57	864.35	ol gb	x	x			
133	138-3-46-50	1	352.40	861.85	ol gb	x	x			
		2	352.42	861.84	ol gb	x	x			
		3	352.30	861.94	ol gb	x	x			
134	140-3-55-59		358.65	856.33	gb	x	x			
135	OM-DP-BI-49		370.11	846.21	ol gb	x	x	x		
136	OM-DP-BI-50		375.49	841.46	ol gb	x	x	x		
137	147-4-56-60		377.80	839.43	ol gb	x	x			
138	148-1-60-64		378.45	838.85	ol gb	x	x			
139	149-1-3-8		380.93	836.66	we	x	x		x	
140	OM-DP-BI-51		383.58	834.32	ol gb	x	x	x		
141	151-1-62-67		387.62	830.75	gb	x	x			
142	152-2-65-68		391.45	827.37	we	x	x			
143	1-154-2		397.17	822.32	ol gb	x	x	x	x	

[a] domains were defined by significant changes in lithology, modal abundances, or texture

[b] Depth in bore hole in meters

[c] Height above the base of the mantle transition zone in meters, calculated with respect to the 28° tilt of the Wadi Tayin massif

[d] lithology defined from visual mode estimates, following the categorization given by Gillis et al. (2014b); an=anorthosite, gb=gabbro, ol-gb=olivine gabbro, tr=troctolite, we=wehrlite; "-b"=bearing (<5% abundance), am=amphibole, ol=olivine, ox=oxide

[e] analytical methods applied to the samples with PO = point counting, EPMA = electron probe micro analysis, EBSD = electron backscattered diffration, BRC = bulk rock chemistry, MC = mineral trace element chemistry; "n/a" indicates "not analyzed" due to strong alteration; dashed boxes mark sample pieces prepared for a single BRC analysis

Table S-3   Samples obtained from drill core GT2A and analytical methods applied to the samples.

#	thin section	D[a]	D[b] [m]	HaM[c] [m]	unit[d]	lithology[e]	Analytical methods[f]		
							PC	EPMA	EBSD
1	5-3-4-9		6.97	2688.03	FG	ox gb	x	x	x
2	10-2-50-55		12.77	2682.23	FG	gb	x	n/a	x
3	10-4-74-79	1	14.70	2680.30	FG		x	x	
		2	14.71	2680.29	FG		x	x	
		3	14.74	2680.26	FG		x	x	
4	2-12-2		18.60	2676.40	LG	gb	x	x	x
5	12-4-32-36		19.71	2675.29	FG		x	x	
6	14-2-21-26		24.63	2670.38	FG	gb	x	n/a	
7	14-4-52-55		26.52	2668.49	FG		x	x	x
8	14-4-74-78	1	26.71	2668.30	FG		x	x	
		2	26.72	2668.29	n/d		x	x	
		3	26.74	2668.27	FG		x	x	
9	2-15-1		27.31	2667.69	LG	am-b gb	x	x	x
10	15-4-32-36	1	29.41	2665.59	FG		x	x	
		2	29.44	2665.56	FG		n/a	n/a	
11	17-1-0-5		32.90	2662.10	FG	gb	x	x	x
12	17-1-59-64		33.49	2661.51	LG		x	x	
13	18-4-26-30	1	38.59	2656.41	LG		x	n/a	x
		2	38.62	2656.38	FG		x	n/a	x
14	2-20-3		44.63	2650.37	LG	am-b gb	x	x	x
15	20-4-4-9		44.87	2650.14	LG	gb	x	x	
16	2-21-3		47.34	2647.66	LG	am-b gb	x	x	x
17	2-24-3		56.01	2638.99	FG	am-b gb	x	x	x
18	25-2-9-14		58.07	2636.93	LG	ol gb	x	n/a	
19	2-27-5Aa		66.25	2628.75	FG	am-b gb	x	x	x
20	2-27-5Ab		66.31	2628.69	FG	ox-b gb	x	x	x
21	28-3-34-37		68.41	2626.60	LG		x	n/a	x
22	31-2-6-10		76.60	2618.41	n/d		x	n/a	
23	2-31-3		77.49	2617.52	FG	am-b gb	x	x	x
24	32-2-73-78		80.20	2614.81	FG	gb	x	x	
25	32-3-49-54	1	80.93	2614.07	FG		n/a	x	
		2	80.96	2614.04	n/d		n/a	n/a	
26	2-35-2		89.22	2605.78	FG	am-b gb	x	x	
27	2-35-3		90.02	2604.98	LG	ol gb	x	x	x
28	36-3-15-20		92.74	2602.26	LG	ol gb	x	n/a	
29	36-5-0-5		93.72	2601.29	LG	ol gb	x	x	
30	40-4-52-57		105.73	2589.27	n/d	we	n/a	x	
31	42-1-36-38		109.51	2585.49	LG		n/a	n/a	
32	2-43-3	1	114.77	2580.24	LG	gb	x	x	x
		2	114.79	2580.21	LG	ol gb	x	x	x

33	44-3-48-53		117.20	2577.80	FG		n/a	x	
34	2-46-1Aa		118.63	2576.37	LG	ol gb	x	x	
35	2-46-1Ab		118.70	2576.30	LG	am-b ol gb	x	x	
36	46-1-63-66		118.93	2576.07	LG		n/a	x	
		1	118.91	2576.09	LG	am-b ol gb	x	x	
37	2-46-1Ca	2	118.93	2576.07	LG	gb	x	x	
		3	118.94	2576.06	LG	ol gb	x	x	
38	2-46-1Cb		118.98	2576.02	LG	ol gb	x	x	
39	2-46-3		119.85	2575.15	LG	am-b ol gb	x	x	x
40	48-2-62-65		126.00	2569.01	LG		x	x	
41	51-2-81-84	1	135.23	2559.78	LG		x	x	
		2	135.25	2559.76	LG		x	x	
42	52-2-43-48		137.86	2557.14	LG	gb	x	x	x
43	53-1-7-12		139.72	2555.28	LG		x	x	
44	53-2-30-35		140.81	2554.20	LG		x	x	
45	53-2-69-74		141.20	2553.81	LG		x	x	
46	55-4-44-49		148.64	2546.36	LG		x	x	x
47	56-2-43-48		150.09	2544.91	n/d	we	x	x	
48	56-3-67-72		151.05	2543.96	LG		x	x	
49	57-1-6-11		151.30	2543.70	LG		x	x	
50	57-1-73-78		151.53	2543.47	LG	an	x	x	
51	63-1-35-40		158.30	2536.70	LG	n/d	n/a	x	
52	63-2-12-16		159.07	2535.93	LG		x	x	
53	63-3-50-55		160.44	2534.57	LG		x	x	x
54	64-1-46-50		161.46	2533.54	LG		x	x	
55	66-3-13-18		168.97	2526.03	LG	ol gb	x	x	x
56	67-3-56-59	1	172.68	2522.32	LG	ol gb	x	x	
		2	172.71	2522.29	LG	ol gb	x	x	
57	2-68-1		173.72	2521.28	FG	gb	x	x	
58	70-2-47-52		180.54	2514.46	FG	gb	x	x	x
59	72-3-55-60		187.41	2507.60	FG	gb	x	x	
60	74-2-14-19		192.58	2502.43	LG	ol gb	x	x	
61	74-4-0-3		194.00	2501.01	LG		x	x	
62	75-2-0-5	1	195.43	2499.57	n/d	we	x	x	
		2	195.46	2499.54	LG	ol gb	x	x	
63	75-2-7-12		195.51	2499.49	FG		x	x	
64	2-75-2A	1	195.81	2499.19	LG	ol-b gb	x	x	x
		2	195.83	2499.17	LG	am-ox-b ol gb	x	x	x
		3	195.84	2499.16	LG	ol gb	x	x	x
65	2-75-2Ca	1	195.86	2499.14	FG	ol-b gb	x	x	
		2	195.89	2499.11	FG	ol gb	x	x	

#	Sample								
66	2-75-2Cb		195.93	2499.07	FG	ol gb	x	x	
67	75-3-47-52	1	196.70	2498.31	LG	ol-b gb	x	x	
		2	196.71	2498.29	n/d	an	x	x	
		3	196.73	2498.28	LG	ol gb	x	x	
68	76-4-38-43		200.41	2494.59	LG		x	x	
69	2-77-3	1	202.40	2492.60	FG	gb	x	x	x
		2	202.42	2492.58	LG	ol gb	x	x	x
70	78-4-17-22		206.40	2488.61	LG	ol gb	x	x	
71	2-79-2	1	207.45	2487.55	LG	ol gb	x	x	x
		2	207.65	2487.35	LG	gb	x	x	x
72	81-4-38-43	1	215.67	2479.33	n/d	we	x	x	
		2	215.71	2479.29	LG	ol-b gb	x	x	
73	2-83-3Aa		221.53	2473.47	LG	ol gb	x	x	x
74	2-83-3Ab		221.59	2473.41	LG	ol gb	x	x	
75	2-83-3Ac		221.65	2473.35	LG	ol gb	x	x	
76	2-87-4A	1	233.65	2461.35	LG	ol gb	x	x	x
		2	233.67	2461.33	LG	ol-b gb	x	x	x
77	2-87-4B		234.02	2460.98	LG	ol gb	x	x	
78	2-88-1A		234.22	2460.78	LG	gb	x	x	
79	2-88-1Ba		234.47	2460.53	LG	ol-b gb	x	x	
80	2-88-1Bb		234.54	2460.46	LG	ol gb	x	x	x
81	89-2-7-10		238.03	2456.97	LG		n/a	n/a	
82	94-2-53-61	1	253.66	2441.34	n/d	an	x	x	x
		2	253.70	2441.30	LG	ol-gb	x	x	x
83	95-2-72-80		257.29	2437.72	LG		x	x	
84	95-4-22-25		258.32	2436.69	n/d	we	x	x	
85	98-1-41-49		262.06	2432.94	LG	ol gb	x	n/a	
86	99-3-56-64	1	266.53	2428.47	FG	ol gb	x	n/a	x
		2	266.55	2428.45	LG	gb	x	x	x
		3	266.57	2428.43	FG	ol gb	x	x	x
87	102-3-37-42		275.96	2419.05	LG	gb	x	x	x
88	103-2-58-63		278.39	2416.62	LG		x	x	
89	110-1-0-8		295.20	2399.80	LG		x	x	
90	111-2-3-7		299.13	2395.87	LG		n/a	n/a	
91	112-3-14-20		303.28	2391.73	LG	am-b ox-ol gb	x	n/a	x
92	114-3-4-12		306.08	2388.93	FG	ol-b gb	x	x	x
93	2-115-1	1	308.16	2386.84	FG	ol gb	x	x	
		2	308.18	2386.82	FG	ol-b gb	x	x	
94	117-1-58-66		314.08	2380.92	LG		x	x	
95	2-117-2		314.75	2380.25	LG	am-b ol gb	x	x	x

166

96	118-1-74-79	1	317.28	2377.73	FG		x	x	
		2	317.29	2377.71	FG		x	x	
		3	317.32	2377.69	FG		x	x	
97	2-119-1	1	319.07	2375.93	LG	ol-b gb	x	x	x
		2	319.09	2375.91	LG	(ox-b?) ol gb	x	x	x
		3	319.10	2375.90	FG	ol gb	x	x	x
98	2-120-2A		321.05	2373.95	FG	ol gb	x	x	x
99	2-120-2B		321.21	2373.79	FG	ol gb	x	x	x
100	2-120-3Aa		321.26	2373.74	FG	ol gb	x	x	
101	2-120-3Ab	1	321.29	2373.71	FG	ol-b gb	x	x	x
		2	321.31	2373.69	FG	ol gb	x	x	x
		3	321.33	2373.67	FG	ol gb	x	x	x
102	120-4-20-28		322.16	2372.85	LG		x	x	
103	121-1-38-43		323.03	2371.97	FG		x	x	
104	125-4-59-65		334.81	2360.19	FG	ox-ol gb	x	x	x
105	2-127-1Aa		338.35	2356.65	LG	(ox-b?) ol gb	x	x	x
106	2-127-1Ab		338.40	2356.60	LG	(ox-b?) ol-b gb	x	x	
107	2-127-1Ac		338.46	2356.54	LG	(ox-b?) ol-b gb	x	x	
108	2-127-1C	1	338.46	2356.54	FG	ol-gb	x	x	x
		2	338.48	2356.52	FG	gb	x	x	x
		3	338.50	2356.50	FG	(ox-b?) ol gb	x	x	x
109	2-133-4A	1	352.25	2342.75	FG	gb	x	x	
		2	352.27	2342.73	FG	ol gb	x	x	
		3	352.29	2342.71	FG	gb	x	x	
110	2-133-4Ba		352.39	2342.61	FG	gb	x	x	
111	2-133-4Bb		352.45	2342.55	FG	(ox-b?) ol-b gb	x	x	
112	2-133-4Bc		352.51	2342.49	FG	(ox-b?) ol gb	x	x	x
114	134-3-53-61		355.27	2339.73	FG	ol-b gb	x	x	
115	136-1-5-12		359.30	2335.70	FG		x	x	
116	137-2-8-14	1	363.16	2331.85	FG		x	x	
		2	363.17	2331.83	LG		x	x	
		3	363.19	2331.81	FG		x	x	
117	138-1-8-13		365.43	2329.57	n/d	we	x	x	
118	138-1-22-30	1	365.57	2329.44	FG	(ox-b?) gb	x	x	
		2	365.57	2329.43	FG	(ox-b?) gb	x	x	
		3	365.59	2329.41	FG	(ox-b?) gb	x	x	
113	2-138-4	1	368.22	2326.78	FG	gb	x	x	x
		2	368.24	2326.76	FG	gb	x	x	x
		3	368.26	2326.74	FG	gb	x	x	x
119	139-3-3-8	1	369.90	2325.10	FG	gb	x	x	x
		2	369.92	2325.09	n/d	px	x	x	x
		3	369.93	2325.07	FG	gb	x	x	x

120	142-1-75-82		378.30	2316.70	FG		x	x	
121	142-2-19-27		378.60	2316.40	n/d	we	x	x	
122	142-4-71-76	1	380.65	2314.36	n/d		x	x	x
		2	380.67	2314.33	FG		x	n/a	x
123	144-3-62-66		385.62	2309.38	n/d	we	x	x	
124	144-3-72-80		385.72	2309.28	FG		x	x	
125	147-2-71-76	1	394.42	2300.59	LG		x	x	
		2	394.43	2300.58	n/d		x	x	
		3	394.44	2300.56	LG		n/a	x	
126	147-3-64-70	1	395.16	2299.84	FG		x	n/a	
		2	395.18	2299.82	FG		n/a	n/a	
		3	395.19	2299.81	FG		x	n/a	
127	148-2-60-66		397.35	2297.66	FG		x	n/a	
128	148-4-19-26	1	398.45	2296.55	LG		n/a	n/a	
		2	398.46	2296.54	LG		x	x	
		3	398.48	2296.52	LG		x	x	
129	151-1-37-42		404.62	2290.38	LG	we	n/a	x	
130	151-2-19-24	1	405.30	2289.71	LG	ol gb	x	x	
		2	405.31	2289.69	LG	ol gb	x	x	
		3	405.33	2289.68	n/d	we	x	x	

[a] domains were defined by significant changes in lithology, modal abundances, or texture

[b] Depth in bore hole in meters

[c] Height above the base of the mantle transition zone in meters, calculated with respect to the 28° tilt of the Wadi Tayin massif

[d] crustal unit with FG=foliated gabbro and LG=layered gabbro, visually defined by overall grain size; "n/d" indicates "not defined" due to heterogeneous grain size distributions or non-gabbroic lithologies

[e] lithology defined from visual mode estimates, following the categorization given by Gillis et al. (2014b); an=anorthosite, gb=gabbro, ol-gb=olivine gabbro, tr=troctolite, we=wehrlite; "-b"=bearing (<5% abundance), am=amphibole, ol=olivine, ox=oxide

[f] analytical methods applied to the samples with PO = point counting, EPMA = electron probe micro analysis, EBSD = electron backscattered diffration; "n/A" indicates not analyzed due to strong alteration

Electronic supplement

Analytical data acquired during this study are available as electronic supplement to the thesis.

Curriculum Vitae

Personal details

Name	Dominik Mock
Date of Birth	12.08.1990
Place of Birth	Trier
Citizenship	German

Work experience

07/2017 – today   Research Assistant
Institut für Mineralogie, Leibniz Universität Hannover, Germany

10/2014 – 07/2017   Student Assistant
Institute für Mineralogie und Geologie, Leibniz Universität Hannover

05/2014 – 06/2014   Intern
Géosciences Montpellier, Centre national de recherches scientifique

Education

07/2017 – today   PhD student
Leibniz Universität Hannover und Université de Montpellier
Thesis: „Magmatic Processes at Various Scales in the Lower Crust of the Samail Ophiolite (Sultanate of Oman)"

10/2014 – 04/2017   Master's studies in Earthsciences with focus on Mineralogy/Geochemistry
Leibniz Universität Hannover
Thesis: "Microanalytical and microstructural investigations on the layering of two gabbro sections in the Oman ophiolite"

10/2011 – 12/2014   Bachelor's studies in Earthsciences
Leibniz Universität Hannover
Thesis: "Einfluss von Anorthitkomponenten auf die Position des eutektischen Punktes im haplogranitischen System bei 200 MPa"

08/2000 – 03/2009   Abitur
Hindenburg Gymnasium Trier, Trier, Germany

List of Publications

Journal Articles

Mock, D., Neave, D., Müller, S., Garbe-Schönberg, D., Namur, O., Ildefonse, B., & Koepke, J. (2020). Formation of igneous layering in the lower oceanic crust from the Samail Ophiolite, Sultanate of Oman. Journal of Geophysical Research: Solid Earth, e2020JB019573.

Mock, D., Ildefonse, B., Müller, T., & Koepke, J. (2021). A reference section through fast-spread lower oceanic crust, Wadi Gideah, Samail Ophiolite (Sultanate of Oman): Insights from Crystallographic Preferred Orientations. Journal of Geophysical Research: Solid Earth, e2021JB021864.

Koepke J., Müller, S., Garbe-Schönberg, D., Müller, T., **Mock D.**, & Nasir, S. A reference section through fast-spreading lower oceanic crust, Wadi Gideah, Samail Ophiolite: petrography and petrology. *submitted to Journal of Geophysical Research: Solid Earth*

Garbe-Schönberg, D., Koepke J., Müller, S., **Mock D.**, & Müller, T. A reference section through fast-spread lower oceanic crust, Wadi Gideah, Samail Ophiolite (Sultanate of Oman): Whole rock geochemistry. *submitted to Journal of Geophysical Research: Solid Earth*

Conference Poster

DFG IODP/ICDP Colloquium 2018
D. Mock, B. Ildefonse, D. Garbe-Schönberg, S. Müller, D.A. Neave, J. Koepke, and the Oman Drilling Project Phase 1 Science Party. Understanding lower crust accretion at fast-spreading mid-ocean ridges: new insights from drill cores obtained by the ICDP Oman Drilling Project: First Results

DFG IODP/ICDP Colloquium 2019
D. Mock, B. Ildefonse, D. Garbe-Schönberg, S. Müller, D.A. neave, J. Koepke, and the Oman Drilling Project Phase 1 Science Party. New Insights into Lower Crustal Accretion at Fast-Spreading Mid-Ocean Ridges – Petrological and Microstructural Results from the ICDP Oman Drilling Project

AGU conference 2020
D. Mock, B. Ildefonse, T. Müller, J. Koepke, and the Oman Drilling Project Science Team. Crystallographic preferred orientations in Wadi Gideah (Oman) – refining a reference profile along lower oceanic crust

DMG virtual poster session 2020
Mock, D., Neave, D.A., Müller, S., Garbe-Schönberg, D., Namur, O., Ildefonse, B., Koepke, J. How does layering in lower oceanic crust form? A high-resolution study

Conference Talks

AGU conference 2016
B. Ildefonse, T. Müller, **D. Mock**, J. Koepke. Formation of fast-spread ocean crust: crystallographic preferred orientations from a reference lower crust section in the Oman ophiolite

DFG IODP/ICDP Colloquium 2017
J. Koepke, D. Garbe-Schönberg, S. Müller, **D. Mock**, and the Oman Drilling Project Science Team. Report from the ICDP Oman Drilling Project: Phase 1 is in progress

Annual DMG Meeting GeoBremen 2017
D. Mock, B. Ildefonse, J. Koepke, T. Müller, D. Garbe-Schönberg. Oman Drilling Project: Crystallographic preferred orientations as indicator for lower crustal formation at fast-spreading mid-ocean ridges – The Wadi Gideah transect

Annual DMG Meeting GeoBremen 2017
J. Koepke, D. Garbe-Schönberg, S. Müller, **D. Mock**, and the Oman Drilling Project Science Team. Progress in the ICDP Oman Drilling Project

AGU conference 2017
J. Koepke, D. Garbe-Schönberg, T. Müller, S. Müller, **D. Mock**, H. Strauss, S. Schuth, B. Ildefonse. A Reference Section through the Lower Fast-spreading Oceanic Crust in the Wadi Gideah (Sumail ophiolite, Sultanate Oman): Drill Sites GT1A and GT2A within the ICDP Oman Drilling Project

Annual DMG Meeting GeoBonn 2018
D. Mock, B. Ildefonse, D. Garbe-Schönberg, S. Müller, K. Faak, O. Namur, J. Koepke. What Causes the Layering of Gabbros? – A Microanalytical and Microstructural Investigation on the Layering of two Gabbro Sections in the Oman Ophiolite

Annual DMG Meeting GeoBonn 2018
J. Koepke, D. Garbe-Schönberg, T. Müller, S. Müller, **D. Mock**, H. Strauss, S. Schuth, B. Ildefonse. Wadi Gideah (Sumail Ophiolite, Sultanate Oman): A reference section through the lower fast-spreading oceanic crust

Annual DMG Meeting GeoMünster 2019
D. Mock, B. Ildefonse, D. Garbe-Schönberg, S. Müller, D. A. Neave, J. Koepke. On the formation of oceanic layered gabbros: drillcore GT1 of the ICDP Oman Drilling Project

Annual DMG Meeting GeoMünster 2019
J. Koepke, D. Garbe-Schönberg, S. Müller, **D. Mock**, and the Oman Drilling Project Science Team. The ICDP Oman Drilling Project: a status report

International Conference on Ophiolites and Oceanic Lithosphere 2020
D. Mock, B. Ildefonse, D. Garbe-Schönberg, S. Müller, D.A. Neave, J. Koepke, and the Oman Drilling Project Phase 1 Science Party. Drillcore GT1 of the ICDP Oman Drilling Project: Implications from the Layered Gabbros on the Accretion of Lower Oceanic Crust

International Conference on Ophiolites and Oceanic Lithosphere 2020
J. Koepke, D. Garbe-Schönberg, T. Müller, S. Müller, **D. Mock**, S. Schuth, B. Ildefonse. A Reference

Section through the lower crust in the Wadi Gideah (Sumail ophiolite, Sultanate Oman): the crustal drill sites within the ICDP OmanDP and related work

International Conference on Ophiolites and Oceanic Lithosphere 2020
D. Garbe-Schönberg, S. Müller, T. Müller, E. Wolff, **D. Mock**, and Jürgen Koepke. A geochemical reference profile through (paleo)oceanic crust: The Wadi Gideah Transect (Oman Ophiolite)

GeoUtrecht 2020
D. Mock, B. Ildefonse, D. Garbe-Schönberg, S. Müller, D.A. Neave, J. Koepke, and the Omand Drilling Project Phase 1 Science Party. Drillcore GT1 of the ICDP Oman Drilling Project: insights into magmatic processes beneath fast-spreading mid-ocean ridges

EGU conference 2021
D. Mock, D. A. Neave, S. Müller, D. Garbe-Schönberg, B. Ildefonse, J. Koepke, and the Oman Drilling Project Science Team. Accretion of fast-spread lower oceanic crust: drill core GT1 from the ICDP Oman Drilling Project

DMG Annual meeting of the section Petrology and Petrophysics 2021
Mock, D., Neave, D.A., Müller, S., Garbe-Schönberg, D., Ildefonse, B., Koepke, J. Rhythmic fracionation trends in lower layered gabbros: Evidence from hole GT1 Oman Drilling Project

European Mineralogical Conference 2021 (September)
D. Mock, D. A. Neave, S. Müller, D. Garbe-Schönberg, B. Ildefonse, J. Koepke, and the Oman Drilling Project Science Team. Sill intrusions in lower oceanic crust: Implications from drill core GT1 of the Oman Drilling Project

GeoKarlsruhe 2021 (September)
D. Mock, D. A. Neave, S. Müller, D. Garbe-Schönberg, B. Ildefonse, J. Koepke, and the Oman Drilling Project Science Team. The ICDP Oman Drilling Project – Implications from drill core GT1 on magmatic processes beneath fast-spreading mid-ocean ridges

GeoKarlsruhe 2021 (September)
J. Koepke, D. Garbe-Schönberg, **D. Mock**, S. Müller, and the Oman Drilling Project Science Team. A profile through ancient fast-spreading oceanic crust in the Wadi Gideah, Oman ophiolite – reference frame for the crustal drillings within the ICDP Oman Drilling Project